Passive Optical Bandwidth Control of Quasi-Phase Matched Optical Parametric Oscillators

Philip Schlup

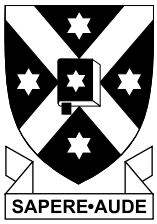

A thesis submitted for the degree of

Doctor of Philosophy

At the University of Otago, Dunedin,
New Zealand

February 2003

Abstract

Passive techniques for optical bandwidth control, in the form of intracavity frequency selective elements, were investigated in quasi-phase matched optical parametric oscillators (OPOs). When pumped by narrowband laser sources, periodically poled $LiNbO_3$ (PPLN) and periodically poled $KTiOPO_4$ (PPKTP) OPOs were operated on a single longitudinal mode with optical bandwidths typically below 250 MHz, limited by the resolution of the detection system. Two configurations were developed: intracavity étalons, and grazing incidence diffraction gratings.

Compared to free running OPOs, the insertion of an intracavity étalon approximately doubled the oscillation threshold, but yielded similar slope efficiencies. A 1.064 μm pumped étalon narrowed PPLN OPO generated up to 130 μJ broadband and 83 μJ single longitudinal mode signal pulse energy, while the output energy of a 532 nm pumped PPKTP OPO was reduced from 149 μJ to 44 μJ on insertion of an étalon. The étalon used to became ineffective in reducing the optical bandwidth when the gain bandwidth of the OPO diverged close to degeneracy.

The diffraction grating at grazing incidence (Littman–Metcalf) configuration was successfully applied to PPLN and PPKTP OPOs to yield single longitudinal mode operation. The high effective output coupling and long cavity lengths yielded high oscillation thresholds so that the OPOs could be operated only to around 1.5 times threshold. Single mode signal pulse energies of 150 μJ and 370 μJ were measured in PPLN and PPKTP OPOs. A large aperture PPKTP optical parametric amplifier (OPA) was used to generate 2.15 mJ of signal radiation at 1.69 μm, and 1.18 mJ of idler at 2.88 μm. A solid state dye laser amplifier generated 115 μJ single longitudinal mode radiation at 615 nm. The spectral behaviour of a 532 nm pumped monolithic PPLN OPO was investigated by injection seeding using a single mode semiconductor diode laser.

A diode pumped, high repetition rate Nd : YAG pump source was constructed and used to pump high repetition rate PPLN OPOs. The free running laser optical bandwidth was reduced to two longitudinal modes separated by 600 MHz using a passive prelase technique and an intracavity étalon. The laser, which generated 10.7 W power

under free running, continuous wave (cw) conditions, provided 400 μJ at 1.064 μm when Q-switched at 5 kHz, and 300 μJ at 532 nm when Q-switched at 1 kHz and frequency doubled in LiB_3O_5.

Thermal lensing of a diode pumped cw $Nd:YVO_4$ laser with intracavity periodically poled $RbTiOAsO_4$ OPO was investigated. The thermal lensing was found to be most significantly influenced by thermal loading of the pump radiation in the laser rod. Using resonator modelling, a system insensitive to thermal lensing in both laser and nonlinear optical crystals was designed, yielding improved idler output power stability. The intracavity singly resonant OPO generated up to 215 mW one-way idler at 3.50 μm.

Contents

List of Figures

List of Tables

List of Symbols

Roman Symbols

Sym.	Definition	Units	Page
$\mathbf{B}$	Magnetic flux density	$\mathrm{Wb/m^2}$	32
$\mathbf{D}$	Electric displacement, $\mathbf{D} = \varepsilon_0 \varepsilon_r \mathbf{E} + \mathbf{P}$	$\mathrm{C/m^2}$	32
d	Nonlinear optical coefficient; d_{ijk} tensor notation; d_{il} reduced notation; d_{eff} effective value	$\mathrm{m/V}$	30
d	Spacing of diffraction grating grooves	m	57
$\mathbf{E}$	Electric field; $E = \lvert\mathbf{E}\rvert$ magnitude of field vector	$\mathrm{V/m}$	30
$\lvert\mathcal{E}\rangle$	Atomic quantum state with energy $\mathcal{E}$	—	14
$\mathcal{F}$	Etalon finesse, $\mathcal{F} = \pi\sqrt{R}/(1-R)$	—	54
g_i	Atomic level degeneracy factor	—	14
$\mathbf{H}$	Magnetic field	$\mathrm{A/m}$	32
$\mathbf{h}$	Heat flux	$\mathrm{W/m^2}$	21
I	Intensity of electromagnetic wave, $I = \frac{1}{2} n \varepsilon_0 \lvert E\rvert^2$	$\mathrm{W/m^2}$	14
I_{sat}	Saturation intensity, $I_{\mathrm{sat}} = \hbar\omega/\sigma\tau_2$	$\mathrm{W/m^2}$	14
$\mathbf{k}$	Wavevector of plane wave, $\lvert\mathbf{k}\rvert = 2\pi n/\lambda$	$\mathrm{m^{-1}}$	32
Δk	Wave vector mismatch, $\Delta k = k_3 - k_2 - k_1$; for quasi-phase matched interaction $\Delta k_{\mathrm{QPM}} = k_3 - k_2 - k_1 - 2\pi m/\Lambda$	$\mathrm{m^{-1}}$	33
L	Passive cavity round trip loss coefficient	—	16
L	Nonlinear optical crystal length	m	34
L_c	Resonator cavity length	m	15
L'	Optical cavity length	m	55
L_g	Diffraction grating length	m	58
l_c	Laser crystal length	m	15
M	Number of cavity round trips	—	52
M^2	Beam quality parameter	—	28
$\mathbf{M}$	Ray transfer matrix	—	26
m	Diffraction order; QPM interaction order	—	37
N	Atomic population inversion density; N_i initial inversion density, population density of state i; N_{thr} threshold inversion density	$\mathrm{m^{-3}}$	14
N	Number of illuminated grooves of diffraction grating	—	56

Sym.	Definition	Units	Page
n	Index of refraction; of uniaxial crystal, n_o ordinary, n_e extraordinary; of biaxial crystal, n_x, n_y, n_z along dielectric axes x, y, z	—	32
P	Power; P_{abs} absorbed pump power; P_{out} output power	W	14
$\mathbf{P}$	Polarisation, $P = \lvert\mathbf{P}\rvert$ magnitude of polarisation	C/m^2	30
Q	Thermal heat load, $Q = \nabla \cdot \mathbf{h}$	W/m^3	21
q	Complex beam parameter, $1/q = 1/R - i\lambda/\pi w^2$	m	27
R	Power reflectivity of mirror	—	16
R	Wavefront radius of curvature	m	27
R_p	Atomic pumping rate density	$\text{m}^{-3}\text{s}^{-1}$	14
T	Temperature, temperature distribution	K	21
U	Pulse energy	J	17
V	Volume; V_p pump volume	m^3	14
w	Beam spot size, radius to $1/e^2$ level	m	27

Greek Symbols

Sym.	Definition	Units	Page
α	Absorption or loss coefficient per unit length	m^{-1}	16
α_{Th}	Linear thermal expansion coefficient	K^{-1}	22
β_{ji}	Group velocity index dispersion, $\beta_{ji} = c(dk_j/d\omega - dk_i/d\omega)$	—	52
Γ	Parametric gain coefficient, $\Gamma^2 = \kappa I$	m^{-1}	34
γ	Gain coefficient per unit length	m^{-1}	16
γ_0	Small-signal laser gain coefficient, $\gamma_0 = \sigma\tau_2 R_p$	m^{-1}	16
θ	Angle; θ_i incidence angle; θ_t internal angle; θ_m diffracted angle	rad	54
κ	Nonlinear optical interaction coefficient, $\kappa = 2\omega_1\omega_2 d_{\text{eff}}^2/n_1 n_2 n_3 \varepsilon_0 c^3$	W^{-1}	34
κ_{Th}	Thermal conductivity	W/m K	21
λ	Wavelength	m	15
σ	Transition cross-section	m^2	14
τ_i	Characteristic lifetime, τ_{ji} lifetime between states j and i	s	14
τ_c	Cavity photon lifetime	s	16
τ	Pulse duration	s	38
$\chi^{(2)}$	Second-order nonlinear optical susceptibility tensor	m/V	30
ω	Angular frequency	rad/s	14
ω_{21}	Atomic transition frequency, $\hbar\omega_{21} = \mathcal{E}_2 - \mathcal{E}_1$	rad/s	14
$\Delta\omega$	Spectral acceptance bandwidth; $\Delta\omega_c$ crystal gain bandwidth; $\Delta\omega_f$ filter pass bandwidth; $\Delta\omega_{\ldots,M}$ multiple pass bandwidth	rad/s	41

Chapter 1

Introduction

Nonlinear optical frequency conversion has become established as an important tool for accessing wavelengths that cannot be generated by conventional laser sources. In particular, optical parametric oscillators (OPOs), such as those investigated in this thesis, provide tuneable radiation in the near to mid-infrared spectral region, which includes important molecular absorption features, and also has potential applicability in the areas of fibre optics, telecommunications, atmospheric and remote sensing, and infrared countermeasures. The high nonlinearity of materials such as periodically poled $LiNbO_3$ (PPLN) and $KTiOPO_4$ (PPKTP) make these attractive for compact, efficient sources with emission energies in the 100 μJ to 10 mJ range. However, the free running gain bandwidths of OPOs are often too broad for certain applications, particularly high resolution spectroscopy, so that optical bandwidth control measures must be implemented.

In this thesis, passive methods of optical bandwidth control, using intracavity étalons and diffraction gratings applied to quasi-phase matched OPOs, are reported. The work represents initial investigations and includes several first reports of these techniques in OPOs based on PPLN and PPKTP. The publication of similar investigations by other authors during the course of the work attested to the relevance and timeliness of this research.

1.1 Lasers

The OPO laser pump source influences many aspects of the OPO performance, including the spectral and temporal characteristics of the output as well as the efficiency of the system. The invention of the laser, first demonstrated in 1960, has had a tremendous impact on society, from providing scientists with a powerful new tool to probe the chemical and physical composition and behavioural characteristics of materials, to making digital en-

tertainment media and high-speed telecommunications links commonplace and readily affordable. From the initial demonstration of amplification by stimulated optical emission in a flashlamp pumped ruby ($Cr:Al_2O_3$) laser [1], a wide variety of laser gain media have been developed, each with unique characteristics making them suitable for different applications. These include gas discharge lasers such as CO_2, Ar^+, and transition metal vapour lasers that typically, with the notable exception of the helium–neon laser, give high continuous-wave (cw) powers but require large discharge tubes; liquid dye lasers, offering wide tunability and high gain at the expense of somewhat complex system architectures; and solid state lasers including semiconductor diodes and transition metal ion doped media like Nd : YAG, used in the work presented here, and Ti : sapphire.

Solid state lasers based on ionic impurities doped into crystalline or amorphous hosts commonly include the trivalent ions Nd, Ti, Cr, Er, Yb, Ho, and Tm, doped into hosts such including YAG, YLF, YVO_4, sapphire, and various glasses [2]. The spectroscopic characteristics of the laser gain medium are determined principally by the active ion impurity, modified by the host field (see, for example, figure 2.5 on page 24), while the host dictates the mechanical and thermal properties as well as possible mechanical configurations. These are often chosen based on thermal management considerations arising from heat deposited by pump sources, with microchips, fibres, rods, and slabs providing relatively efficient heat removal for increasing power levels.

Nd : YAG

Nd : YAG, emitting at 1.064 μm, has become one of the most widely used solid state laser media and has been successfully applied to operating regimes including cw and various laser pulsing strategies such as Q-switching, and modelocking [2, 3]. Due to a combination of good optical and thermo-mechanical characteristics, efficient, high power Nd : YAG lasers are useful for numerous applications including material processing, tissue manipulation, and laser ranging. Nd : YAG is an important pump source for both laser and nonlinear optical frequency conversion chains such as those used in this work; modest, diode pumped frequency doubled systems have recently been demonstrated to offer a viable alternative to Ar^+ lasers as an optical pump source [4]. Besides the strong 1.064 μm Nd : YAG transition, useful output powers have been recently demonstrated at 946 nm [5, 6], 1.123 μm [7, 8], and 1.33 μm [9].

Pulsed laser operation allows access to high peak powers with modest average powers and pump requirements. Active Q-switching and modelocking has been routinely used for many years [2], including in commercial systems such as the pump lasers used in chapters 5, 6, and 7, and recent research has focused on advanced methods in active

and passive Q-switching and modelocking. A form of prelase Q-switching, initially developed by Hanna *et al.* [10], was used in the laser constructed in chapter 7. In this technique, a partially opened Q-switch allows a cw field to build up before the laser pulse, resulting in narrowband, or even single longitudinal mode [11–13], self seeded pulses with reduced temporal jitter, improved polarisation characteristics [14], and actively damped relaxation oscillations that permit higher repetition rates [15]. Passive Q-switching by saturable absorption yields particularly simple system configurations with no active elements. The saturable absorber typically takes the form of an unpumped laser material, such as Cr^{4+}: YAG [16–19]. The laser pulse repetition frequency and pulse energy are in this case governed by the interplay between the population dynamics of the saturable absorber and laser gain medium [16, 20–22]. Passive Q-switching was tested in this work, but unsuccessfully, and no results are presented.

The performance of Nd : YAG lasers may be adversely affected by energy transfer upconversion [23, 24], excited state absorption [20, 21, 25], the formation of colour centres [26], and, more commonly, thermal lensing [6, 24, 27–32]. The refractive index, thermal conductivity, and thermal expansion coefficients of Nd : YAG have unfavourable temperature dependence [24, 33], and strong thermal lensing and depolarisation losses may be observed under high thermal loading. Improved performance is typically observed with more efficient cooling of the laser rod, or operation at cryogenic temperatures. Thermal lensing effects are discussed in section 2.1.

These thermal issues in Nd : YAG have contributed to interest in research of other laser media. Nd : YLF [34, 35] has similar gain due to an almost identical $\sigma\tau_2$ product, but a lower susceptibility to thermal lensing and reduced depolarization losses due to natural birefringence [36, 37]. A long upper state lifetime and low thermal lensing of Nd : YLF make it an attractive material for multiwatt diode-pumped, Q-switched solid-state lasers with good beam quality [24], such as the high repetition rate laser developed in chapter 7. Although Nd : YLF rods were tested in that laser, catastrophic crystal damage prevented the application of the Nd : YLF laser as a pump source for OPOs. For cw lasers emitting in the $\sim$10 W range, such as the laser head used in chapter 8, Nd : YVO_4 has been found to be superior to Nd : YAG, primarily due to a high stimulated emission cross-section and strong absorption of semiconductor diode pump lasers [38]. This has facilitated the development of ultracompact microchip and mini lasers [39] and stimulated interest in lower doping concentrations [40, 41]. Despite the short upper state lifetime, Nd : YVO_4 may also be Q-switched, with Du *et al.* [42] recently demonstrating 5.6 mJ pulses at 10 kHz from an electro-optically Q-switched Nd : YVO_4 laser.

Semiconductor Diodes

Solid state semiconductor diode lasers offer high electrical to optical efficiencies, and choice of the semiconductor composition, typically combinations of In, Ga, Al, As, and P, permits the emission wavelength to be selected. Common wavelengths include 635–670 nm, 780 nm, 808 nm, 980 nm, 1.3 μm, and 1.5 μm. Of particular importance to this work are the InGaAlAs diodes emitting around 808 nm, which may be used to diode pump Nd : YAG on a strong absorption peak (see figure 2.6 on page 25) with high efficiency and modest thermal loading [9, 43]. Catastrophic material damage due to heating often limits the power emitted by single diode junctions to a few hundred mW, but arrangement into arrays, bars, and stacks offers a convenient pathway to power scaling. Current state of the art 100 W cw diode bars available are from Coherent Inc. Beam confinement within the short resonators results in diode lasers emitting astigmatic and highly diverging beams, so that beam reshaping is normally required for pumping solid state lasers. Fibre coupling of diode bars offers benefits including beam reshaping, isolation of thermal loads, and convenient replacement of pump source, such as in the lasers described in chapters 7 and 8. In addition, 635 nm AlGaInP diodes were used separately to injection seed a monolithic OPO, as outlined in section 7.3. Before the advent of diode pumping, lamp pumping of Nd : YAG lasers employed Xe, Kr or tungsten-iodide arc or flashlamps [2], and the pump source used in chapters 5, 6, and 7 was pumped by a flashlamp, powered by the discharge of a high-voltage capacitor bank via a suitable pulse forming network.

Solid State Dyes

Liquid dye lasers comprise large organic molecules in solvents such as methanol, glycerol, or water [44]. Recent efforts have been made to suspend the dye molecules within solid host matrices such as poly(methyl-methacrylate) (PMMA) and sol-gel [45]; one such dye amplifier was used in chapter 6. Dyes are characterised by wide absorption and emission profiles, resulting in broadly tuneable laser output and allowing optical pumping by short pulse flashlamps or another laser. Laser pumping is typically necessary to sustain cw dye laser operation due to extremely short ($\sim$ns) upper state lifetimes [46]. As observed in chapter 6, poor output beam quality can arise from large thermal gradients of the dye suspended in the host matrix; in addition, dye molecule degradation, in the form of bleaching or triplet state formation, necessitates replenishing of the dye. Besides the Perylene red dye used here, an extensive array of laser dyes has been developed and investigated, with emission wavelengths ranging from the blue of Coumarin dyes to the

near-infrared of the polymethine family [44].

Perylene red, a large, non-ionic, nonpolar dye, has limited solubility in many commonly used liquid solvents, but dissolves readily in methyl methacrylate. Excited state absorption restricts the laser efficiency of Perylene red to below that of most other commonly used dyes in the orange–red spectral region, but it remains one of the most photostable dyes available. The normalised photostability of Perylene red has been quoted to be $80 \pm 15\,\mathrm{GJ\,mol^{-1}}$ in PMMA when pumped by 6 ns pulses [45], although a number of studies have shown that the photostability depends on many different operating parameters, including pump fluence, pump repetition rate, and doping concentration. The laser damage threshold of PMMA has been published to be around $0.2\,\mathrm{GJ\,cm^{-2}}$ [45].

1.2 Nonlinear Optics

The strong electric fields generated by focused high intensity laser beams led to the early discovery, in crystal quartz, of the nonlinear optical generation of optical harmonics [47]. As described in chapter 3, nonlinear optical processes including harmonic generation, difference frequency generation, parametric generation and oscillation, and Raman shifting can be used to yield radiation that retains many of the advantageous properties of laser radiation at otherwise inaccessible wavelengths.

The development of nonlinear optics was, for some time, hindered by the lack of large, high quality nonlinear optical crystals, and of suitable pump sources. Advances in pump lasers, especially diode laser pumped solid state lasers, have led to renewed research interest in the field of nonlinear optics. Nonlinear optical crystals, such as β-BaB_2O_4 (BBO) [48–50], $LiNbO_3$ (LN) [51–53], $KTiOPO_4$ (KTP) [54], and LiB_3O_5 (LBO) [55], with high purity, high damage thresholds, and low absorption were developed, whose high nonlinear optical coefficients somewhat relaxed the energy requirements placed on the pump lasers. Increased crystal size and high power cw pump lasers, combined with novel interaction geometries, made feasible the development of cw nonlinear optical systems.

For high conversion efficiency, the nonlinear optical interaction must be phase matched. The traditionally common birefringent phase matching technique relies on fortuitous refractive index properties, which limits the range of interaction wavelengths. More recently, research has concentrated on quasi-phase matching (QPM), which any interaction, subject to absorption and fabrication constraints, to be phase matched with the highest nonlinear optical coefficient [56, 57]. Quasi-phase matching has been achieved by stacking polished plates, diffusion bonded wafers, controlled growth conditions [58],

electron beam scanning, and periodic poling.

Periodically Poled $LiNbO_3$

In the early 1990s, the successful periodic poling of the ferroelectric material $LiNbO_3$, by the application of high voltage pulses via patterned electrodes, was demonstrated [59, 60], and numerous applications of PPLN were rapidly developed [56, 61]. Field poling has since been demonstrated in $LiTaO_3$, attractive for its short wavelength cut-off [62–65]; $KNbO_3$ [66]; KTP [67–70], and its isomorphs $RbTiOAsO_4$ (RTA, [71]), $RbTiOPO_4$ (RTP [72]) and $KTiOAsO_4$ (KTA [73]).

After initial reports of PPLN used for of second harmonic generation (SHG) [59, 60, 74–76], the first PPLN OPOs were demonstrated by Pruneri *et al.* [77] and Myers *et al.* [56] in 1995. In rapid succession, OPOs pumped by a diode pumped high repetition rate Q-switched Nd : YAG laser, a long pulse Nd : YAG oscillator–amplifier, and a cw semiconductor diode oscillator–amplifier system, were demonstrated [61]. Even during these early experiments, thresholds as low as 12 μJ, in good agreement with the threshold model of Brosnan and Byer [78], were measured for a nominally singly resonant OPO pumped by 7 ns pump pulses, although imperfect mirror coatings resulted in some pump and idler enhancement. Reductions in OPO thresholds by as much as a factor of 3 have been observed on double-passing of the pump [79]. The flexibility of domain patterning resulted in multiple grating crystals being developed [77, 80]. In 1997, Jundt used the phase matching wavelengths of PPLN OPOs to establish an accurate Sellmeier equation for n_e of $LiNbO_3$ [81]. Ultrafast PPLN OPOs, synchronously pumped by modelocked lasers, have been reported with pulse durations as short as 60 fs and average output powers of up to 1 W [82–88]. Although the crystal length is typically limited by group delay dispersion considerations, pumping directly by modelocked diode lasers has been demonstrated, with up to 78 mW generated in 8 ps pulses at a repetition rate of 2.5 GHz [89].

The thickness of crystal that can be electric field poled is limited by the ionic conductivity. PPLN wafers have been poled to 1 mm thickness, but the effective aperture has been enlarged by diffusion bonding a stack of PPLN plates. In one result, a 3 mm thick stack allowed the generation of 2 mJ pulses when pumped with up to 22 mJ of pump pulse energy [90], although up to 7.4 mJ (3.6 mJ) signal (idler) pulses have been generated in a 1 mm thick monolithic PPLN OPO [91]. Scaling plane parallel OPOs to larger crystal apertures comes at the expense of a deterioration in beam quality [91] due to larger signal mode waist and simultaneously increased beam divergence as the range of signal spatial modes that can be phase matched increases with the higher cavity Fresnel

number. Non-collinear phase matching, at the same time, broadens the spectral output of the OPO.

The high gain in PPLN makes it possible to construct optical parametric generators, amplifiers, and monolithic oscillators. Agnesi *et al.* [92] demonstrated a travelling wave ps OPG–OPA configuration by double passing the same crystal, while a two-crystal configuration was used by Aniolek *et al.* [93]. Monolithic resonators, where the crystal end faces are coated to form the resonant cavity, are particularly attractive due to their simplicity [91] and potentially efficient conversion [94–97]. In a comparative study between 50 mm long PPLN OPGs and 20 mm long monolithic OPOs, Missey *et al.* [98] found the devices to exhibit similar performances. In chapter 7, results are presented of a PPLN crystal whose Fresnel reflectivities supported monolithic oscillation.

A significant factor limiting the applications of PPLN is its susceptibility to photorefractive effects, arising from refractive index variations due to photo-generated carriers via the electro-optic effect. Taya *et al.* presented a model [99] of photorefractive effects in which the space charge concentration is reduced by longitudinal currents arising from the field between the poled domains. A more comprehensive study, taking into account the photovoltaic effect, and drift and diffusion of photo-generated electrons, was presented by Sturman *et al.* [100]. Although the effects have been observed to be less severe in PPLN than in bulk $LiNbO_3$, the crystals are commonly maintaining at an elevated temperature above 100°C as a precaution [56, 61, 101]. Doping PPLN with MgO has also been demonstrated to avert photorefractive damage.

Periodically Poled $KTiOPO_4$ and $RbTiOAsO_4$

Second harmonic generation in field poled PPKTP gained prominence in the mid-1990s and was developed rapidly [67–69, 102–106]. The coercive field of KTP is an order of magnitude lower than that of $LiNbO_3$ and the highly anisotropic crystalline structure prevents domain broadening, allowing crystals of 1–3 mm thickness to be poled [107–109]. In addition, the absence of photorefractive effects in PPKTP allows this material to be operated at room temperature, simplifying the experimental configuration [8, 105, 107, 110]. Using 8 mm long PPKTP crystals, Pasiskevicius *et al.* [107] have demonstrated 81 mW of cw, 1.34 W of modelocked, and 0.4 mJ of Q-switched SHG output using extracavity frequency doubling of Nd : YAG lasers. Intracavity doubling of a 946 nm Nd : YAG laser yielding 750 mW at 473 nm was reported by Pierrou *et al.* [8]. More recently, Woll *et al.* [110] reported frequency doubling of an InGaAs oscillator–amplifier, yielding up to 250 mW of 460 nm radiation by single-pass frequency doubling of 13 ps pulses at a pulse repetition frequency of 4.8 GHz.

Difference frequency generation in PPKTP was first demonstrated in 1998 by Gibson *et al.* [111] and independently by Fradkin *et al.* [112, 113]. Around the same time, PPKTP was applied to OPOs, initially in synchronously pumped systems [108], and subsequently in cw [109, 114–116] and *Q*-switched pumped [117] OPOs. The OPOs investigated by Hellström *et al.* were similar to those presented in this work. Pumping at 3.5 mJ in 5 ns pulses, a total signal plus idler combined output energy of 1.8 mJ was measured in a 25 mm long plane–plane cavity [117]. Fresnel reflections were observed to support monolithic oscillation. In a more recent study [118], the authors generated 12.5 mJ unidirectional output within a 3 mm thick PPKTP crystal, limited by the available pump energy, and a similar OPO was pumped at up to 15 times threshold [118]. These results may be compared to the 18 mJ reported in chapter 5 from an OPO pumped at 18 times threshold.

Periodic poling of RTA was first demonstrated in 1996 by Karlsson *et al.* [119], and independently by Hu *et al.* [120], for SHG of Ti : sapphire lasers. The first PPRTA OPO was demonstrated by Reid *et al.* in 1997 using a fs Ti : sapphire pump laser [121] and PPRTA has since been employed in OPOs in the cw [122, 123], ns [124], ps [125], and fs [126] time domains. The relatively recent development of PPRTA, which built on extensive experience gained from poling of KTP, meant that few performance improvements have been reported since the initial demonstrations. Poling to 3 mm apertures allowed a Nd : YVO_4 pumped PPRTA OPO to generate 1.3 W average output power for a pump power of 8 W at 20 kHz, and single pulse energies of 18 mJ when pumped by 56 mJ from a flashlamp pumped Nd : YAG laser [127]. Virtually identical results had been reported in the initial demonstration two years previously [124].

Continuous-Wave and Intracavity OPOs

The large nonlinearities accessible by quasi-phase matching, particularly in PPLN, allowed the development of cw OPOs with modest pump sources [61, 128], including direct pumping by tuneable diode lasers [129, 130]. These narrowband tuneable cw devices are particularly suited for chemical detection [130, 131]. For example, Strößner *et al.* [132] recently demonstrated a remarkable tuning range, between 550 nm and 2.83 μm, of a single frequency (20 kHz optical bandwidth) cw OPO based frequency conversion system that generated up to 800 mW output power using either PPLN or PPKTP. Early demonstrations of cw OPOs employing birefringent phase matched nonlinear optical crystals were most commonly doubly resonant [133, 134]; theoretical treatments of these have been presented by a number of authors [94, 135, 136]. Low thresholds have allowed these devices to be pumped directly by semiconductor oscillator–amplifier systems [137]

and diode lasers [138, 139]. The spectral sensitivity of doubly resonant OPOs, due to the multiple resonance constraints, can be mitigated by employing dual cavity configurations [137, 140]. Pump enhanced OPOs have also been shown to give low thresholds and efficient conversions [141–143], with the theoretical aspects being treated by Schiller *et al.* [144].

The intracavity, singly resonant OPO (ICSRO) configuration, used in chapter 8, was initially applied to fs [145], and subsequently *Q*-switched systems [17, 146, 147]. In 1996, Colville *et al.* reported the first demonstration of a cw ICSRO using bulk KTP intracavity to a Ti : sapphire laser [148]. This was followed in 1997 by the first multiple-parameter tuned ICSRO by Turnbull *et al.* [149], using a 19 mm long PPLN crystal within a Ti : sapphire laser cavity. Significant thermal lensing in PPLN was observed. Subsequently, Edwards *et al.* extensively investigated intracavity OPOs in Ti : sapphire lasers, including the nonlinear optical materials KTA [150], which generated 0.8 W idler output power with 90% conversion efficiency; PPRTA [122], which generated 270 mW idler at a reduced conversion efficiency of 43% due to focusing requirements in the short nonlinear optical crystal; and PPKTP [116], which generated up to 455 mW at the non-resonant idler wavelength.

The intracavity OPO configuration was thereby shown to be feasible for both birefringent and quasi-phase matched nonlinear optical materials. A theoretical treatment of intracavity doubly resonant oscillators was given in an early paper by Oshman and Harris [151], followed by an analysis of the cw conversion efficiencies and optimum focusing conditions of intracavity singly resonant oscillators by Tran-Ba-Chu and Boyer [152]. Colville *et al.* [148] found the conditions required for an optimum 100% conversion efficiency by solving the laser and coupled nonlinear optical rate equations under steady state. A more exhaustive treatment was presented by Turnbull *et al.* [153], including relaxation oscillations and power stability with a multi-frequency laser field. Under steady state, the authors showed that below the ICSRO threshold, the system operates as a conventional laser cavity, whereas above OPO threshold the laser field is clamped at the threshold value. Different expressions optimising idler power, signal power, and total power were derived in terms of laser cavity and ICSRO threshold pump powers. Analytic and numerical analysis of relaxation oscillations in ICSROs demonstrated a substantially increased damping time with the OPO above threshold. Turnbull *et al.* investigated such transient dynamics and found the numerical treatment to agree with the experimental results of a PPLN OPO intracavity to an Nd : YVO_4 laser [154]. The dynamics of ICSROs under pulsed operation were investigated by Debuisschert *et al.* [147].

A cw ICSRO based on system similar to the one in chapter 8 of this thesis was used

by Stothard *et al.* [123], who were able to generate up to 70 mW of idler power using a 50 mm long PPLN crystal driven by a 1 W-diode pumped Nd : YVO_4 minilaser. This configuration was used in a comparative study between PPLN and PPRTA [155], and the results of a PPRTA-Nd : YVO_4 cw ICSRO pumped by a 3 W diode was recently presented by Carleton *et al.* [156].

1.3 Optical Bandwidth Control

A number of authors have presented spectroscopic measurements using the output from pulsed, tuneable OPOs. The free-running optical bandwidths of birefringently phase matched ($\sim$10 cm^{-1}) or quasi-phase matched ($\sim$5 cm^{-1}) ns pulsed OPOs are typically too broad for all but the coarsest spectroscopic features [157], and useful devices have, in the past, been based primarily on cw or injection seeded OPOs [158]. Photoacoustic and direct absorption spectroscopy of a number of pollutant molecules, including CH_4 [109, 131, 159–162], CO_2 [158, 163], C_2H_2 [157, 158], N_2O [130], and NO [158], has been demonstrated. The short, high energy pulses of seeded OPOs have been shown to be suitable for differential absorption lidar of atmospheric methane [164] and water [165]. Other spectroscopic applications include coherent anti-Stokes Raman and cavity ring-down spectroscopy [166].

Narrowing the optical bandwidth of OPOs using active techniques such as injection seeding [167] can lead to complex system architectures [168]. In this work, optical bandwidth control using passive frequency filters, including étalons and diffraction gratings, are investigated, resulting in narrowband radiation that would be suitable for applications previously demonstrated using OPOs.

In two early papers on intracavity étalon OPOs, Kreuzer [169] and Young *et al.* [170] demonstrated single mode and narrowband, respectively, output from bulk $LiNbO_3$ OPOs. Such OPOs are still of interest for high pulse energy work, and étalon narrowing was used by Long *et al.* [171] in a bulk $LiNbO_3$ OPO–OPA system to generate up to 180 mJ of narrowband ($\leq$1.5 GHz) radiation. Robertson *et al.* [172] narrowed the optical bandwidth of an excimer laser pumped birefringently phase matched β-BaB_2O_4 OPO using two intracavity étalons. The authors observed a significant increase in threshold on insertion and tilting of the étalons. This may be attributed to losses introduced by the étalon [173], in terms of walkoff and build-up time effects, which may also reduce the effective finesse [174]. In a more recent publication, Richman *et al.* [162] reported on a ring cavity PPLN OPO that included an air spaced étalon; simultaneous sweeping of the étalon spacing and cavity length allowed 10 cm^{-1} continuous frequency tuning. The sys-

tem provided up to 10 μJ of tuneable output pulse energy, which was used to measure a cavity ring-down absorption spectrum of methane. In cw OPOs, thin, low finesse étalons are often used to select the resonating wavelength, and the output power is usually not greatly affected by the insertion and angle tuning of these étalons [128, 130, 143, 163].

The first grazing incidence diffraction grating cavities were independently demonstrated in dye lasers by Shoshan *et al.* [175] and Littman and Metcalf [176]. Subsequent studies, also performed with pulsed dye lasers, showed the importance of short cavity lengths [177] and the choice of tuning mirror pivot point for synchronous tuning of cavity length and tuning mirror angle [178]. The grazing incidence cavity has since been used successfully to narrow the optical bandwidth of Ti : sapphire lasers [179] as well as OPOs based on bulk KTP [180], BBO [181, 182], and PPLN [161]. Due to the low output efficiency of the grazing incidence cavity, nonlinear optical amplifier chains have been implemented [183, 184], resulting in mJ-class, reliable, practical systems suitable for spectroscopy. A grazing incidence KTP OPO and amplifier chain has been commercialised by Continuum Inc.

The key operating parameters of a grazing incidence OPO were investigated by Gloster *et al.* [181] using a walkoff compensated BBO OPO, pumped by the third harmonic of a Nd : YAG laser. The optical bandwidth of the pump laser was found to be critical in determining the optical bandwidth of the OPO, with a single frequency pump being necessary to achieve single longitudinal mode OPO oscillation. Other passively line narrowed OPOs have agreed with this observation, but single longitudinal mode signal output has also been demonstrated under broadband pumping [169, 170, 183]. Nonetheless, Gloster *et al.* [181] could not achieve reliable single mode operation under broadband pumping, which could be explained by the geometric considerations presented by Kangas *et al.* [179].

A grazing incidence PPLN OPO similar to the one presented in chapter 5 was reported by Yu and Kung [161] shortly after the experiments reported in section 5.2.4 had been completed. The authors demonstrated the suitability for such OPOs as spectroscopic sources by the successful measurement of photo-acoustic absorption spectra of CH_4. The OPO optical bandwidth was reduced to 9 GHz in that case, with 50 μJ of output energy. These values may be compared to those reported in chapter 5, where a diagnostic instrument limited optical bandwidth of $\leq$250 MHz and signal output pulse energies of up to 170 μJ were measured.

1.4 Thesis Outline

The thesis is arranged into two parts: theoretical background and experimental results. Chapters 2, 3 and 4 review the theoretical foundations for lasers, nonlinear optics, and the passive methods of optical bandwidth control used, with emphasis on areas of relevance to the experimental work. Summaries of important properties of the laser and nonlinear optical media used are presented in sections 2.2 and 3.4.

The second part of the thesis presents results from experimental work carried out on quasi-phase matched OPOs. The results are divided into 10 Hz OPOs pumped at 1.064 μm (chapter 5); 10 Hz OPOs pumped at 532 nm (chapter 6); OPOs pumped by a high repetition rate laser, both at 1.064 μm and 532 nm (chapter 7); and the design and construction of a thermal lensing tolerant cw intracavity OPO pumped at 1.064 μm (chapter 8). The pulsed OPO chapters include performance results of OPOs based on PPLN and PPKTP, incorporating either intracavity étalons or diffraction gratings as a means to obtain single mode or narrowband operation. An overall summary and general conclusions drawn from the experimental results are presented in chapter 9.

A list of publications arising from the work presented in this thesis is given in appendix A, while the circuit diagram used to generate an error signal from a scanned grazing incidence PPLN OPO described in section 5.2.5 is included in appendix B.

Chapter 2

Laser Sources

The theoretical foundations for the laser were formulated in the 1920s by Einstein, but it was not until 1960 that the first optical frequency laser was demonstrated [1]. Lasers have since become invaluable to many fields of research, including nonlinear optics. Section 2.1 describes the laser rate equation models for both continuous-wave (cw) and Q-switched modes of operation, and the method by which thermal lensing may be calculated. Relevant properties of laser gain materials used are briefly outlined in section 2.2, and the $ABCD$ law and its application to resonator design is summarised in section 2.3.

2.1 Laser Theory

2.1.1 Rate Equations

The performance of lasers can be predicted with remarkable accuracy using semi-classical equations as derived in optics texts [2, 46, 185–187]. In a system of ideal four-level atoms, with energy levels as illustrated in figure 2.1, the population density

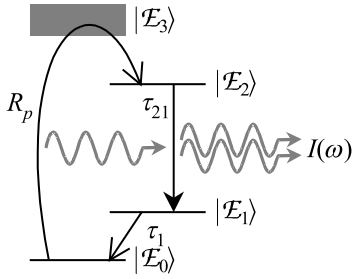

Figure 2.1: Atomic system comprising four levels $|\mathcal{E}_i\rangle$. A pump source R_p excites the atoms from the ground state $|\mathcal{E}_0\rangle$ to the upper laser level via a band of pump levels $|\mathcal{E}_3\rangle$. A radiation field $I(\omega)$ may be amplified by stimulated emission between the upper $|\mathcal{E}_2\rangle$ and lower $|\mathcal{E}_1\rangle$ laser levels.

rate equations for the upper N_2 and lower N_1 transition states may be written as the sum of pumping, decay, and stimulated transition terms as

$$\begin{aligned} \frac{dN_2}{dt} &= R_p - \frac{N_2}{\tau_2} - \left(\frac{\sigma I}{\hbar\omega}\right)\left[N_2 - \frac{g_2}{g_1}N_1\right] \\ \frac{dN_1}{dt} &= \frac{N_2}{\tau_{21}} - \frac{N_1}{\tau_1} + \left(\frac{\sigma I}{\hbar\omega}\right)\left[N_2 - \frac{g_2}{g_1}N_1\right]. \end{aligned} \tag{2.1}$$

Here, σ is the transition cross-section; g_i is the degeneracy of state $|\mathcal{E}_i\rangle$, which has energy $\mathcal{E}_i$; τ_{ji} is the characteristic relaxation lifetime from level $|\mathcal{E}_j\rangle$ to $|\mathcal{E}_i\rangle$; and $1/\tau_j \equiv \sum_{i<j} 1/\tau_{ji}$ is the total level decay rate. The atoms interact with a radiation field of intensity I and angular frequency ω, assumed to be close to the atomic transition frequency $\omega_{21} = (\mathcal{E}_2 - \mathcal{E}_1)/\hbar$.

In equations (2.1), R_p is an effective pump rate density from the ground state into the upper laser level $|\mathcal{E}_2\rangle$. For an ideal laser material with a branching ratio $\tau_3/\tau_{32} = 1$, an optical pump source of absorbed power P_{abs} injected into a pumped volume V_p yields a pump rate of

$$R_p = \frac{P_{\text{abs}}}{\hbar\omega_p V_p}, \tag{2.2}$$

where ω_p is the angular frequency of the pump radiation. Optical pumping can assume many forms, including flashlamp and diode laser pumping as discussed in chapter 1, and efficiency coefficients may be introduced to account for imperfect spectral and spatial overlap [2].

To simplify the notation, it is customary to define a population inversion density $N \equiv [N_2 - (g_2/g_1)N_1]$ where $N \approx N_2$ in four-level laser systems. Under equilibrium conditions, we may set the temporal derivatives $d/dt = 0$ and solve equations (2.1) for the steady-state inversion density. Assuming ideal lifetime, branching, and degeneracy ratios [186], the steady-state inversion density is

$$N = \frac{\tau_2 R_p}{1 + I/I_{\text{sat}}}, \tag{2.3}$$

where the saturation intensity

$$I_{\text{sat}} = \frac{\hbar\omega}{\sigma\tau_2} \tag{2.4}$$

is the field intensity required to deplete the inversion to half of its small-signal value. The saturation intensity is found to be an important figure of merit for comparing laser media.

2.1.2 Atomic Lineshape

The laser transition of Nd : YAG is homogeneously broadened, principally by phonon collision dephasing processes. We may use a plausibility argument to derive the homogeneously broadened lineshape of the stimulated emission cross-section $\sigma(\omega)$ by considering the one-dimensional equation of motion of the polarisation $P(t)$ induced by an applied electric field $E(t)$ in a system of $\mathcal{N}$ dipoles [185],

$$\frac{d^2P(t)}{dt^2} + \Delta\omega\frac{dP(t)}{dt} + \omega_{21}^2 P(t) = \frac{\mathcal{N}e^2}{m}E(t), \tag{2.5}$$

where e and m are the electronic charge and mass, and $\Delta\omega$ the linewidth. For a monochromatic applied electric field of frequency $\omega \approx \omega_{21}$, the complex atomic susceptibility can be derived as $\chi_{\text{at}} \equiv P(t)/E(t) \propto 1/(\omega_{21}^2 - \omega^2 + i\omega\Delta\omega)$ [185]. The imaginary part of χ_{at} is related to the strength of the transition lineshape, which, under typical lasing conditions, is the dominant factor determining the frequency dependence of the cross-section $\sigma(\omega)$. A more detailed derivation of the stimulated emission cross-section results in the Lorentzian distribution

$$\sigma(\omega) = \frac{\lambda^2}{8\pi n^2\tau_2}\left[\frac{4/\Delta\omega}{1 + \{2(\omega - \omega_{21})/\Delta\omega\}^2}\right], \tag{2.6}$$

where λ is the laser wavelength. The spontaneous emission lifetime τ_2 may, at least in principle, be derived from quantum mechanics [46, 185].

The natural transition linewidth $\Delta\omega$ in equation (2.6) arises from the Fourier transform of the spontaneous emission decays via the damping term in equation (2.5). In Nd : YAG, the contribution from the $\tau_2 = 230\,\mu$s lifetime is overwhelmed by phonon broadening, resulting in a typical pulsed free-running spectral width of $\Delta\omega'/2\pi \sim 30\,$GHz. Under cw conditions, the combination of gain saturation and homogeneous broadening results in narrowband laser output, whereas injection seeding or frequency selective filters may be used to control the optical bandwidth of Q-switched systems [2].

2.1.3 Continuous-Wave Operation

A laser material with a suitable population inversion may act as a laser amplifier, or, when placed within a resonant cavity, a laser oscillator. Analogously to equations (2.1), we may write a rate equation for the intracavity field intensity I,

$$\frac{dI}{dt} = -\frac{I}{\tau_c} + \frac{l_c}{L_c}c\sigma NI, \tag{2.7}$$

where spontaneous emission has been neglected. The ratio between crystal l_c and cavity L_c lengths accounts for the intensity experiencing gain only within the laser crystal on

each round trip. The cavity photon lifetime is denoted τ_c. The intensity gain γ per unit length is defined as

$$\gamma \equiv \sigma N = \frac{\sigma \tau_2 R_p}{1 + I/I_{\text{sat}}} \tag{2.8}$$

in steady state using equation (2.3). The losses experienced by the field are due to the output coupler reflectivity R and a cavity loss coefficient L, to which absorption and scattering losses contribute. The round trip intensity survival factor is $R(1-L)e^{2\gamma l_c} = e^{2l_c(\gamma-\alpha)}$ with an effective loss coefficient α per unit length within the crystal of

$$\alpha = \frac{-\ln[R(1-L)]}{2l_c}. \tag{2.9}$$

Under steady-state conditions, $dI/dt = 0$ and $\gamma = \alpha$, which leads to an expression for the cavity lifetime $\tau_c = L_c/l_c c\alpha$.

Below threshold, there exists a negligible intensity within the cavity and the gain coefficient in equation (2.8) reduces to the small-signal gain coefficient, denoted $\gamma_0 = \sigma\tau_2 R_p$. The laser oscillation threshold is reached when $\gamma_0 = \alpha$, and combining equations (2.2), (2.8) and (2.9) gives the pump power required to maintain threshold [2],

$$P_{p,\text{thr}} = -\frac{\hbar\omega_p V_p}{2l_c\sigma\tau_2}\ln[R(1-L)]. \tag{2.10}$$

For low losses $L \ll 1$, this may be simplified using $-\ln[R(1-L)] \approx L - \ln R$, yielding a linear relationship between $P_{p,\text{thr}}$ and $-\ln R$. This provides a method for experimentally determining the resonator cavity losses L by measuring the threshold power for varying output coupler reflectivities R, as first outlined by Findlay and Clay [188].

Above threshold, the intracavity intensity grows until gain saturation depletes the gain coefficient γ. Under steady-state conditions, the intracavity intensity is given by $I = (\gamma_0/\alpha - 1)I_{\text{sat}}$ from equation (2.7). This is the sum of counter-propagating field components, and for low output coupling approximately $-(\ln R)/2$ of the intensity is transmitted as useful laser output [2]. Provided the losses L are known, the equation for the output power

$$P_{\text{out}} = \frac{-\ln R}{2}\frac{V_p}{l_c}\left[2l_c\frac{\sigma\tau_2 R_p}{-\ln\{R(1-L)\}} - 1\right] I_{\text{sat}} \tag{2.11}$$

can be used to find the optimum output coupler reflectivity.

The performance of the diode-pumped Nd:YAG laser reported in chapter 7 was modelled using the following parameters: pump volume $V_p = 1.5\,\text{mm}^2$; crystal length $l_c = 10\,\text{mm}$; cavity length $L_c = 250\,\text{mm}$; output coupler reflectivity $R = 0.8$; and cavity round trip loss coefficient $L = 0.1$. Equation (2.10) predicted a threshold power

of $P_{\text{thr}} = 0.95\,\text{W}$, while an absorbed pump power $P_{\text{abs}} = 24\,\text{W}$ led to an output power $P_{\text{out}} = 11.9\,\text{W}$. Both values are in good agreement with the values measured experimentally. A more detailed analysis of a diode-pumped $\text{Nd}:\text{YVO}_4$ laser, including Findlay–Clay and output power analyses of the cavity losses and optimum output coupling, is presented in chapter 8.

2.1.4 Q-Switching

One method for increasing the peak power levels for applications such as the nonlinear optical frequency conversion investigated in this thesis is to store energy in the form of a population inversion within a high-loss cavity in which laser oscillation is suppressed, followed by rapid depletion of the inversion and simultaneous generation of an intense laser pulse by switching the cavity losses L (cavity Q factor). The evolutions of the population inversion density $N(t)$ and the intracavity laser intensity $I(t)$ are still governed by the coupled rate equations (2.1) and (2.7), but time-dependent functions are substituted for the pumping rate $R_p(t)$ and the cavity losses $\alpha(t)$.

Approximate analytic evolution solutions can be found by partitioning the Q-switch pulse into build-up, emission and decay time periods [185]. During inversion build-up, integration of equation (2.1) with $I = 0$ and a constant pumping rate R_p yields a population inversion density that grows as $N(t) = \tau_2 R_p(1 - e^{-t/\tau_2})$, limiting the useful build-up time to a few fluorescence lifetimes τ_2. After the Q-switch is opened, the radiation field grows exponentially at a rate determined by γ_0 until the gain begins to saturate, and intensity growth continues until the inversion density is reduced below the cw threshold inversion density $N_{\text{thr}} = \alpha/\sigma$. The final part of the pulse comprises an exponential tail $I(t) \propto e^{-t/\tau_c}$ as the intracavity intensity decays due to cavity losses.

In the period during which the Q-switched laser pulse is emitted, the rate equations (2.1) and (2.7) may be manipulating to yield a differential equation of the form $dI(t)/dN(t) \propto \left[N_{\text{thr}}/N(t) - 1\right]$. Integration leads to [185]

$$I(t) = \hbar\omega c \frac{l_c}{L_c}\left[N_i - N(t) - N_{\text{thr}} \ln \frac{N_i}{N(t)}\right], \tag{2.12}$$

where N_i is the population inversion density when the Q-switch is opened. This expression may be used to calculate the inversion density N_f remaining after the Q-switch pulse has finished, and it is found that for initial inversions in excess of $\sim 2N_{\text{thr}}$, virtually all of the stored inversion is converted into photons [2]. The output pulse energy U is given by the useful fraction of these photons,

$$U_{\text{out}} = \hbar\omega V_p (N_i - N_f) \frac{\ln(R)}{\ln[R(1-L)]}. \tag{2.13}$$

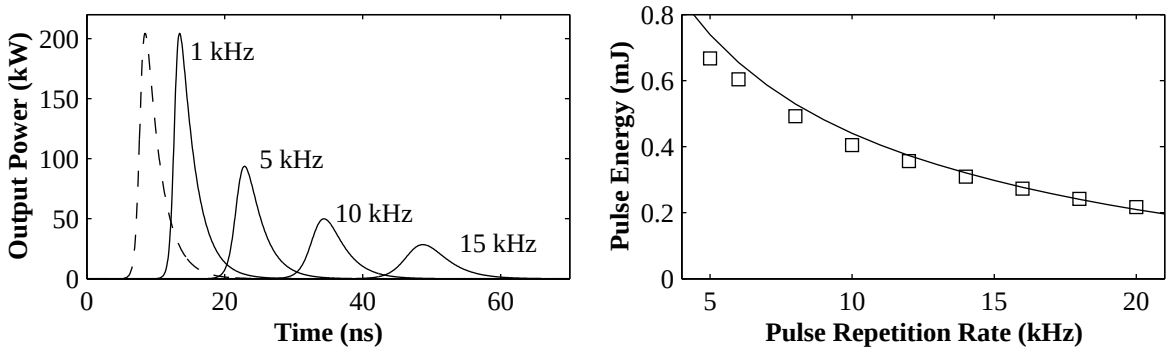

Figure 2.2: Modelling of a diode-pumped high repetition rate Nd : YAG laser performance. (a) Laser output pulse evolution obtained by numerical integration of equations (2.1) and (2.7). (b) Output pulse energy as a function of repetition rate. Squares, experimental data reported in chapter 7; solid line, theory from equation (2.13). For further information, see text.

The peak output power $P_{\text{out,pk}}$ is generated when the inversion is reduced to the cw threshold value, $N(t) = N_{\text{thr}}$, and may be calculated directly using equation (2.12). An estimate of pulse duration can then be found from the ratio $U_{\text{out}}/P_{\text{out,pk}}$. For systems pumped well above threshold, the pulse duration approaches the cavity lifetime τ_c. Combining the expressions for the inversion build-up and output pulse energy, the average Q-switched power P_{avg} at a laser repetition rate f can be related to the cw output power P_{out} by [35]

$$P_{\text{avg}} \approx P_{\text{out}} \tau_2 f (1 - e^{-1/\tau_2 f}). \tag{2.14}$$

Numerical integration of the population (2.1) and intensity (2.7) rate equations is required to obtain accurate pulse shapes. Such a model was developed for the diode-pumped Nd : YAG laser reported in chapter 7, with most of the parameters as outlined at the end of section 2.1.3. Figure 2.2 (a) shows the output power evolution after the Q-switch is opened obtained using such calculations, which included a low intracavity seed field from which the laser pulse started. The output pulse energy as a function of repetition frequency is shown in figure 2.2 (b) together with experimentally measured values reported in chapter 7. To obtain agreement between the theoretical model and experiment, the round trip loss coefficient L was set to 0.4. The corresponding cavity lifetime $\tau_c = 2\,\text{ns}$ was in agreement with the pulse decay tails of experimentally recorded pulses, and the high loss coefficient was attributed in part to the introduction of an intracavity aperture, used to ensure fundamental transverse mode oscillation. The durations of the modelled pulses shown in figure 2.2 (a) were consistently $\sim$5 times shorter than those measured in the laboratory. Introducing into the model switching times of around 50 ns,

comparable to the beam traverse time of a sound wave in silica, reduced the predicted output pulse energies due to inefficient extraction of the population inversion but did not match the experimentally measured pulse durations.

The pulse build-up time can be reduced by injection seeding, as shown by the dashed line in figure 2.2 (a), or by lowering the cavity losses, which also modifies the decay constant of the pulse tail. Minimisation of the build-up time can thus be used experimentally to optimise resonator alignment and to ensure successful seeding. The rate equations (2.1) and (2.7) can be extended to include other phenomena, such as injection seeding, variable pumping and hold-off, excited state absorption (ESA) [20], energy transfer upconversion (ETU) [23], and the influence of intracavity components such as saturable absorbers [21], intracavity frequency doubling, or OPO crystals [153].

Acousto-Optic Q-Switching

The high repetition rate Nd : YAG laser described in chapter 7 employed an acousto-optic Q-switch, in which an acoustically induced Bragg grating causes a beam deflection. The acousto-optic effect arises from an acoustic wave, generated by an rf-driven transducer, inducing a strain wave that modifies the refractive index within the material via the photoelastic, or strain-optic, coefficient p. It can be shown [187] that the magnitude of the change in refractive index is given by $\Delta n = \sqrt{\mathcal{M} I_s/2}$, where I_s is the sound wave intensity and

$$\mathcal{M} = \frac{p^2 n^6}{\rho v_s^3} \tag{2.15}$$

is a material figure of merit parameter. In equation (2.15), ρ is the mass density of the medium and v_s the velocity of sound. Typical figures of merit are around $\mathcal{M} \sim 1 \times 10^{-14}\,\mathrm{m^2/W}$.

In deriving the resulting Bragg diffraction, the strain-induced refractive index grating is assumed to be stationary during the radiation transit time, as shown in figure 2.3. A beam incident at the Bragg angle θ_B, where $\sin\theta_\mathrm{B} = \lambda/2\Lambda_s$ with λ the optical and Λ_s the acoustic wavelength, is partially reflected. A detailed power diffraction calculation [187] leads to an expression for the power reflectivity R of the deflected beam,

$$R = \sin^2\left[\frac{2\pi n L \Lambda_s}{\lambda^2}\sqrt{\frac{\mathcal{M} I_s}{2}}\right], \tag{2.16}$$

where L is the length of the Q-switch. The extinction ratio is thus determined by the applied rf power, with typical diffraction efficiencies of around 1–5% per Watt of rf power [14, 187].

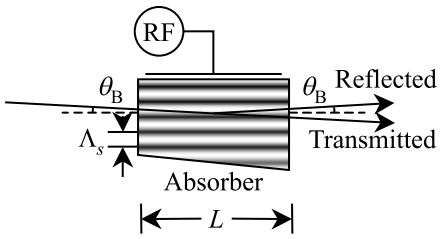

Figure 2.3: Acousto-optic Q-switch of length L. An rf signal applied to a transducer generates an acoustic wave of wavelength Λ_s, which induces a refractive index grating. A beam incident at the Bragg angle θ_B is partially reflected by the grating.

The switching time is determined by the transit time of the acoustic wave across the beam diameter, and the hold off of acousto-optic Q-switches is often insufficient for high gain lasers. However, the modest power requirements and low insertion losses ($\sim$0.5%) make these switches ideal for cw-pumped solid-state lasers.

An alternative method for obtaining Q-switched pulses relies on the electro-optic effect in birefringent media. Electro-optic Pockels cell Q-switches are commonly designed to give an orthogonal polarisation after a round trip, which is rejected by the polariser, and a quarter wave voltage applied to the Q-switch to open it. Electro-optic Q-switches require fast, high voltage drive circuits, but offer higher extinction ratios and faster switching times than acousto-optic Q-switches. The commercial flashlamp pumped Nd : YAG lasers employed as pump sources in chapters 5 and 6 were electro-optically Q-switched.

Prelase Q-Switching

The variable diffraction efficiency of acousto-optic Q-switches determined by the applied rf power may be used as a variable output coupler to optimise the laser Q-switching efficiency and beam quality [12], to enforce unidirectional oscillation in a ring cavity [12, 189], or to control the transient build-up of the laser intensity within the cavity before the laser pulse is emitted [10, 15].

In the last of these, which is known as prelase Q-switching and has also been demonstrated using electro-optic Q-switches [10, 13, 189], the hold off is adjusted to maintain a low seeding intensity within the resonator before the Q-switch is opened for the laser pulse. Gain saturation of this cw prelase results in a narrowing of the optical bandwidth of the emitted laser pulse, as well as improved amplitude and temporal stability. Intensity spiking and relaxation oscillations during the prelase period are often suppressed with electronic feedback [15]. A form of prelase Q-switching without feedback was im-

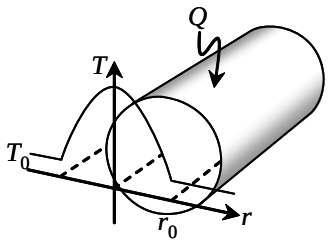

Figure 2.4: Thermal distribution $T(r)$ generated within an infinitely long rod by a uniform heat load Q per unit volume. The resulting temperature distribution is quadratic, leading to a spherical thermal lens. The rod has radius r_0 and surface temperature T_0.

plemented as described in chapter 7 by tilting the acousto-optic Q-switch to reduce the hold-off. The spectral narrowing was, in this case, observed at the expense of somewhat degraded temporal and amplitude stability.

2.1.5 Thermal Lensing

Within the laser crystal, thermally induced changes in the refractive index cause phase front deformations. For extreme heat loads with inadequate cooling, thermally induced stresses can lead to catastrophic crystal damage [2]. In moderate power solid-state lasers end-pumped by semiconductor diode lasers, the thermal load arises largely from the pump quantum defect ω_p/ω, whereas in other configurations additional heat loads due to absorption and spectral or spatial matching of the pump and laser may contribute [2].

Under steady state thermal loading, a heat flux $\nabla \cdot \mathbf{h}(\mathbf{r}) = Q(\mathbf{r})$ is generated [190] by the heat load $Q(\mathbf{r})$. The heat flux is related to the temperature distribution by $\mathbf{h}(\mathbf{r}) = -\kappa_{\mathrm{Th}} \nabla T(\mathbf{r})$, where κ_{Th} is the material thermal conductivity, from which we may write the heat conduction equation [190]

$$\nabla \Big[\kappa_{\mathrm{Th}} \nabla T(\mathbf{r}) \Big] + Q(\mathbf{r}) = 0. \tag{2.17}$$

To simplify the calculation, we assume constant κ_{Th} and a heat load $Q = P_{\mathrm{abs}}/V$ uniformly distributed within an infinitely long laser rod of radius r_0, as illustrated in figure 2.4. The thermal gradients are then purely radial and the radially symmetric temperature distribution is given by [2]

$$\Delta T(r) = T(r) - T(r_0) = \frac{Q}{4\kappa_{\mathrm{Th}}} \left(r_0^2 - r^2 \right). \tag{2.18}$$

This quadratic temperature profile gives rise to a spherical thermal lens due to spatial variations in the refractive index arising through the material dn/dT coefficient, thermal

stresses leading to stress-induced changes in the refractive index via the photo-elastic effect, and bulging of the crystal ends due to the coefficient of thermal expansion α_{Th}. The effective focal length may be calculated by treating the rod as a thick lens [2], which yields

$$\frac{1}{f_{\mathrm{Th}}} = \frac{P_{\mathrm{abs}} l_c}{\kappa_{\mathrm{Th}} V} \left[\frac{1}{2} \frac{dn}{dT} + \alpha_{\mathrm{Th}} C_{r,\phi} n_0^3 + \frac{\alpha_{\mathrm{Th}} r_0 (n_0 - 1)}{l_c} \right], \tag{2.19}$$

where each of the terms on the right hand side corresponds to a contributing lensing process. The radial and azimuthal components of the photoelastic coefficient $C_{r,\phi}$ may be derived from the laser material stress optic tensor and have values $C_r \approx 0.017$ and $C_\phi \approx -0.0025$ in Nd : YAG [2]. The unequal values result in a polarisation dependent lens. This effect is usually dominated by surface bulging in end-pumped configurations [27], or the dn/dT term in flashlamp and side-pumped geometries [190], but can lead to thermal depolarisation losses. Knowledge of material parameters allowed equation (2.19) to be used directly to calculate the thermal lens in the diode pumped Nd : YAG (yielding $f_{\mathrm{Th}} \approx 75\,\mathrm{mm}$) and Nd : YVO_4 ($f_{\mathrm{Th}} \approx 150\,\mathrm{mm}$) lasers, described in chapters 7 and 8, respectively.

Thermal lensing within laser rods has been extensively modelled both analytically [28, 32, 190] and numerically [23, 27, 31, 191], and results have been compared to experimental measurements of beam distortions arising from thermal effects [43]. In Nd : YAG, the quantum defect places a lower limit of $(1 - \omega_p/\omega) = 24\%$ on the fractional thermal heat load [192], whereas values of up to 40% have been measured experimentally [29, 30]. Thermal distortions have been observed to be substantially stronger under nonlasing conditions applicable to the pulse build-up period of Q-switched systems [24, 192] as compared to cw lasing conditions. Comparison between face and edge cooling geometries [32, 191] have shown that the centre-to-edge temperature gradient is reduced in face cooled configurations, and the contribution to the thermal lens due to bulging of the end faces can be substantially reduced by diffusion-bonded, undoped end caps [27, 193]. In general, thermal lensing and the risk of fracture can be mitigated by reducing the absorbed power density, by lowering the dopant concentration [41, 194], dual-end pumping [32], or by distributing the pump across multiple laser rods within the same cavity [27].

2.2 Laser Gain Materials

The Nd^{3+} active laser ion has been doped into numerous hosts, including Nd : YAG, Nd : YLF and Nd : YVO_4, discussed in the following sections. Since the active $4f$ electrons

Table 2.1: Properties of laser media [2, 24, 38, 41, 46, 185, 191, 192].

	Nd : YAG	**Nd : YLF**		**Nd : YVO_4**	
Property		π	σ	π	σ
Pump Wavelength λ_p (nm)	808.7	797		808.5	
Pump Absorption (cm^{-1}, 1% at.)	9.1	4.5		31	10
Laser Wavelength λ (nm)	1064.2	1047	1053	1064.3	1066
Fluorescence Lifetime τ_2 (μs)	230	480	520	98	
Cross-Section σ ($\times 10^{-19}\,cm^2$)	2.8	1.8	1.2	15.6	
Refractive Index n	1.82	1.47 (n_e)	1.45 (n_o)	2.17 (n_e)	1.96 (n_o)
dn/dT ($\times 10^{-6}\,K^{-1}$)	7.3	−4.3	−2.0	3.0	8.5
Thermal Expansion α_{Th} ($\times 10^{-6}\,K^{-1}$)	7.5	8 (c)	13 (a)	11 (c)	4 (a)
Thermal Conductivity κ_{Th} (W/m K)	14	5.8	7.2	5	

are partially shielded from the host surroundings by the $5s^2$ and $5p^2$ shells, the materials exhibit similar energy level structures, shown in figure 2.5. By contrast, the thermo-optic and mechanical properties, summarised in table 2.1, are determined largely by the host crystal, making the different materials attractive for different applications. The properties of Nd : YAG have been widely researched in many operating regimes including the cw and Q-switched applications used here, making it a benchmark material with excellent and reliable performance. Due to its lower propensity to thermal lensing, Nd : YLF was investigated for the high repetition rate laser reported in chapter 7, and Nd : YVO_4 was chosen for the cw laser results presented in chapter 8 because it offers superior cw laser efficiency and pump absorption characteristics.

2.2.1 Nd : YAG

Since the first report in 1964 [3], Nd : YAG (Nd : $Y_3Al_5O_{12}$) has become the most widely used solid state laser material. Its widespread success for many diverse applications including scientific, medical, industrial, and commercial uses is due to the combination of favourable bulk material characteristics of the YAG host and the excellent laser properties of the Nd^{3+} active centre [2]. The cubic YAG garnet host is naturally isotropic, and offers a high thermal conductivity suitable for high power applications. Due to its mechanical hardness it can be machined well, resulting in high quality crystal faces. Typically 1% of the Y^{3+} lattice sites are replaced by Nd^{3+}; higher impurity concentrations lead to heavily strained crystals due to the ∼3% size difference between the ions.

A number of pump bands, in particular around 730 and 810, are available for pumping Nd : YAG. The absorption spectrum for the latter is illustrated in figure 2.6 and 808.7 nm semiconductor diodes are often employed for pumping to the $^4F_{5/2}$ manifold. From these levels, excited atoms decay rapidly to the metastable upper $^4F_{3/2}$ laser level,

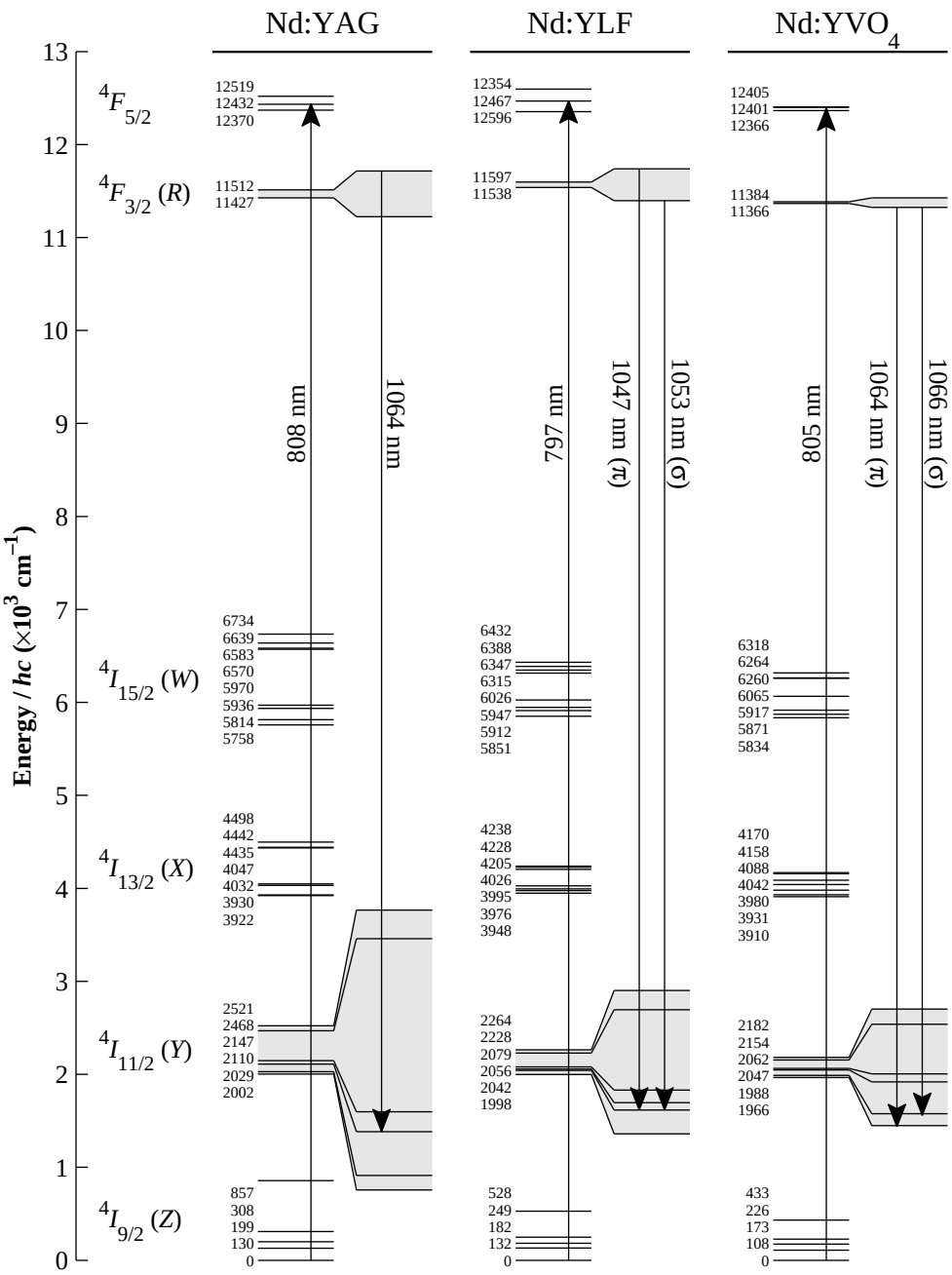

Figure 2.5: Energy level diagrams for Nd : YAG, Nd : YLF and Nd : YVO_4 laser gain materials [2, 24, 34, 186, 195]. Pump diodes at $\sim$0.8 μm raise atoms from the $^4I_{9/2}$ ground level to the $^4F_{5/2}$ pump band, whence they decay to the $^4F_{3/2}$ upper laser level. The $\sim$1 μm laser transition occurs between the $^4F_{3/2}$ and $^4I_{11/2}$ manifolds, shown in detail at right; in the uniaxial Nd : YLF and Nd : YVO_4 crystals, lasing occurs on two discrete polarisations, labelled π and σ. Other laser transitions terminating on the $^4I_{15/2}$, $^4I_{13/2}$ and $^4I_{9/2}$ manifolds occur at wavelengths $\sim$2.0 μm, $\sim$1.3 μm and $\sim$0.9 μm, respectively.

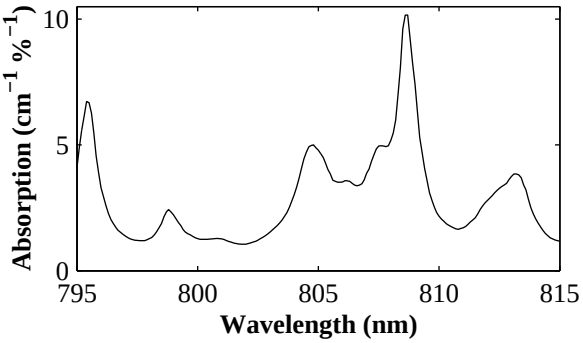

Figure 2.6: Absorption coefficient α_{abs} per atomic doping percent in Nd : YAG, as a function of wavelength λ, near the 808 nm band commonly used for optical pumping by semiconductor diodes. (Litton data sheet.)

which has a lifetime $\tau_2 = 230\,\mu$s. Laser transitions ending on a number of different lower states have been demonstrated, including ${}^4I_{15/2}$ ($\lambda = 1.74$–$2.13\,\mu$m), ${}^4I_{13/2}$ (1.319–1.356 μm), ${}^4I_{11/2}$ (1.052–1.226 μm) and ${}^4I_{9/2}$ (890–946 nm). The thermal population of the ${}^4I_{9/2}$ terminal level results in a quasi-three level laser system at this wavelength that requires bleaching and is subject to reabsorption losses [6]. The strongest transition, employed in the work presented here, occurs between sublevels R_2 and Y_3, at a wavelength of 1.064 μm. The lower level decays rapidly ($\tau_1 \sim 30$ ns [186]) to the ground level, making this Nd : YAG transition close to an ideal four-level laser system.

2.2.2 Nd : YLF

In diode pumped Q-switched and cw systems such as those described in chapter 7, the improved thermal lensing properties of Nd : YLF (Nd : $YLiF_4$) make it an attractive alternative to Nd : YAG [35, 37, 196]. Despite a lower thermal conductivity, partial cancellation between the negative dn/dT and positive end-face contributions to the thermal lens in equation (2.19) results in reduced thermal aberrations [191]. Depolarisation losses are also reduced due to the strong natural birefringence of the uniaxial YLF crystal host [2]. An intracavity polariser can be used to discriminate between the higher gain π transition at 1.047 μm (electric field $E \parallel c$ axis) and the lower lensing σ transition at 1.053 μm ($E \perp c$). The cw thresholds for Nd : YLF are lower than comparable Nd : YAG systems on account of the slightly larger $\sigma\tau_2$ product [197]. Under Q-switched operation, a longer upper state lifetime can lead to an enhanced energy storage capability [37]. Careful attention must be paid to heat removal from Nd : YLF, and detuning the pump diode wavelength by up to 8 nm may be used to reduce the absorbed power density [198]. Nonetheless,

thermal fracture prevented an experimental realisation of a Q-switched Nd : YLF laser in this work.

2.2.3 Nd : YVO_4

Nd : YVO_4 offers laser characteristics that are uniquely suited to cw diode end pumped lasers in the $\sim$10 W domain [38]. Nd : YVO_4 has a strong pump absorption coefficient of $\alpha_{abs} = 31\,cm^{-1}$ for 1% at. doped Nd : YVO_4 [41] and a reduced Stark splitting in the $^4F_{5/2}$ pump manifold (see figure 2.5), leading to an absorption some 20 nm wide, both broader and smoother than Nd : YAG [38]. Typical Nd : YVO_4 crystals need thus only be a few millimetres long for good pump absorption and the temperature stability tolerance on the pump diodes is substantially eased. The short crystal length allows high brightness TEM_{00} modes to be generated with high efficiencies, since the resonated mode radius need be constrained over only a short length [95]. In addition, like Nd : YLF, natural birefringence overwhelms thermal induced birefringence, reducing the susceptibility to depolarisation losses.

The cross-section for the π-polarised 1.064 μm transition in Nd : YVO_4 is greater than for the corresponding transition in Nd : YAG, leading to lower thresholds in Nd : YVO_4 systems. Crystals doped with up to 3% at. Nd^{3+} [39, 41] have been demonstrated, allowing Nd : YVO_4 microchip and minilasers to be constructed [39], including minilasers with intracavity nonlinear optical frequency conversion with excellent spatial qualities [95]. In recent years, upconversion and thermal problems, associated with the high thermal loading of highly doped Nd : YVO_4 crystals and a low thermal conductivity, have resulted in crystals with lower doping levels of around 0.5% at. to be increasingly favoured [39–41, 194]. The short upper state lifetime $\tau_2 = 98\,\mu s$, shown to be dependent on doping concentration [41], makes Nd : YVO_4 less attractive for pulsed systems due to the limited energy storage, although both modelocked and Q-switched pulsed operation have been demonstrated [88, 95], with up to 5.6 mJ at 10 kHz [42].

2.3 Resonator Design

For the intracavity OPO design work reported in chapter 8, the $ABCD$ matrix formalism of optical cavities was used to find cavity configurations that remained stable even in the presence of thermal lensing in the laser and nonlinear optical crystals. Geometric ray tracing optics describes each optical element by a 2×2 matrix $\mathbf{M}$, with unity determinant $AD - BC = 1$ [185]. The transfer matrix $\mathbf{M}$ for a system comprising a sequence

Table 2.2: Useful Gaussian beam propagation formulae relating the $1/e^2$ radius $w(z)$ and the wavefront curvature $R(z)$ at propagation distance z from the beam waist, with the waist radius w_0 at $z = 0$.

$w^2(z) = w_0^2\left[1+\left(\frac{\lambda z}{\pi w_0^2}\right)^2\right]$	$w_0^2 = w^2\left[1+\left(\frac{\pi w^2}{\lambda R}\right)^2\right]^{-1}$
$R(z) = z\left[1+\left(\frac{\pi w_0^2}{\lambda z}\right)^2\right]$	$z = R\left[1+\left(\frac{\lambda R}{\pi w^2}\right)^2\right]^{-1}$

of elements $\mathbf{M}_1, \mathbf{M}_2, ..., \mathbf{M}_i$ may be obtained by pre-multiplying the individual element transfer matrices, $\mathbf{M} = \mathbf{M}_i \times \cdots \times \mathbf{M}_2 \times \mathbf{M}_1$.

Diffractive beams in resonators may be treated by expanding in terms of Gaussian modes, of which the fundamental TEM_{00} is often of most interest [185]. At a given longitudinal coordinate position z, this mode is characterised by a $1/e^2$ beam spot radius $w(z)$ and a wavefront curvature $R(z)$. Separation of the lowest order Gaussian beam mode into transverse and longitudinal spatial functions gives rise to the complex beam parameter $q(z)$, defined as

$$\frac{1}{q} = \frac{1}{R} - i\left(\frac{\lambda}{\pi w^2}\right). \tag{2.20}$$

Its evolution in free space from the beam waist value q_0 where $z = 0$, $w(0) \equiv w_0$, $R(0) = \infty$, is given by $q(z) = q_0 + z$, from which we can derive a number of useful formulae, listed in table 2.2, relating the propagated parameters to the values at the waist. The evolution of a complex beam parameter q to q' through a system with transfer matrix $\mathbf{M}$ can be calculated using the matrix elements as

$$\frac{1}{q'} = \frac{C + \frac{1}{q}D}{A + \frac{1}{q}B}. \tag{2.21}$$

If $\mathbf{M}$ is the transfer matrix for a complete round-trip of a resonator, then a self-consistent solution with $q' = q$ leads to an expression for q at the reference plane of [199]

$$\frac{1}{q} = \frac{D-A}{2B} - \frac{i}{2|B|}\sqrt{4-(A+D)^2}. \tag{2.22}$$

Equations (2.21) and (2.22) facilitate numerical calculations of resonant mode dimensions, with unstable resonators readily identified as having $(A + D)^2 \geq 4$. For the cavity design process described in chapter 8, cavity round trip transfer matrices were calculated for a range of parameters, from which resonator mode spot sizes at the laser rod and nonlinear

optical crystal were determined using equations (2.20) and (2.22). The same principles may be extended to higher order Gaussian beams by the introduction of the M^2 beam quality parameter [200] and the replacement $\lambda \rightarrow M^2\lambda$ in the equations above.

2.4 Conclusion

Modelling of laser performance as described in this section was applied to the lasers developed in chapters 7 and 8. Numerical modelling of Q-switched pulses are compared to experimental data measured for a high repetition rate Q-switched Nd : YAG laser in chapter 7. The threshold predictions of equation (2.10) and the output power modelling of equation (2.11) were applied to the cw pump laser for the intracavity OPO constructed as described in chapter 8, the cavity configurations for which were designed using the techniques of section 2.3. Generally, good agreement between the theory and measured data was found.

Chapter 3

Nonlinear Optics

In this chapter, the theoretical foundations for nonlinear optical processes are presented. In section 3.1, Maxwell's equations are solved with a nonlinear polarisation term, leading to coupled energy transfer equations and phase matching (section 3.2). Threshold and acceptance bandwidths of optical parametric oscillators are derived in section 3.3, and relevant properties of the nonlinear optical materials used are summarised in section 3.4.

3.1 Nonlinear Optics

This section investigates the second order nonlinear polarisation term that gives rise to the nonlinear optical processes discussed in this thesis. In centro-symmetric crystals that feature inversion symmetry, a crystal symmetry results in a zero $\chi^{(2)}$ coefficient and third order nonlinear optical phenomena such as an intensity-dependent refractive index, Kerr lensing, self-focusing, two-photon absorption, and stimulated Raman scattering may be observed.

3.1.1 Origin of Susceptibility

The instantaneous electric field-induced polarisation at position $\mathbf{r}$ and time t may be expressed in its most general form as a Volterra expansion [201]

$$\begin{aligned}\mathbf{P}(\mathbf{r},t) &= \mathbf{P}^{(0)}(\mathbf{r},t) + \sum_{n=1}^{\infty} \varepsilon_0 \int dV_1 \int dt_1 \cdots \int dV_n \int dt_n \\ &\qquad \times \chi^{(n)}(\mathbf{r},t;\mathbf{r}_1,t_1;\ldots;\mathbf{r}_n,t_n)\, \mathbf{E}(\mathbf{r}_1,t_1)\cdots\mathbf{E}(\mathbf{r}_n,t_n), \quad (3.1)\end{aligned}$$

where $\chi^{(n)}$ is a tensor of rank $n+1$ that characterises the noninstantaneous and nonlocal dependence of $\mathbf{P}$ on $\mathbf{E}$ within the material, and ε_0 is the permittivity of free space. The in-

trinsic polarisation term $\mathbf{P}^{(0)}$ can exist without an external field, but at optical frequencies only dipole fluctuations contribute and the average value of this term vanishes.

In order to apply equation (3.1), we assume that the region of nonlocality is small compared to the wavelength of the electric field, eliminating $\mathbf{r}$. Causality leads to the polarisation $\mathbf{P}(t)$ being influenced only by the electric field $\mathbf{E}(t)$ at times $t_i \leq t$ and the material response function $\chi^{(n)}$ depending only on the response time $\tau_i = t - t_i$. Transforming into the more convenient frequency domain, we write the electric field in terms of positive and negative frequencies as $\mathbf{E}(t) = \int d\omega\ \mathbf{E}^{(\pm)}(\omega)\, e^{\pm i\omega t}$ with $\mathbf{E}^{(+)}(\omega) = [\mathbf{E}^{(-)}(-\omega)]^*$ to guarantee that $\mathbf{E} = \frac{1}{2}\left[\mathbf{E}^{(+)} + \mathbf{E}^{(-)}\right]$ is a real-valued function. Applying analogous relations to $\mathbf{P}$ and a two-dimensional Fourier transform to the second-order susceptibility $\chi^{(2)}$ yields

$$\mathbf{P}^{(2)}(\omega) = \varepsilon_0 \int_{-\infty}^{\infty} d\omega_1'\ \chi^{(2)}(\omega;\omega_1', \omega - \omega_1')\, \mathbf{E}(\omega_1')\mathbf{E}(\omega - \omega_1'). \tag{3.2}$$

The notation $\chi^{(n)}(\omega;\omega_1,\ldots,\omega_n)$, with $\omega = \sum_{j=1}^{n} \omega_j$, is introduced to emphasise the constrained relationship between ω and the ω_j, and, since both $\mathbf{E}(\omega)$ and $\mathbf{P}(\omega)$ are real, we have that $\chi^{(n)}(\omega;\omega_1,\ldots,\omega_n) = [\chi^{(n)}(-\omega;-\omega_1,\ldots,-\omega_n)]^*$.

Using the Einstein tensor notation listing vector components explicitly, it can be shown [57, 201] that the second order susceptibility obeys the symmetry relation $\chi^{(2)}_{ijk}(\omega;\omega_1,\omega_2) = \chi^{(2)}_{ikj}(\omega;\omega_2,\omega_1)$, which reduces the number of independent elements in $\chi^{(2)}_{ijk}$ from 27 to 18. It is therefore customary to introduce a contracted 3×6 element notation $\chi^{(2)}_{il}$ that allows the second-order nonlinear polarisation components to be written explicitly as

$$\begin{bmatrix} P_x^{(2)} \\ P_y^{(2)} \\ P_z^{(2)} \end{bmatrix} = 2\varepsilon_0 \begin{bmatrix} d_{11} & d_{12} & d_{13} & d_{14} & d_{15} & d_{16} \\ d_{21} & d_{22} & d_{23} & d_{24} & d_{25} & d_{26} \\ d_{31} & d_{32} & d_{33} & d_{34} & d_{35} & d_{36} \end{bmatrix} \begin{bmatrix} E_x^2 \\ E_y^2 \\ E_z^2 \\ 2E_yE_z \\ 2E_xE_z \\ 2E_xE_y \end{bmatrix}, \tag{3.3}$$

where, in common with experimental nonlinear optics, we have introduced the nonlinear optical coefficient $d = \chi^{(2)}/2$. In the case of second harmonic generation, the factors of 2 in of the compound electric field vector must be omitted, since in that case the interacting fields are indistinguishable [202].

Crystal symmetries, i.e., mapping operations that reproduce the crystal structure, force a number of d elements to be zero. Two crystal classes of relevance to the work presented in this thesis are the uniaxial 3m point group, of which $LiNbO_3$ is a member, and the biaxial mm2 point group, of which $KTiOPO_4$, $RbTiOAsO_4$, and LiB_3O_5 are

members. It can be shown that [202–204]

$$\begin{aligned} d_{il}^{(3\mathrm{m})} &= \begin{bmatrix} 0 & 0 & 0 & 0 & d_{15} & -d_{22} \\ -d_{22} & d_{22} & 0 & d_{15} & 0 & 0 \\ d_{31} & d_{31} & d_{33} & 0 & 0 & 0 \end{bmatrix} \\ d_{il}^{(\mathrm{mm}2)} &= \begin{bmatrix} 0 & 0 & 0 & 0 & d_{15} & 0 \\ 0 & 0 & 0 & d_{24} & 0 & 0 \\ d_{31} & d_{32} & d_{33} & 0 & 0 & 0 \end{bmatrix} \end{aligned} \tag{3.4}$$

An additional symmetry condition, formulated by Kleinman [205, 206], holds when the spectral range covered by the interacting frequencies does not include a crystal absorption band, and permits all elements of $\chi_{ijk}^{(2)}$ to be freely permuted with i, j, and k. As these permutations are effectively removing the significance of the frequencies of the respective electric fields, this is equivalent to neglecting dispersion of the nonlinear optical coefficient. In the collapsed notation of equation (3.3), Kleinman's symmetry yields the following simplifications [202, 204, 207]: $d_{12} = d_{26}$; $d_{13} = d_{35}$; $d_{14} = d_{36} = d_{25}$; $d_{21} = d_{16}$; $d_{23} = d_{34}$; $d_{31} = d_{15}$; and $d_{32} = d_{24}$.

For a given nonlinear interaction geometry, the multiplication of equation (3.3) can be performed to establish an effective nonlinear optical coefficient d_{eff}, such that $P^{(2)} = 2\varepsilon_0 d_{\mathrm{eff}} E_1 E_2$, rendering the interaction essentially one-dimensional with implied polarizations. The algebraic expression for d_{eff} will be determined by crystal class, phase matching geometry, and field polarisations of the interaction, and its definition may be extended to include quasi-phase matching, as discussed below.

We may consider the effect on the polarisation of a polychromatic field containing frequency components $\pm\omega_1$ and $\pm\omega_2$. The integration in equation (3.2) becomes a sum over the positive and negative frequencies that includes terms at the second harmonics (used for second harmonic generation, SHG) as well as the sum (sum frequency generation, SFG) and difference (difference frequency generation, DFG) of the incident frequencies. In addition, steady state terms proportional to $|E_j|^2$ account for the electro-optic effect of the material. Optical parametric oscillation may be regarded as a process analogous to sum frequency generation where a pump wave at frequency ω_3 generates the signal ω_2 and idler ω_1 frequencies via the $\chi^{(2)}(\omega_3; \omega_2, \omega_1)$ term, such that

$$\omega_3 = \omega_2 + \omega_1. \tag{3.5}$$

3.1.2 Coupled Rate Equations

The induced polarisation, in turn, affects the electric field, so that Maxwell's equations must be solved including the nonlinear term $\mathbf{P}^{(2)}$ term. In a lossless material, they may

be expressed as

$$\nabla \cdot \mathbf{D} = \rho \tag{3.6}$$

$$\nabla \times \mathbf{E} + \frac{\partial \mathbf{B}}{\partial t} = \mathbf{0} \tag{3.7}$$

$$\nabla \cdot \mathbf{B} = 0 \tag{3.8}$$

$$\nabla \times \mathbf{H} - \frac{\partial \mathbf{D}}{\partial t} = \mathbf{J} \tag{3.9}$$

We consider a nonmagnetic material that is non-conducting ($\mathbf{J} = \mathbf{0}$) and without free charges ($\rho = 0$). The magnetic field is then $\mathbf{H} = \mathbf{B}/\mu_0$, with μ_0 the magnetic permeability of free space. The electric displacement $\mathbf{D} = (\varepsilon_0 \mathbf{E} + \mathbf{P})$ may be rewritten as

$$\mathbf{D} = \varepsilon_0 \varepsilon_r \mathbf{E} + \mathbf{P}^{(2)}, \tag{3.10}$$

where the relative permittivity $\varepsilon_r = (1 + \chi)$ incorporates the linear polarisation term from equation (3.1). Higher order nonlinear terms may be included on the right hand side of equation (3.10).

The standard derivation of Maxwell's equations is followed [204, 208, 209]. The curl of equation (3.7) is taken, the identity $\nabla \times \nabla \times \mathbf{E} = (\nabla \nabla \cdot \mathbf{E} - \nabla^2 \mathbf{E})$ is employed; it is assumed that the order of temporal and spatial derivatives may be exchanged freely and that $\nabla \cdot \mathbf{E} = 0$. The terms of the resulting expression are replaced using (3.9) and (3.10), which leads, after some rearranging, to

$$\nabla^2 \mathbf{E} = \mu_0 \frac{\partial^2}{\partial t^2} \left[\varepsilon_0 \varepsilon_r \mathbf{E} + \mathbf{P}^{(2)} \right]. \tag{3.11}$$

In the absence of the $\mathbf{P}^{(2)}$ nonlinear term, equation (3.11) simplifies to Maxwell's famous wave equation whose general solution is a superposition of real-valued electromagnetic waves of the form

$$\mathbf{E}(\mathbf{r}, t) = \sum_j \frac{1}{2} \left[\mathbf{E}_j(\mathbf{r}) e^{i(\mathbf{k}_j \cdot \mathbf{r} - \omega_j t)} + \text{C.C.} \right], \tag{3.12}$$

where C.C. denotes the complex conjugate and ensures $\mathbf{E}(\mathbf{r}, t)$ is real. Upon substitution, we find that the propagation constants $k_j = |\mathbf{k}_j|$ are related to the material property parameters implicitly included in Maxwell's equations as

$$k_j = \frac{n_j \omega_j}{c} = \frac{2\pi n_j}{\lambda_j}, \tag{3.13}$$

where the refractive index $n_j = [1 + \chi^{(1)}(\omega_j)]^{1/2}$ and the speed of light $c = (\varepsilon_0 \mu_0)^{-1/2}$.

We simplify the solution of the nonlinear wave equation (3.11) with the nonlinear term $\mathbf{P}^{(2)}$ included by reducing the problem to a single spatial dimension. From the frequency cross-terms discussed above, we are motivated to propose a solution of the form

(3.12) consisting of a superposition of three frequency components satisfying equation (3.5), whose amplitudes $E_j(z)$ vary with distance z through the material. Substitution of the trial solution into equation (3.11) results in a large number of terms of the possible frequency combinations. In order for (3.11) to be satisfied over all z and t, individual frequency components must independently satisfy the wave equation. For the component at $\omega_3 = (\omega_1 + \omega_2)$, equation (3.11) yields

$$\begin{aligned}\left[\frac{d^2E_3(z)}{dz^2} + 2ik_3\frac{dE_3(z)}{dz} - k_3^2E_3(z)\right]\exp i(k_3z - \omega_3t) \; = \\ -\mu_0\varepsilon_0\varepsilon_r\omega_3^2E_3(z)\exp i(k_3z - \omega_3t) \\ + 2d\mu_0\varepsilon_0E_1(z)E_2(z)(\omega_1+\omega_2)^2\exp i[(k_1+k_2)z - (\omega_1+\omega_2)t].\end{aligned} \tag{3.14}$$

In general, $E_3(z)$ will be changing sufficiently slowly with z for the slowly varying envelope approximation $d^2E_3/dz^2 \ll k_3dE_3/dz$ to be valid [202]. The temporal dependence in (3.14) may be thus eliminated by dividing both sides by $\exp(-i\omega_3t) = \exp i[-(\omega_1+\omega_2)t]$ to yield an equation that describes the evolution of $E_3(z)$ as a function of the other two field amplitudes, and $\mu_0\varepsilon_0\varepsilon_r\omega_3^2 = k_3^2$ may be identified. Following a similar procedure for the other two components, $\omega_1 = (\omega_3 - \omega_2)$ and $\omega_2 = (\omega_3 - \omega_1)$, yields a set of equations known as the coupled rate equations,

$$\begin{aligned}\frac{dE_1(z)}{dz} &= -i\frac{\omega_1 d}{n_1c}E_3(z)E_2^*(z)\,e^{i\Delta kz} \\ \frac{dE_2(z)}{dz} &= -i\frac{\omega_2 d}{n_2c}E_3(z)E_1^*(z)\,e^{i\Delta kz} \\ \frac{dE_3(z)}{dz} &= -i\frac{\omega_3 d}{n_3c}E_1(z)E_2(z)\,e^{-i\Delta kz}\end{aligned} \tag{3.15}$$

where the wave vector mismatch Δk, generalised to a vector relation, is defined by

$$\Delta\mathbf{k} = \mathbf{k}_3 - \mathbf{k}_2 - \mathbf{k}_1. \tag{3.16}$$

The coupled rate equations (3.15) can be extended to include losses due to spatial mismatching of the interacting waves, incorporated by a multiplicative mode overlap factor g [78], and crystal absorption, by the inclusion of decay terms $-\alpha_jE_j$ [56]. Equations (3.15) may be combined to yield a set of equations known as the Manley–Rowe relations [210], with the physical interpretation of photon conservation, with each pump photon destroyed resulting in the generation of one pair of signal and idler photons, or vice versa.

3.1.3 Parametric Gain

The coupling of the field amplitudes by the rate equations (3.15) results in nontrivial general solutions that cannot be expressed in terms of algebraic functions unless approximations can be made. To find the small-signal gain in an optical parametric amplifier (OPA), we make the assumptions that pump depletion is negligible, so that $dE_3(z)/dz = 0$, and that the gain is sufficiently small that the signal or idler field may be approximated by the incident amplitude $E_j(0)$. Equations (3.15) may then be integrated directly over the crystal length L, with the first yielding an idler field gain

$$E_1(L) - E_1(0) = \frac{2\omega_1 d}{n_1 c} L E_3 E_2^*(0)\ \mathrm{sinc}\,(\Delta k L/2), \tag{3.17}$$

where $\mathrm{sinc}\,(x) \equiv (\sin x)/x$. A similar relation may be derived for $E_2(L)$. The OPA intensity gain thus varies as $\mathrm{sinc}^2(\Delta k L/2)$, and efficient nonlinear optical conversion necessitates matching of the phases such that $|\Delta k L| \leq \pi$.

For a phase matched interaction $\Delta k = 0$, the evolution of the signal and idler fields through the gain medium, in the negligible pump depletion approximation, can be found by combining the coupled rate equations (3.15) to obtain second-order differential equations for E_1 and E_2 of the form $d^2E_j/dz^2 - \Gamma^2 E_j(z) = 0$. The parametric gain coefficient Γ is related to the nonlinear interaction coefficient, denoted κ, by [211]

$$\kappa = \frac{\Gamma^2}{I_3} = \frac{2\omega_1\omega_2 d^2}{n_1 n_2 n_3 \varepsilon_0 c^3}, \tag{3.18}$$

where $I_3 = \frac{1}{2} n_3 \varepsilon_0 c |E_3|^2$ is the pump intensity. The general solutions have the form $E_j(z) = a_j e^{i\Gamma z} + a_j' e^{-i\Gamma z}$ with the integration constants a_j, a_j' determined by the boundary conditions. In a typical OPA configuration we may assume no initial idler field, $E_1(0) = 0$, and some weak initial signal field $E_2(0)$ arising from the $I_2 \sim 10^{-10}$ W quantum noise within the cavity. Numerical OPO models tend to not be sensitive to the exact value [212]. These boundary conditions lead to the solutions [78, 201, 204, 213]

$$\begin{aligned} E_1(z) &= i\left(\frac{n_2\omega_1}{n_1\omega_2}\right)^{1/2} \frac{E_3}{|E_3|} E_2^*(0) \sinh \Gamma z \\ E_2(z) &= E_2(0) \cosh \Gamma z \end{aligned} \tag{3.19}$$

so that the intensity gain for large z is approximately proportional to $e^{2\Gamma z}$.

To include a phase mismatch $\Delta k \neq 0$, we propose trial solutions of the form $e^{(Q \pm i\Delta k/2)z}$, whereupon the substitution into the equations (3.15) yield the relation $Q = \pm\Gamma'$, where

$$\Gamma' = \sqrt{\Gamma^2 - \left(\frac{\Delta k}{2}\right)^2} \tag{3.20}$$

represents the gain coefficient reduced by the phase mismatch. The solutions for the fields $E_j(z)$ are formally similar to those of equation (3.19), with multiplicative phase factors $e^{\pm i\Delta k/2}$ introduced in the trial solutions [201, 204].

3.2 Phase Matching

Normal dispersion typically yields a nonzero phase mismatch Δk for waves satisfying the energy conservation equation (3.5), precluding efficient nonlinear optical conversion. Compensating for dispersion, termed phase matching, may be achieved, for example, in anisotropic crystals by careful choice of the polarisation and crystal angle [214, 215], or by quasi-phase matching (QPM) [57].

3.2.1 Birefringent Phase Matching

In anisotropic media, there exists a selection of coordinate axes, in the representation of which $\chi^{(1)}_{ij}$, or equivalently the refractive index n_{ij}, is diagonal [206]. The diagonal elements in this frame, which is parallel to the principal dielectric axes and may be mapped to the crystallographic axes by a suitable tensor transformation, are denoted n_x, n_y and n_z. The mapping of crystal frames is the subject of some discussion in the literature [216] but common practices will be followed here [207].

The number of independent n_{ii} elements allows crystals to be classified into isotropic (all n_{ii} equal), uniaxial ($n_x = n_y \neq n_z$) and biaxial ($n_x \neq n_y \neq n_z$). In order to visualise the distribution of the refractive index tensor, we may use the bilayer index ellipsoid construction, applicable to orthogonal polarisations, defined by the parametric equation

$$\frac{x^2}{n_x^2} + \frac{y^2}{n_y^2} + \frac{z^2}{n_z^2} = 1 \tag{3.21}$$

and illustrated in figure 3.1 for uniaxial and biaxial crystals. Uniaxial and biaxial crystals are classified into positive ($n_e > n_o$, or $n_x > n_y > n_z$) or negative ($n_e < n_o$, or $n_x < n_y < n_z$).

Optic axes are defined by propagation directions for which the refractive index is independent of the polarisation. In a uniaxial crystal such as $LiNbO_3$, there exists one optic axis that is parallel to the Z axis. The refractive index $n^e(\theta)$ for an extraordinary ray, polarised within the principal plane, follows an ellipse with axes n_o and n_e,

$$n^e(\theta) = n_o \left[\frac{1 + \tan^2\theta}{1 + (n_o/n_e)^2 \tan^2\theta} \right]^{1/2}, \tag{3.22}$$

whereas the refractive index for the ordinary ray is constant at n_o, as shown in figure 3.1 (a). Biaxial crystals such as $KTiOPO_4$ have two optic axes at angle V_Z to Z in the XZ

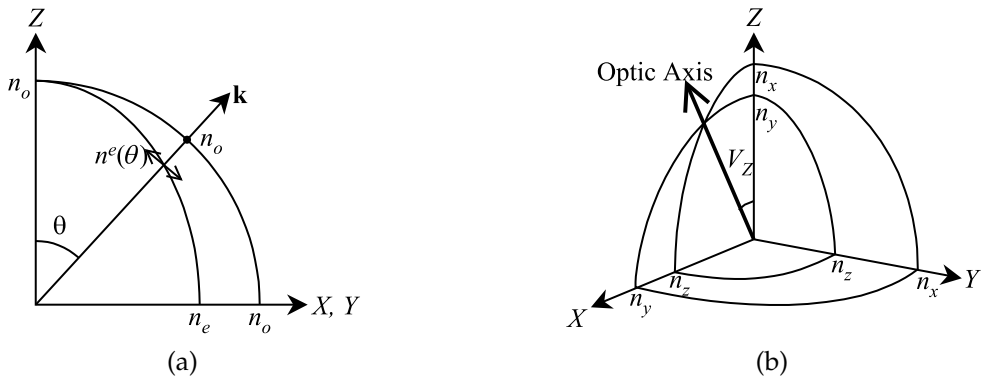

Figure 3.1: Index ellipsoids in anisotropic crystals. (a) Negative uniaxial crystal ($n_e < n_o$) with optic axis parallel to Z. (b) Positive biaxial crystal ($n_x > n_y > n_z$); the angle between the optic axis and Z is defined as V_Z. The field propagation vector is $\mathbf{k}$.

plane, with $V_Z < 45^\circ$ for positive biaxial crystals. To simplify the discussion, it is common [202, 207] to consider interactions in biaxial crystals only in the principal XY, XZ and YZ planes, whereupon the interactions become analogous to those in uniaxial crystals.

Under some circumstances, the appropriate choice of polarisations and interaction direction allows dispersion to be cancelled by birefringence so that $\Delta\mathbf{k} = \mathbf{0}$ in equation (3.16), either with all three $\mathbf{k}_i$ parallel (collinear interaction) or nonparallel (non-collinear interaction). The choice of polarisations allows interactions to be further categorised into type I and II. For example, a type I interaction in a negative uniaxial crystal is denoted *eoo* since the components at ω_3, ω_2, ω_1 respectively *e*, *o* and *o* polarised; while type II interactions are *eoe* or *eeo*. The wavelengths of critically phase matched interactions in anisotropic crystals may be tuned by the crystal temperature or by the crystal angle θ.

The application of Maxwell's equations (3.7) and (3.9) to a monochromatic plane wave in nonmagnetic and nonconducting anisotropic media shows that the wave vector $\mathbf{k}$ and Poynting vector $\mathbf{S} = \mathbf{E} \times \mathbf{H}$ are generally not parallel for an *e*-polarised wave [202]. This phenomenon, termed Poynting vector walkoff, places an upper limit on the interaction length for critically phase matched interactions in birefringent crystals [217]. Poynting vector walkoff may be avoided by phase matching along the principal axes, termed non-critical or 90° phase matching, but this is not always possible. Alternatively, non-collinear phase matching [218] or geometries using two walkoff compensating crystals [183, 219] may be used to partially compensate for the walkoff.

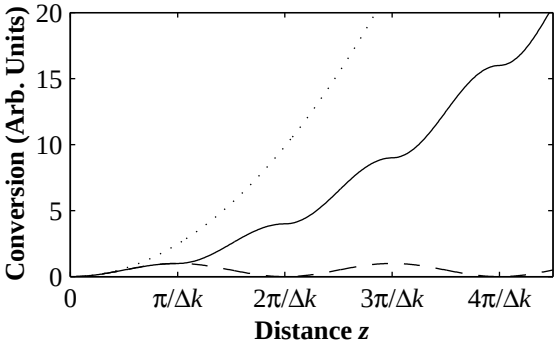

Figure 3.2: Conversion efficiency for quasi-phase matching. Dashed line, no phase matching; dotted line, ideal phase matching with $\Delta k = 0$; solid line, first order quasi-phase matching.

3.2.2 Quasi-Phase Matching

For a given phase mismatch Δk, the $e^{\pm i\Delta kz}$ factors in the coupled rate equations (3.15) result in a cycling of growth and decay (backconversion) of the frequency components, illustrated by the dashed line in figure 3.2, as dispersion shifts their relative phases. If the relative field phases are reset after every coherence length $\pi/\Delta k$, the generated wave experiences monotonic growth, a configuration termed first-order quasi-phase matching. The phase reset may be achieved by the periodic reversal, or modulation, of the nonlinear coefficient d with distance z. The periodicity may be formalised by expressing $d(z)$ as a Fourier series [56, 59]

$$d(z) = d_{\mathrm{b}} \sum_{m=-\infty}^{\infty} G_m e^{-iK_m z}, \tag{3.23}$$

where d_{b} is the effective nonlinear optical coefficient for the bulk material interaction, derived as outlined in the previous section. The Fourier component vectors are given by $K_m = m(2\pi/\Lambda)$, where Λ is the period of the modulated $d(z)$ coefficient.

Since only one phase matched Fourier component G_m contributes significantly to the nonlinear optical interaction, we may neglect the other terms in the sum of equation (3.23) and write, for interactions over many grating periods Λ, an effective nonlinear optical coefficient as $d_{\mathrm{QPM}} = d_{\mathrm{b}} G_m$ [56]. The parameter m is then termed the order of the quasi-phase matched interaction. For a complete periodic reversal of $d(z)$, such as that imparted by periodic poling, the Fourier coefficient G_m for order m may be written $G_m = (2/m\pi)\sin m\pi D$, where D is the duty factor of the poled grating [59]. It can be seen that for odd-order interactions, the effective nonlinear optical coefficient d_{QPM} is maximised with a 50% duty factor. The largest d_{QPM} is accessible in first order interactions, used in

the OPOs reported in this thesis, for which

$$d_{\mathrm{QPM}} = \frac{2}{\pi} d_{\mathrm{b}}. \tag{3.24}$$

In practice, the conversion efficiency may be lower than that predicted using equation (3.24) due imperfect poling or domain errors [59], which can arise by domain broadening due to the tangential electric field under the patterned electrode [220].

The periodicity of $d(z)$ expressed by equation (3.23) may be conveniently incorporated into the coupled rate equations (3.15) by the modified definition of the phase mismatch applicable to quasi-phase matched interactions,

$$\Delta k_{\mathrm{QPM}} = k_3 - k_2 - k_1 - \frac{2\pi m}{\Lambda}. \tag{3.25}$$

This expression emphasises the engineering flexibility imparted by the choice of grating period Λ, which permits any frequency interaction within the material transparency to be noncritically phase matched using the highest material d_{il} coefficient, with $\Delta k_{\mathrm{QPM}} = 0$. In addition, the flexibility in grating design has been exploited for applications such as smooth wavelength tuning using fan-out gratings [75, 131, 163], phase matching OPO and SHG interactions in the same crystal [221, 222], broadening of the acceptance bandwidth [76], and simultaneous SHG and pulse compression of fs pulses using a chirped grating [223]. A chirped grating has also been used to obtain pulses of $3\,\mu$m radiation only five optical cycles long [224].

3.3 Optical Parametric Oscillation

An optical parametric oscillator (OPO) is constructed by placing an OPA within a resonant cavity. A strong pump wave at frequency ω_3 generates signal and idler waves at ω_2 and ω_1, with enhanced conversion due to the resonator feedback. The devices used in this work, termed singly resonant OPOs, employed feedback only at the signal frequency.

3.3.1 Oscillation Threshold

Near threshold, the negligible pump depletion assumption made in deriving equations (3.19) applies. A temporal model presented by Brosnan and Byer [78] can be used to calculate approximate pulsed OPO threshold pump fluences. The time dependent pump intensity $I_3(t)$ may be conveniently expressed as a time-dependent parametric gain coefficient $\Gamma(t) = \Gamma e^{-(t/\tau)^2}$, with Γ as defined in (3.18), representing a Gaussian time profile of duration τ.

The signal power $P_{2,j}$, at frequency ω_2, after j round trips may be calculated using equation (3.19). Under the assumption that the pump intensity stays constant on a single round trip, we may write the recursive relation

$$P_{2,j} = P_{2,(j-1)} \left[R\, e^{-4\alpha L} \cosh^2 \left(\Gamma L e^{-(t_j/\tau)^2} \right) \right], \tag{3.26}$$

where α is the linear absorption within the nonlinear optical crystal; R the power reflectivity of the output coupler, which may be extended to include the effects of reflections from other cavity optics and the crystal faces; and L the crystal length. In birefringently phase matched interactions, the effective interaction length may be reduced from the crystal length by beam walkoff and overlap effects [78].

Equation (3.26) may be integrated by numerical methods to find a threshold pump intensity. An approximate analytic expression for the pump threshold fluence J_0 may be found by assuming a flat top pump temporal profile of duration 2τ. An iterative method is used to find the pump pulse energy required to yield a power to noise ratio $\ln(P_n/P_0) = 33$ during the pump pulse, corresponding to a signal energy of around 100 μJ. The threshold is then given by [78]

$$J_{3,\mathrm{thr}} = \frac{2.25\tau}{\kappa g_2 L^2} \left[\frac{L_c}{2\tau c} \ln \frac{P_n}{P_0} + 2\alpha L + \ln \frac{1}{\sqrt{R}} + \ln 2 \right]^2, \tag{3.27}$$

where L_c is the cavity length and κ is defined in equation (3.18). The signal mode coupling coefficient is given by $g_2 = w_3^2/(w_3^2 + w_2^2)$, where gain guiding and resonator mode considerations determine the signal mode waist w_2 [78]. The terms on the right hand side may be identified as contributions to the threshold arising from build-up time, crystal absorption loss, and output coupling, while the $\ln 2$ term arises from the singly resonant operation. Despite its broad simplifications, equation (3.27) is often in reasonable agreement with measured OPO thresholds and has been used to determine approximate d_{eff} values for periodically poled nonlinear optical crystals where a qualitative assessment of poling fidelity was difficult [117].

Threshold calculations are modified when focussed Gaussian beams are used. Guha *et al.* [225] used a Green's function approach in the calculation of cw OPO thresholds and found that the lowest threshold was, in general, achieved with unequal confocal parameters. The Brosnan and Byer model was extended by Terry *et al.* to include focusing and unequal absorption effects [226], with thresholds determined by integrating the modified gain equations over the duration of the pump pulse. The model predicted the measured performance of a bulk KTP more accurately than the Brosnan and Byer model, but an approximate analytic solution, such as that given by equation (3.27), was not established.

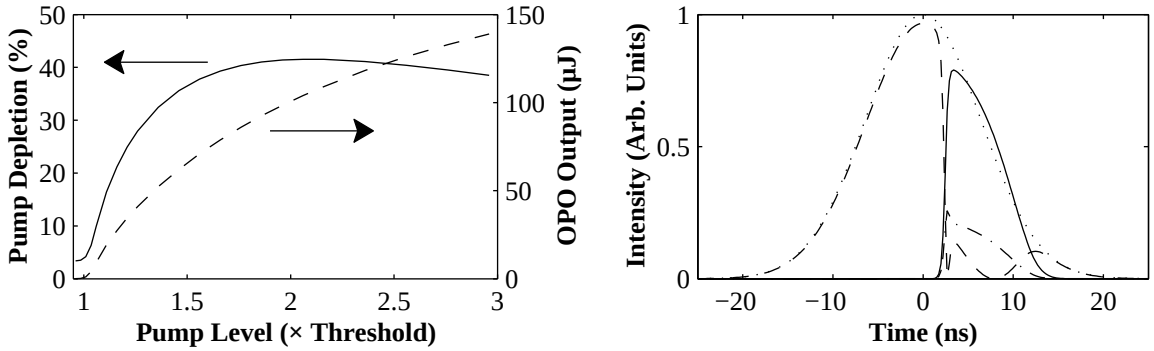

(a) (b)

Figure 3.3: Numerical integration of the coupled rate equations (3.15) for a pulsed PPLN OPO. (a) Pump depletion (solid line) and OPO output energy (dashed) as a function of pump level above threshold. (b) Temporal profiles of incident pump (dotted line); depleted pump (dashed); signal (solid); and idler (dash-dot); at 1.4 times threshold.

Models such as those presented in references [78] and [226] assume no pump depletion, and OPO behaviour above threshold typically requires the coupled rate equations (3.15) to be integrated directly using numerical methods. A simple model was developed to simulate a free running, 1.064 μm pumped PPLN OPO similar to those described in chapter 5, with a 20 mm long crystal and a cavity output coupler reflectivity of 60% at the signal wavelength. Results are shown in figure 3.3. A pump threshold energy of 90 μJ was established, compared to 300 μJ predicted using equation (3.27) and 220 μJ measured in chapter 5. The modelled pump depletion and OPO output energy are shown in figure 3.3 (a) as a function of pump level. To a good approximation, the fractional pump depletion at N times threshold is given by $\delta E_3/E_3 \propto (1 - 1/N)$, although this approximation neglects pulse build-up time effects [226]. The roll-over in the pump depletion was due to backconversion, as can be seen in the temporal profiles shown in panel (b), modelled at 1.4 times threshold. Qualitatively, the results of the numerical model of figure 3.3 agreed with experimental results, although absolute output energies and thresholds differed by factors of two or more. The differences may be due to a number of factors, including the plane wave approximation of the model, which tended to predict lower thresholds and higher output energies than the experimental devices pumped by Gaussian spatial distributions. The performance of a ns pulsed, injection seeded, bulk KTP ring OPO were modelled by Smith *et al.*, whose spatially resolved model included birefringence walkoff, diffraction, and absorptive losses in the crystal [212]. The model accurately predicted efficiencies, spectral profiles, beam quality, and spatially resolved temporal profiles in close agreement with measured data. Backconversion, the existence of which has been

established directly in a dual-wavelength seeded pulsed β-BaB_2O_4 OPO [227], was found to limit OPO efficiency and significantly influence all aspects of the OPO performance. Backconversion may also lead to self-focusing of the pump beam [228].

3.3.2 Acceptance Bandwidth

The phase mismatch tolerance of $|\Delta kL| \leq \pi$ discussed in reference to the OPA intensity gain equation (3.17) leads to acceptance bandwidths for interaction parameters such as wavelength, temperature, or angle. Quasi-phase matched interactions tend to have larger acceptance bandwidths compared to critical phase matching, since the interactions are noncritically phase matched with parallel polarised waves [59].

The OPA full width acceptance bandwidth $\Delta\zeta$ with respect to a general parameter ζ can be derived by expanding equation (3.16), or equation (3.25), as a Taylor series about $\Delta k = 0$,

$$\Delta k(\zeta) = \frac{\partial \Delta k}{\partial \zeta}\Delta\zeta + \frac{1}{2}\frac{\partial^2 \Delta k}{\partial \zeta^2}\Delta\zeta^2 + \ldots, \tag{3.28}$$

and, to first order, setting $\Delta kL = 2\pi$, where L is the crystal length [59, 78, 201, 208, 213]. For example, the temperature acceptance bandwidth ΔT may be calculated by setting

$$2\pi = 2\pi L\left(\frac{1}{\lambda_3}\frac{\partial n_3}{\partial T} - \frac{1}{\lambda_2}\frac{\partial n_2}{\partial T} - \frac{1}{\lambda_1}\frac{\partial n_1}{\partial T} + \frac{\alpha_{\mathrm{Th}}}{\Lambda}\right)\Delta T. \tag{3.29}$$

Using the Sellmeier equations of Jundt [81], we may calculate a temperature acceptance of $\Delta TL \sim 20\,^{\circ}\mathrm{C\,cm}$ for a general 1 μm pumped PPLN OPA.

The signal spectral acceptance bandwidth $\Delta\omega$ for a monochromatic plane wave pump may be calculated in a similar fashion. Since empirical Sellmeier equations are typically expressed as functions of the wavelength λ, identifying the group velocity index $c(dk/d\omega) = [n - \lambda(dn/d\lambda)]$ leads to a useful form of the spectral acceptance bandwidth,

$$\Delta\omega = \frac{2\pi c}{L} \times \left| n_2 - n_1 + \lambda_1 \frac{dn}{d\lambda}\bigg|_{\lambda_1} - \lambda_2 \frac{dn}{d\lambda}\bigg|_{\lambda_2} \right|^{-1}. \tag{3.30}$$

The spectral acceptance depends strongly on the wavelength and diverges as the OPO approaches degeneracy. An example of the spectral acceptance bandwidth of a 1.064 μm pumped PPLN OPO is shown in figure 5.11 on page 78. The OPA acceptance bandwidth is further broadened by the divergence and optical bandwidth of the pump radiation, since different wavevector components can phase match different wavelengths [59, 213, 225, 229, 230].

Table 3.1: Properties of nonlinear optical crystals used in this work [55, 211, 231–239].

Parameter		$LiNbO_3$	$KTiOPO_4$	$RbTiOAsO_4$	LiB_3O_5
Point Group		3 m	mm 2	mm 2	mm 2
Transparency (μm)		0.33–5.5	0.35–4.4	0.35–5.3	0.16–2.6
Refractive Index n_e or n_z at 1 μm and 25°C		2.16	1.83	1.88	1.61
Thermal Conductivity κ_{Th} (W/m K)		4.6	2.8		3.5
Thermal Expansion α_{Th} ($\times 10^{-6}$ K^{-1})		15.4	6.9	15.1	
Damage Threshold (MW/cm^2)		270	900	800	600
Figure of Merit d_{eff}^2/n^3 ($\times 10^{-24}$ m^2/V^2)		29	14	15	0.17
Nonlinear Coefficients (pm/V)	d_{15}	4.4	3.7	1.4	0.71
	d_{22}	2.1	0	0	0
	d_{31}	4.4	3.7	1.4	−0.67
	d_{32}	4.4	2.2	3.8	0.83
	d_{33}	27.2	14.6	15.8	0.04

3.4 Nonlinear Optical Materials

Good nonlinear optical materials, besides having large nonlinear optical coefficients d_{il}, should have a good transparency range without absorption, which could lead to heating and thermal focusing, and a high optical damage threshold, which scales approximately with $\tau^{1/2}$ for a pulse duration τ [78, 213]. For birefringent phase matching, the material must possess sufficient birefringence to permit phase matching but not so large as to restrict the acceptance bandwidths [213]. Nonhygroscopic materials are preferred since this eases operating environment requirements. Relevant crystal properties of the materials used in this work are summarised in table 3.1. Periodically poled $LiNbO_3$ (PPLN), $KTiOPO_4$ (PPKTP), and $RbTiOAsO_4$ (PPRTA) were used for various OPO interactions reported in the chapters 5–8, and bulk LiB_3O_5 was used to frequency double a high repetition rate Nd : YAG laser as reported in chapter 7.

3.4.1 Lithium Niobate

The negative uniaxial crystal $LiNbO_3$ offers one of the highest nonlinear optical coefficients $d_{33} = 27.2$ pm/V [78, 211] of any material suitable for 1 μm pumped OPO, and was the first electric field poled material to gain prominence [60]. The damage threshold for lithium niobate has been measured to be 2.7 J/cm^2 in a 10 ns pulse, with higher values measured for SiO_2 coated crystals on account of oxygen diffusion [78]. A relatively high coercive field of 21 kV/mm limits the thickness of periodically poled wafers to around 1 mm [61].

Sellmeier equations for congruent lithium niobate ([Li]/[Nb] = 0.946) were presented by Edwards *et al.* [240]. Based on their refractive index data, figure 3.4 (a) illustrates differ-

ent degenerate OPO, or, equivalently, SHG, interactions in quasi-phase matched PPLN, together with the effective nonlinear coefficient for each configuration. The heavy line indicates the phase matching periods for the type I quasi-phase matched interaction used in this work, employing the large d_{33} coefficient. At the expense of reduced nonlinearity, type II quasi-phase matched interactions can offer some benefits, especially for SHG to the blue and ultraviolet spectral region where short poling periods are required for first order type I phase matching. The longer periods ease fabrication tolerances and allow thicker, more uniformly poled crystals to be obtained, and the larger acceptance bandwidths permit the use of longer crystals, thereby compensating, in part, for the lower effective nonlinear coefficient [66, 241]. The use of off-diagonal tensor coefficients allowed Yu *et al.* to demonstrate broadband SHG in PPLN [242]. From figure 3.4 (a), birefringent phase matching is possible where $\Lambda \to \infty$ for the $e \to o + o$, type I birefringently phase matched interaction.

Improved long wavelength accuracy and temperature dependence of n_e was provided by the equation of Jundt [81] using phase matching wavelength measurements of mid-infrared PPLN OPOs,

$$\begin{aligned} n_e^2 &= 5.35583 + 4.629 \times 10^{-7} f + \frac{0.100473 + 3.862 \times 10^{-8} f}{\lambda^2 - (0.20692 - 0.89 \times 10^{-8} f)^2} \\ &\quad + \frac{100 + 2.657 \times 10^{-5} f}{\lambda^2 - 11.34927^2} - 1.5334 \times 10^{-2} \lambda^2, \end{aligned} \tag{3.31}$$

where λ is the wavelength in μm and the temperature parameter $f = (T - 24.5^\circ\text{C})(T + 570.82^\circ\text{C})$. The thermal expansion in lithium niobate may be described more accurately by adding a quadratic term $5.3 \times 10^{-9}(T - 25^\circ\text{C})^2$ to the linear expression given in table 3.1. The Sellmeier equations and thermal expansion expression have been found to accurately predict phase matching periods for as long as $6.6\,\mu$m [243], and were found to agree with experimentally measured wavelengths in this work. However, some published work has indicated that under short wavelength, high temperature conditions, the Sellmeier equations of Edwards *et al.* remain more accurate [132]. Other compositions of lithium niobate, such as stoichiometric, lithium-rich, or MgO-doped, exhibit different refractive index dependences [244].

Tuning curves for $1.064\,\mu$m and 532 nm pumped PPLN OPOs are shown in figures 3.4 (b) and (c), with the shaded regions showing the wavelength ranges accessible with the crystals used in this work. The curves were obtained by calculating, for a given set of frequencies satisfying equation (3.5), the corresponding first-order ($m = 1$) phase matched period Λ by setting $\Delta k_{\text{QPM}} = 0$ in equation (3.25). The thermal expansion of Λ was taken into account, and refractive indices given by equation (3.31) were used.

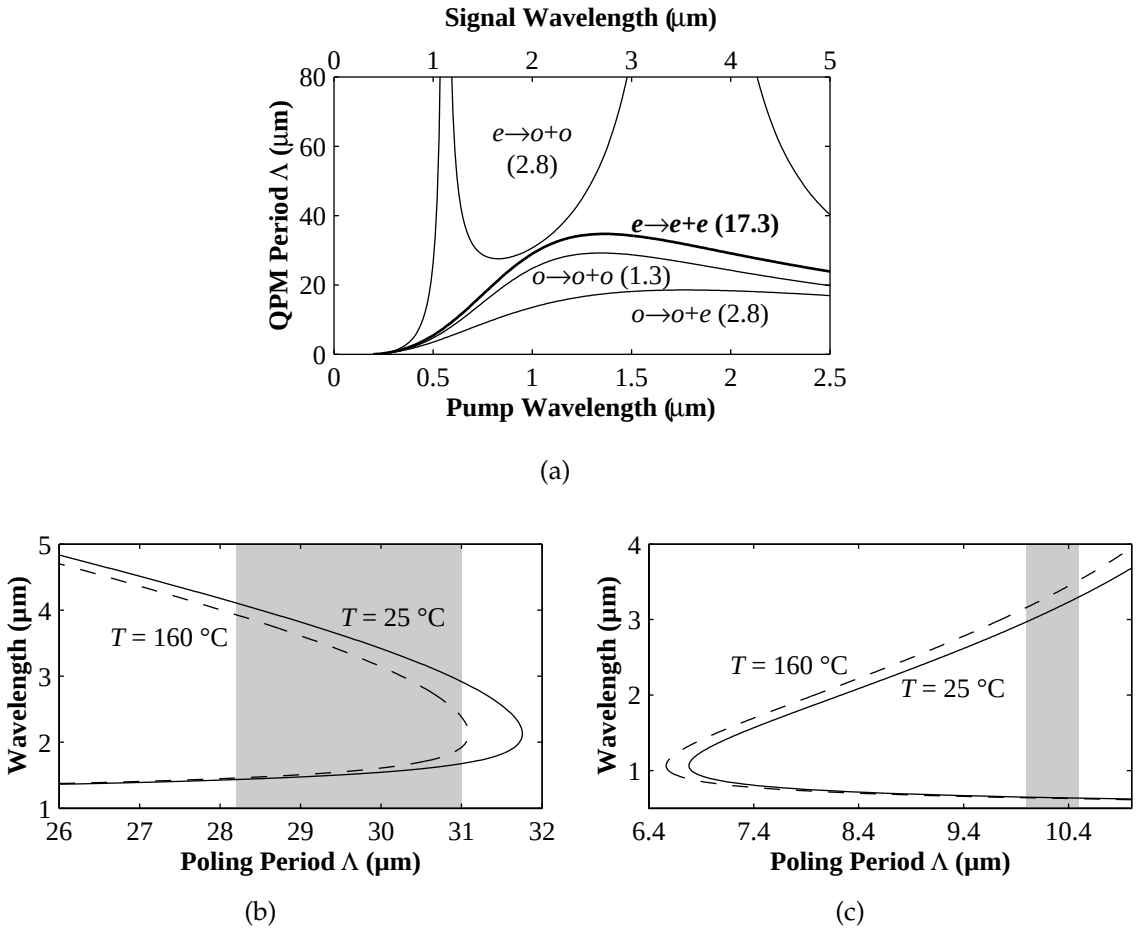

Figure 3.4: Quasi-phase matched interactions in PPLN. (a) Grating period Λ for degenerate OPOs (lower axis) or SHG (upper axis) for different interactions in $LiNbO_3$ at 160°C, and the effective nonlinear coefficient for each. (After [56].) (b) Theoretical PPLN tuning curves for OPOs pumped at 1.064 μm, and (c) at 532 nm, as a function of poling period Λ. The interaction used in this work is marked with a heavy line in (a), while the shaded regions in (b) and (c) indicate periods and wavelengths accessible through crystals available for the work presented here.

The high nonlinear optical gain in PPLN has enabled oscillation even under strong idler absorption. Generation of ps and fs idler pulses beyond 5 μm was demonstrated by Burr *et al.* [84] and Lefort *et al.* [87, 245]. An idler wavelength of 6.6 μm was generated by pumping with a Q-switched laser by Sato *et al.* [243], who found that the attenuation coefficient in $LiNbO_3$ drops from $\alpha = 40\,\mathrm{cm}^{-1}$ at $\lambda = 5.7\,\mu$m to $\alpha \sim 10\,\mathrm{cm}^{-1}$ around 6.2 μm. At such wavelengths, the transmission of the extraordinary polarisation was determined to be better than the ordinary [80]. The longest wavelengths generated in the work reported here were typically around 4.5 μm, where idler absorption was less severe [80].

3.4.2 Potassium Titanyl Phosphate

KTP is a member of the orthorhombic mm2 family of isomorphs $M\mathrm{TiO}X\mathrm{O}_4$, where M can be K, Rb, Tl, NH_4 or Cs, and X can be P or As [235, 237], the members of which typically offer high nonlinear optical d_{33} coefficients and a high optical damage threshold. KTP offers good transparency over the visible range, with an absorption coefficient of $0.5\%\,\mathrm{cm}^{-1}$ at 1.064 μm [246], but with an infrared cut-off around 4.4 μm [235, 247] and strong absorption features at 2.8 μm, due to OH^- absorption [248], and at 3.5 μm, due to PO_4 overtones [249]. The arsenates, such as RTA, exhibit a longer wavelength infrared cut-off of around 5.3 μm and reduced absorption features around 3.3 μm [71, 239, 248, 250]. $KTiOAsO_4$ (KTA) has properties similar to RTA, but a higher ionic conductivity [73, 115, 248, 251]; while $RbTiOPO_4$ (RTP) is less readily available but potentially offers the highest nonlinear optical coefficient of the family [72, 237].

The availability of high quality bulk KTP has resulted in the properties being generally well researched. The values for thermal conductivity κ_{Th} and expansion α_{Th} presented in table 3.1 are averages over the published values, parallel to the a, b, c axes, of $\kappa_{\mathrm{Th}} = 2, 3, 3.3\,\mathrm{W/m\,K}$ and $\alpha_{\mathrm{Th}} = 11, 9, 0.6 \times 10^{-6}\,\mathrm{K}^{-1}$ [211, 231, 235]. The value for the d_{33} nonlinear optical coefficient has been variously published to be between 10.7 pm/V and 18.8 pm/V [102–104, 110, 118, 235–237, 252, 253]; the value $d_{33} = 14.6\,\mathrm{pm/V}$ shown in table 3.1 is taken from the comprehensive study of nonlinearities presented by Shoji *et al.* [236].

A number of KTP dispersion relations, determined either by direct measurements using specifically cut prisms or by fitting experimentally observed phase matching wavelengths, as well as refractive index temperature derivatives, have been published in the literature. Table 3.2 summarizes the published coefficients for the n_z component of the refractive index of KTP. The Sellmeier equation of Fradkin *et al.* [112],

Table 3.2: Published Sellmeier equation coefficients for n_z of KTP (λ in μm).

		Sellmeier Coefficient							
Reference (Authors, Year)	**Eq.**	a_1	a_2	a_3	a_4	a_5	a_6	a_7	a_8
Fan *et al.* [254] (1987)	(a)	2.25411	1.06543	0.05486	—	—	—	—	0.02140
Liao *et al.* [255] (1988)	(a)	0.1494	3.1315	0.0236	—	—	—	—	—
Kato [256] (1988)	(b)	3.3209	0.05305	0.05960	—	—	—	—	0.01763
Anthon *et al.* [257] (1988)	(b)	2.006239	1.2965213	0.04807691	1.1329810	100	—	—	—
Vanherzeele *et al.* [258] (1988)	(a)	2.3136	1.00012	0.0567917	—	—	—	—	0.01679
Dyakov *et al.* [259] (1988)	(a)	1.94460	1.36170	0.04700	—	—	—	—	0.01491
Kato [247] (1991)	(b)	3.3134	0.05694	0.05658	—	—	—	—	0.01682
Boulanger *et al.* [260] (1997)	(a)	1.6539	1.6482	0.038825	0.34767	29.378	—	—	—
Fradkin *et al.* [112] (1999)	(a)	2.12725	1.18431	0.00514852	0.6603	100.00507	—	—	0.00968956
Katz *et al.* [261] (2001)	(a)	1	1.71645	0.013346	0.5924	0.06503	0.3226	67.1208	0.01133
Kato *et al.* [262] (2002)	(b)	4.59423	0.06206	0.04763	110.80672	86.12171	—	—	—
Kato [263] (1992)	(c)	0.3896	−1.3332	2.2762	2.1151	—	—	—	—
Wiechmann *et al.* [264] (1993)	(c)	1.2415	−4.4414	5.9129	1.2101	—	—	—	—
Kato *et al.* [262] (2002)	(d)	−0.5523	3.3920	−1.7101	0.3424	—	—	—	—

Dispersion Equations		**Temperature Derivatives**	
$n_z^2 = a_1 + \frac{a_2}{1-a_3/\lambda^2} + \frac{a_4}{1-a_5/\lambda^2} + \frac{a_6}{1-a_7/\lambda^2} - a_6\lambda^2$	(a)	$\frac{dn_z}{dT} = \left(\frac{a_1}{\lambda^3} + \frac{a_2}{\lambda^2} + \frac{a_3}{\lambda} + a_4\right) \times 10^{-5}$	(c)
$n_z^2 = a_1 + \frac{a_2}{\lambda^2-a_3} + \frac{a_4}{\lambda^2-a_5} + \frac{a_6}{\lambda^2-a_7} - a_8\lambda^2$	(b)	$\frac{dn_z}{dT} = \left(\frac{a_1}{\lambda} + a_2 + a_3\lambda + a_4\lambda^2\right) \times 10^{-5}$	(d)

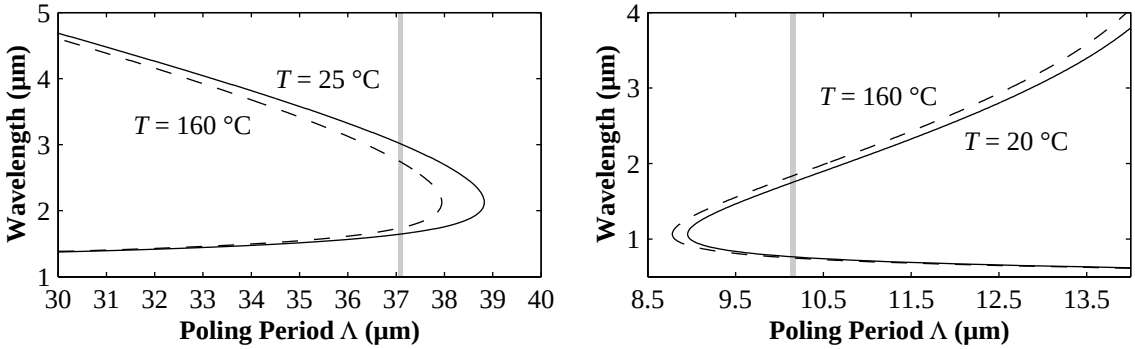

(a) (b)

Figure 3.5: Theoretical PPKTP tuning curves for OPOs pumped at (a) 1.064 μm and (b) 532 nm, as a function of poling period Λ. The Sellmeier equation of Fradkin *et al.* [112] was used in conjunction with the temperature dependence of Kato [263]. The shaded regions indicate periods and wavelengths accessible through crystals available for the work presented here.

$$n_z^2 = 2.12725 + \frac{1.18431}{1 - 5.148252 \times 10^{-2}/\lambda^2} + \frac{0.6603}{1 - 100.00507/\lambda^2} - 9.68956 \times 10^{-3}\lambda^2, \quad (3.32)$$

together with the temperature derivative of Kato [263],

$$\frac{dn_z}{dT} = \left(\frac{0.3896}{\lambda^3} + \frac{-1.3332}{\lambda^2} + \frac{2.2762}{\lambda} + 2.1151\right) \times 10^{-5}\ \mathrm{K}^{-1}, \quad (3.33)$$

was found to provide the best fit to the experimental data. Tuning curves for 1.064 μm and 532 nm pumped OPOs are presented in figure 3.5 as a function of poling period. At elevated temperatures, the more recent temperature dependent Sellmeier equation of Kato *et al.* [262] was found to give satisfactory agreement between predicted and measured wavelengths.

Laser induced photochromatic damage, commonly termed grey-tracking, has been observed in KTP with high intensity, short wavelength pulses. Proposed mechanisms for the formation of grey tracks include the formation of colour centres at Fe and Ti ion sites and two-photon absorption [265, 266]. The relaxation time for grey tracks can be accelerated by heating, and at crystal temperatures above $\sim$150°C the formation of grey tracks is typically suppressed [265]. In common with published reports pumping PPKTP under similar conditions [117], grey tracking was not observed in this work.

3.4.3 Rubidium Titanyl Arsenate

Of the KTP isomorph family, RTA is perhaps the most widely researched; nonetheless, its properties are much less accurately known. A low ionic conductivity, due to the larger

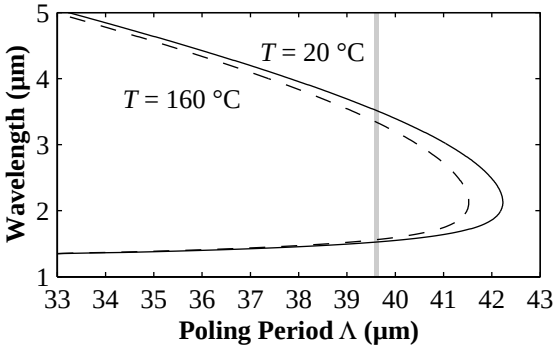

Figure 3.6: Theoretical PPRTA tuning curve for OPO pumped at 1.064 μm as a function of poling period Λ. The Sellmeier equation of Fradkin-Kashi *et al.* [250], was used in conjunction with the temperature dependence of Peltz *et al.* [127]. The shaded region indicates the period and wavelengths accessible with the crystal used in the work presented here.

size of the Rb ion compared to K, allows high quality bulk crystals to be periodically poled with thicknesses up to 3 mm [72, 121, 124, 127, 239, 267], and, unlike KTP, no pretreatment is required for room-temperature poling [250]. A number of different Sellmeier equations have been published for RTA [124, 234, 237, 250, 268]. The equation of Fradkin-Kashi *et al.*,

$$n_z^2 = 2.182064 + \frac{1.307519}{1-(0.228244/\lambda)^2} + \frac{0.354743}{1-(9.010959/\lambda)^2} - 0.008921\lambda^2, \tag{3.34}$$

determined using phase matching measurements of DFG in PPRTA [250], was found to agree most closely with wavelengths measured in this work. Of the published expressions for the n_z temperature variation [124, 127], closest agreement with measurements was found using the equation of Peltz *et al.* [127],

$$\frac{dn_z}{dT} = \left(\frac{0.1867}{\lambda^3} + \frac{13.2760}{\lambda^2} - \frac{12.2556}{\lambda} + \text{arb.}\right) \times 10^{-6}\ \text{K}^{-1}. \tag{3.35}$$

The PPRTA tuning curve is shown in figure 3.6 for a 1.064 μm pumped OPO. Additional properties are summarised in table 3.1 [234, 237].

3.4.4 Lithium Triborate

The growth of the negative biaxial, orthorhombic crystal LiB_3O_5 (LBO) was first reported in 1989 [55]. The material is particularly attractive for upconversion to visible and ultraviolet frequencies due to low absorption and a high damage threshold, and it has been widely used, for example in section 7.3, for SHG of the 1.064 μm Nd : YAG transition, which can be noncritically phase matched (yzz-polarised) with large acceptance angles

at 151°C [55]. For frequency doubling of 1.3 μm Nd : YLF, LBO was found to be superior to KTP due to reduced walkoff [269]. Sum frequency generation [270], optical parametric amplification [271] and oscillation [272] have also been demonstrated in LBO.

Dispersion relations have been published by a number of authors, [55, 238, 273], most recently by Mao *et al.* [271],

$$\begin{aligned} n_x^2 &= 2.45414 + \frac{0.011289}{\lambda^2 - 0.01135} - 0.014591\lambda^2 - 0.000066\lambda^4 \\ n_y^2 &= 2.53907 + \frac{0.012711}{\lambda^2 - 0.012523} - 0.01854\lambda^2 + 0.0002\lambda^4 \\ n_z^2 &= 2.586179 + \frac{0.013099}{\lambda^2 - 0.011893} - 0.017968\lambda^2 - 0.000226\lambda^4 \end{aligned} \tag{3.36}$$

The temperature derivatives have been published to be $dn_{x,y,z}/dT = (-1.8, -13.6, -6.3) \times 10^{-6}\,\mathrm{K}^{-1}$ [55]. Additional properties are summarised in table 3.1 [55, 232, 233, 238].

3.5 Conclusion

This chapter summarised the theoretical aspects of nonlinear optics. In practice, OPO design relies on the selection of an appropriate nonlinear optical crystal, chosen for high nonlinearity and damage thresholds as outlined in section 3.4. The crystal properties determine the range and acceptance bandwidths of interactions that can be phase matched with $\Delta k = 0$ in equation (3.16), or (3.25) in quasi-phase matched materials, while satisfying the energy conservation equation (3.5). Subsequently, OPO resonators are designed to yield a suitable combination of threshold and output power or energy at the desired wavelength, for which modelling of the coupled rate equations (3.15) is an invaluable tools.

Chapter 4

Optical Bandwidth Control

In the devices investigated in the subsequent chapters, the free running optical parametric oscillator (OPO) optical bandwidth was reduced by the implementation of passive intracavity frequency selective filters. Two types of filters were investigated, étalons and diffraction gratings. In this chapter, the narrowing of the OPO optical bandwidth due to the filter pass bandwidths, as well as multiple passes through the crystal and filters, are discussed. A review of the literature of the development and practical implementation of these techniques in OPOs was given in section 1.3.

The chief advantage of using passive filters lies in their simplicity. A minimal number of optical components is required so that compact and robust cavity configurations are maintained. However, passive band pass filters typically increase the effective cavity losses, resulting in increased thresholds and reduced output energies, especially if an extension of the cavity length, and a corresponding reduction in the number of cavity round trips, is necessary to accommodate the optical elements. Coupled cavities, not discussed in this work, can be constructed to partly compensate for the reduced OPO efficiency [274].

4.1 OPO Gain Bandwidth

The free-running optical bandwidth of an OPO depends on a number of parameters including the refractivity, dispersion, and absorption of the crystal, and the bandwidth, divergence, pulse duration and energy of the pump [157, 158, 227]. The single pass optical bandwidth of an optical parametric amplifier (OPA) may be estimated using a procedure similar to the acceptance bandwidth calculations in section 3.3. The gain bandwidth is broadened from the monochromatic plane wave pumped signal spectral acceptance given in equation (3.30) by the pump optical bandwidth $\Delta\omega_3$ as well as the pump full

angle beam divergence $\Delta\theta_3$. The resulting expression for the crystal gain bandwidth is [230, 275]

$$\Delta\omega_c = \left| \frac{1}{\beta_{21}} \left(\frac{2\pi c}{L} + \frac{2\pi c}{2\lambda_3} \frac{\partial n_3}{\partial \theta} \Delta\theta_3 + \Delta\omega_3 \beta_{31} \right) \right|, \tag{4.1}$$

where the group velocity index dispersion coefficient β_{ji} is given by

$$\beta_{ji} = c \left[\left. \frac{dk_j}{d\omega} \right|_{\omega_j} - \left. \frac{dk_i}{d\omega} \right|_{\omega_i} \right]. \tag{4.2}$$

In a free-running OPO, multiple passes through the crystal result in a narrowing of the optical bandwidth [78, 161, 213]. For M passes of a Gaussian gain profile, the bandwidth is narrowed to $\Delta\omega_{c,M} = \Delta\omega_c / M^{1/2}$. A potentially more accurate approximation that emphasises the significance of the pump divergence contribution to the optical bandwidth, by replacing the crystal length L with an effective length $L_{\text{eff}} = M^{1/2} L$, was found by Haub *et al.* to give better agreement with free running optical bandwidths of β-BaB_2O_4 OPOs [230]. Under free running pulsed conditions, the intensities of the OPO output spectral components are determined by starting conditions, typically resulting in irregular spectra that vary from pulse to pulse.

The introduction of an intracavity spectral filter with a single pass filter bandwidth of $\Delta\omega_f$, such as an étalon or diffraction grating, causes a reduction in the OPO optical bandwidth. The characteristics of the individual band pass functions are discussed in the sections below. Multiple traverses contribute to additional narrowing, and the multiple pass filter bandwidth is also given approximately by $\Delta\omega_{f,M} = \Delta\omega_f / M^{1/2}$ [78, 161].

Using these multiple pass gain and filter bandwidth expressions, the line narrowed OPO optical bandwidth can be written as [78]

$$\frac{1}{\Delta\omega_{\text{OPO}}} = \sqrt{\frac{1}{\Delta\omega_{c,M}^2} + \frac{1}{\Delta\omega_{f,M}^2}}, \tag{4.3}$$

where terms corresponding to additional band pass mechanisms may be added to the series within the radical. For the OPOs described here, the spectral filter term dominates. For example, the single pass gain bandwidth for a 20 mm long PPLN crystal, pumped at 1.064 μm to generate signal and idler wavelengths of 1.5 μm and 3.66 μm, may be calculated to be $\Delta\omega_c / 2\pi \approx 400\,\text{GHz}$ ($13\,\text{cm}^{-1}$) using equation (4.1). During a typical 5 ns OPO pulse, the crystal is passed $M \approx 30$ times, assuming a physical cavity length of $L_c = 50\,\text{mm}$, narrowing the free running OPO optical bandwidth to around 70 GHz. This value was in reasonable agreement with measurements of single shot spectra recorded for a free running PPLN OPO, such as those shown in figure 5.2 (a) on page 65. By

contrast, the multiple pass bandwidth of an intracavity étalon or diffraction grating was calculated as outlined below to be around $\Delta\omega_{f,M}/2\pi \sim 1\,\mathrm{GHz}$.

The OPO output spectrum is constrained by the frequency comb of standing wave modes of the OPO cavity. For most of the experiments reported in this work, the output coupler reflectivity was around $R \sim 0.7$, from which a cavity finesse of $\mathcal{F} = 8$ may be calculated. The cw cavity mode bandwidth for a 50 mm long cavity is then 250 MHz. This width may be broadened by the reduced effective pulsed finesse effects described by Daussy *et al.* [174], as well as reduced by the multiple cavity round trips. A comprehensive study of the relative magnitude of these effects was not undertaken here. The narrowest optical bandwidth resolvable by the Fabry–Pérot interferometers used as measurement devices was 250 GHz, which was sufficient to verify the desired single longitudinal mode oscillation, but not to yield high precision optical bandwidth measurements.

Some studies have reported that a single longitudinal mode signal can be achieved using passive line narrowing with a multi-mode pump, resulting in a broadband idler [78, 170]. Gloster *et al.* found that, although some of the excess pump bandwidth may be carried away by the non-resonant wave, a single longitudinal mode pump was required for single mode operation of a grazing incidence OPO [181, 219]. In the work presented here, single mode operation could not be achieved with broadband pumping. By contrast, cw pumped OPOs reach the limit of large M, and saturation commonly results in oscillation on a single mode, even with a multiple mode pump and no frequency selective elements [115, 128, 169].

4.2 Fabry–Pérot Etalon

One example of a frequency selective filter is the Fabry–Pérot étalon, where interference between successive internally reflected beams results in transmission occurring preferentially at specific wavelengths. The intensity transmission function, normalized to the incident intensity I_0, is determined by the interference between multiple reflections, and is given by [187, 208]

$$\frac{I(\phi)}{I_0} = \frac{1}{1 + \left(\frac{2}{\pi}\mathcal{F}\right)^2 \sin^2\left(\frac{\phi}{2}\right)}, \tag{4.4}$$

known as the Airy function. The relative phase between successive interfering fields at angular frequency ω in an étalon of refractive index n and thickness l is given by

$$\phi = \frac{2nl\cos\theta_t}{c}\omega, \tag{4.5}$$

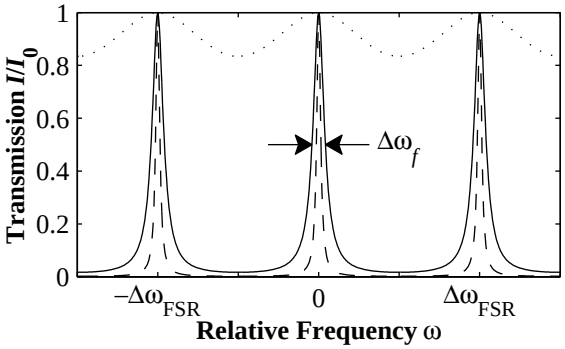

Figure 4.1: Normalised étalon transmission (Airy) function, defined in equation (4.4), as a function of relative frequency ω. The dotted, solid and dashed lines correspond to finesses $\mathcal{F} = 0.7$, 12, and 35. The étalon fringe optical bandwidth $\Delta\omega_f$ is indicated for the $\mathcal{F} = 12$ case, and $\Delta\omega_{\mathrm{FSR}}$ denotes the étalon free spectral range.

where the internal angle θ_t is related to the external incident angle θ_i by Snell's law. The period of the Airy function in frequency space is termed the free spectral range (FSR) and is given by $\Delta\omega_{\mathrm{FSR}} = 2\pi(c/2nl\cos\theta_t)$. The Airy function is shown in figure 4.1.

The finesse parameter $\mathcal{F}$ introduced in equation (4.4) is related to the intensity reflectivity of the étalon faces R by [187]

$$\mathcal{F} = \frac{\pi\sqrt{R}}{1-R}. \tag{4.6}$$

As can be seen from figure 4.1, the finesse determines both the contrast I_0/I_{min} and the optical bandwidth $\Delta\omega_f$ of each étalon fringe. For étalons with $\mathcal{F}^2 \gg \pi^2/2$ (corresponding to $R \gg 25\%$), the width of the fringes is approximately given by [187]

$$\Delta\omega_f \approx \frac{\Delta\omega_{\mathrm{FSR}}}{\mathcal{F}}. \tag{4.7}$$

The transmission contributions in an étalon narrowed OPO are sketched in figure 4.2. The conditions illustrated were chosen to model the experimental results presented in chapter 5, where single longitudinal mode operation of pulsed 1.064 μm pumped PPLN and periodically poled $KTiOPO_4$ OPOs was demonstrated using an intracavity étalon. A typical crystal gain bandwidth of $\Delta\omega_c/2\pi = 400\,\mathrm{GHz}$, shown by the dotted line, was assumed to be narrowed by $M = 30$ cavity round-trips to yield an OPO gain bandwidth as shown by the dashed line. The product of gain and transmission of an intracavity étalon of free spectral range $\Delta\omega_{\mathrm{FSR}}/2\pi = 30\,\mathrm{GHz}$ and a finesse $\mathcal{F} = 12$ is shown as the solid line in the lower panel, and may be regarded as a net gain–loss curve. Finally, the longitudinal cavity modes supported by the resonator, separated by $\Delta\omega_{\mathrm{mode}}/2\pi =$

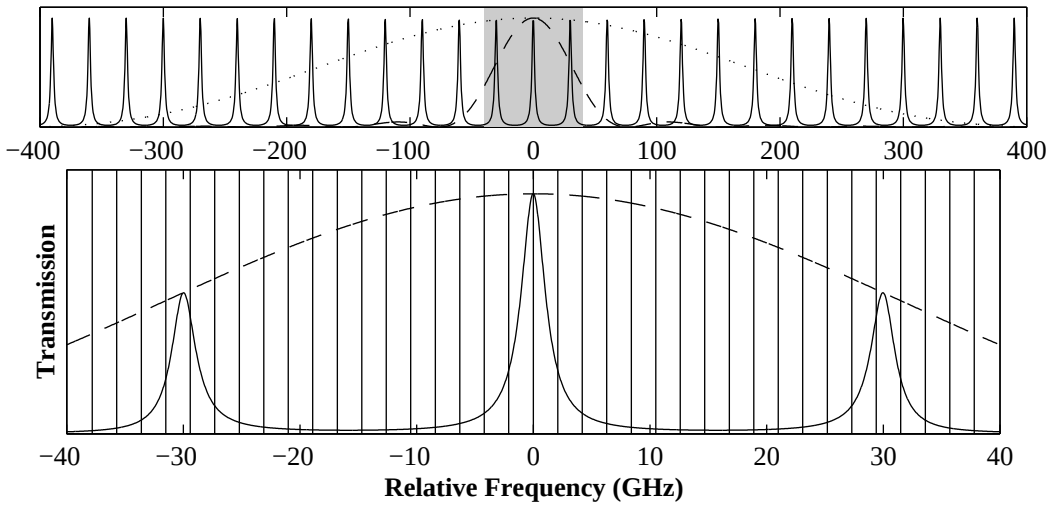

Figure 4.2: Combined OPO gain and cavity transmission characteristics with intracavity étalon. The crystal gain bandwidth (dotted line) is narrowed (dashed) by multiple passes and filtered by the intracavity étalon transmission function (solid) and the cavity modes (vertical strokes). For further discussion, see text.

$c/2L' = 2.1\,\mathrm{GHz}$, where L' is the optical length of the cavity, are shown as vertical strokes in the lower panel.

Under pulsed illumination the étalon transit time restricts the number of interfering fields, reducing the effective finesse if the number of étalon passes becomes small, as calculated by Daussy *et al.* [174]. In the experiments presented here, the ratio of cavity to étalon round trip times was usually in excess of 15, and an explicit summation of interfering fields yielded a pass bandwidth within 10% of the cw case. The residual finesse effects were assumed to be small, allowing the cw Airy function characteristics to be used in the bandwidth analysis.

The success of an étalon in narrowing the optical bandwidth of an OPO to a single longitudinal mode depends on a number of factors. It can be seen in figure 4.2 that an increase in the OPO gain bandwidth will decrease the relative losses of cavity modes that simultaneously satisfy the étalon transmission requirement. Especially under pulsed conditions, where gain saturation is typically not reached, above a certain OPO gain bandwidth there will be many modes that experience comparable gain, and the OPO output spectrum will be determined by incidental factors. An intracavity étalon is thus anticipated to become ineffective where the free-running OPO bandwidth diverges, such as near degeneracy. This was observed as reported in section 5.3. The periodicity of the Airy function potentially permits hopping between étalon modes if they shift rela-

tive to the cavity modes, such as when the étalon is tilted. Experimentally, such effects were observed but not investigated, and fine angle adjusts were typically necessary to obtain stable single longitudinal mode operation. Under broadband pumping, an étalon was expected be unable to restrict the signal optical bandwidth to a single mode due to frequency cross-terms between the broadband idler and the pump modes.

Insertion of an intracavity étalon results in higher thresholds, reduced output efficiencies, and lower pump depletions due to walkoff losses, acceptance angle constraints, and intensity build-up delays within the étalon [78, 172–174, 276, 277]. The round-trip loss coefficient L arising from multiple reflection walkoff within the étalon is given in the low-loss approximation by [173]

$$L \approx \frac{2R}{(1-R)^2}\left(\frac{2l\theta_i}{nw_0}\right)^2, \tag{4.8}$$

where w_0 the spot size perpendicular to the rotation axis. This approximation was not valid for the intracavity étalon configurations implemented in chapters 5 and 6, characterised by $R \approx 0.8$, $l = 3\,\text{mm}$, $\theta_i = 11\,\text{mrad}$, $n = 1.5$ and a resonated mode volume radius $w_0 \approx 200\,\mu\text{m}$. The beam distortion caused by walkoff of successive reflections within the étalon was calculated numerically, and round trip losses of up to $\sim$35%, subject to uncertainties in the spot size and divergence of the resonated signal wave, were calculated, in agreement with the modelling results presented by Leeb [173].

From equation (4.5), it can be seen that ϕ is determined the incident angle θ_i, the étalon thickness l, and the illumination wavelength λ. The dependence of ϕ on l and θ allows étalons to be used as frequency analysis tools, typically called Fabry–Pérot interferometers. The angular dependence of ϕ gives rise to the characteristic concentric rings of interference fringes when an interferometer is illuminated by a diverging source, and this effect was used to obtain the interference fringes presented in the results chapters of this thesis. The analysing interferometers comprised solid fused silica substrates in-house coated with silver to yield approximately constant reflectivity coefficients over the wavelength range used. The finesse in each case was determined by measurements of the injection seeded OPO pump laser, whose quoted optical bandwidth of around 10 kHz was substantially below the resolution limit of the interferometer.

4.3 Diffraction Grating

The general treatment of diffraction, which is somewhat lengthy, is given in many standard optics texts [185, 208, 209]. The normalised diffracted intensity distribution for N

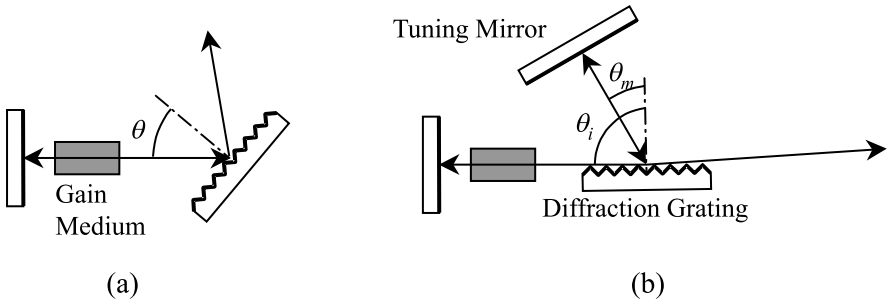

Figure 4.3: Intracavity diffraction grating configurations. (a) Littrow configuration, where the first diffracted order is coupled back into the gain medium. (b) Littman–Metcalf or grazing incidence configuration adopted for the work presented in this thesis.

illuminated grooves of width b and spacing d may be written as

$$\frac{I(\theta)}{I_{\max}} = \operatorname{sinc}^2\beta\left(\frac{\sin N\alpha}{\sin\alpha}\right)^2, \tag{4.9}$$

where $\alpha = \pi d(\sin\theta_i + \sin\theta_m)$ and $\beta = (b/d)\alpha$. The angles of incidence θ_i and diffraction θ_m are measured with the same sense relative to the grating normal. Since the groove spacing d exceeds the groove width b, the principal maxima are determined by the $(\sin N\alpha/\sin\alpha)^2$ term and occur at

$$d(\sin\theta_i + \sin\theta_m) = m\lambda, \tag{4.10}$$

where m is the diffraction order. In many practical situations the groove spacing d is chosen such that only one diffraction order is physically possible in the range of $|\theta_{i,m}| \leq 90^\circ$, which eliminates the spatial overlap of adjacent free spectral ranges in étalons and allows diffraction gratings to be used for line narrowing even close to OPO degeneracy [278].

Figure 4.3 shows the two intracavity diffraction grating configurations that have most commonly been used for wavelength selectivity. In the Littrow configuration illustrated in figure 4.3 (a), the first order of diffraction is used directly as feedback into the cavity, constraining the incidence and diffracted angles to be equal [277–279]. The minimum resolvable wavelength difference is inversely proportional to the illumined grating width [176], so that the resolution of a diffraction grating in the Littrow configuration is limited by the beam diameter. The resolution may be improved by the use of beam expansion optics, usually at the expense of additional losses and increased resonator lengths [78, 277].

The Littman–Metcalf, or grazing incidence, configuration was adopted for the work presented here [175, 176]. The diffraction grating was inserted into the cavity with a high

incidence angle, $\theta_i \geq 85^\circ$, and a separate tuning mirror completed the resonant cavity as illustrated in figure 4.3 (b). In this geometry, the number of illuminated grooves can be controlled by the grating angle, independent of the wavelength. A fortuitous advantage of the large incidence angle is a reduced risk of laser induced grating damage, since the beam is distributed across a large area of the diffraction grating.

The single pass resolution of a grazing incidence diffraction grating illuminated by a Gaussian beam of width w_g, limited by the divergence of the incident beam, is given by $\Delta\lambda = \lambda^2/\pi w_g \tan\theta_i$ [161, 175]. This expression remains valid until the beam fills the width of the grating L_g, and it can be shown that the highest resolution is achieved when the grating is placed at the Rayleigh length from the focus [176]. In this case, and the minimum resolvable wavelength difference becomes

$$\Delta\omega_f = 2\pi c \frac{2\sqrt{2}}{\pi L_g(\sin\theta_i + \sin\theta_m)}. \tag{4.11}$$

The efficiency of a diffraction grating depends on the shape of the individual grooves, independently of the diffraction equation (4.10), allowing blazed gratings with improved efficiencies at specific wavelengths and angles to be manufactured [208, 280]. In the work of this thesis, holographic gratings with sinusoidal grooves were used, which have no blaze angle. For this groove profile, the s polarisation, perpendicular to the grooves, is diffracted more efficiently than the p polarisation [280]. The specular reflection (zeroth diffraction order) has the highest power efficiency and constituted the OPO output. On one cavity round trip, the resonant beam was diffracted twice, so that the effective output coupling of the cavity was estimated to be around $\sim$90%, increasing with increasing grating angle θ_i [161]. In addition, physical constraints when constructing the cavity mean that long average cavity lengths are required for large tuning mirror angles θ_m. From the results presented in chapters 5 and 6, the grazing incidence cavity was found to be suited mainly to high gain, low output energy systems operating at ≤ 1.5 times threshold, which were also used as seed sources for amplifiers.

Cavity Length Stabilisation

Tuning in the grazing incidence configuration is accomplished by tilting of the tuning mirror. This changes both the cavity length and angle θ_m, and continuous single-mode tuning requires that the pivot point of the tuning mirror coincides with the end mirror of the optical cavity [178, 219, 281]. In practice, a cavity length servo is often used both for continuous tuning and to stabilise the single mode output against mechanical disturbances [183, 282].

A cavity stabilisation scheme proposed by Raymond *et al.* [282], and previously implemented in a bulk KTP [183] OPO, detects small changes in output pointing direction that result from detuned wavelengths resonating within the cavity. A wavelength detuned by $\Delta\lambda$ from λ, for which the grating equation (4.10) results in a closed path through the cavity, will exit the grazing incidence cavity with an angular deviation $\Delta\theta \approx 2\Delta\lambda/d\cos\theta_i$, where the factor of 2 arises from the beam being diffracted twice [282]. These angular deviations may be detected using a suitably placed split photodiode and processed to generate an error signal to lock the grazing incidence cavity to a single longitudinal mode. An adjacent cavity mode, separated by $\Delta\lambda = \lambda^2/2L'$, will be separated by angular deviation

$$\Delta\theta_{\text{mode}} \approx \frac{\lambda^2}{L'd\cos\theta_i}. \tag{4.12}$$

Raymond *et al.* proposed that the beam deflection would be more difficult to detect if the beam divergence $\lambda/\pi w_0$ exceeded the angular separation of adjacent cavity modes, thereby placing a lower limit on the waist size $w_0 \geq L'd\cos\theta_i/\pi\lambda$. This condition was not satisfied in the OPO presented in chapter 5. The success of this stabilisation relies on stable short-term single mode operation of the OPO, and mechanical vibrations, air currents, and pump instabilities must be minimised. Due to the $\cos\theta_i$ term in the denominator of equation (4.12), good locking performance requires the largest possible grating angle θ_i. However, this simultaneously decreases the feedback efficiency from the grating, so a compromise between large dispersion and low diffraction efficiency must be reached. Investigations of the influence of grating angle have been carried out in grazing incidence BBO and PPLN OPOs [161, 181]. An alternative locking scheme was reported by Boon-Engering *et al.* in a BBO OPO, in which the error signal was determined by a computer evaluating single shot Fabry–Pérot interferometer spectra of the signal radiation [219]. This technique was not attempted here.

4.4 Injection Seeding

Injection seeding provides an alternative approach for obtaining narrowband OPO output, and was demonstrated in a monolithic PPLN OPO in chapter 7. The method involves a low power, narrowband seed that injected into the resonant cavity, from which the seeded frequency grows rapidly as determined by the coupled rate equations (3.15). The operating range of injection seeding is restricted to that accessible by suitable seed sources, and, since the injection seed wavelength must satisfy the standing wave criterion of the resonator, active locking of the cavity length or seed source is usually necessary for

successful long term seeding.

Injection seeding has been extensively studied in lasers and OPOs, being first applied to pulsed OPOs by Bjorkholm and Danielmeyer [167]. Baxter *et al.* [160, 168] developed a particularly effective spectroscopic source based on a PPLN OPO injection locked by a tuneable semiconductor laser and subsequently amplified in a bulk $LiNbO_3$ amplifier. The tuned optical bandwidth of the system was established to be 130 MHz by means of coherent anti-Stokes Raman spectroscopy in methane. Maintaining the OPO cavity on resonance with the seed source required active cavity locking [168]. A novel technique for rapid pulse to pulse tuning in PPLN was demonstrated by Yang and Velsko [283] using an acousto-optically tuned pump angle to select phase matching for one of two simultaneously injected single mode semiconductor seed sources.

4.5 Conclusion

The contributions to the OPO output optical bandwidth were considered in this chapter, including the crystal gain bandwidth, intracavity filter pass bandwidth, and narrowing due to multiple pass effects. The passive line narrowing techniques discussed in this chapter were implemented in the experimental OPO devices reported in the following chapters. Both intracavity étalons and diffraction gratings were demonstrated to yield single longitudinal mode OPO operation.

Chapter 5

Infrared Pumped OPOs at 10 Hz Repetition Rate

Optical parametric oscillators (OPOs) pumped $\lambda_3 \approx 1\,\mu$m are typically employed to generate a near-IR signal wavelength around $\lambda_2 \sim 1.5\,\mu$m and a mid-IR idler wavelength $\lambda_1 \sim 3.5\,\mu$m. The strong $1.064\,\mu$m laser transition in Nd : YAG yields efficient, reliable, high power pump sources whose spatial, spectral, and temporal characteristics can be finely controlled, making these lasers uniquely suited for pumping OPOs. This chapter reports on experiments on $1.064\,\mu$m pumped OPOs that incorporated passive frequency selective filters to narrow the emitted optical bandwidths. The OPOs were based on the quasi-phase matched materials periodically poled $LiNbO_3$ (PPLN) (section 5.2) and $KTiOPO_4$ (PPKTP) (section 5.3), with OPO tuning curves presented in figures 3.4 (b) (page 44) and 3.5 (page 47) respectively. Within each section, the experimental results are presented for different cavity configurations; in particular, intracavity étalon or a diffraction grating in the grazing incidence configuration. A direct comparison between the two nonlinear optical materials was often not possible, since the crystals had different characteristics, including operating wavelengths. Some general conclusions between the relative merits of the materials are presented in the conclusion, section 5.4.

5.1 Continuum Powerlite 7000

The pump source used for the experiments in this chapter, with the exception of the cavity scanning results of section 5.2.5, was a modified Continuum Powerlite PL7000 oscillator–amplifier system. The laser comprised two Nd : YAG rods, both 115 mm long with 6 mm diameter, pumped by one Xe flashlamp at a pulse repetition rate of 10 Hz. The single-rod oscillator was electro-optically Q-switched by a KD^*P Pockels cell and thin film polariser,

and quarter-wave plates were used to yield circular polarisation within the laser rod to prevent spatial hole burning. The cavity was seeded by a single frequency (90 kHz specified optical bandwidth) non-planar ring Nd : YAG laser [284] injected via the polarizer. An electronic feedback circuit locked the resonator length to the seed signal until the Q-switch opened. The resonator was completed by a Gaussian reflectivity output coupler. The output was single-pass amplified in the second Nd : YAG rod and could be passed through KD*P frequency doubling and sum frequency mixing crystals to yield output at 532 nm or 355 nm. A custom addition of an apodiser between oscillator and amplifier yielded an excellent spatial quality output beam ($M^2 \leq 1.1$) at the expense of pulse energy. The laser generated up to 400 mJ in 8 ns pulses at 1.064 μm and 180 mJ in 6 ns pulses at 532 nm. For many of the experiments described below, the oscillator-only output was used, and the Q-switch delay was extended from the optimum 185 μs to obtain pulse durations of $\sim$15 ns while maintaining successful seeding.

5.2 OPOs Based on Periodically Poled $LiNbO_3$

Two PPLN crystals were available for pumping at 1.064 μm. Both crystals had dimensions $20 \times 11 \times 0.5\,\text{mm}^3$ (length $\times$ breadth $\times$ thickness). One of the crystals was supplied by Crystal Technologies, Inc. The crystal had eight adjacent tracks of $\Lambda = 28.5, 28.7, \ldots, 29.9\,\mu$m. The crystal end faces were single layer antireflection coated with SiO_2 ($n = 1.45$) to yield $\leq 0.5\%$ reflectivity over the range 1.4–1.7 μm. Due to the high refractive index of $LiNbO_3$ ($n \approx 2.2$), significant residual reflectivity existed at the pump and idler wavelengths. The second crystal was obtained from Deltronic Crystal Industries. This had 14 poling periods of $\Lambda = 28.2, 28.5, 28.7, \ldots, 29.9, 30.2, 30.4, \ldots, 31.0\,\mu$m, and the end faces were multilayer antireflection coated at the pump, signal and idler wavelength ranges. The crystals were housed in a temperature controlled oven capable of maintaining temperatures up to 220°C with $\pm$0.1°C accuracy. The crystal oven was mounted on a precision three-axis translation stage to permit accurate crystal positioning and track selection. Although no photorefractive effects were observed here, due to low average powers even at the maximum pump levels used, the crystals were operated at 160°C as a precaution [56, 61, 101].

5.2.1 Linear Cavity PPLN OPO

A linear, plane–plane cavity, with a physical length of 39 mm, sufficient to accommodate an étalon between crystal and output coupler, was constructed to determine a reference for OPO performance. One mirror, through which the pump entered the OPO cavity, was

a 2° wedged fused silica substrate coated for $R > 99\%$ over 1.35–1.60 μm while maintaining $T > 70\%$ at the 1.064 μm pump wavelength. A number of different output coupling optics were available: Two dielectric mirrors on fused silica substrates providing reflectivities of 95% and 66% over the signal wavelength range, and an uncoated ZnS window with a reflectivity of 14% by Fresnel reflection. The lack of coating on the ZnS window meant similar reflectivities were present at the pump and idler wavelengths. The 4% Fresnel reflection from a fused silica window was found to be too low to bring the OPO above threshold.

The modified Continuum PL7000 oscillator was used as a pump source. A half wave plate and polariser combination permitted smooth, variable control of the pump energy incident on the OPO up to 1.5 mJ. The pump beam was focused by a 500 mm focal length achromat, with the PPLN crystal placed beyond the waist of the pump beam to avoid the effects of optical damage and monolithic oscillation [285]. When the PPLN crystal was located at the waist of the pump beam, a measurable depletion of the pump pulse was observed for pump energies in excess of 480 μJ, even without cavity optics, with the depletion reaching 40% at a pump pulse energy of 1 mJ. As the pump energy was increased to 2 mJ, damage to the PPLN crystal occurred after a few minutes of operation, setting an upper limit on the pump fluence used subsequently. The observed pump depletion could be attributed to single pass optical parametric generation (OPG), or to the crystal faces forming a low finesse monolithic resonator. Since OPG under these operating conditions usually requires longer crystals and monolithic oscillation was subsequently observed in other OPO experiments presented here, the observations were attributed to the latter. Parametric generators and monolithic oscillators have been identified as useful systems for robust, broadband, tuneable near or mid infrared sources [91, 96, 98, 193, 286–289], but the generation of output was in this case a parasitic process. When the PPLN crystal was placed before the waist of the beam, damage to the output coupler was observed when an étalon was inserted into the cavity, possibly as a result of misaligned multiple reflections between étalon and output coupler. The centre of the PPLN crystal was accordingly positioned 40 mm beyond the waist formed by the pump focusing lens. This pump configuration resulted in a slightly diverging pump beam with an average waist of 170 μm ($1/e^2$ radius) inside the crystal and avoided spatial aperturing at the faces of the PPLN crystal.

The OPO performance results for this simple cavity with different output coupling optics are summarised in table 5.1 and served as a benchmark for comparison with the frequency narrowed cavities discussed below. The 95% reflective output coupler resulted in the lowest OPO threshold of 190 μJ, while the 14% optic generated the greatest signal

Table 5.1: Performance of a linear cavity PPLN OPO with different output coupling optics. The highest pump pulse energy used was 1 mJ.

Parameter	$R = 95\%$	$R = 66\%$	$R = 14\%$
Threshold (μJ)	190	240	580
Peak Signal Energy (μJ)	21	155	175
Signal Slope Efficiency (%)	2.8	22	35
Pump Depletion (%)	68	68	44

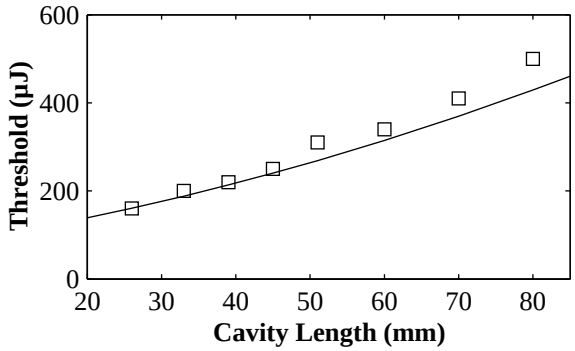

Figure 5.1: Threshold of a linear cavity PPLN OPO as a function of cavity length. Squares, values measured using a $R = 66\%$ output coupler; solid line, theoretical prediction using equation (3.27).

output pulse energy, 175 μJ. The 66% reflecting output coupler was selected for the remainder of experiments, since it provided a suitable compromise between threshold and output the energy. The idler pulse energy could not be measured since the idler wavelength was absorbed by the output coupler optic substrates.

Although the cavity length was constant at 39 mm for the work presented in this section, more complex OPO resonators required an increased cavity length. The oscillation threshold was measured as a function of cavity length by moving the output coupler. The data showed a factor of 2.3 increase in threshold when the cavity length was doubled to 80 mm, and is presented in figure 5.1 together with a solid fit line calculated using the simplified threshold model, equation (3.27), of Brosnan and Byer [78]. The threshold model parameters used were pump spot size $w_3 = 180\,\mu$m, pump pulse duration $\tau = 10$ ns, and $\ln(P_n/P_0) = 150$. The model agreed satisfactorily with the measured threshold energies.

5.2.2 Etalon Narrowed PPLN OPO

In order to narrow the optical bandwidth of the OPO, a number of étalons were tested in the OPO cavity. Three different étalons were available, with free spectral ranges (FSR) of 400 GHz, 100 GHz, and 30 GHz. Only the last of these was successful in narrowing

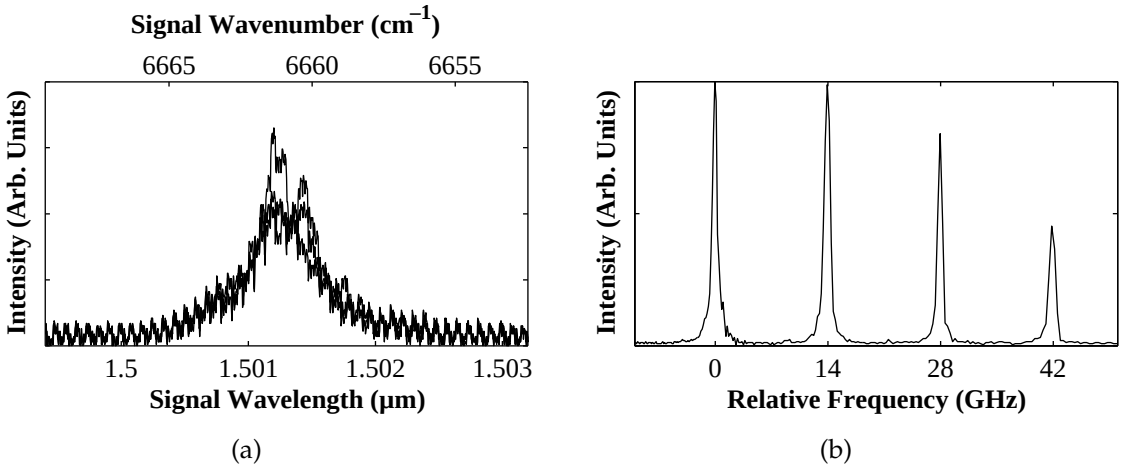

Figure 5.2: Signal spectra of an étalon narrowed PPLN OPO. (a) Free-running spectrum measured using a 0.75 m monochromator; the ripples are due to electronic noise. (b) Line profile through fringes produced by a 14 GHz free spectral range Fabry–Pérot interferometer indicating an instrument limited étalon narrowed optical bandwidth of 450 MHz.

the OPO spectral bandwidth to a single longitudinal mode. This solid fused silica étalon (TecOptics, ES-251-189-189) had broadband dielectric coatings with reflectivity $R \approx 78\%$ per face over the wavelength range 1.06–1.50 μm, and was absorptive at idler wavelengths. This corresponded to a finesse $\mathcal{F} = 12$. The laser damage threshold of the étalon coatings was specified to be $8\,\mathrm{J/cm^2}$.

The free running OPO signal optical bandwidth was determined from the signal plus pump sum frequency component, measured using a 0.75 m grating monochromator. The broadband spectrum varied from shot to shot but had a $\sim$1 nm ($\sim$120 GHz) optical bandwidth at the signal wavelength. This is illustrated in figure 5.2 (a) with the OPO operating at a signal wavelength of 1.501 μm. The rapid oscillatory structure was spurious, resulting from the detection system electronics used.

The intracavity étalon was typically introduced into the OPO cavity at a small tilt to prevent pump retroreflections, as well as coupled cavity geometries between the étalon and crystal faces or cavity optics. The OPO performance was observed to deteriorate with increasing étalon tilt, yielding both higher thresholds and lower output pulse energies. Since temporal delays introduced by the étalon interference [174] were calculated to be negligible for the étalon used, the performance degradation was primarily attributed to beam walkoff effects within the étalon [173]. Such losses may be reduced by the use of thinner, lower finesse étalons, but these were found to be ineffective in obtaining single mode operation. A coarse étalon tilt of around 11 mrad was used throughout, with

fine adjustments to obtain reliable single longitudinal mode operation. Single mode oscillation was readily obtained when the OPO was tuned to wavelengths throughout the range between 1.449 μm and 1.594 μm using a combination of crystal track and temperature adjustments.

In order to assess the influence of the étalon, the output of the OPO was monitored using different Fabry–Pérot interferometers with FSRs between 5 GHz and 100 GHz, in-house coated with metallic silver. In each case a cylindrical lens was used to expand the beam in the horizontal plane prior to entering the interferometer. An achromat lens was used to image the interferometer fringes on a CCD camera. The signal and pump sum frequency component, generated within the PPLN crystal to detectable but negligible pulse energies, was used for spectral measurements since InGaAs or similar detector arrays capable of detecting signal wavelengths around 1.5 μm were not available [285]. As the linewidth of the pump was well below the instrument resolution, the bandwidth of the sum frequency radiation could be attributed solely to the signal. Figure 5.2 (b) shows a characteristic single mode signal spectrum measured using a 14 GHz FSR FPI. The $\mathcal{F} = 30$ finesse of this interferometer was sufficient to resolve OPO resonator modes (mode spacing 2.7 GHz), and the measurement confirmed single axial mode operation of the OPO. The instrument limited FWHM optical bandwidth was 450 MHz. Similar measurements using a 100 GHz FSR interferometer with finesse $\mathcal{F} = 50$ confirmed that oscillation was occurring under only a single étalon mode.

The OPO output signal pulse energy, with and without the intracavity étalon, is shown in figure 5.3 (a) as a function of pump energy, with the OPO was operating at a signal wavelength of 1.501 μm. On insertion of the étalon, the oscillation threshold increased from the free running value of 220 μJ to 410 μJ, while the signal output pulse energy at the maximum 1 mJ pump energy dropped from 140 μJ to 78 μJ. The lines in figure 5.3 had slope efficiencies of approximately 18% and 14% respectively for the free running and étalon narrowed cavities. The decreasing slope at high pump energies on both lines is attributed to backconversion effects that become significant above $\sim$2 times threshold [117].

Measured pump depletions are plotted in figure 5.3 (b) as a function of pumping level. The increased threshold of the étalon narrowed cavity and the limited damage threshold of the PPLN crystal and the étalon coatings restricted the pumping level to just below 2 times threshold in the single mode cavity, while the free running OPO could be pumped at nearly 4 times threshold. From figure 5.3 (b) it was concluded that the raised threshold on insertion of the étalon, due to increased cavity losses, accounted for most of the performance degradation compared to the free running cavity.

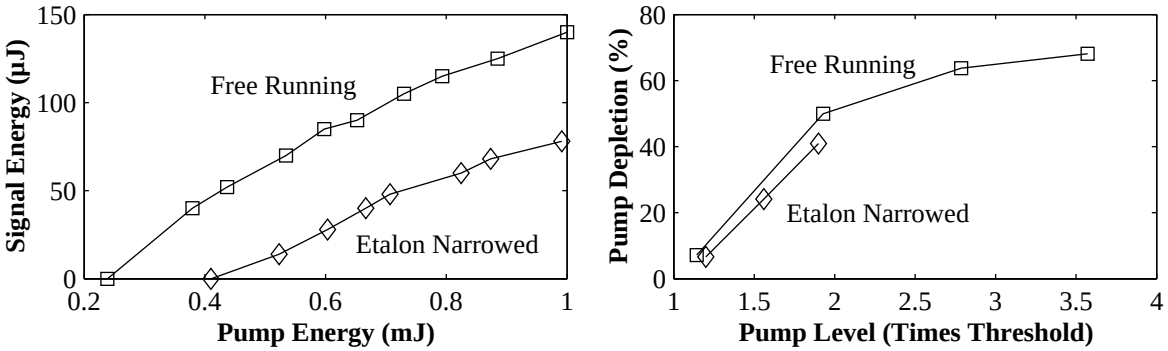

(a) (b)

Figure 5.3: (a) Signal pulse energy and (b) pump depletion of a PPLN OPO, in free running broadband (squares) and étalon narrowed single longitudinal mode (diamonds) oscillation. Panel (b) is plotted against the number of times above threshold. The OPO was operating on a signal wavelength of 1.501 μm.

Temporal profiles for the PPLN OPO, illustrated in figure 5.4, were recorded using fast photodiodes: The incident (dotted line) and depleted (dashed line) pump pulses were recorded using Si photodiodes, while an InGaAs photodiode was used to monitor the generated 1.5 μm signal pulses (solid line). Both varieties of photodiode were reverse biased to yield nominal 1 ns rise times. A Tektronix TDS 350 digital storage oscilloscope, with a bandwidth of 200 MHz, was used to sample and store the traces. The pulses demonstrated standard characteristics of OPOs pumped at several times above threshold. Close to threshold, trace (c), the output signal pulse shape is short and somewhat symmetric. As the pump energy is increased (d) to (a), the build-up time of the signal pulse decreases and the pulse widens, with a slowly decaying trailing edge. In common with other findings [56, 212, 227], traces (a) and (b) indicate the presence of backconversion when the OPO is pumped at more than $\sim$2 times threshold. This is indicated by a regrowth in the pump field resulting in a lobe at the centre of the depleted pump profile. From the pulse profiles, it can be seen that the temporal characteristics of the OPO with an intracavity étalon remained largely unchanged except for the increased threshold.

The threshold of the free-running OPO did not show significant variations over the OPO tuning range, whereas the étalon narrowed threshold decreased from 510 μJ at a signal wavelength of 1.45 μm to 340 μJ at 1.59 μJ. This effect may have been due to wavelength dependent loss in the étalon, indicating that optimum étalon coatings should lead to threshold increases of 1.5 times across the tuning range of the OPO[285]. Similarly, pump depletion was typically between 60% and 70% for the free running cavity, while the étalon narrowed cavity gave slightly lower results, consistently across the wavelength

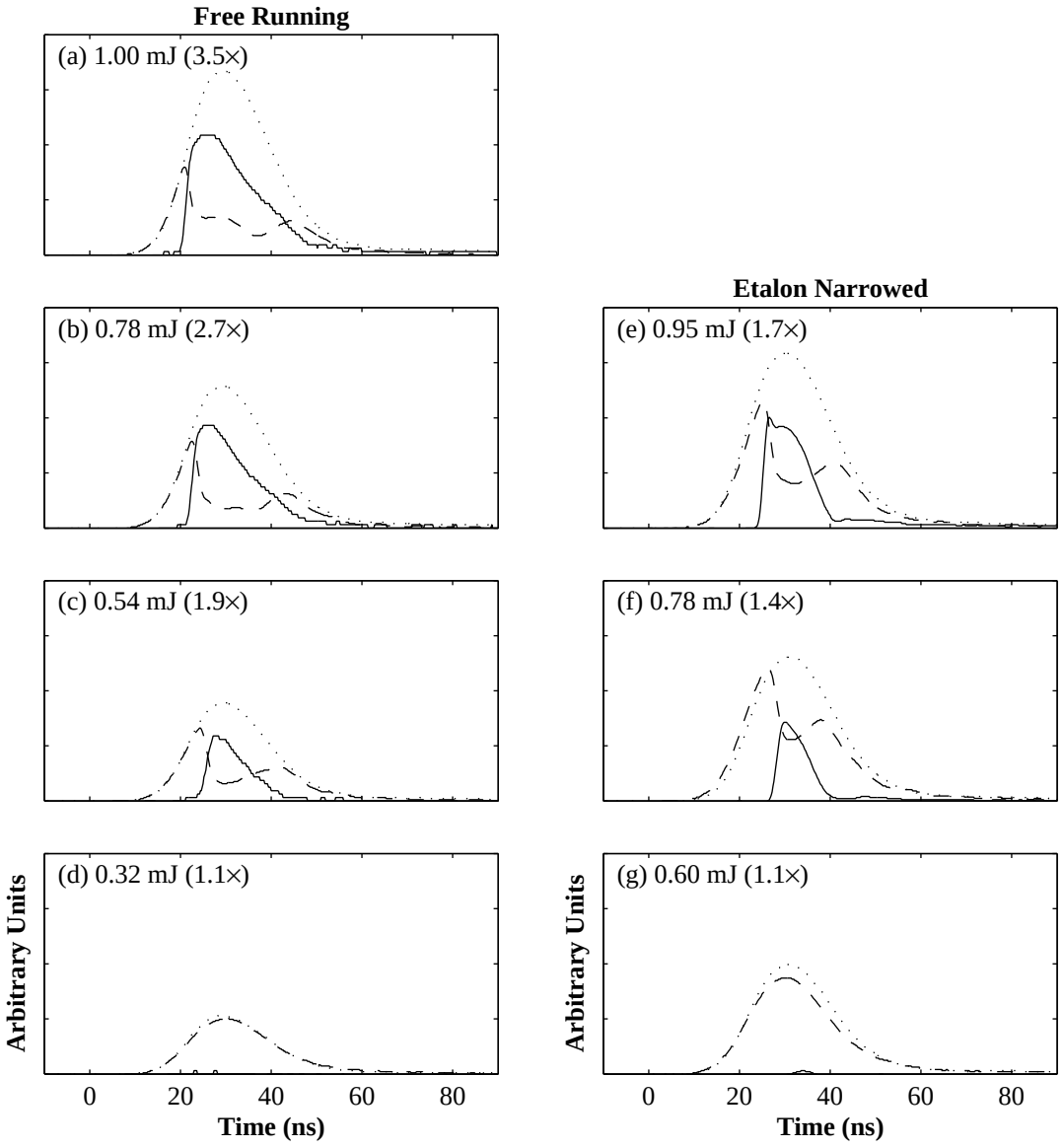

Figure 5.4: Temporal profiles of a PPLN OPO, without (left column) and with (right) intracavity étalon. Solid line, OPO signal pulse; dashed line, depleted pump; dotted line, incident pump. The pump pulse energy and times above OPO threshold is shown in each case. The vertical axes are constant within each group of plots.

range measured.

Beam profile measurements were taken by scanning a 100 μm aperture InGaAs photodiode through the signal beam. The signal from the photodiode was averaged over 10 pulses using a Stanford Research Systems SR250 gated boxcar integrator, and the measured intensity spatial distributions were fitted to Gaussian curves in order to establish $1/e^2$ intensity radii. While the OPO was operating successfully on a single longitudinal mode, the output beam was observed to be smooth and with a Gaussian spatial distribution. Vertical and horizontal slice measurements of the single longitudinal mode signal beam were taken at various propagation distances from the OPO,. Estimating a signal beam waist of 230 μm within the PPLN crystal from pump overlap considerations, the single mode signal beam was estimated to have a beam quality parameter $M^2 = 1.5$. Multimode OPO operation resulted in an unstable output beam with shot to shot fluctuations, arising from the plane–plane cavity configuration allowing higher order transverse modes to oscillate [91], that could not be profiled using the scanning photodiode technique.

The influence of pump bandwidth on the single mode OPO signal output was investigated by blocking the injection seed to the pump laser. This resulted in the Nd : YAG pump laser operating on around 50 axial modes within a 15 GHz envelope. Since the sum frequency mixing process between signal and pump convoluted the spectral bandwidths of both wavelength components, the radiation from this process could not in this case be used to establish the optical bandwidth of the signal beam. Instead, the non-phase matched second harmonic of the signal at ~750 nm was used. Under multimode pumping the OPO signal output became more erratic, with significant fluctuations in output energy, and the étalon was not sufficient to yield a single mode signal output. This suggested, consistent with the observations of other authors [181], that stable single frequency operation of ns OPOs required a single axial mode pump source.

5.2.3 Cascaded Oscillation

The collinear interaction and inherent periodicity of the phase matching configuration in QPM can result in the phase matched generation of frequency components other than the primary signal and idler waves, although fortuitous coincidence of multiple wavelength phase matching is not restricted to QPM [290]. One possible QPM interaction is a cascaded OPO [291], in which one of the fields generated by the primary OPO becomes sufficiently intense to drive a cascaded OPO interaction. A signal wave driven cascaded OPO was observed experimentally; a cascaded OPO driven by the idler was considered

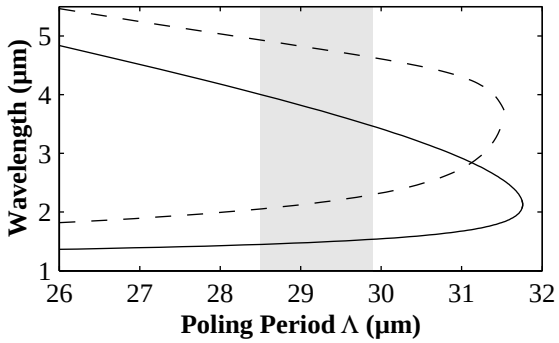

Figure 5.5: Tuning curve for a 1.064 μm pumped cascaded PPLN OPO, operated at $T = 25°$C. The solid line is the conventional OPO interaction as shown in figure 3.4 (b) on page 44. The dashed line shows the cascaded OPO wavelengths. The shaded region indicates periods and wavelengths accessible with the crystal used.

less likely, since the idler was not resonated, suffered absorption in the étalon substrate, and had a lower photon energy.

The cascaded signal ω_2' and idler ω_1' frequencies of a cascaded OPO, driven by the primary signal field ω_2, must satisfy the energy conservation and phase matching conditions

$$\begin{aligned} \omega_2 &= \omega_2' + \omega_1' \\ \Delta k'_{\mathrm{QPM}} &= k_2 - k_2' - k_1' - \frac{2\pi m}{\Lambda} = 0, \end{aligned} \tag{5.1}$$

where $k_i' = n(\omega_i')c\omega_i'$. A tuning curve for the cascaded OPO was calculated by simultaneously solving the set of equations (3.5), (3.25), and (5.1) for given pump frequency ω_3, poling period Λ, and crystal temperature T, using the Sellmeier equation of Jundt [81]. The tuning curve for a $\omega_3 = 1.064\,\mu$m pumped cascaded PPLN OPO, operating at $T = 25°$C, is shown in figure 5.5.

A cascaded OPO may offer a cost-effective and potentially robust way to obtain mid-IR radiation, or tailored multiple wavelength emission, provided that the long wavelength cascaded idler is not absorbed within the crystal. Under most circumstances, cascading may limit the primary OPO efficiency by depleting the intracavity signal field, similarly to backconversion. It can be eliminated by degrading the OPO cavity efficiency at the cascaded wavelengths, e.g. by specific anti-reflection coatings on the cavity mirrors, or by introducing an intracavity dispersive element such as a prism to ensure singly resonant oscillation.

Cascaded oscillation was observed while operating a linear cavity PPLN OPO as described in the previous section. The round trip mirror reflectivities at the cascaded signal

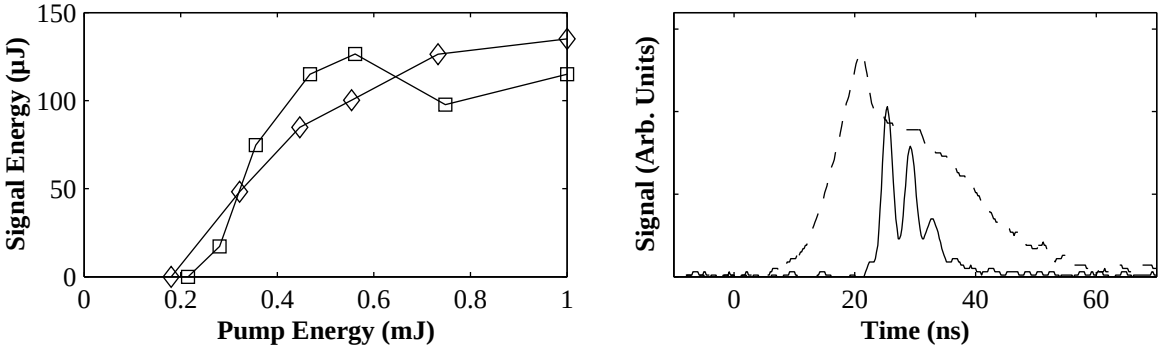

(a) (b)

Figure 5.6: Performance of a PPLN OPO, showing the onset and elimination of cascading. (a) Signal pulse energy with the cavity aligned and subject to cascaded operation(squares); and cavity misaligned by $\sim$2 mrad to eliminate cascading up to the maximum pump pulse energies used (diamonds). (b) Temporal profiles of the signal (solid line) and depleted pump (dashed line) of the aligned cavity. The oscillatory structure visible on the signal pulse was not present on the depleted pump, indicating that the structure arose from cascading rather than backconversion.

wavelengths varied between 30% and 90% over the wavelength range 1.7–2.0 μm. For the results presented here, a set of wavelengths $\lambda_2 = 1.55\,\mu$m, $\lambda_1 = 3.39\,\mu$m, $\lambda_2' = 2.34\,\mu$m, $\lambda_1' = 4.58\,\mu$m was arbitrarily chosen by crystal track selection. A primary OPO oscillation threshold of 200 μJ (26 MW/cm^2) was measured. Cascaded OPO operation was first indicated by a roll-over in the signal output energy, as shown by the squares in figure 5.6 (a), at around three times threshold. Simultaneously, the signal output pulse, shown as the solid line in figure 5.6 (b), was observed to have an oscillatory structure that indicated a dynamic nonlinear interaction with another field. In an OPO pumped well above threshold, backconversion can yield a similar temporal structure through a pump–signal interaction, but the absence of corresponding structure on the residual pump temporal profile, shown as a dashed line, precluded this possibility.

Cascaded operation was confirmed by measuring the wavelengths of weak output beams arising from non-phase matched upconversion interactions of the cascaded OPO frequency components. The output of the OPO, with the residual pump radiation eliminated by a dichroic optic with adequate transmission at visible wavelengths, was delivered to a 0.75 m grating monochromator via a fibre patchcord. An Ikegami CCD camera was placed in the focusing plane of the monochromator output slit and used to observe the frequency components in the range 300–1000 nm. Several OPO wavelength components were detected, as shown in figure 5.7. The intensity of individual frequency components varied greatly, but no attempt was made to quantify the strength or optical

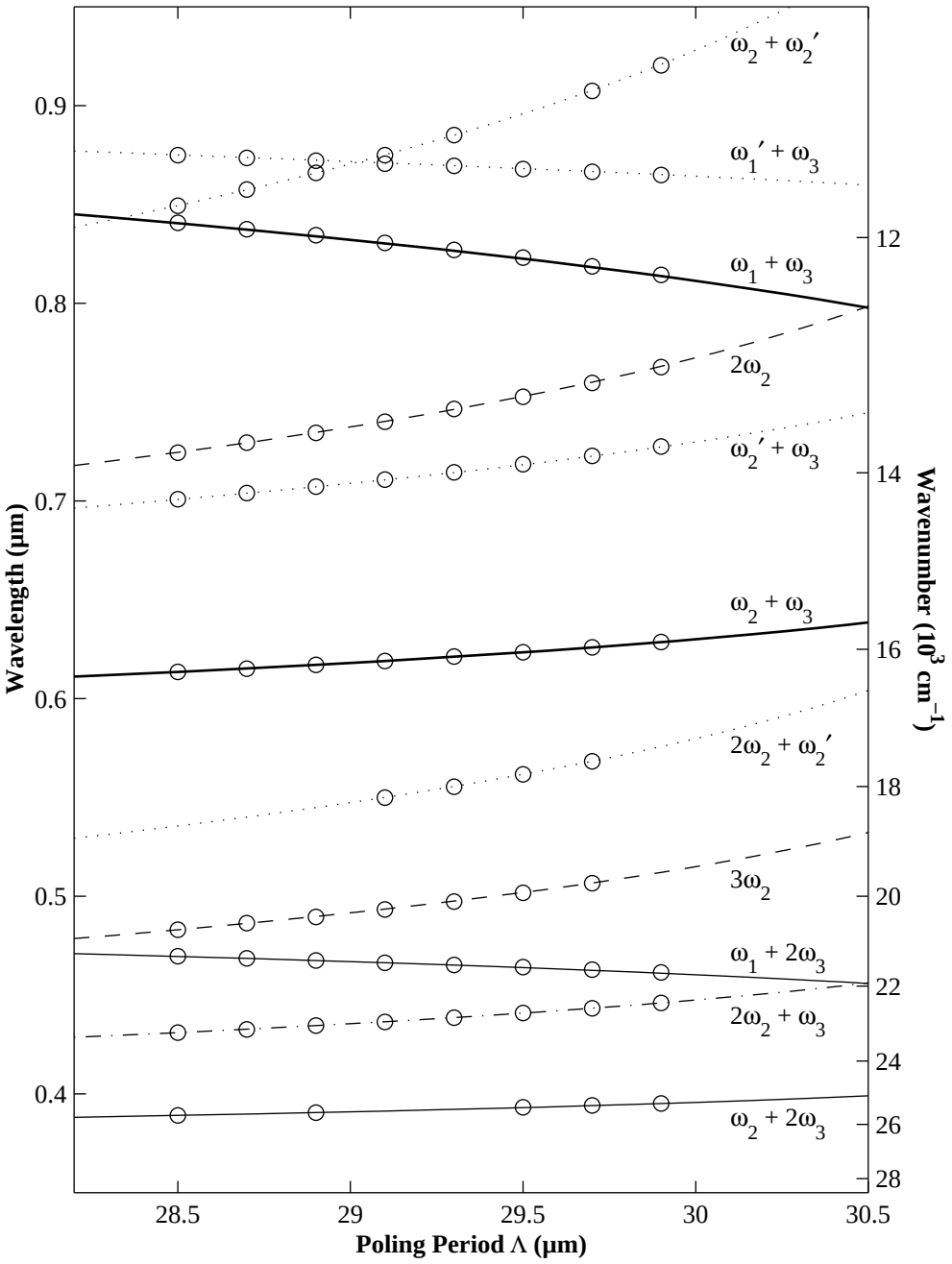

Figure 5.7: Upconverted frequency components from a cascaded PPLN OPO, as a function of poling period. The PPLN crystal was held at ∼25°C. Circles, measured wavelengths; lines, theoretical values calculated using the Sellmeier equations from reference [81] and equations (3.5), (3.25), and (5.1). The solid lines indicate the commonly observed upconversion frequencies based on pump ω_3, signal ω_2, and idler ω_1 photons. Dashed lines indicate higher harmonics of the resonated signal field. Dotted lines show frequency components arising on account of the cascaded signal ω_2' and idler ω_1' components. Not shown are the pump harmonics that were observed even under single-pass conditions.

bandwidth of each component, with the input slit width adjusted to control the intensity incident on the CCD. The lines indicate wavelengths predicted using the procedure outlined above, and the slope and curve of each line confirm that the modelled processes agree with the detected frequency components. Not included in the figure are the strong pump second and third harmonics, at wavelengths of 532 nm and 355 nm, that were also detected.

The heavy lines in figure 5.7 indicate the signal plus pump ($\omega_2 + \omega_3$) and idler plus pump ($\omega_1 + \omega_3$) components, the former of which was often used as a convenient indication that the OPO was above threshold and for spectral bandwidth measurements. The light solid lines indicate signal and idler interactions with the pump second harmonic ($\omega_i + 2\omega_3$), while the dashed lines indicate further components arising from signal wavelength harmonics. The dotted lines in figure 5.7 mark wavelength components arising from the cascaded OPO. The cascaded signal ω_2' and idler ω_1' interacted particularly with the strong pump and resonated signal fields. The excellent agreement between measured and calculated wavelengths was attributed to the accuracy of the Sellmeier equations [81] in this wavelength region.

The cascaded OPO was found to be highly sensitive to cavity alignment. A misalignment of the output coupling mirror by 2 mrad was sufficient to suppress cascading up to the maximum 1 mJ pump pulse energies (130 MW/cm^2) used in these experiments. The absence of cascading was reflected in a monotonically increasing signal output efficiency curve (figure 5.6 (a), diamonds) and the absence of an oscillatory structure on the temporal profile of the signal pulse. In a linear cavity with a line-narrowing étalon, cascaded operation was not observed. This was attributed to an increased threshold due to the added étalon losses; an investigation of passively narrowed cascaded OPOs could not be carried out due to bulk crystal damage considerations.

Prism Cavity

To ensure truly singly resonant oscillation, a prism was introduced into the linear cavity to eliminate cascaded OPO operation as well as residual pump or idler resonance. Two uncoated Brewster-angled prisms were tested, one of SF10 glass substrate and the other of ZnS. Since the OPO threshold was consistently around 200 μJ higher over the entire tuning range when the ZnS prism was used, the SF10 prism was selected for the remainder of the measurements. In order to accommodate the prism, it was necessary to extend the physical cavity length to 75 mm; insertion of the SF10 prism then increased the threshold by only 10% with respect to a linear resonator of the same length, to around 410 μJ. Spectral components corresponding to cascaded interactions were found to be absent,

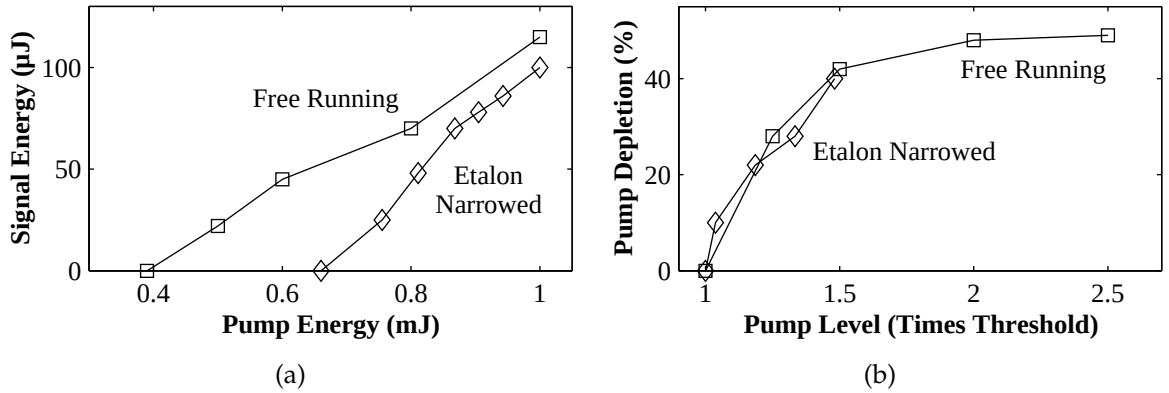

Figure 5.8: (a) Signal pulse energy and (b) pump depletion of a singly resonant, 1.064 μm pumped PPLN OPO with intracavity SF10 prism, under free running broadband (squares) and étalon narrowed single longitudinal mode (diamonds) operating conditions. Panel (b) is plotted against the number of times above threshold.

and structure observed on the signal pulse was matched by corresponding fluctuations in the depleted pump pulse, indicating backconversion but an absence of cascading.

As in section 5.2.2, a single fused silica étalon with a free spectral range of 30 GHz and a finesse of 12 over the signal wavelength range was inserted into the cavity, between the prism and output coupler, to obtain single longitudinal mode operation. Without the étalon, the OPO operated with a signal optical bandwidth of around 1.7 nm (FWHM), with considerable shot to shot variation. An étalon tilt of 11 mrad was sufficient to ensure single longitudinal mode operation over the full 1.47–1.59 μm OPO signal tuning range. Single mode operation was not sensitive to the alignment or position of the PPLN crystal within the OPO cavity, confirming that the residual reflections from the crystal faces did not play a role in mode selection. Measurements using a 5 GHz FSR Fabry–Pérot interferometer indicated that the OPO operated with an optical bandwidth of less than 240 MHz, limited by the interferometer resolution. The improved interferometer resolution, compared to the results presented in section 5.2.2, was due to increased reflectivity coatings on the interferometer. A 100 GHz FSR interferometer was used to confirm the absence of other modes of the intracavity étalon in the OPO spectrum. The OPO output could be set to any arbitrary operating wavelength within its gain bandwidth, and the wavelength was stable with regard to shot to shot as well as longer term fluctuations.

The addition of the intracavity étalon increased the threshold, from 400 μJ to 660 μJ, and reduced the efficiency of the OPO. Figure 5.8 shows for comparison the signal output energy and pump depletion as a function of pump pulse energy for the broadband and single longitudinal mode OPOs, at a signal wavelength of 1.55 μm. At the 1 mJ max-

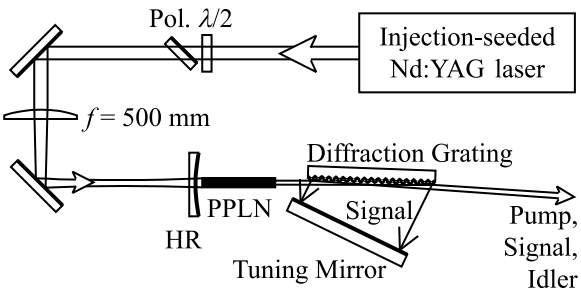

Figure 5.9: Schematic of a PPLN OPO with a diffraction grating at grazing incidence. $\lambda/2$, half wave plate; Pol., polariser; HR, signal high reflector.

imum pump energy, the signal output energy dropped only from 115 μJ to 100 μJ when the étalon was inserted. The resulting increase in slope efficiency for the étalon narrowed OPO was not fully understood [292]. Figure 5.8 (b) shows the pump depletion as a function of pumping level and shows that the degraded OPO performance could be attributed largely to an increased oscillation threshold, as in the case of the linear cavity.

A slight wavelength dependence of the OPO threshold and pump depletion was observed. A similar trend was also observed in the broadband OPO but was enhanced here, possibly as a result of the wavelength dependence of the étalon coatings. The single mode OPO threshold decreased from 700 μJ at a signal wavelength of 1.47 μm to 570 μJ at 1.59 μm. Over the same wavelength range, a corresponding increase in pump depletion from 40% to 47% was measured.

5.2.4 Grating Narrowed PPLN OPO

A PPLN OPO with grazing incidence diffraction grating was constructed and its performance compared to that of the étalon narrowed OPOs presented in the previous section. After the major part of the work presented here had been completed, Yu and Kung reported a similar grazing incidence PPLN OPO [161].

The OPO configuration is shown in figure 5.9. The 20 mm long Deltronic Crystal Industries PPLN crystal, with poling periods between 28.2 μm and 31.0 μm, was used. The crystal end faces were coated to have low reflection losses at the pump ($R \sim 0.2\%$), signal ($R \sim 0.5\%$) and idler (R between 6% at 2.6 μm and 1% at 3.8 μm) wavelengths. The crystal was operated at $160.0 \pm 0.1^{\circ}$C throughout the experiments to prevent possible photorefractive effects. The high reflecting cavity end mirror (HR) had $R > 99\%$ reflectivity over the 1.35–1.60 μm signal range, while maintaining $T > 95\%$ transmission at the pump wavelength. A concave optic with a 250 mm radius of curvature was used, since

it was found that the OPO operated with better amplitude and frequency stability than when a plane optic was used. This phenomenon was attributed to a better mode definition within the near hemispherical signal resonant cavity, as compared to a plane–plane cavity, as well as improved mode matching within the PPLN crystal.

From the grating equation (4.10), the ratio of wavelength to groove spading should satisfy $1 \leq \lambda_2/d \leq 2$ for operation in first order, with a value close to 1 preferred to minimize the tuning mirror angle θ_m. For $\lambda_2 = 1.5\,\mu$m, this corresponds to a groove density $650 \leq 1/d \leq 1300\,\text{mm}^{-1}$; of the available gratings, a 50 mm long holographic diffraction grating ruled at $900\,\text{mm}^{-1}$ and coated with metallic gold was used. The first diffracted order of the signal wavelength was retroreflected by a $50 \times 11\,\text{mm}^2$ plane tuning mirror, also coated with metallic gold for a reflectivity $R > 96\%$ across the near-infrared. The zeroth diffraction order (specular reflection) from the grating provided the output from the OPO, with superimposed signal, idler, and depleted pump beams. The cavity was constructed to yield the shortest possible physical length of 70 mm measured to the centres of diffraction grating and tuning mirror, corresponding to a longitudinal mode spacing of 1.6 GHz. Pivot point considerations for continuous tuning [178, 219, 281] were not taken into account.

The OPO was pumped by a small fraction of the output of the Continuum PL7000 laser, injection seeded and operated with a Q-switch delay of 260 μs to generate 15 ns oscillator-only pulses of $\sim$1.5 mJ energy. As before, a half wave plate ($\lambda/2$) and polariser (Pol.) combination allowed smooth variable control of the pump energy, and the PPLN crystal was positioned 50 mm beyond the pump beam waist formed by an antireflection coated 500 mm focal length achromat to fill the available crystal volume while reducing the risk of surface damage. In this configuration a pump spot size of between 170 μm and 250 μm in the PPLN crystal was adequately matched to the OPO signal mode spot size of $\sim$270 μm for efficient conversion [293]. Positioning the PPLN crystal before the pump beam waist would have provided better pump–signal beam wavefront curvature matching, but this configuration was not adopted here due to the risk of diffraction grating damage by the 90 μm pump waist. In previously reported grazing incidence OPOs, an intracavity pump filter was necessary to prevent damage to the grating [181, 219].

A diffraction grating incidence angle of $\theta_i = 88.6^\circ$ was found to be optimal for efficient single longitudinal mode operation. A decrease in incidence angle resulted in the OPO oscillating on several longitudinal modes, while an increase led to lower output efficiencies without enhancing the single mode stability. Quantitative studies of the effects of diffraction grating angle on optical bandwidth and threshold have been reported for BBO [181] and PPLN OPOs [161], but were not undertaken here. Yu and Kung [161]

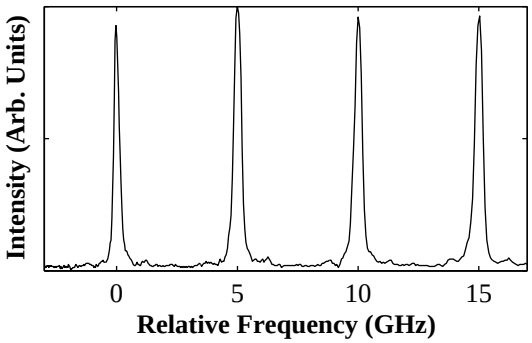

Figure 5.10: Line profile taken through the centre of a 5 GHz free spectral range Fabry–Pérot interferometer fringe pattern of a PPLN OPO with grazing incidence diffraction grating. The fringes were taken with the OPO operating at a signal wavelength 1.796 μm, where tuning across 110 cm^{-1} was demonstrated.

found that grating angles in excess of 88° raised the OPO threshold, due to increased losses at the diffraction grating, without contributing to further line narrowing of the signal output.

High resolution OPO spectra were obtained using a 5 GHz FSR Fabry–Pérot interferometer, the fringes from which were imaged onto a CCD camera. The resolution limit of the Fabry–Pérot interferometer was measured to be 250 MHz at 532 nm using the frequency doubled output from the injection seeded pump laser. The OPO signal optical bandwidth was deduced from measurements of the ∼650 nm signal plus pump sum frequency; in a similar study with a multimode pump source, the second harmonic of the signal was used [161]. As the optical bandwidth of the injection seeded pump was below the measurable limit, the bandwidth measured was attributed solely to the signal radiation. Energy conservation requires an idler frequency bandwidth comparable to that of the signal. A line profile taken through the Fabry–Pérot interferometer fringes is shown in figure 5.10, with the OPO operating on the $\Lambda = 30.8\,\mu$m poling period, corresponding to signal (idler) wavelengths of 1.796 μm (2.611 μm). Single axial mode operation was demonstrated over the wavelength range 1.48–1.80 μm (signal) and 2.61–3.82 μm (idler), with each poled track yielding an instrument limited measured bandwidth of ≤ 250 MHz.

The single longitudinal mode output could be tuned by adjustment of the tuning mirror angle. In agreement with the results of Yu and Kung [161], tuning to almost twice the calculated crystal gain bandwidth of each track was observed, as shown in figure 5.11. The experimental tuning range for each poling period was determined by adjusting the tuning mirror and measuring the wavelength range over which oscillation at the signal

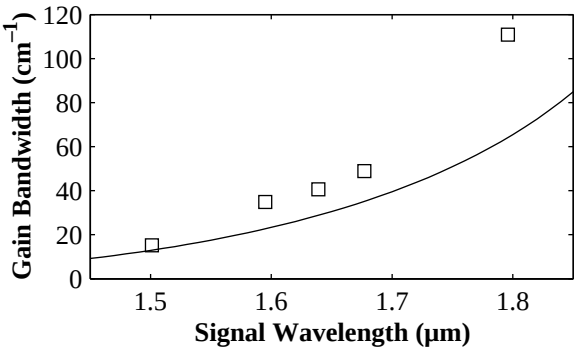

Figure 5.11: Measured single longitudinal mode signal tuning range of a PPLN OPO with grazing incidence diffraction grating (squares), and OPO gain bandwidth calculated as outlined in section 4.1 (solid line), as a function of signal wavelength.

Table 5.2: Performance of a PPLN OPO with grazing incidence diffraction grating.

	Poling Period Λ (μm)				
Parameter	28.9	29.9	30.2	30.4	30.8
Signal Wavelength λ_2 (μm)	1.501	1.595	1.639	1.677	1.796
Idler Wavelength λ_1 (μm)	3.655	3.198	3.034	2.912	2.611
Threshold (mJ)	1.28	1.06	1.10	1.15	1.09
Signal Slope Efficiency (%)	36.8	30.4	30.5	30.9	30.8
Idler Slope Efficiency (%)	8.4	8.9	6.8	8.4	10.7
Tuning Range (cm^{-1})	15.1	34.8	40.6	48.9	110.9

plus pump sum frequency was observed. The solid line indicates the crystal single pass signal gain bandwidth, calculated as described in section 4.1. The acceptance bandwidth was observed to diverge as degeneracy was approached. At the longest 1.796 μm signal wavelength accessible, single mode signal could be tuned across 30 nm (110 cm^{-1}), with a bandwidth of less than 250 MHz (0.008 cm^{-1}).

The high effective loss introduced by the grazing incidence diffraction grating resulted in a comparatively high oscillation threshold of 1.1 mJ ($\sim$90 MW/cm^2) across the operating wavelength range, which may be compared to a threshold of 410 μJ measured in section 5.2.2 for a similar linear cavity OPO. The grazing incidence OPO was pumped with no more than 1.6 mJ due to the risk of bulk crystal and coating damage to the PPLN.

The output signal beam was separated from the residual pump and output idler beams using a Brewster angled ZnS prism, while a polished germanium window allowed the idler to be isolated. A summary of the measured performance parameters of the grazing incidence PPLN OPO is presented in table 5.2 for a number of different wavelengths. In part, the performance variations between different poled tracks was attributed to dif-

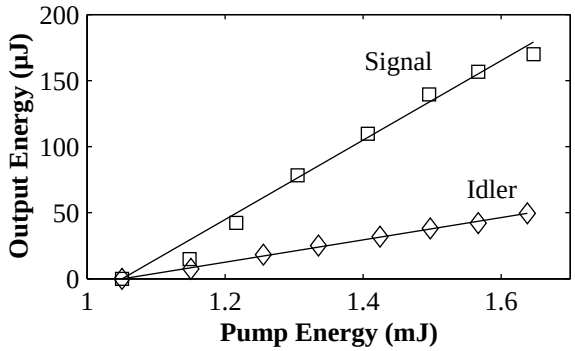

Figure 5.12: Signal (squares) and idler (diamonds) output pulse energies of a PPLN OPO with grazing incidence diffraction grating, as a function of pump pulse energy. The OPO was operating on a signal (idler) wavelength of 1.677 μm (2.9 μm).

ferences in the precise cavity conditions, in particular, the diffraction grating angle θ_i. The highest output signal (170 μJ) and idler (49.6 μJ) pulse energies were measured with the $\Lambda = 30.4\,\mu$m poling period, at a signal wavelength of 1.677 μm, and are shown in figure 5.12. Over the full tuning range, output pulse energies of 139–170 μJ at the signal and 37–52 μJ at the idler wavelengths were observed, corresponding to slope efficiencies of 31% to 37% for the signal and 7% to 11% for the idler. The signal to idler output energy ratio trend was consistent with the ratio between the photon energies, although the extraction efficiency at the signal wavelength was higher. At all wavelengths, the total (pump to signal + idler) OPO efficiency exceeded 11%.

Temporal profiles of the signal pulses were measured using a 1 ns rise time InGaAs photodiode. Typical signal pulse durations between 3 ns and 5 ns were measured. The pulse shapes qualitatively followed the characteristics of standard OPOs pumped to less than twice threshold, such as those illustrated in figure 5.4 on page 68. While the OPO operated on a single axial mode, the temporal profiles indicated less than 10% amplitude and only $\sim$1 ns timing jitter, which were attributable to timing jitter of the pump laser.

The spatial profile of the signal beam was recorded by translating a 100 μm aperture photodiode through the signal beam. A sample data set measured at a distance of 1 m from the OPO is shown in figure 5.13. The solid lines were calculated by fitting a Gaussian profile to the data points. The fitted spot sizes were used to calculate far field divergences of 4.22 mrad and 2.93 mrad in the horizontal and vertical planes respectively. Assuming a waist size of 200 μm inside the PPLN crystal, a beam quality factor of $M^2 = 1.3 \pm 0.2$ was calculated for the OPO operating on a single mode. The stability of the single mode OPO spectral and temporal behaviour depended critically on the exact alignment of the cavity

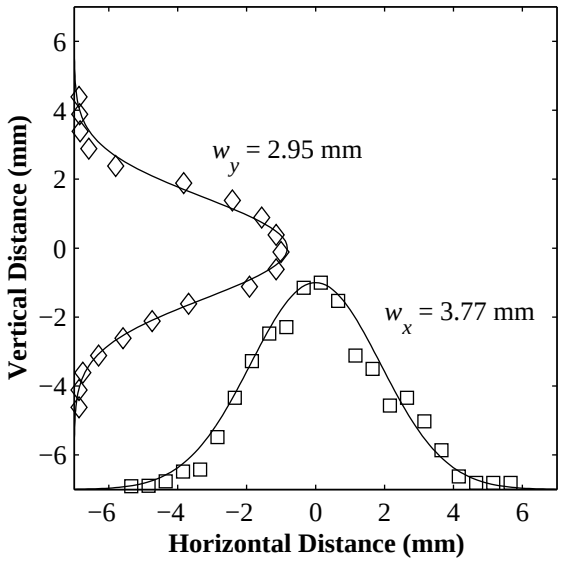

Figure 5.13: Horizontal and vertical spatial intensity distributions of the signal output beam from a PPLN OPO with grazing incidence diffraction grating, measured at a distance of 1 m from the OPO. The solid lines indicate a Gaussian fit.

optics and on precise control of the temperature of the PPLN crystal. Yet despite no active cavity stabilisation, the OPO regularly operated with a stable single mode output for tens of seconds. Cavity misalignments resulted in shot to shot fluctuations of the output beam and a multiple mode output spectrum.

A grazing incidence PPLN OPO similar to the one presented here was reported by Yu and Kung [161] shortly after the experiments in this section had been completed. The authors demonstrated the suitability for such OPOs as spectroscopic sources by the successful measurement of photoacoustic absorption spectra of CH_4. A multiple mode Nd : YAG laser, emitting 28 ns pulses of 18 GHz optical bandwidth, was focused to a 220 μm waist within the PPLN crystal. The bandwidth of the pump permitted the OPO optical bandwidth to be reduced only to 9 GHz in that case. The substantially higher gain provided by the 50 mm long PPLN crystals of Yu and Kung allowed their OPO to be operated in excess of 2.5 times the threshold energy, which they measured to be around 200 μJ, but also provided sufficient gain for a broadband parametric generation pedestal to be observed on the OPO spectra. Pump depletions of 46% were reported. At the peak signal wavelength, 50 μJ of signal was generated. This value was almost three times lower than that presented here, partly on account of a 20% reduction in the number of cavity round trips during the pump pulse (160 mm cavity length and 28 ns pump pulse duration in [161], compared to 70 mm cavity length and 15 ns pulse duration used here).

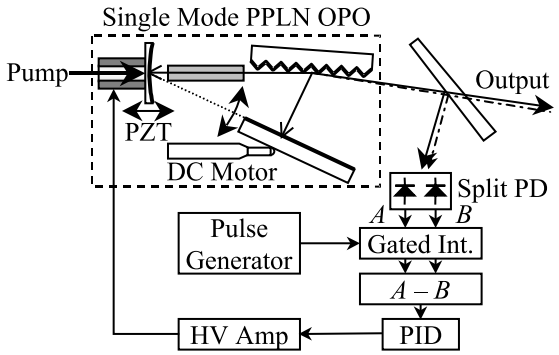

Figure 5.14: Schematic of a grazing incidence PPLN OPO with active cavity length stabilisation and computer controlled wavelength selection.

5.2.5 Cavity Length Control

As described in section 4.3, the single mode output from a grazing incidence diffraction grating cavity can be actively stabilized by controlling the cavity length. The initial promising performance of the grazing incidence PPLN OPO presented in the previous section prompted an attempt at such cavity length locking using a different, but similarly constructed, OPO. The work described in this section was carried out during a research visit to Macquarie University under the guidance of Prof. Brian Orr.

Figure 5.14 shows the modified grazing incidence PPLN OPO. The OPO cavity comprised the same diffraction grating, tuning mirror, and -250 mm radius of curvature dielectric coated signal high reflector, but employed a different pump source and PPLN crystal, and was constructed to allow piezoelectric translation (PZT) of the high reflector and computer controlled tuning mirror rotation by DC motor. The cavity was constructed on a custom built platform, approximately satisfying the tuning mirror pivot point criteria necessary for synchronous tuning of angle and cavity length [178].

The OPO was pumped by a small fraction of the output from a 10 Hz Q-switched, injection seeded SpectraPhysics GCR250 Nd : YAG laser [166]. The 8 mm pump beam diameter was reduced using a Galilean telescope with 50 mm and -25 mm focal length achromats, and subsequently focused using a 1 m focal length lens to yield a 140 μm waist within the PPLN crystal. The $20 \times 7 \times 0.5\,\text{mm}^3$ PPLN crystal (Crystal Associates Inc) had eight adjacent poled tracks with periods between 28.5 μm and 29.9 μm. The end faces were polished with a 2° wedge angle to prevent monolithic resonance, and antireflection coated at the 1.064 μm pump and $\sim$1.5 μm signal wavelengths. An oscillation threshold of 530 μJ was measured. The non-phase matched signal plus pump upconverted signal generated within the PPLN was monitored using a Burleigh W4500-1 Wavemeter that

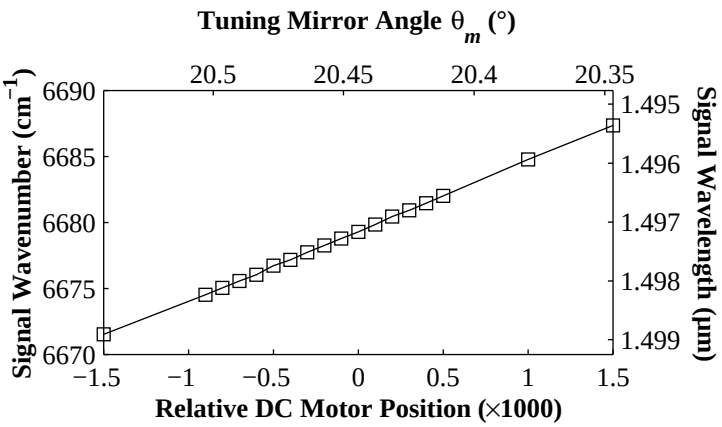

Figure 5.15: Signal frequency of a grazing incidence PPLN OPO as a function of DC motor position, controlled via computer. The scan rate was determined to be $5.3\,\mathrm{cm}^{-1}$ per 1000 motor steps.

simultaneously determined the optical bandwidth and wavelength of the upconverted wave.

The DC motor (Physik Instrumente, M224,20) was driven via a GPIB connection and a Physik Instrumente C-812 motor controller. An existing collection of Pascal procedures for low-level control of the DC motor was modified and combined for convenient motor control. Figure 5.15 shows a computer-actuated wavelength scan for the OPO operating on the $\Lambda = 28.9\,\mu$m poling period. From the data, an approximately linear tuning rate of $5.3\,\mathrm{cm}^{-1}$ per 1000 motor steps was determined. Under these conditions, a scan of 6000 motor steps was sufficient to cover the $\sim 30\,\mathrm{cm}^{-1}$ gain bandwidth of the OPO.

To obtain a suitable error signal as outlined by Raymond *et al.* [282], a fused silica wedge directed part of the generated signal beam onto a quadrant Ge photodiode (EG&G Inc). The photodiode was operated in the photovoltaic configuration without bias or amplification, leading to long decay tails on the detected pulses. The signals of two horizontally adjacent photodiode cells were, initially, processed using an in-house built circuit, described in appendix B, but that was subsequently replaced by commercial gated integrator / averager and analogue processor (Stanford Research Systems, models 250 and 235). The error signal was generated from the comparison level between the gated, integrated photodiode signals, processed using standard proportional–integral–derivative (PID) processing.

Applying a linear ramp to the PZT (Physik Instrumente, P305.40) yielded an error signal as shown in figure 5.16. As expected [282], the error signal was approximately linear and crossed through the zero level for every $\lambda/2$ cavity length change; in this region, cavity length locking to a single longitudinal mode should be possible. The error

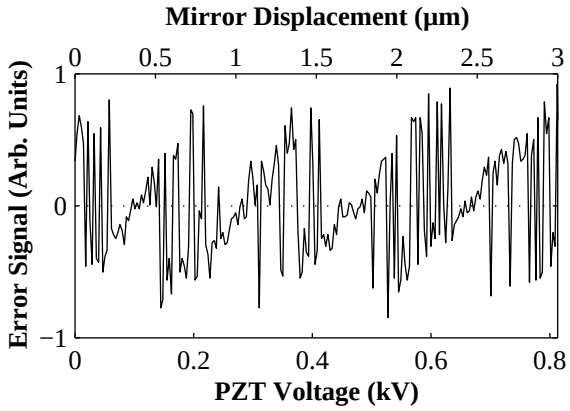

Figure 5.16: Error signal obtained using split photodiode, as the cavity length of a grazing incidence PPLN OPO is ramped using a piezoelectric translator.

signal shape in regions where the OPO does not operate on a single mode depends on the geometry of the detection system. The characteristic parallelogram shape between the cavity resonances was here attributed to the OPO hopping between cavity modes on successive pump pulses. Closing the cavity length feedback loop yielded a minor qualitative improvement in the medium-term stability of the OPO spectrum, but mode hopping typically occurred after a few hundred pulses.

Grazing incidence diffraction grating cavities have been stabilised in the past using this technique [183, 282], and the lack of success here was not attributed to PPLN as a nonlinear optical medium. Qualitatively, it was found that the free running OPO operated less reliably on a single longitudinal mode compared to the one described in section 5.2.4. This may have been due to the 20% decrease in pump pulse duration [219], or to the spectral bandwidth of the pump laser, as there was subsequent evidence to suggest the injection seed was lasing on two modes. It was found that the locking electronics required some significant modifications and further testing, for which insufficient time was available. The divergence of the signal beam, constrained within the PPLN crystal, may have contributed to a lack of fidelity in the error signal [282]. Nonetheless, the initial experimental results indicated that the development of a passively narrowed quasi-phase matched OPO with active cavity length control, yielding continuously tuneable, single longitudinal mode output, should be possible.

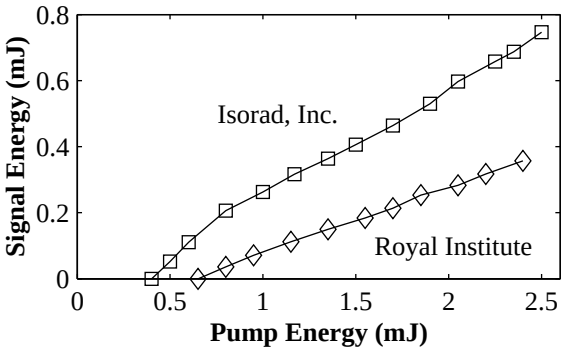

Figure 5.17: Signal pulse energy performance PPKTP OPOs, as a function of input pulse energy, for the two available PPKTP crystals. Squares, crystal obtained from Isorad, Inc; diamonds, crystal supplied by the Royal Institute of Technology.

5.3 OPOs Based on Periodically Poled KTP

Two PPKTP crystals suitable for 1.064 μm pumped OPOs were available. Both crystals were 20 mm long and poled with a single track of period $\Lambda = 37.4\,\mu$m, yielding 1.064 μm pumped OPO signal and idler wavelengths of 1.68 μm and 2.9 μm, respectively. The first crystal was supplied by Dr. Fredrik Laurell of the Royal Institute of Technology (Stockholm, Sweden) in a collaborative effort to develop and characterise PPKTP for nonlinear optical frequency conversion. The crystal was poled by Jonas Hellström as part of his PhD thesis at the Royal Institute [294]. The 1 mm thick KTP wafer was poled at room temperature using the poling technique described in by Karlsson *et al.* [70], with three 2.2 kV electrical pulses of 6 ms duration. The second crystal was a commercial sample obtained from Isorad, Inc (Israel), and was 1.4 mm thick. The end faces of the Isorad PPKTP crystal were antireflection coated at the 1.064 μm pump and 1.7 μm signal wavelengths, while the crystal from the Royal Institute was initially uncoated.

5.3.1 Linear Cavity PPKTP OPO

To compare the performance between the two available crystals, both were operated in a linear OPO configuration with a 70% reflective output coupler. The OPOs were pumped by up to 2.5 mJ of 15 ns pump pulses, and placed $\sim$50 mm beyond the waist formed by a 500 mm focal length achromat to preclude monolithic oscillations observed when the crystals were placed at the focus. In this configuration, the pump spot size within the PPKTP crystals was around 180 μm and the peak pump intensity was 350 MW/cm^2.

The output 1.68 μm signal pulse energies are shown in figure 5.17. The commercial

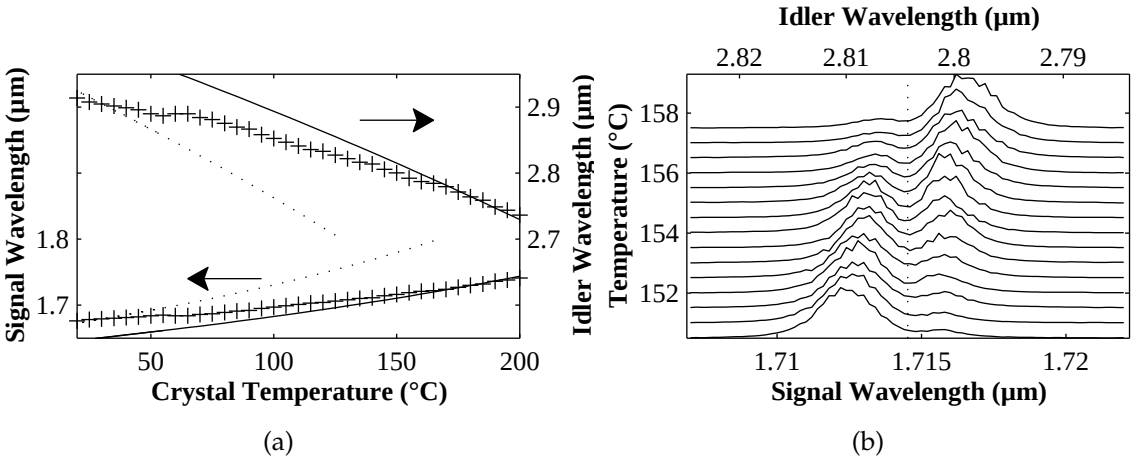

(a) (b)

Figure 5.18: (a) Measured signal and deduced idler tuning curve for a PPKTP OPO with poling period $\Lambda = 37.4\,\mu$m, with predicted curves using Sellmeier equations of reference [262] (solid line); and references [112] and [263] (dotted line). (b) Signal spectra of the OPO operating near the 2.804 μm OH^- absorption feature [248].

crystal had superior performance, with lower threshold (0.41 mJ compared to 0.65 mJ), higher slope efficiency (34% compared to 20%) and higher signal pulse energy (0.75 mJ compared to 0.36 mJ at 2.5 mJ pump) than the crystal from the Royal Institute. The performance difference between the two crystals was attributed to the end face coatings, and to potential differences in the uniformity of the poled regions. The passive losses at the 1.68 μm signal wavelength were measured to be 2% for the Isorad crystal and 15% for the crystal from the Royal Institute. The latter losses were attributed to Fresnel surface reflection losses of the uncoated crystal. For later experiments, presented in section 5.3.3, the Royal Institute crystal was repolished to yield Brewster-angled end faces, thereby all but eliminating reflection losses at the faces.

Since only one poling period was available, tuning was achieved by varying the crystal temperature. Typically, the PPKTP OPOs were operated at room temperature, since KTP was not susceptible to the photorefractive effects that required PPLN to be operated at elevated temperatures. Figure 5.18 (a) presents signal and idler wavelength tuning measured by varying the temperature of the Isorad crystal. From the different published Sellmeier equations and refractive index temperature variation coefficients presented in table 3.2 on page 46, the Sellmeier equations of Fradkin *et al.* [112] provided the best agreement between predicted and measured wavelengths at room temperature. The dn/dT coefficients best matching the measured temperature tuning rates were found to be those presented by Kato [263]. At elevated temperatures, the temperature dependent Sellmeier equations published recently by Kato *et al.* [262] satisfactorily predicted the OPO wave-

lengths. Figure 5.18 (b) shows signal spectra measured using a 0.5 m diffraction grating monochromator, as the OPO idler wavelength tuned across the 2.804 μm OH^- feature, where Hansson *et al.* [248] have measured an absorption coefficient of around 2 cm^{-1}, but found some variation between crystals. Due to the absorption, the OPO output energy was observed to decrease by 24%.

Spectral measurements using the 650 nm signal plus pump sum frequency component indicated a free running OPO optical bandwidth of around 280 GHz (9 cm^{-1}). This was consistent with a calculation of the theoretical single pass crystal gain bandwidth of 26 cm^{-1}, based on the Sellmeier equation of Fradkin *et al.* [112], and narrowed by multiple cavity passes as discussed in section 4.1. Attempts to implement an étalon narrowed configuration similar to that of the PPLN OPO described in section 5.2.2 were unsuccessful. This was attributed to feedback from the crystal faces reducing the effectiveness of the étalon, as well as the broad optical gain bandwidth, since, as reported in section 7.2, line narrowing to a single longitudinal mode using the same intracavity étalon could not be achieved for single pass crystal gain bandwidths in excess of 29 cm^{-1}.

The high damage threshold of KTP, as compared to $LiNbO_3$, combined with the larger crystal apertures available, make PPKTP an attractive candidate for high power quasi-phase matched OPOs. This possibility was investigated using the Isorad PPKTP crystal. The OPO was pumped by the modified Continuum PL7000 operating at a Q-switch delay of 240 μs to yield up to 150 mJ pulses of 12 ns duration. The free propagation of the beam resulted in a spot size of $\sim$3 mm ($1/e^2$ radius) at the OPO. In the horizontal plane, corresponding to the 1.4 mm thickness of the crystal, a spatial filter was used to aperture the beam to an approximately flat top spatial profile of 1.3 mm full width. The singly resonant OPO cavity was formed by two plane mirrors; a signal wavelength high reflector, through which the pump entered the OPO cavity, and a CaF_2 substrate coated for 70% reflectivity at the signal wavelength as the output coupler.

The total signal plus idler output pulse energy is shown in figure 5.19 as a function of incident pulse energy. The crystal was pumped with up to 70 mJ, corresponding to a peak intensity of 450 MW/cm^2, safely below the reported damage thresholds of PPKTP [117]. The total output energy of 18.3 mJ was, at the time of the experiment, higher than previously published output energies from OPOs based on periodically poled materials [124]. Crystal or coating damage was not observed.

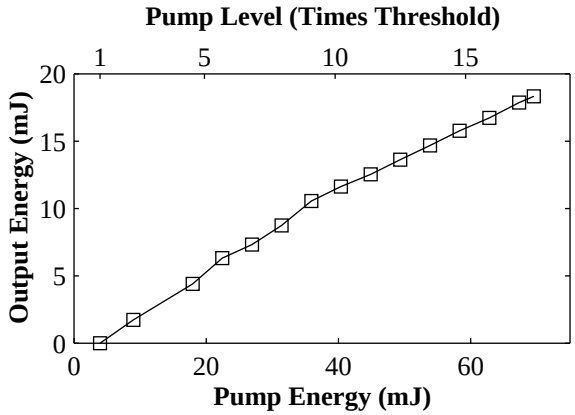

Figure 5.19: Total signal plus idler output pulse energy of a high pulse energy PPKTP OPO, as a function of pump energy.

5.3.2 Brewster Cut PPKTP OPO

The theoretically vanishing reflection loss for p-polarised light at a Brewster angled face is often exploited in laser crystals to reduce cavity losses and oscillation thresholds [185]. In type I quasi-phase matched OPOs, a crystal cut at the Brewster angle can have low loss at all interacting fields, since they propagate collinearly through the crystal and have the same polarisation. The Brewster angle was calculated to be 61° for KTP at the $1.68\,\mu$m signal wavelength. The PPKTP crystal from the Royal Institute was repolished to parallel Brewster angled faces, which reduced the crystal length to 17 mm.

The Brewster cut crystal was placed within a resonator formed between a high reflector at the signal wavelength, through which the pump entered, and an output coupler with reflectivity $R \approx 70\%$ at the signal wavelength. The high reflector coating provided $R = 97\%$ reflectivity at the signal and $T = 92\%$ transmission at the pump wavelengths. Potential interference effects from the optics were avoided by employing substrates wedged by 2° in the plane orthogonal to the Brewster angled crystal faces.

Because of dispersion, the refraction angles at the crystal faces were different for the pump, signal, idler, as well as upconverted frequencies, as illustrated in figure 5.20. In particular, the pump beam entered the cavity at a 1° angle to the signal resonator axis, somewhat complicating the practical alignment of the OPO cavity. To facilitate alignment of the Brewster angled OPO, a plane–plane linear cavity OPO, comprising a signal high reflector, the Isorad PPKTP crystal, and a 66% reflective output coupler, was constructed, and the $1.68\,\mu$m signal radiation used as an alignment beam.

The output from the modified Continuum PL7000, focused using a 1 m focal length

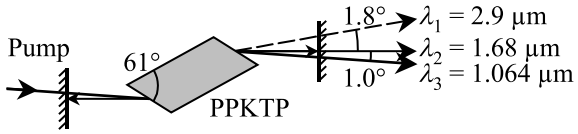

Figure 5.20: Refraction at the Brewster angled PPKTP faces leading to angular spread between the λ_3 pump, λ_2 signal, and λ_1 idler. The diagram is not drawn to scale.

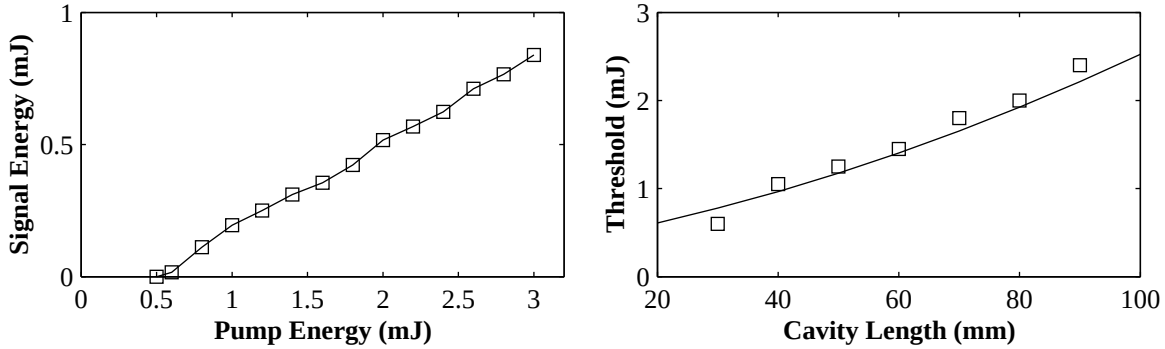

(a) (b)

Figure 5.21: Performance of a Brewster angled PPKTP OPO. (a) OPO signal efficiency as a function of pump energy, with a cavity length of 30 mm. (b) Measured threshold as a function of cavity length (squares) and theoretical prediction using equation (3.27).

achromat, was used to pump the OPO. Due to refraction at the Brewster faces, the spot size within the crystal was elliptical with dimensions $230 \times 470\,\mu\text{m}^2$. The OPO performance is summarised in figure 5.21. For the shortest possible cavity length of 30 mm, a threshold of 0.51 mJ was measured, and pumping with 3 mJ yielded 0.84 mJ of signal energy. This corresponded to a slope efficiency of 34%. An increase in the physical cavity length to 90 mm raised the threshold to 2.4 mJ, close to the 3 mJ limit imposed by crystal damage considerations. The theoretical curve in figure 5.21 (b) was calculated using equation (3.27) with parameters pump pulse duration $\tau = 10$ ns and $\ln(P_n/P_0) = 120$, and gave satisfactory agreement with the measured data.

5.3.3 Grating Narrowed PPKTP OPO

In order to demonstrate single longitudinal mode operation, the Brewster angled crystal was incorporated into a grazing incidence diffraction grating cavity. The output from the OPO was subsequently used to seed a single pass PPKTP optical parametric amplifier (OPA) as described in the following section. The experimental configuration is illustrated in 5.22. The pump laser used was the injection seeded modified Continuum

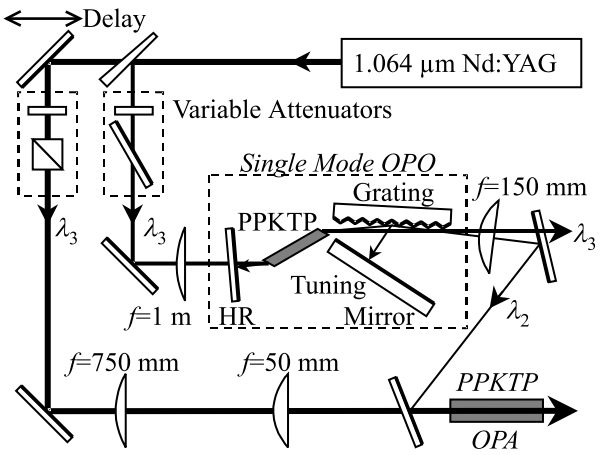

Figure 5.22: Experimental configuration of PPKTP grazing incidence OPO and OPA. HR, high reflector at signal wavelength λ_2. A second PPKTP crystal was used to amplify the generated signal and idler wavelengths to 2.15 mJ and 1.18 mJ respectively.

PL7000 Nd : YAG oscillator, producing 14 ns pulses at a repetition rate of 10 Hz, with the Q-switch delay adjusted to yield a pulse energy of approximately 20 mJ. A ZnS wedge directed approximately 3 mJ pump energy to the grazing incidence cavity, with the remaining pump energy used to drive the amplifier. Separate variable attenuators permitted smooth, independent control of the pump energies incident on the OPO and OPA crystals.

A 1 m focal length achromat focused the pump beam to a waist of $230 \times 470\,\mu\text{m}^2$ within the crystal as before. The OPO cavity was formed by a plane dielectric high reflector, a diffraction grating, and a plane metallic tuning mirror. A $900\,\text{mm}^{-1}$ holographic diffraction grating coated with metallic gold was introduced into the cavity with an incidence angle between grating normal and cavity axis of $\theta_i = 86.6°$. A plane metallic gold mirror, with a reflectivity of $R = 94\%$ at $1.68\,\mu$m, completed the cavity by retroreflecting the first diffracted order from the grating. The specular reflection (zeroth diffraction order) from the grating was used as the OPO output.

The $1°$ deviation between pump and signal wavelengths allowed the depleted pump beam to be coupled out of the cavity without contacting the diffraction grating. Considerations of the high pump fluence potentially damaging the grating surface were thereby simplified, and no separate intracavity dichroics were necessary to protect the grating [181, 219]. The $1.8°$ idler deviation resulted in the idler being clipped by the grating, and no idler output could be extracted from the OPO. This issue could be addressed by mechanical construction considerations. The cavity was built to yield the shortest possible

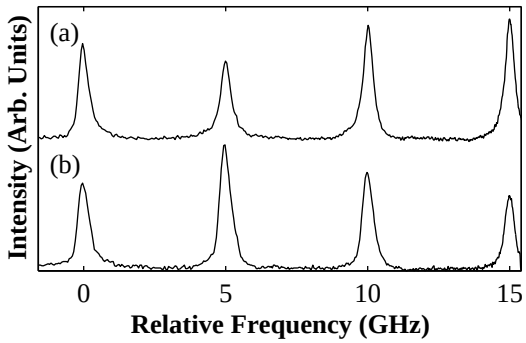

Figure 5.23: Line profiles taken through the fringe pattern produced by a 5 GHz free spectral range Fabry–Pérot interferometer, for (a) PPKTP OPO with grazing incidence diffraction grating; (b) output from PPKTP OPA seeded by the single longitudinal mode OPO signal.

cavity length of 60 mm, measured to the centres of the grating and tuning mirrors. Continuous single-mode tuning considerations regarding the tuning mirror pivot point [178] were not taken into account.

The diffraction grating successfully narrowed the OPO optical bandwidth to a single longitudinal mode. The optical bandwidth was deduced from Fabry–Pérot interferometer measurements on the signal plus pump upconverted frequency component. A trace through the fringe pattern of a Fabry–Pérot interferometer with a free spectral range of 5 GHz, imaged onto a CCD camera, is shown as trace (a) in figure 5.23. The trace indicated a single longitudinal mode signal bandwidth of less than 400 MHz, limited by the resolution of the interferometer. The bandwidth could be attributed solely to the signal, since the bandwidth of the pump radiation was substantially below the interferometer resolution. Energy conservation requires that the idler radiation had a similar optical bandwidth.

The signal wavelength could be tuned by tilt adjustments to the tuning mirror. As in the case of the grazing incidence OPOs reported in section 5.2 and by Yu and Kung [161], the OPO could be tuned substantially beyond the single pass crystal gain bandwidth. Single mode operation was observed across 1300 GHz (44 cm^{-1}). Continuous single mode tuning was not attempted. A sequence of line profiles recorded with a 400 GHz free spectral range Fabry–Pérot interferometer and normalised in amplitude is shown in figure 5.24, with the dotted lines indicating the frequency progression. The OPO exhibited a tuning range of 1.678–1.691 μm (full width to $1/e^2$ level) with highest output energies measured at 1.685 μm. The corresponding idler tuning range was 2.869–2.907 μm, and the peak idler wavelength 2.887 μm.

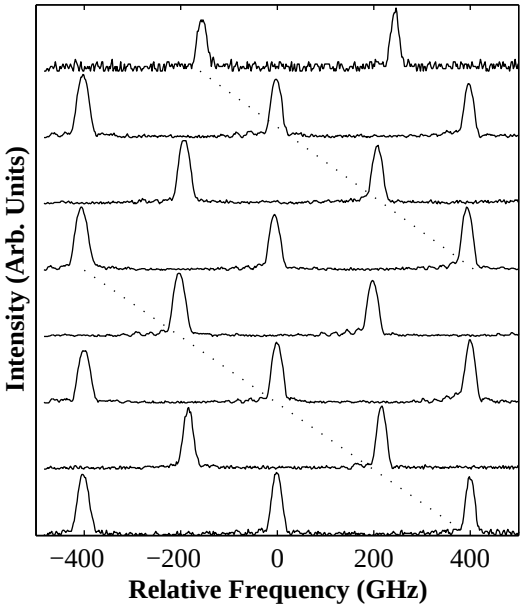

Figure 5.24: Normalised line profiles taken through the fringe pattern produced by a 400 GHz free spectral range Fabry–Pérot interferometer, indicating the tuning range of a single longitudinal mode PPKTP OPO with grazing incidence diffraction grating. A tuning range of 1300 GHz (44 cm^{-1}) was recorded.

An oscillation threshold of 2.3 mJ ($\sim$56 MW/cm^2) was measured for the OPO at the optimum signal wavelength of 1.685 μm. At a pump energy of 3.1 mJ (1.3 times threshold), 370 μJ of signal radiation was generated, corresponding to a slope efficiency of 46%. The high threshold and high slope efficiency were characteristic of all the grazing incidence diffraction grating OPOs investigated. The pump, depleted pump and signal pulse temporal profiles were recorded using fast rise time Si and InGaAs photodiodes and a 200 MHz digital oscilloscope. Pulse durations of $\sim$2.5 ns full width at half maximum intensity for pump energies below 2.6 mJ were recorded. At a pump level of 3.1 mJ, a signal pulse duration broadening to $\sim$5 ns and structure on the signal and depleted pump pulse, potentially indicative of backconversion were observed, as illustrated in figure 5.25 (a). The pump depletion was estimated to be $\sim$15% at the highest pump energies used.

Fundamental signal beam far field spatial distributions were measured using a 100 μm active area InGaAs photodiode scanned through the beam on a micrometer translation stage. The beam intensities at each position were averaged over four pulses using a gated boxcar integrator and recorded in horizontal and vertical slices through the beam. The single longitudinal mode OPO signal radiation was observed to have a smooth Gaussian spatial distribution with far field divergences of 5.55 mrad (5.84 mrad) in the

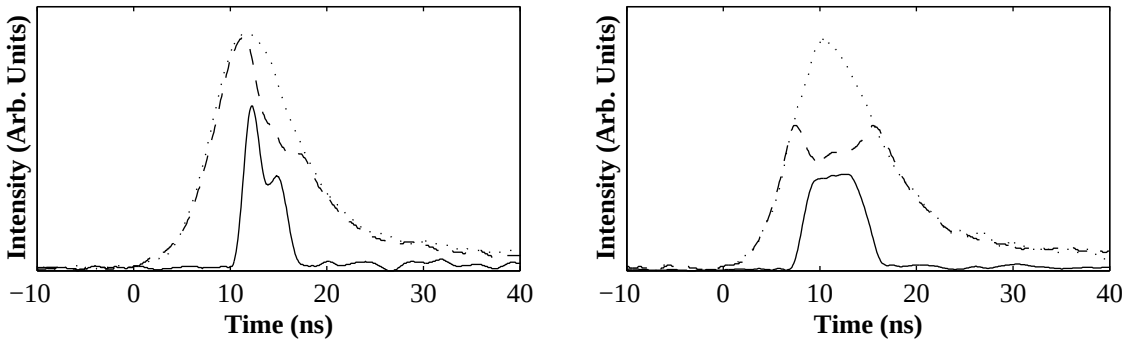

Figure 5.25: Temporal profiles for a single longitudinal mode PPKTP OPO–OPA system. Solid line, signal; dashed line, depleted pump; dotted line, incident pump. (a) Single longitudinal mode OPO with grazing incidence diffraction grating. (b) PPKTP OPA seeded by the single mode output from the OPO.

horizontal (vertical) planes. From these values a signal M^2 beam quality parameter of 1.6 ± 0.1 was calculated with an estimated resonated signal waist of $\sim$170 μm within the cavity.

5.3.4 Amplification in Bulk PPKTP

In order to increase the single longitudinal mode output pulse energy from the grazing incidence diffraction grating cavity, a single pass OPA was implemented using the Isorad PPKTP crystal. The OPA crystal axis was tilted by 5° in the horizontal plane (1.4 mm dimension) relative to the pump beam in order to eliminate monolithic oscillations supported by idler wavelength Fresnel reflections from the crystal faces, which were observed at pumping levels above 8 mJ when the crystal was aligned on axis. The temporal overlap between the OPA pump and OPO signal pulses was adjusted using the variable length beam delay path as indicated in figure 5.22 on page 89 for optimum output energy, which was found to correspond to a delay of 4 ns between the $1/e^2$ amplitude levels of the OPA pump and seed signal pulses. The pump beam was shaped to an approximately collimated beam with 450 μm $1/e^2$ radius at the position of the OPA crystal using a Keplerian telescope comprising $f = 750$ mm and 50 mm focal length achromat lenses. A dichroic mirror coated for $R = 99\%$ at the 1.68 μm signal and $T = 95\%$ at the pump wavelength was used to spatially overlap the pump and OPO signal beams within the OPA crystal. An $f = 150$ mm lens collimated the signal beam and weakly focused it to a large waist within the OPA crystal.

The single pass PPKTP amplifier increased the output signal and idler energies with

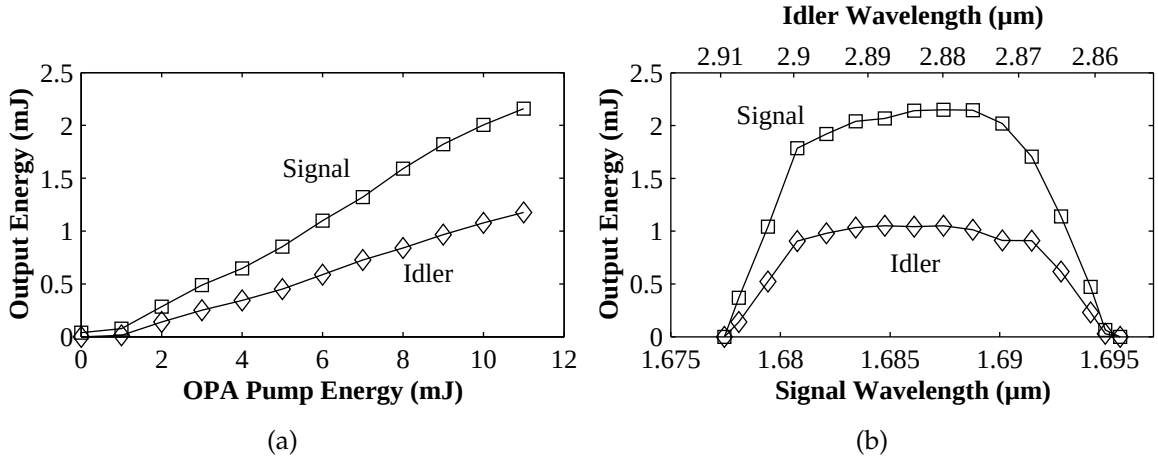

Figure 5.26: Signal (squares) and idler (diamonds) output energies of a PPKTP OPA, seeded by the single longitudinal mode signal of a PPKTP OPO. (a) Efficiency at a peak signal wavelength 1.687 μm, where 11 mJ pump generated signal (idler) pulse energies of 2.15 mJ (1.18 mJ). (b) Amplifier tuning range, with the signal (idler) wavelength tuning over 1.679–1.694 μm (2.861–2.905 μm) by adjusting the tuning mirror angle of the OPO.

no measurable broadening of the signal optical bandwidth. Figure 5.23 (b) shows a trace through the fringe pattern of a 5 GHz free spectral range Fabry–Pérot interferometer of the pump plus amplified signal sum frequency component. This trace indicated an instrument limited optical bandwidth of 400 MHz, comparable to the bandwidth of the OPO seed signal.

An efficiency curve for the PPKTP amplifier is shown in figure 5.26 (a) for a signal (idler) wavelength of 1.687 μm (2.881 μm). At a maximum pump energy of 11 mJ, the OPA amplified the 0.37 mJ single longitudinal mode OPO seed to 2.15 mJ, and generated 1.18 mJ of idler radiation, corresponding to efficiencies of 19.6% and 10.7% respectively. The amplified signal radiation could be tuned across the wavelength range 1.679–1.694 μm by adjusting the OPO tuning mirror angle; no adjustments to the OPA were necessary. The corresponding idler tuning range was 2.861–2.905 μm. A tuning curve showing amplified signal and idler pulse energies is shown in figure 5.26 (b). The highest output energies were measured at a signal (idler) wavelength of 1.687 μm (2.881 μm). An observed difference of 2 nm between optimum performance signal wavelengths for OPO and OPA was attributed to minor inconsistencies in poling period and heating effects in the OPA crystal, where the peak pumping intensities approached 150 MW/cm^2. Over the signal (idler) wavelength range 1.682–1.690 μm (2.873–2.896 μm), the OPA output pulse energies were approximately constant, to within 10% of the maximum generated output. This was attributed to saturation and backconversion effects in the OPA limiting the

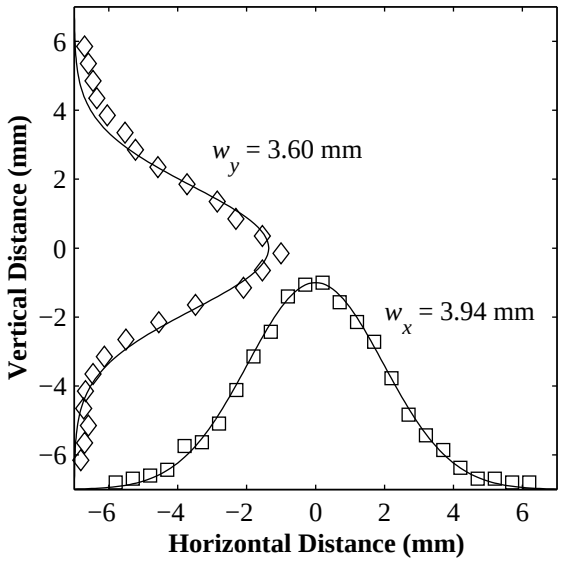

Figure 5.27: Horizontal and vertical spatial intensity distributions of the signal output beam from a PPKTP OPA seeded by the single longitudinal mode signal from a PPKTP OPO with grazing incidence diffraction grating, measured at a distance of 1 m from the amplifier. The solid lines indicate a Gaussian fit.

conversion efficiency, visible in the flat top signal pulse temporal profile shown in figure 5.25 (b). A 7 ns OPA signal pulse duration was recorded at the highest pump energies used, with corresponding depleted pump traces indicating a pump depletion reaching 25%.

As with the grazing incidence OPO, the OPA signal output beam spatial profile was recorded by translating a 100 μm aperture InGaAs photodiode through the beam. Sample horizontal and vertical intensity distributions, measured at a distance of 1 m from the OPA, are shown in figure 5.27, with a Gaussian fit. A far field divergence of 3.7 ± 0.2 mrad was measured. The lack of knowledge about the amplified signal beam waist within the OPA crystal makes M^2 beam quality deductions unreliable in this case.

5.4 Conclusion

In this chapter, passive optical bandwidth control of PPLN and PPKTP OPOs, pumped at 1.064 μm, was successfully demonstrated. Both intracavity étalon and grazing incidence diffraction grating configurations resulted in simple, compact cavities. In all cases, the measured single longitudinal mode optical bandwidths were below the 250–400 MHz resolution limits of the analysing interferometers used, and beams with excellent spatial

profiles were generated. The experiments indicated that, of the two methods for optical bandwidth control, the grazing incidence diffraction grating was superior. Despite higher thresholds, the grazing incidence cavities operated with higher slope efficiencies than étalon narrowed OPOs and typically generated similar levels of output energy. Qualitatively, the stability of the single mode in the grazing incidence OPOs was more reliable, and the absence of transmissive intracavity and resonator optics allowed the mid-infrared idler wavelengths to be extracted without specific optic substrates. In addition, the feasibility of implementing a cavity length stabilisation scheme was demonstrated.

Line narrowing using an intracavity étalon was found to only be successful in a PPLN OPO; in a PPKTP OPO, the crystal gain bandwidth was believed to have been too broad. The étalon approximately doubled the oscillation threshold and reduced the output signal pulse energy from 140 μJ to 78 μJ when the OPO was pumped with 1 mJ. In a short linear cavity PPLN OPO, cascaded oscillations [291] were observed and characterised, and subsequently suppressed using an intracavity prism that increased the oscillation threshold by 10% with respect to a linear cavity of the same length.

Single longitudinal mode OPOs based on PPLN and PPKTP were demonstrated in the grazing incidence diffraction grating configuration, with measurements of the resulting optical bandwidth limited by the resolution of the analysing interferometer. The performance of the $\Lambda = 30.4\,\mu$m period of the PPLN crystal may be compared to the $\Lambda = 37.4\,\mu$m period in the Brewster angled PPKTP crystal. The OPOs were constructed using the same diffraction grating and tuning mirror and exhibited similar threshold intensities of around 55 MW/cm^2. In agreement with similar reports in the literature [161], the grazing incidence OPOs could be tuned across almost twice the respective single pass crystal gain bandwidth, with 45 cm^{-1} (1300 GHz) of single longitudinal mode tuning demonstrated at a signal (idler) wavelength of 1.68 μm (2.9 μm). The PPLN and PPKTP OPOs were operated at up to 1.5 and 1.3 times threshold, respectively. The PPKTP OPO generated higher energy signal pulses, of up to 370 μJ, compared to the PPLN OPO that yielded up to 170 μJ. The power scaling possibilities in the large aperture PPKTP crystal were explored, with a free running OPO generating up to 18.3 mJ of output with a 70 mJ pump, and the same crystal used in an OPA to amplify the single longitudinal mode signal from the grazing incidence PPKTP OPO to 2.15 mJ signal and 1.18 mJ idler.

Chapter 6

Visible Region Pumped OPOs at 10 Hz Repetition Rate

Quasi-phase matched optical parametric oscillators (OPOs) pumped at 532 nm by the second harmonic of Nd : YAG were investigated, as reported in this chapter. The OPOs, based on periodically poled $LiNbO_3$ (PPLN) and periodically poled $KTiOPO_4$ (PPKTP), generated tuneable radiation in the 600–800 nm wavelength range. The optical bandwidths were narrowed using the passive line narrowing techniques discussed in chapter 4 to yield single longitudinal mode output. A PPLN OPO with grazing incidence diffraction grating is described in section 6.1, where a Perylene red poly(methyl methacrylate) (PMMA) solid state laser sample was used as a laser amplifier. In section 6.2, results from high pulse energy PPKTP OPOs are presented, as well as experiments in which the optical bandwidth was narrowed using an intracavity étalon.

The OPOs were pumped by the 532 nm output of an modified Continuum Powerlite PL7000. The injection seeded, flashlamp pumped, Q-switched Nd : YAG oscillator–amplifier system is described in section 5.1. The amplified pulses were frequency doubled in a type-I birefringent phase matched KD^*P nonlinear optical crystal. The system generated output energies of up to 180 mJ at 532 nm with a specified optical bandwidth of less than 90 kHz. In practice, only a small fraction of the output pulse energy was used to pump the OPOs, and the Q-switch trigger delay was adjusted from the optimum 185 μs to yield longer pulse durations and reduced output pulse energies.

6.1 OPOs Based on Periodically Poled $LiNbO_3$

The PPLN crystal used was obtained from Deltronic Crystal Industries and had physical dimensions (length $\times$ breadth $\times$ thickness) of $20 \times 5 \times 0.5\,\mathrm{mm}^3$. The crystal was

poled using a six track custom specified mask with poling periods of $\Lambda = 6.5$, 10.0, 10.3, 10.5, 10.8 and 12.1 μm. The 6.5 μm and 12.1 μm grating periods were chosen for quasi-phase matched second harmonic generation (SHG) experiments of 1.064 μm Nd : YAG and 1.295 μm LiF : F_2^- colour centre lasers, respectively, that were not related to this work. As can be seen from figure 3.4 (c) on page 44, careful temperature control of the crystal could yield a near degenerate 532 nm pumped OPO using the $\Lambda = 6.5$ μm poling period, but this was not attempted. The $\Lambda = 12.1$ μm poling period was not expected to yield efficient 532 nm pumped OPO configurations due to the strong absorption at the corresponding 5.2 μm idler wavelength [80]. Accordingly, the following sections present results from the remaining $\Lambda = 10.0$–10.8 μm poling periods, for which the resulting signal (idler) wavelengths ranged from 619 nm to 639 nm (3.16 μm to 3.77 μm).

The PPLN crystal end faces were polished and coated to yield low reflectivity over the 532–640 nm and 1.20–1.30 μm wavelength ranges. The latter was specified for the LiF : F_2^- SHG experiments mentioned above. Due to residual Fresnel reflections at the idler wavelengths, estimated to exceed 10% per face, monolithic OPO resonance at the idler was observed for pump energies in excess of $\sim$300 μJ, limiting the pump energies that could be used for passively line narrowed OPO configurations. The crystal was held in a temperature controlled oven and operated at 160.0 ± 0.1°C to prevent photorefractive effects, to which PPLN is susceptible, particularly at visible wavelengths [99, 100, 295]. Mounting of the crystal oven on a precision three axis translation stage permitted accurate control of the crystal placement as well as track selection.

6.1.1 Grating Narrowed PPLN OPO

The pump laser was operated with a Q-switch delay of 261 μs to yield smooth and stable 7 ns duration (FWHM) pulses with 20 mJ energies at 532 nm. The Fresnel reflection from the front face of a fused silica wedge directed up to 500 μJ of the pump to the OPO, and a half wave plate and polariser combination was used to allow smooth variable control of the incident energy and to select the correct pump polarisation (parallel to the z axis of the crystal). The pump beam was focused using an antireflection coated 500 mm focal length achromat. The PPLN crystal was placed $\sim$50 mm beyond the waist formed so that the pump beam filled the entire crystal volume [296]. In an initial test with a 25 mm long linear cavity employing a $R = 70\%$ reflective optic at the signal wavelength as the output coupler, an oscillation threshold energy of 25 μJ was measured, and at 300 μJ incident pump energy the OPO generated 64 μJ of signal energy.

The grazing incidence diffraction grating OPO is shown schematically in figure 6.1.

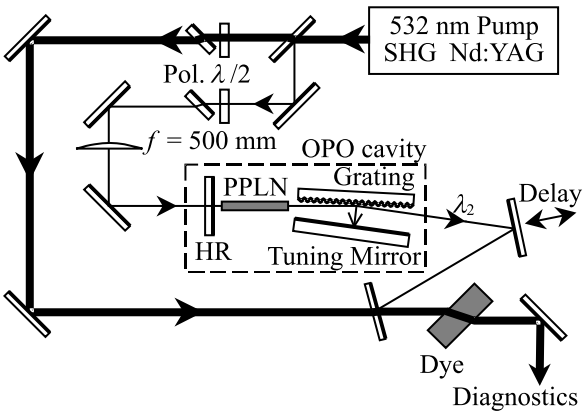

Figure 6.1: Experimental configuration of a PPLN OPO with grazing incidence diffraction grating, and laser amplifier. $\lambda/2$, Half wave plate; Pol, thin film polariser; HR, signal high reflector. The single mode OPO signal beam was amplified in a Perylene red doped PMMA solid state dye amplifier.

The pump beam entered the OPO cavity through a plane dielectric mirror coated for high reflectivity over 555–640 nm and a transmission of $T \approx 76\%$ at 532 nm. A 50 mm long holographic diffraction grating (Optometrics Group, 5-2407), dielectric coated for high reflectivity at visible wavelengths, was introduced at grazing incidence, with incidence angle $\theta_i \approx 86^\circ$ (see figure 4.3 on page 57). The cavity was completed by a plane metallic aluminium mirror retroreflecting the first diffraction order of the signal beam. For diagnostic measurements and the amplification experiments, the OPO output was collimated by a 200 mm focal length lens and a dichroic mirror was used to discard the depleted pump. Signal wavelength spectroscopic measurements were obtained by spatially dispersing the OPO output using a Brewster cut ZnS prism. The idler pulse energies were too low to be measured accurately.

Two diffraction gratings, ruled at 2400 mm^{-1} and 1800 mm^{-1}, were tested. The tuning mirror angles $\theta_m \approx 31^\circ$ and $\approx 7^\circ$ relative to the grating normal resulted in minimum physical cavity lengths of 75 mm and 40 mm. It was found that the dispersion provided by the 1800 mm^{-1} grating was sufficient to yield single mode operation, and the shorter cavity length and therefore lower threshold resulted in more efficient and more stable OPO performance. This was attributed to operation closer to threshold in the case of the 2400 mm^{-1} grating at the pump energy corresponding to the monolithic resonance threshold. The 1800 mm^{-1} grating was used for the remaining experiments.

The diffraction grating restricted the OPO to oscillate on a single longitudinal mode. The performance of the grazing incidence OPO at the different wavelengths is summarised in table 6.1. An oscillation threshold of 230 μJ was measured. Single mode op-

Table 6.1: Performance summary of PPLN OPO with grazing incidence diffraction grating. The maximum pump energy used was 300 μJ.

	Grating Period Λ (μm)			
Parameter	10.0	10.3	10.5	10.8
Signal Wavelength λ_2 (nm)	639.7	631.7	626.7	619.4
Idler Wavelength λ_1 (μm)	3.16	3.37	3.52	3.77
Threshold (μJ)	230	230	230	210
Max. Signal Energy (μJ)	9.1	9.1	9.2	10.0

eration could be maintained only for pump energies below 330 μJ; beyond this level, the OPO operated on many modes with large pulse to pulse variation in the output spectrum, and the external cavity was ineffective in controlling the optical bandwidth. This was established to be caused by monolithic resonance at the idler wavelength, supported by the reflections at the crystal face. In subsequent experiments, reported in section 7.3, a monolithic PPLN OPO was successfully injection seeded by laser diodes. The idler resonance could have been overcome by more optimum antireflection coatings or by employing a crystal with wedged end faces, such as the Brewster cut PPKTP crystal used to inhibit monolithic oscillation in section 5.3, as well as in a number of published works [91, 96, 98, 287]. In the present case, the OPO was operated at pump energies below the onset of monolithic oscillation. At a pump pulse energy of 300 μJ, up to 10.0 μJ of signal energy was obtained, with the OPO operating at $\approx$1.3 times threshold. The highest signal slope efficiency measured was 15%.

High resolution spectra were obtained by imaging the fringe pattern produced by a 5 GHz free spectral range (FSR) solid fused silica Fabry–Pérot interferometer onto an Ikegami silicon CCD camera. The narrowband 532 nm radiation from the pump laser was used to establish a resolution limit of 300 MHz at 532 nm for the interferometer, which had been in-house coated with metallic silver. Sample single mode spectra are shown in figure 6.2 for the OPO operating at wavelengths of 619 nm and 639 nm; the other crystal periods yielded similar spectra. The optical bandwidth measured from the traces indicated that the OPO operated on a single cavity mode with a signal bandwidth of 350 MHz, close to the interferometer limit. The OPO operated stably on a single mode over many pulses despite no active stabilization.

A CCD camera was used to measured beam profiles in the vicinity of a secondary waist formed by a 400 mm focal length lens. The single mode OPO signal radiation had a smooth, Gaussian spatial profile, and from the variation in spot size with propagation distance, a beam quality parameter of $M^2 = 1.2$ was calculated. Temporal profiles of the OPO signal output pulses, measured using a 1 ns rise time Si photodiode, indicated

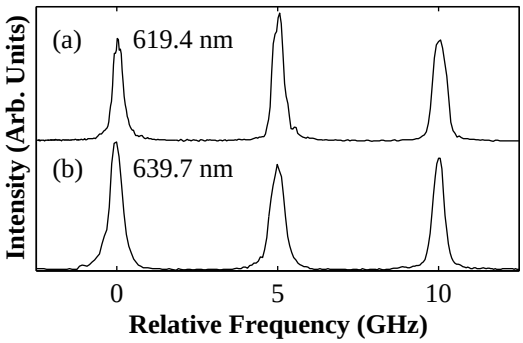

Figure 6.2: Line profiles taken through the fringe pattern produced by a 5 GHz FSR Fabry–Pérot interferometer by a PPLN OPO with grazing incidence diffraction grating, at a signal wavelength of (a) 619.4 nm and (b) 639.7 nm.

smooth signal pulses with FWHM duration of around 2 ns. The pulses had a temporal stability of $\sim$1 ns, attributed to the timing jitter of the pump pulses, and an amplitude stability of $\pm$10%. Pump depletion was estimated to be less than 10%.

Pumping with a broadband pump was investigated by blocking the injection seed to the pump laser, which resulted in a multiple mode pump spectrum with an estimated optical bandwidth of 15 GHz. Under these conditions, the grazing incidence OPO was observed to operate on many modes. Use of the higher dispersion 2400 mm^{-1} grating was also ineffective in obtaining single mode oscillation under broadband pumping.

6.1.2 Amplification in Solid State Dye

In order to increase the output energy of the single mode PPLN OPO, a single pass solid state dye amplifier was constructed, using a solid state dye disc supplied by Industrial Research Ltd (Wellington, New Zealand). A 9.2 mm thick PMMA sample, doped with Perylene red at a concentration of 1.25×10^{-4} M, was used. The dye was chosen since the 532 nm second harmonic of Nd : YAG is adequately matched to the 567 nm absorption peak, while the fluorescence spectrum encompasses the 619–640 nm signal wavelength of the OPO described in the previous section. No attempts were made to optimise the properties of the sample due to the large number of variables in such investigations [45]. The disc was mounted at Brewster's angle for the $\sim$620 nm OPO signal wavelength to minimise reflection losses. Up to the 20 mJ maximum pump energy used, the dye absorbed all of the pump radiation with no detectable spontaneous lasing or ASE, confirming that the sample was operating as a single pass amplifier.

As illustrated in figure 6.1 on page 99, the dye amplifier was pumped by the residual

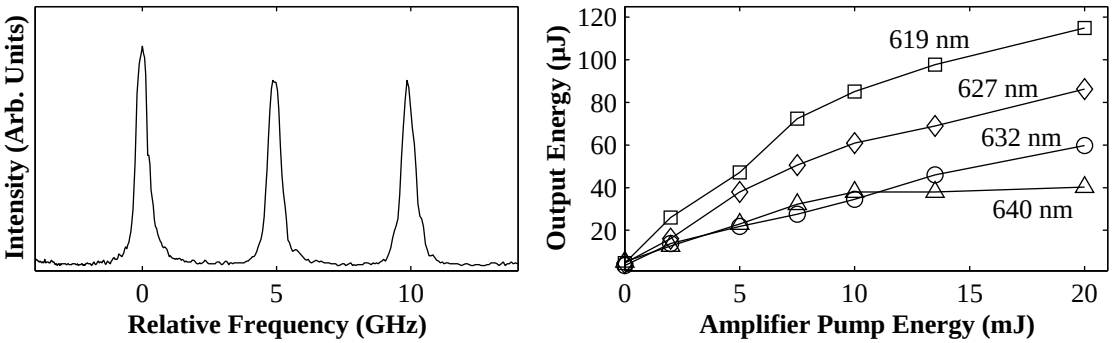

Figure 6.3: Performance of a Perylene red doped PMMA amplifier, seeded by the single mode signal output of a PPLN OPO. (a) Line profile through the fringe pattern produced by a 5 GHz FSR Fabry–Pérot interferometer for an OPO signal wavelength of 619.4 nm. (b) Amplifier pulse energy, for seed wavelengths of 619.4 nm (squares); 626.7 nm (diamonds); 631.7 nm (circles); 639.7 nm (triangles).

energy from the pump laser not used to drive the grazing incidence OPO. A separate half wave plate and polariser combination permitted independent control of the energy incident on the dye sample, which was restricted to below 20 mJ to prevent physical damage to the sample. The pump spot size at the dye sample was 1.5 mm, and no focusing or other control of the pump mode size was implemented. Spatial overlap between the pump and OPO signal beams was accomplished by the use of a plane dielectric mirror coated for high reflectivity over 555–640 nm while maintaining $T \approx 70\%$ transmission at the 532 nm pump wavelength. Temporal overlap was optimised by adjusting the position of a beam steering mirror, as shown in figure 6.1, to yield the highest output pulse energy.

Figure 6.3 (a) shows a representative spectrum of the amplified radiation, measured using a 5 GHz FSR solid fused silica Fabry–Pérot interferometer. From the spectrum, the optical bandwidth of the amplifier output was determined to be $\leq$400 MHz, close to the interferometer limit and comparable to that of the OPO. The difference between the two spectral widths was not considered significant [296]. The single pass amplifier configuration did not contribute additional spectral structure, making the system suitable for amplifying a single mode, continuously tuned OPO in this spectral region.

Figure 6.3 (b) shows the amplifier efficiency for different seed wavelengths. For these measurements, the OPO was pumped with 300 μJ to maintain single mode operation. With the pump to the amplifier blocked, typically 5 μJ of signal radiation was measured passing through the solid state dye disc. At the highest amplifier pump energy of 20 mJ,

Table 6.2: Beam quality parameters M^2 and astigmatism for PMMA amplifier as a function of amplifier pump energy.

Pump	M^2 Beam Quality		Astigm.
Energy (mJ)	Horizontal	Vertical	(mm)
0	1.2	1.2	13
7.5	1.8	1.3	32
20	7.4	2.1	39

the signal energy varied between 115 μJ at 619.4 nm and 40.2 μJ at 639.7 nm, with a slight roll-over observed for pump energies in excess of 10 mJ. This corresponded to a single pass gain of between 20 and 4. The wavelength dependence of the amplification efficiency was partly attributed to the profile of the Perylene red dye fluorescence spectrum [45]. From the spectrum, higher output energies would be expected at shorter wavelengths around 600 μJ.

The beam quality measurements of the amplifier beam were carried out using a 500 mm focal length lens to form a secondary waist. Measurements were made at pump energies of 7.5 mJ and 20 mJ, as well as with the dye sample unpumped. The horizontal and vertical M^2 parameter values measured are listed in table 6.2. The table also shows the astigmatism (separation in the z propagation axis between the horizontal and vertical waists) recorded in the emitted beam. The amplifier beam quality degradation from that of the seed OPO was attributed to thermal lensing in the dye sample. The astigmatism and difference in M^2 for horizontal and vertical directions were attributed to the Brewster angle configuration of the dye sample. In the far field, the beam profiles were found to be somewhat round but noisy, as illustrated in figure 6.4, recorded at a distance of 620 mm after the lens, with the amplifier pumped at 20 mJ.

6.2 OPOs Based on Periodically Poled KTP

A PPKTP crystal suitable for 532 nm pumped OPO was obtained from Isorad Inc. The crystal had dimensions $20 \times 7 \times 0.5\,\mathrm{mm}^3$ (length $\times$ width $\times$ thickness) and was poled with a single $\Lambda = 10.15\,\mu$m poling period across 5 mm of the crystal width. The crystal end faces were polished parallel and dual band antireflection coated at the 532 nm pump and 770 nm signal wavelengths.

The signal wavelength of the crystal could be tuned across 755.5 nm to 770.8 nm (idler wavelength range 1.717 μJ to 1.798 μm) by changing the temperature from 20°C to 150°C, as shown in figure 6.5. The tuning curve was measured using a 30 mm long plane–plane cavity with a 50% reflective output coupler, and the pump beam focused to a 170 μm

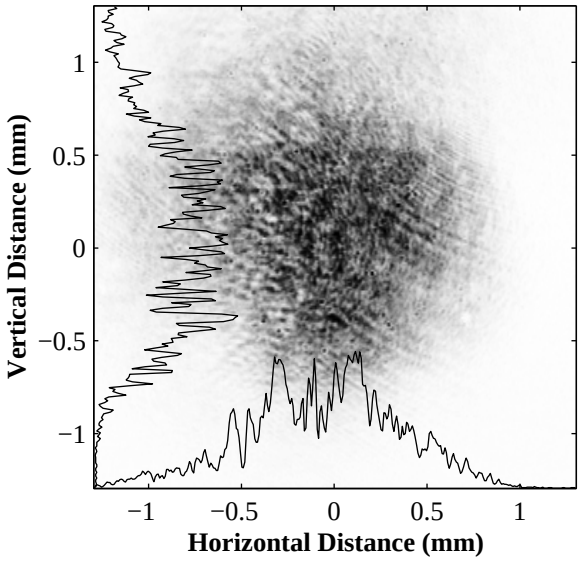

Figure 6.4: Horizontal and vertical spatial intensity distributions of the amplified single mode PPLN OPO signal amplified in Perylene red doped PMMA solid state dye, pumped at 20 mJ.

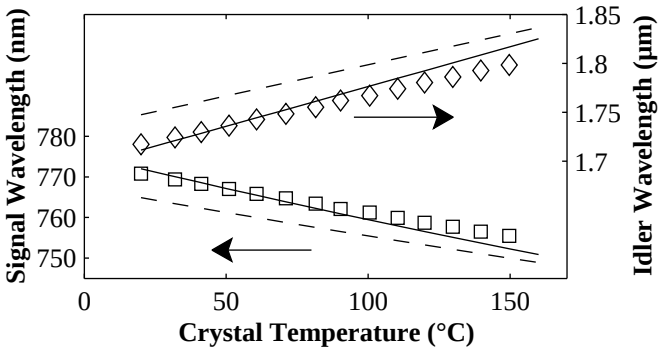

Figure 6.5: Measured signal (squares) and deduced idler (diamonds) temperature tuning curve for a PPKTP OPO with poling period $\Lambda = 10.15\,\mu$m, with predicted curves using Sellmeier equations of reference [262] (solid line); and references [112] and [263] (dashed line).

waist using a 1 m focal length lens. For the wavelengths of this OPO, the temperature dependent Sellmeier equation of Kato *et al.* [262] satisfactorily predicted the phase matching wavelengths, as shown by the solid line. For comparison, the tuning curve predicted using the Sellmeier equations of Fradkin *et al.* [112] and the refractive index temperature derivatives of Kato [263], found to give better agreement in chapter 5, is shown by the dashed line.

6.2.1 Etalon Narrowed PPKTP OPO

Residual feedback from the crystal faces at the idler wavelength, where the crystal coating was not specified, permitted the PPKTP crystal to support monolithic oscillations. The resonated wave was determined by tilting the crystal in the vertical plane and observing non-collinear phase matching, where the idler was constrained by the crystal axis and a signal beam deflection opposite to the crystal tilt was observed. In this PPKTP the thresholds of the monolithic oscillations were within an order of magnitude of those of short external cavities with signal reflectivities of up to 95%, as described in the following section. A grazing incidence diffraction grating cavity was constructed, but the increased threshold due to the longer cavity length and higher cavity losses resulted in this configuration being ineffective in restricting the OPO optical bandwidth.

Single longitudinal mode operation of the PPKTP OPO was demonstrated using an intracavity étalon for pump powers below the onset of monolithic resonance. A 60 mm long plane–plane OPO cavity was constructed, using a 70% reflective output coupler at the signal wavelength. The OPO was placed 300 mm beyond the line focus formed by a 1 m focal length cylindrical lens, with a spatial aperture used to restrict the beam to the thickness of the crystal. The resulting pump spot within the PPKTP crystal was approximately flat-top, of diameter 350 μm, in the narrow dimension and Gaussian with $1/e^2$ radius 2.3 mm in the unconstrained dimension, to fill the available crystal volume.

The free running optical bandwidth of the OPO was measured using a 0.75 m diffraction grating monochromator equipped with a linear CCD array. The resolution of the monochromator was 0.2 nm. Spectra of three arbitrary OPO pulses are shown superimposed in figure 6.6 (a), in which the fast oscillations arose from the CCD reading electronics. The free running optical bandwidth was 1.1 nm FWHM with $\sim$0.1 nm pulse to pulse variation.

A solid fused silica étalon (TecOptics, ES-251-779-779) was inserted between the PPKTP crystal and the output coupler and tilted by 11 mrad in the crystal thickness plane to prevent feedback from the étalon faces. The étalon had a FSR of 20 GHz, and the faces

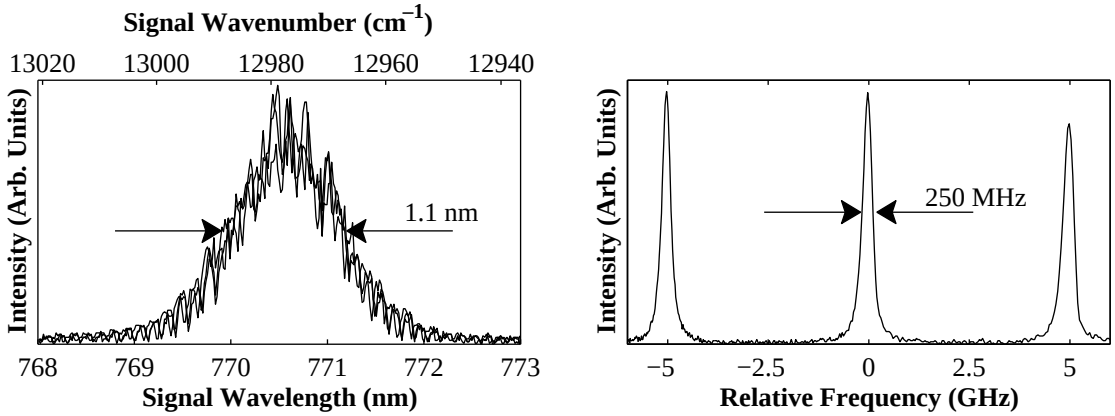

Figure 6.6: Signal spectra of an étalon narrowed PPKTP OPO. (a) Free running spectrum; (b) Line profile through the fringe pattern produced by a 5 GHz Fabry–Pérot interferometer.

were coated for $R = 90 \pm 2.5\%$ over the 580–860 nm wavelength range, from which a finesse of $\mathcal{F} = 30 \pm 8$ was calculated. The étalon restricted the OPO to oscillate on a single longitudinal mode of the cavity. The optical bandwidth of the line narrowed OPO was recorded using a 5 GHz FSR Fabry–Pérot interferometer, yielding a fringe profile as shown in figure 6.6 (b). An optical bandwidth of 250 MHz was measured, limited by the resolution of the interferometer. The OPO operated on a single mode reliably over several pulses. There was qualitative evidence of the crystal faces aiding in the single mode operation in the form of coupled cavities, with the single mode performance being affected by changes in the crystal position relative to the cavity optics. The pump pulse energy was restricted to below 1 mJ by the low damage threshold of the étalon coatings, specified at 150 mJ/cm^2. An oscillation threshold of 0.4 mJ was measured, and at the maximum 1 mJ pump energy, up to 44 μJ of signal pulse energy was generated.

6.2.2 High Pulse Energy PPKTP OPOs

In order to exploit the high power scaling capabilities of PPKTP at visible wavelengths, a number of pump shaping geometries, designed to fill the available crystal volume, were investigated. The Q-switch delay of the pump laser was adjusted in each case to yield suitable pulse energies. Peak pump intensities at the crystal were restricted to 250 MW/cm^2 to prevent crystal and coating damage. The combination of a half wave plate and thin film polariser allowed for variable control of the pump energy incident on the OPO, in addition to ensuring correct polarisation of the pump wave.

In each of the pump focusing geometries, the performance characteristics of a num-

ber of plane–plane OPO cavities were compared in terms of threshold and maximum output energy. All cavities employed the same input coupler, through which the pump entered the cavity, a plane dielectric optic coated for high reflectivity between 700 nm and 900 nm, while maintaining T = 78% transmission at the 532 nm pump wavelength. For the monolithic OPO results presented, the input coupling optic was misaligned to prohibit feedback into the cavity but left in place to enable direct comparison of the pump energies of the monolithic and external cavities.

The generated OPO signal and idler beams were spatially isolated using an uncoated Brewster angled ZnS prism, with the residual pump radiation eliminated by a dielectric coated 45°, 532 nm beam steering mirror. For idler measurements, an additional RG850 glass filter (transmission $T \geq 90\%$ 850–2200 nm; absorption $> 99\%$ below 800 nm) was used to eliminate visible wavelengths. The signal and idler output energy measurements were corrected for transmission losses of the diagnostic optics, measured to be 35.1% at the 770 nm signal wavelength, largely due to the high loss at the pump dichroic, and 10.9% at the 1.7 μm idler wavelength.

Beam quality M^2 measurements were calculated by focusing the PPKTP OPO signal beam to a secondary waist using a 200 mm focal length lens and recording beam spatial distributions at a number of positions along the z propagation axis using a silicon CCD camera. Gaussian distributions were fitted to each beam profile, and the progression of mode sizes was used to derive an M^2 value.

The pump spatial profile shaping geometries used are illustrated in figure 6.7. The configurations included a 1 m focal length lens; focusing with a 500 mm focal length lens and positioning the PPKTP crystal beyond the waist so that the pump filled the available crystal volume; focusing with a 1 m cylindrical lens leaving the beam dimension in the direction parallel to the crystal width unchanged; and focusing with a 1 m cylindrical lens, placing the crystal beyond the waist in the focused dimension and using a rectangular aperture to generate a flat top profile filling the entire available crystal volume. The highest output pulse energies generated in each configuration are tabulated in table 6.3.

1 m Spherical Lens

In the first configuration, a 1 m focal length lens weakly focused the pump beam to a waist of 170 ± 10 μm within the crystal to approximate a collimated beam. The pump laser Q-switch delay was set to 330 μs to yield pulses of 15 ns duration. The energy incident on the PPKTP crystal was restricted to below 1 mJ (150 MW/cm^2).

With this configuration, threshold pump energies of between 15 μJ and 22 μJ were measured for the different output couplers. The signal and idler output energies as a

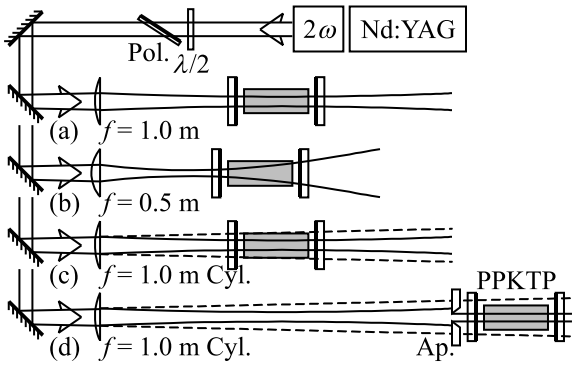

Figure 6.7: Experimental configurations of high pulse energy PPKTP OPOs, with the pump spatial profile configured to fill the available crystal aperture. $\lambda/2$, half-wave plate; Pol., polariser. (a) 1 m focal length spherical lens, crystal at the pump beam waist. (b) 500 mm focal length spherical lens, crystal beyond the waist. (c) 1 m focal length cylindrical lens to focus the beam in the plane corresponding to the 0.5 mm crystal thickness (solid line); in the other dimension, the beam divergence was left unmodified (dashed line). (d) 1 m focal length cylindrical lens, crystal beyond the waist and a rectangular aperture (Ap.) used to restrict the beam to the aperture of the crystal.

Table 6.3: PPKTP OPO output pulse energies using different beam shaping geometries, given for different output coupler reflectivities at the signal wavelength.

	Max	**Signal Pulse Energy (mJ)**				
Pump Shaping Geometry	**Pump (mJ)**	**95% R**	**70% R**	**50% R**	**30% R**	**Monol.**
1 m Lens, at focus	1	0.046	0.232	0.268	0.339	0.223
0.5 m Lens, beyond focus	3	0.10	0.62	0.74	1.12	0.93
1 m Cylindrical lens	10	0.15	1.12	1.54	2.17	2.10
1 m Cylindrical lens and aperture	20.3	0.38	2.60	3.36	4.06	3.74
	Max	**Idler Pulse Energy (mJ)**				
Pump Shaping Geometry	**Pump (mJ)**	**95% R**	**70% R**	**50% R**	**30% R**	**Monol.**
1 m Lens, at focus	1	0.106	0.104	0.088	0.078	0.048
0.5 m Lens, beyond focus	3	0.215	0.233	0.190	0.179	0.126
1 m Cylindrical lens	10	0.68	0.58	0.54	0.44	0.24
1 m Cylindrical lens and aperture	20.3	1.17	1.26	1.09	0.89	0.81

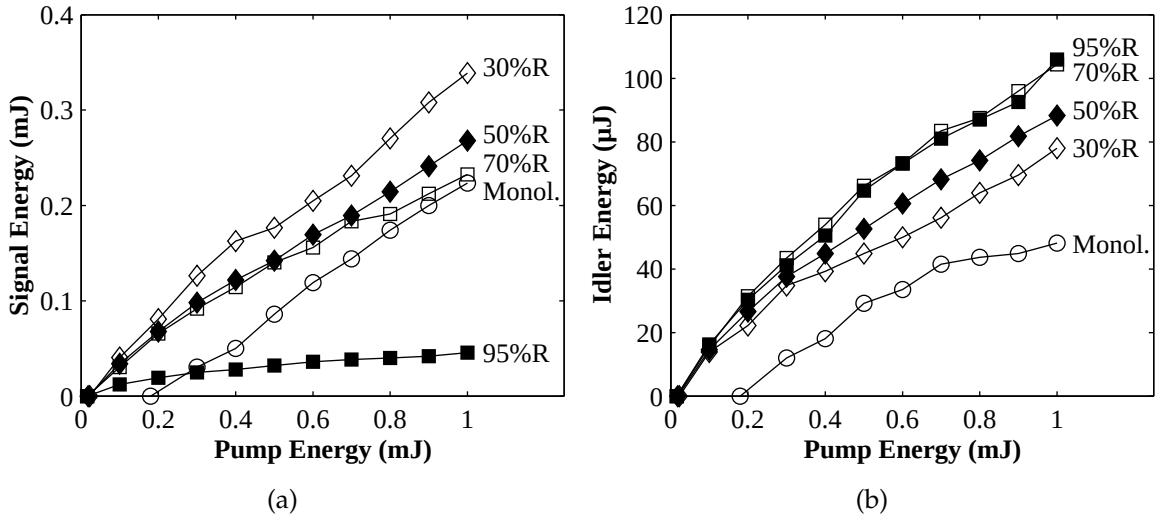

Figure 6.8: Signal (a) and idler (b) output energies of a PPKTP OPO, as a function of pump energy, for the OPO configuration of figure 6.7 (a). The output coupler reflectivity at the signal wavelength was 95% (filled squares); 70% (open squares); 50% (filled diamonds); 30% (open diamonds). The open circles line was measured for monolithic operation without cavity optics.

function of incident pump energy are shown in figure 6.8 (a) and (b) respectively. A 30% reflective output coupler was found to yield the highest signal output pulse energy of 339 μJ, corresponding to an efficiency of 34%. For the highest idler output pulse energy, the 95% and 70% reflective output couplers yielded similar performance with a highest measured idler energy of 106 μJ (10% efficiency). The trends of the 30% reflective output coupler yielding the highest signal output pulse energy, and the highest idler being generated using reflectivities above 70%, were observed for all OPO configurations. The signal beam was observed to have a smooth far field spatial profile, and a beam quality parameter of $M^2 = 3.1 \pm 0.1$ was measured.

Monolithic operation was observed above 200 μJ pump energy: peak signal and idler energies were 223 μJ and 48 μJ, respectively (slope efficiencies 27% and 5.8%). The threshold for monolithic oscillation was 180 μJ, approximately a factor of 10 higher than that measured with output couplers with signal reflectivities in excess of 50%. The idler output pulse energy showed a distinct roll-over above three times threshold, whereas the signal output was consistently 200 μJ lower than the output using the 30% reflective output coupler.

500 mm Spherical Lens

It was found in earlier PPLN experiments (chapter 5) that the onset of monolithic resonance could be delayed to higher pump energies by placing the crystal beyond the focus so that the diverging pump beam filled the entire crystal volume. This focusing geometry was investigated for the high pulse energy PPKTP OPO, with the crystal placed 50 mm beyond the waist formed by a 500 mm focal length achromat, which resulted in a pump spot size of $190 \pm 10\,\mu$m at the input face and $270 \pm 10\,\mu$m at the output face of the PPKTP crystal. In this configuration, the pump energy was limited to 3 mJ (250 MW/cm^2).

The threshold of oscillation of the OPO was measured to be $\approx$30 μJ. At the highest pump energy of 3 mJ, the highest signal output pulse energy of 1.12 mJ was measured using a 30% reflective output coupler at the signal wavelength, whereas the highest idler output pulse energy of 0.23 mJ was reached with a 70% reflective output coupler at the signal wavelength. The peak signal and idler efficiencies were thus 37% and 7.8%. Monolithic oscillations were observed above a pump energy of 0.4 mJ and provided peak signal and idler output energies of 0.93 mJ and 0.13 mJ respectively. Consistent with PPLN and PPKTP OPOs using similar pump focusing geometries, a satisfactory beam quality was measured for both horizontal and vertical axes, with $M^2 = 2.7 \pm 0.5$, where the comparatively large error resulted principally from the uncertainty in the focused waist size.

In this configuration, a comparison between PPKTP and the PPLN OPO of section 6.1 section could be made, even though some of the operating parameters were dissimilar. Principally, whereas the signal (idler) wavelengths of the PPKTP OPO were 770 nm (1.7 μm), for the PPLN OPO these were 626 nm (3.5 μm). The different refractive indices ($\approx$2.2 in PPLN and $\approx$1.8 in PPKTP) and nonlinear coefficients ($d_{33} = 27$ pm/V in PPLN compared to 14.6 pm/V in PPKTP) combined to give a similar nonlinear interaction coefficients $\kappa_{\mathrm{PPLN}} = 3.84 \times 10^{-7}\,\mathrm{W}^{-1}$ and $\kappa_{\mathrm{PPKTP}} = 3.06 \times 10^{-7}\,\mathrm{W}^{-1}$. Incorporating the remainder of the parameters required for the threshold model of Brosnan and Byer [78], equation(3.27), in particular a pump pulse duration of 15 ns (FWHM) for the PPLN and 10 ns for the PPKTP OPO, threshold pump energies of 43 μm and 41 μJ were predicted for the two OPOs. These values were in acceptable agreement with the 41 μm and 30 μJ thresholds measured. Despite similar thresholds, it was clear from the above efficiency curves that the PPKTP OPO could be driven to produce significantly higher output pulse energies than the PPLN OPO.

As the dynamic range accessible with this configuration included two orders of magnitude between threshold and maximum pump energy, temporal profiles were measured using a 1 ns rise time photodiode and a Tektronix TDS350 digital storage oscilloscope.

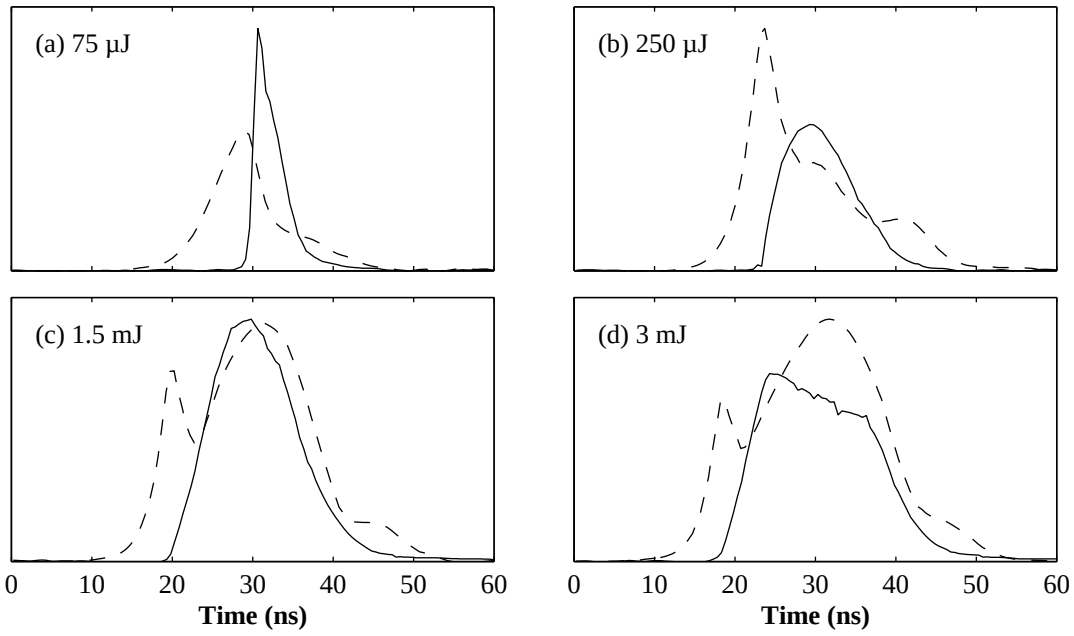

Figure 6.9: Temporal profiles of the signal (solid line) and depleted pump (dashed) pulses of a PPKTP OPO, in the configuration of figure 6.7 (b). The pump energy was (a) 75 μJ; (b) 250 μJ; (c) 1.5 mJ; and (d) 3 mJ.

Figure 6.9 shows traces of the signal and depleted pump pulses taken at different pump levels. Close to threshold, a short signal pulse was emitted after the peak of the pump pulse, with depletion visible on the depleted pump profile. With increased pumping, signal pulse build-up time decreased and backconversion of signal and idler became visible in the regrowth at the centre of the depleted pump pulse.

1 m Cylindrical Lens

In order to make use of the entire 5 mm width of the poled track within the PPKTP crystal, a 1 m focal length cylindrical lens was employed to create a 180 μm waist line focus in the crystal thickness plane. In the crystal width plane, the pump beam was allowed to freely propagate over 3 m, which yielded an approximately Gaussian distribution with a 1.5 mm radius. By measuring the OPO output pulse energy as a function of transverse crystal translation, it was concluded that the crystal thickness was adequately filled, whereas the beam diameter in the crystal width direction could have been enlarged by $\sim$0.5 mm without clipping at the edges of the poled region. The pump Q-switch delay was adjusted to 298 μs to obtain at most 10 mJ incident on the PPKTP crystal in a 9 ns pulse.

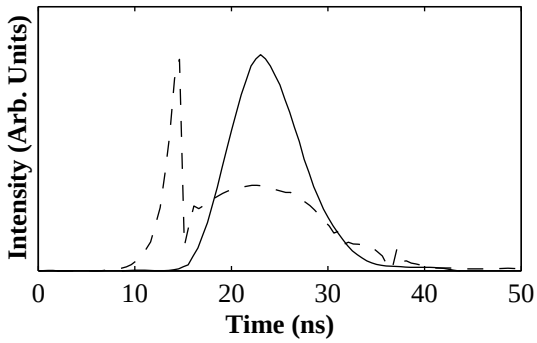

Figure 6.10: Temporal profiles of the signal (solid line) and depleted pump (dashed line) pulses of a OPO in the configuration of figure 6.7 (c), pumped at 10 mJ pulse energy.

The OPO threshold was measured to be ≈150 μJ. At the highest pump energy used, the highest signal and idler energies were 2.17 mJ and 0.69 mJ, obtained with output coupler signal wavelength reflectivities of 30% and 95% respectively (efficiencies 22% and 6.9%). Monolithic oscillations were observed above 2.4 mJ pump energy, and although the signal slope efficiency was higher than the highest external OPO efficiency, a slightly lower pulse energy of 2.10 mJ was generated. The output energy was unstable from pulse to pulse, varying by as much as 30 μJ. Since dynamic amplitude and spectral instabilities are characteristic of doubly resonant oscillators, which have been treated extensively in the literature [140], this led to the speculation that the OPO was operating as a coupled system between the signal radiation resonated by the cavity optics and the idler radiation resonated by the crystal faces.

The large vertical dimension of the pump beam within the plane–plane resonator resulted in a significantly increased signal beam quality parameter if $M^2 = 18 \pm 2$ in this dimension. The observation of this phenomenon in PPLN OPOs and OPGs was subsequently reported by Missey *et al.* [91], who found that flood pumping large crystal apertures yielded a significant increase in divergence and spectral bandwidth, and gave an explanation for this in terms of the phase matching geometry. In the horizontal dimension, the narrow pump waist constrained the resonated signal to $M^2 = 2.6 \pm 0.1$, comparable to the circularly symmetric beam quality measured when spherical lenses were used to focus the pump.

Temporal profiles of the signal and depleted pump showed similar characteristics to those shown in figure 6.9 at low to moderate pump energies. At the highest pump energies used, different dynamics between the interacting waves caused qualitatively different profiles, as illustrated in figure 6.10. The traces indicated a rapid depletion of

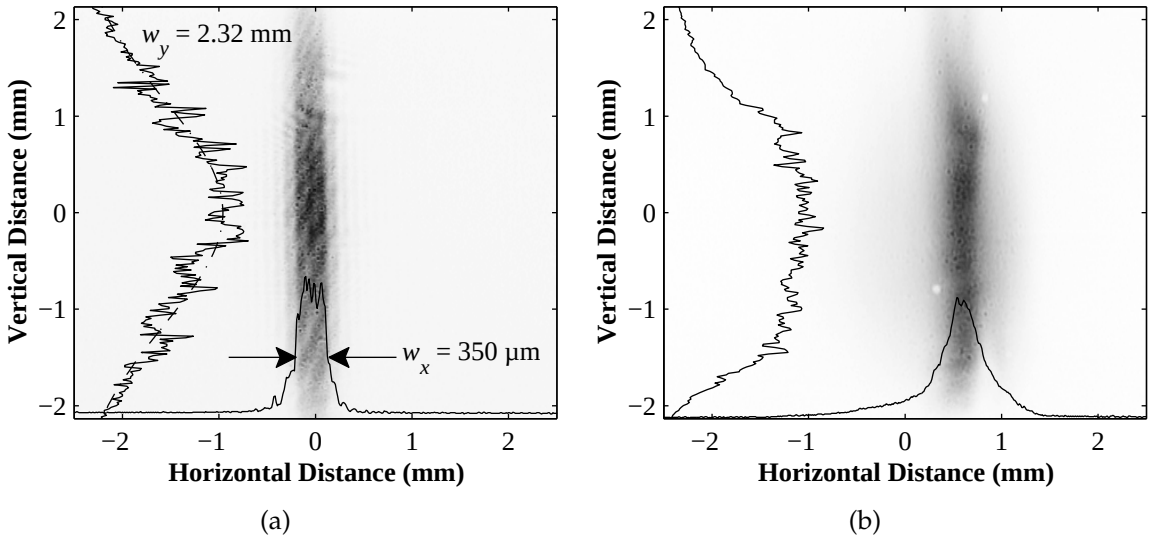

Figure 6.11: Horizontal and vertical intensity distributions of a PPKTP OPO, in the configuration of figure 6.7 (c). (a) Apertured OPO pump beam at crystal position; (b) far field signal output beam.

the pump wave as the OPO pulse energy grew, followed by significant backconversion. Such depleted pump profiles were commonly observed in numerical modelling of OPOs pumped far above threshold, as discussed in section 3.3. The signal profile, in this case, maintained a quasi-Gaussian pulse shape up to the highest energies used, with a pulse duration of around 8 ns.

Cylindrical Lens and Aperture

For the final power scaling experiment, the crystal was moved 0.3 m beyond the pump waist formed by the 1 m focal length cylindrical lens. A rectangular aperture was placed between the lens and crystal, with a narrow dimension that could be adjusted to yield an approximately flat top pump intensity profile, with a full width of 350 μm. In the orthogonal plane, the pump beam maintained a quasi-Gaussian intensity distribution with a spot size of 2.3 mm. The resulting pump beam profile at the PPKTP crystal is shown in figure 6.11 (a). The pump laser Q-switch delay was adjusted to 256 μs to yield 20 mJ incident on the OPO in a 8 ns pulse.

The signal and idler output energies from this configuration are presented in figure 6.12. The oscillation threshold of 0.2 mJ was a factor of 100 below the highest pump energy of 20.3 mJ used. The highest signal and idler pulse energies were 4.06 mJ and 1.27 mJ, measured with a 30% and 70% reflective output coupler respectively (efficien-

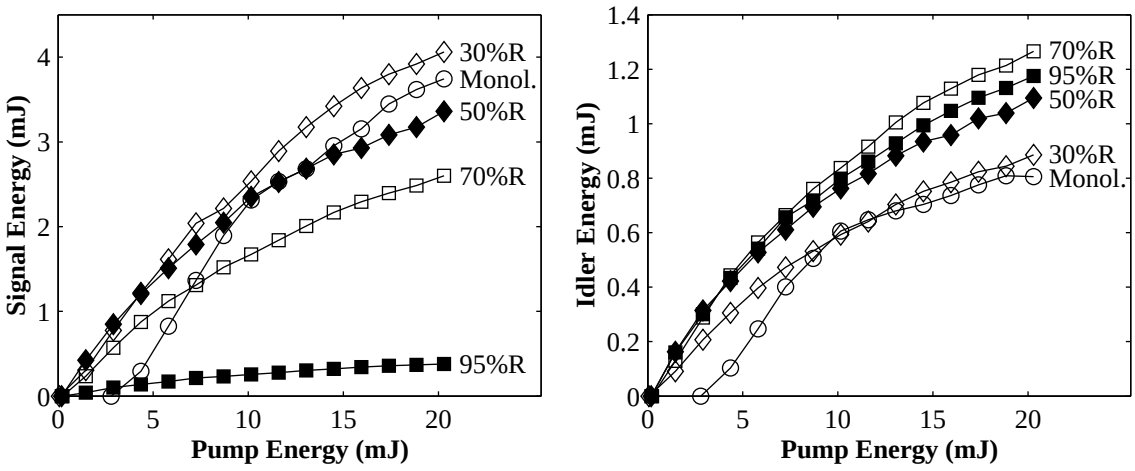

Figure 6.12: Signal (a) and idler (b) output energies of a PPKTP OPO, as a function of pump energy, for the OPO configuration of figure 6.7 (d). The output coupler reflectivity at the signal wavelength was 95% (filled squares); 70% (open squares); 50% (filled diamonds); 30% (open diamonds). The open circles line was measured for monolithic operation without cavity optics.

cies 20.2% and 6.3%). The threshold of monolithic oscillation was 2.78 mJ, an order of magnitude higher than that from a resonant cavity, and peak signal and idler output energies were measured to be 3.74 mJ and 0.81 mJ respectively.

As described above, the large pump spot size in the unfocused vertical dimension resulted in a poor beam quality in this dimension. In a similar fashion, the flat-top intensity distribution degraded the beam quality in the crystal thickness dimension. The far field intensity distribution is shown in figure 6.11 (b). The profile was recorded at a distance of 250 mm beyond the waist formed by a secondary lens, of focal length 200 mm. From a sequence of such images, a beam M^2 quality parameter of 7 ± 1 in the horizontal and 100 ± 30 in the vertical plane was calculated.

The maximum output energies and efficiencies obtained using the different pump focusing geometries are summarised in table 6.4. The intensity values show that each OPO was operated in a similar regime, with a typical threshold intensity of around 2.5 MW/cm^2 and a peak pump intensity of 250 MW/cm^2. The degradation in relative efficiencies with increasingly elaborate pump shaping strategies was attributed to a poorer pump beam quality, which also resulted in increasing M^2 parameters as shown in the table. The significant output energies generated by monolithic OPO suggested that this device could be developed into a robust, efficient device without the need for an external cavity. Some such devices, based on PPLN, have been reported in the literature [91, 98].

Table 6.4: Summary of PPKTP OPO performances using different pump beam shaping geometries.

	Pump Shaping Geometry			
Parameter	**1 m FL Lens**	**0.5 m FL Lens**	**1 m FL Cylindrical**	**1 m FL Cyl., Aperture**
Threshold Energy (mJ)	0.02	0.03	0.1	0.2
Threshold (MW/cm^2)	2.8	2.5	2.6	2.5
Pump Energy (mJ)	1	3	10	20
Signal Energy (mJ)	0.339	1.12	2.17	4.06
Idler Energy (mJ)	0.106	0.233	0.68	1.27
Signal Efficiency (%)	34.6	37.3	21.7	20.2
Idler Efficiency (%)	10.8	7.8	6.9	6.3
Beam Quality M^2	3.1$\pm$ 0.1	2.7$\pm$ 0.5	2.5 (h), 20 (v)	7 (h), 100 (v)

6.3 Conclusion

The development of passively line narrowed, 532 nm pumped PPLN and PPKTP OPOs reported in this chapter was impeded by the observation of monolithic resonance within the crystal, supported by the face Fresnel reflectivities at the idler wavelength. This was attributed, in part, to a higher nonlinear optical gain at shorter wavelengths, and overwhelmed the influence of external cavities in controlling the optical bandwidth. Single longitudinal mode operation was demonstrated for pump pulse energies below the onset of monolithic oscillation.

In a PPLN OPO with grazing incidence diffraction grating, single longitudinal mode operation was demonstrated between the external cavity threshold of 230 μJ and the onset of monolithic oscillation at 300 μJ. Up to 10 μJ of signal radiation was generated. This was sufficient for the successful implementation of a single pass amplifier based on a solid state dye disc of Perylene red doped PMMA, without measurable broadening of the optical bandwidth. The amplifier generated up to 115 μJ single longitudinal mode radiation at 619 nm.

In a PPKTP OPO, an intracavity étalon was used to yield single longitudinal mode signal radiation. Up to 44 μJ single mode pulses were generated, where the pump energy was limited to 1 mJ to prevent étalon coating damage. The oscillation threshold increased from 0.2 mJ to 0.4 mJ on insertion of the étalon.

Flood pumping of PPKTP OPOs was investigated using a number of different pump focusing geometries to fill the available crystal volume, with the OPOs operating up to 100 times above threshold. In one configuration, similar PPKTP and PPLN OPOs were calculated to have comparable nonlinear optical gain coefficients and thresholds, but in the case of PPLN, crystal damage considerations would have limited the OPO to less than

ten times threshold. In the PPKTP OPO, up to 4.06 mJ of signal radiation at 770 nm, and 1.27 mJ of idler at 1.72 μm, was generated, although it was believed that the performance of the OPOs was a combination of external cavity and monolithic resonance in each case. The crystal acting as a monolithic OPO generated up to 3.74 mJ of signal and 0.81 mJ of idler radiation, demonstrating the feasibility of exploiting such configurations without external cavities.

Chapter 7

High Repetition Rate Lasers and OPOs

Diode pumped Nd : YAG lasers are particularly well suited to pumping mJ-class optical parametric oscillators (OPOs) based on periodically poled $LiNbO_3$ (PPLN), with the high efficiency of Nd : YAG and large nonlinear optical coefficient of PPLN yielding compact systems with only modest primary pump power and cooling requirements. The development of such a laser source (section 7.1) and its application to pumping narrowband OPOs (sections 7.2 and 7.3) is reported in this chapter.

7.1 High Repetition Rate Nd : YAG Laser

The continuous wave (cw) diode pumped Nd : YAG laser was based a Light Solutions LightBook, customised to allow external cavities to be constructed around the laser head. A 3 mm diameter, 10 mm long 1% at. doped Nd : YAG rod was dual end pumped by 18 W fibre coupled diode arrays emitting at 808 nm. The outputs from the fibres were collimated and focused into the rod using lens pairs and dichroic mirrors, yielding a spot size of $\sim$200 μm. The diode arrays were water cooled using a recirculating chiller with heat exchanger, and the diode wavelength was optimised for highest laser output power by adjustment of the coolant temperature. About the head, a number of symmetric linear resonators were constructed using available optics.

The cavity configuration used to pump the OPOs described in the following sections is illustrated in figure 7.1. Both the cavity high reflector (HR) and the 80% reflective output coupler (OC) were concave with 300 mm radius of curvature. As described in chapter 2, the thermal lens was used to calculate a predicted thermal lens within the Nd : YAG rod of as short as $f_{\mathrm{Th}} \approx 75$ mm, with the dominant contribution arising from the dn/dT term

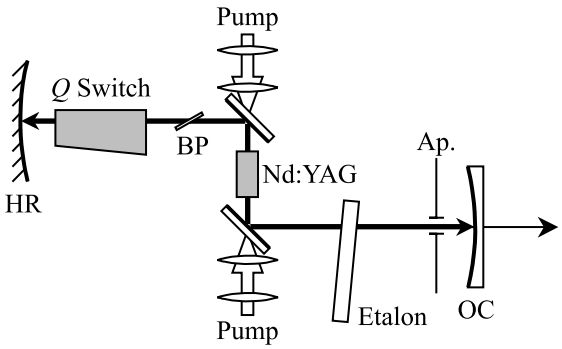

Figure 7.1: Cavity layout of a high repetition rate Nd : YAG laser. HR, high reflector; OC, output coupler; BP, Brewster plate; Ap., aperture.

of equation (2.19). Using the resonated mode stability considerations discussed in section 2.3, resonator lengths in excess of 300 mm were predicted to be unstable with such lensing. A detailed investigation into thermal lensing in this laser was not undertaken. The lensing and a limited selection of available cavity optics precluded the construction of complex resonators with longer cavity lengths, such as ring resonators, which have been shown to yield radiation with high spatial and spectral purity [12]. The laser was constructed with a cavity length of 220 mm, which was found to yield the optimum output power.

In this configuration with no intracavity optics, the laser exhibited an oscillation threshold of $\approx$1.5 W and generated up to 10.7 W cw at the maximum pump power of 33 W. Insertion of a Brewster plate (BP), used to ensure a linearly polarised output with polarisation ratio in excess of 100 : 1, reduced the output power to 10.1 W, resulting in an optical to optical slope efficiency of around 32%.

The introduction of a crystal quartz acousto-optic Q-switch into the cavity permitted pulsed operation at arbitrary pulse repetition frequencies. The Q-switch was 30 mm long, with a 2 mm clear aperture, and was modulated at 27.12 MHz to provide a 5 mrad beam deflection with $\geq$85% diffraction efficiency at 25 W rf power. The Q-switch end faces were dielectric v-coated for minimum reflectivity at 1.064 μm to provide low insertion loss. At a repetition frequency of 35 kHz, the maximum average power was 9.1 W, less than 10% lower than the cw level, and a pulse duration of 70 ns was measured. At 5 kHz the laser produced up to 5.5 W in 20 ns pulses, corresponding to 1.1 mJ.

In most operating configurations, the spatial quality of the laser beam was observed to deteriorate above $\sim$20 W diode power, attributed to thermal lensing and an under-filled pumped volume in the Nd : YAG rod, which could be addressed with different fibre fo-

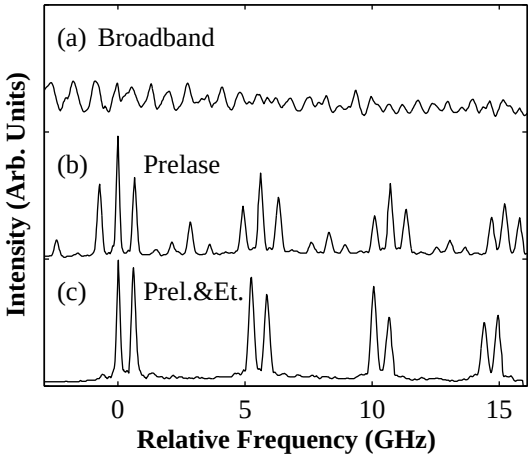

Figure 7.2: Line profiles through the fringe pattern produced by a 5 GHz FSR Fabry–Pérot interferometer for a Nd : YAG laser operating at 5 kHz. (a) Free running laser with optical bandwidth ∼25 GHz; (b) Q-switch tilted to allow prelase Q-switching; (c) prelase Q-switching and 14 GHz FSR intracavity étalon.

cusing optics. To prevent higher order transverse modes from oscillating, an 864 μm diameter aperture (Ap) was inserted into the cavity near the output coupler where resonator modelling predicted a mode waist due to the rod thermal lens. The resulting laser output beam quality was measured to be 1.5 ± 0.2 at 5 kHz. The aperture was observed to qualitatively improve Q-switch hold off by preventing off-axis oscillation. The aperture introduced significant cavity losses, with the cw output power dropping to 7.08 W and the average Q-switched power at 5 kHz to 4.46 W.

The pulsed laser optical bandwidth was measured to be 20–25 GHz, corresponding to around 40 longitudinal cavity modes [297]. A technique of passive prelase Q-switching, in conjunction with an intracavity étalon, was employed to reduce the optical bandwidth. The spectral characteristics of the laser output, monitored with a 5 GHz free spectral range (FSR) Fabry–Pérot interferometer, are illustrated in figure 7.2. The optical bandwidth of the free running laser was too broad to result in interference fringes, figure 7.2 (a). Tilting the Q-switch by 2 mrad in the deflection plane reduced the Q-switch hold off and allowed a small number of high gain modes to oscillate before the Q-switch was opened. Self-seeding by these modes subsequently resulted in narrowband Q-switched pulses. In this mode of operation, the laser typically oscillated on 3–5 cavity modes, as shown in 7.2 (b). Insertion of an uncoated solid fused silica étalon, with a 14 GHz FSR and finesse $\mathcal{F} \approx 0.7$, the oscillating bandwidth was reduced less than 1 GHz, with the laser consistently operating on two axial modes, as shown in figure 7.2 (c). The étalon was

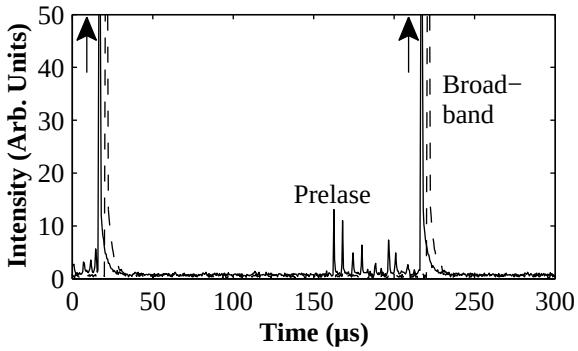

Figure 7.3: Temporal profiles of diode pumped Nd : YAG laser. Solid line, Q-switch tilted to allow prelase Q-switching; dashed line, broadband free running operation. The main laser pulse level exceeded the vertical scale of the figure.

tilted by a small amount to prevent on-axis feedback of laser radiation. The transmission function for a $\mathcal{F} = 0.7$ étalon is shown in figure 4.1 on page 54.

Figure 7.3 shows temporal profiles taken with (solid line) and without (dashed) prelase Q-switching. The reduced hold off with the Q-switch tilted resulted in characteristic prelase spikes before the opening of the Q-switch. The duration of the prelasing could be varied by adjusting the Q-switch tilt between complete suppression and continuous prelase spiking between the laser pulses. A prelase duration of $\sim$80 μs in association with the intracavity étalon was found to be sufficient to reduce the optical bandwidth to two longitudinal cavity modes. Prelase Q-switching resulted in a 35 ns reduction of laser pulse build-up time, while temporal and amplitude jitter increased from 12 ns to 17 ns and from 10% to 25%, respectively, under prelase Q-switching conditions. These instabilities were caused by the laser pulses starting from the spiked prelase levels; using active feedback to control the prelase level has been demonstrated to suppress the spiking and yield prelase Q-switched output with improved stability over corresponding free running systems [14, 15], but this was not attempted. Measurements of the cw output as a function of Q-switch angle indicated that the reduction in output power arising from the tilt of the Q-switch was less than 5%.

The pulse duration and energy for both free-running and prelase Q-switched laser operation are summarised in figure 7.4 as a function of laser repetition rate. The $\sim$10% drop in pulse energy was attributed to losses introduced by the étalon confirmed by similar losses observed when the étalon was added to free running cw cavities. For comparison, the performance of the laser was modelled using the theory developed in chapter 2. Given the output coupler reflectivity $R = 0.8$, cavity length $l_c = 220$ mm, pump mode

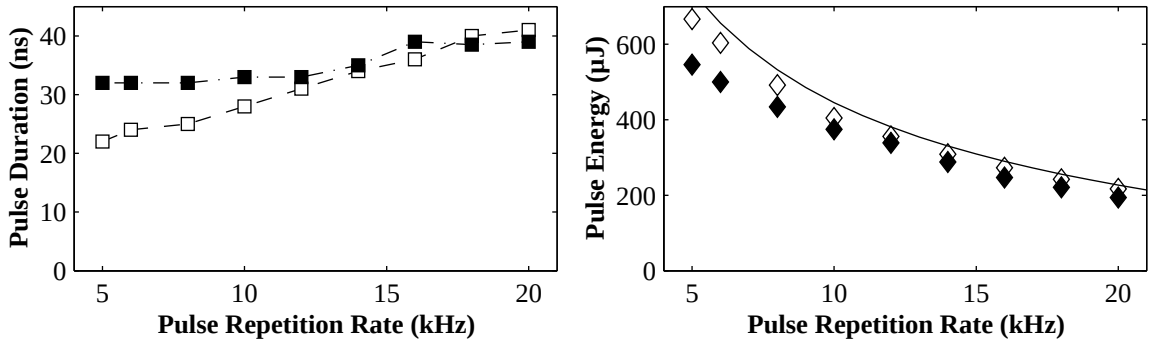

Figure 7.4: Performance of diode pumped Nd : YAG laser as a function of pulse repetition frequency. Open symbols, broadband operation; filled symbols, narrowband operation with prelase Q-switching and intracavity étalon. (a) Pulse duration. (b) Pulse energy, with solid line showing modelled energies assuming output coupler reflectivity $R = 0.8$ and cavity losses $L = 0.1$.

radius $w_p = 220\,\mu$m through the 10 mm long Nd : YAG rod, and a loss coefficient $L = 0.1$, a threshold pump power of $P_{\text{thr}} = 0.95\,$W and a cw output power of $P_{\text{out}} = 11.9\,$W for 24 W absorbed pump power were predicted by equations (2.10) and (2.11), respectively. Calculations of the Q-switched output pulse energies with different repetition rates, using equation (2.13), were in good agreement the measured data, as shown as the solid line in figure 7.4.

7.2 High Repetition Rate PPLN OPO

The high repetition rate laser characterised in the previous section was used to pump a PPLN OPO in a configuration similar to that described in section 5.2. The same PPLN crystal and mounting configuration were used. The OPO cavity was formed between a concave high reflector, with 250 mm radius of curvature, and a plane output coupler with 66% reflectivity over the signal wavelength range. Both mirrors had $> 90\%$ transmission at the pump wavelength and were absorptive with $< 15\%$ reflectivity at the idler wavelength. The physical cavity length was 30 mm, corresponding to a FSR of 2.7 GHz, which was sufficient to accommodate an étalon between the PPLN crystal and the output coupler. The pump beam was focused to a spot size of 120 μm using a 500 mm focal length achromat. The crystal was located 50 mm beyond the waist of the pump beam, to avoid parasitic monolithic oscillations [297].

Instabilities in the spectral, temporal and pulse amplitude characteristics of the pump laser were observed when it was first used to pump the OPO. The cause of the instabilities

was traced to weak feedback of pump radiation from the OPO cavity optics to the laser. In the absence of an optical isolator, the implementation of an 8 m delay line and a $\sim$2 mrad tilt of the OPO cavity relative to the pump beam axis eliminated the feedback and the instabilities.

A Brewster-cut SF10 glass prism was used to separate the OPO signal radiation from a number of non phase matched output beams arising from frequency-doubled signal, signal and pump sum frequency, and the frequency doubled pump radiation. The depleted pump radiation was eliminated using a dichroic coated optic. The OPO output was analysed using a range of Fabry–Pérot interferometers with FSRs between 5 GHz and 100 GHz. The OPO signal radiation could not be directly measured as only silicon-based CCD arrays were available. Previous spectral measurements in chapter 5 relied on the sum frequency radiation of pump and signal, but this method could not be used in this case since the pump was not single mode. Spectral measurements were thus carried out using the non phase matched second harmonic of the signal output generated within the PPLN crystal.

To narrow the optical bandwidth of the OPO, a 30 GHz FSR étalon with a finesse of $\mathcal{F} = 12$ at signal wavelengths was inserted into the cavity. An étalon tilt of $\sim$5 mrad was introduced to prevent feedback from the faces. The spectral output of the OPO was measured at a range of operating signal wavelengths by translating the crystal to access different PPLN grating periods. Figure 7.5 shows OPO spectral profiles, taken through a line of the fringe pattern of a 5 GHz FSR interferometer for six signal wavelengths between 1.46 μm and 1.73 μm (idler wavelengths 2.77–3.93 μm). Single longitudinal mode operation was demonstrated for signal wavelengths up to 1.639 μm. Closer to degeneracy, multiple mode operation was obtained, which was attributed to the increasing PPLN crystal gain bandwidth, which nearly doubled to 42 cm^{-1} as the signal wavelength increased from 1.6 μm to 1.73 μm. The silica substrates of the étalon and output coupler absorbed the OPO idler radiation and residual idler properties were not measured.

The efficiency and threshold of the OPO signal output were measured for a range of pulse repetition frequencies between 5 kHz and 20 kHz. A typical efficiency curve, recorded at 5 kHz, is shown in figure 7.6 (a) for the free running broadband, and single longitudinal mode étalon narrowed, OPO operation. The results were measured at a signal wavelength of 1.501 μm using the $\Lambda = 28.9$ μm PPLN grating period, and no significant variation in OPO performance was observed at different wavelengths. Similar thresholds of 350 mW were obtained for both free running and étalon narrowed OPOs; it was found that at low pump powers the OPO resonated weakly between the cavity high reflector and the misaligned étalon surface closest to the PPLN crystal, resulting in mul-

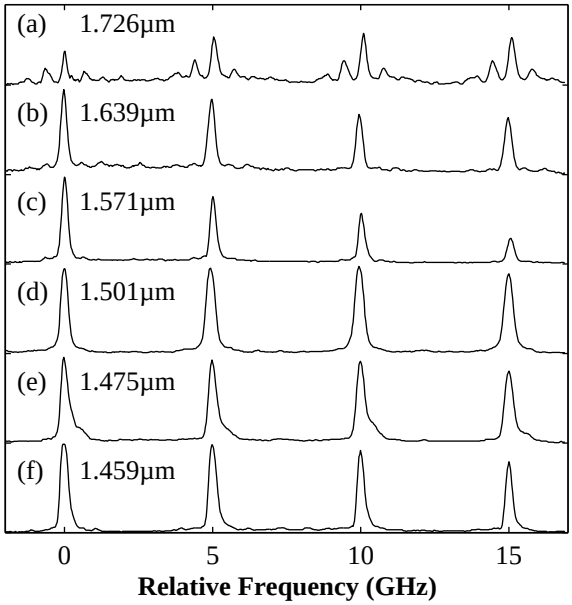

Figure 7.5: Line profile through fringes produced by a 5 GHz FSR Fabry–Pérot interferometer, for a 1.06 μm pumped étalon narrowed PPLN OPO operating at signal wavelength (a) 1.726 μm; (b) 1.639 μm; (c) 1.571 μm; (d) 1.501 μm; (e) 1.475 μm; and (f) 1.459 μm.

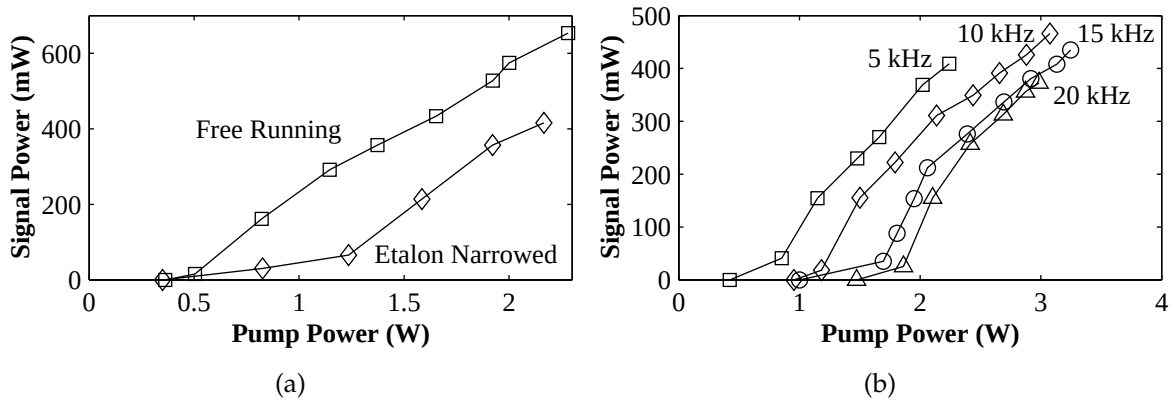

Figure 7.6: Signal pulse energy performance of a 1.064 μm pumped PPLN OPO, operating on a signal wavelength of 1.501 μm. (a) OPO performance at 5 kHz under free running broadband (squares) and étalon narrowed single longitudinal mode (diamonds) operation. (b) Etalon narrowed performance with the OPO operating at 5 kHz (squares); 10 kHz (diamonds); 15 kHz (circles); 20 kHz (triangles).

tiple mode oscillation even with the étalon inserted. This effect became insignificant for pump powers in excess of 1 W when the OPO began to oscillate predominantly between the high reflector and output coupler, and in this region single cavity longitudinal mode operation was obtained with the intracavity étalon. In this region of operation, both free running and étalon narrowed OPOs yielded slope efficiencies of ≈30%, from which a factor of two effective increase in threshold was determined on insertion of the étalon. These characteristics were consistent with other étalon narrowed OPOs investigated in chapter 5. At the maximum pump power used, the free running cavity generated up to 650 mW of signal output, while the étalon narrowed OPO provided 415 mW.

The OPO performance at different pulse repetition frequencies is shown in figure 7.6 (b). The trend in output power near threshold, discussed above, was observed at all repetition rates. In terms of pulse energy, the OPO performance was independent of repetition rate, with a threshold of around 80 μJ (7 MW/cm^2) and a slope efficiency of 27%. The highest signal pulse energy of 82 μJ was generated at 5 kHz with a pump pulse energy of 450 μJ. The OPO spectral characteristics were not affected by the pulse repetition frequency.

Far field divergence measurements of the fundamental OPO signal beam profile, made by scanning a 100 μm diameter photodiode through the beam at a range of distances from the OPO, allowed a beam quality parameter $M^2 = 1.3$ to be calculated. The high spatial quality beam was attributed to a good resonant mode definition in the OPO and adequate spatial purity of the high repetition rate Nd : YAG pump laser.

7.3 Injection Seeded Monolithic PPLN OPO

The diode pumped, high repetition rate Nd : YAG laser described in section 7.1 was frequency doubled and used to pump a visible wavelength monolithic PPLN OPO, injection seeded by a semiconductor diode laser. Around the time this work was carried out, Bäder *et al.* reported seeding of 532 nm pumped monolithic PPLN OPOs using a fixed wavelength 632 nm He–Ne laser [96].

In order to yield sufficient pulse energy to bring the OPO above threshold, a pulse repetition frequency of 2.5 kHz was used, unless otherwise noted. The laser radiation was focused into a 6 mm long LiB_3O_5(LBO) frequency doubling crystal for single pass second harmonic generation (SHG). The LBO crystal was cut with angles $\phi = 0^\circ$ and $\theta = 90^\circ$ for noncritical phase matching parallel to the X tensor axis. A resistively heated oven maintained an LBO crystal temperature of $149.9 \pm 0.1^\circ$C to provide an optical conversion efficiency in excess of 35%. The focusing lens had a focal length of 150 mm, resulting in

a 60 μm spot size within the LBO crystal. A 250 mm focal length achromat was used to collimate the generated 532 nm radiation, and a dichroic mirror eliminated the residual 1.064 μm laser radiation.

The spectra and temporal profiles of the pump laser and its second harmonic are illustrated in figures 7.7 (a) and 7.7 (b). The spectra were obtained using a 5 GHz FSR Fabry–Pérot interferometer, while a 1 ns rise time photodiode and a 200 MHz digital storage oscilloscope (Tektronix TDS 350) were used to record the temporal profiles. The Nd : YAG laser operated principally on two longitudinal cavity modes (left panel), separated by around 600 MHz, leading to mode beating visible on the pump pulse evolution (right panel). From the frequency separation of adjacent cavity modes, a mode beating period of 1.7 ns was expected; the lack of detail in resolving the mode beating structure on the pulse was attributed to an insufficient frequency response of the detection system, but oscillations faster than those visible were not expected. The temporal ripples from the laser pulse were also evident in the second harmonic and OPO pulse profiles. Frequency mixing cross terms between the laser cavity modes resulted in the second harmonic spectral mode structure and temporal profile shown in figure 7.7 (b). The second harmonic pulse duration was shortened to 22 ns from the fundamental laser pulse duration of 25 ns.

A 500 mm focal length achromat was used to focus the 532 nm pump radiation into the PPLN crystal previously described in section 6.1 to generate signal wavelengths between 620 and 640 nm. The crystal was held at around 77°C in a resistively heated temperature controlled oven. This temperature was chosen such that the free running OPO spectrum encompassed the wavelength of the semiconductor diode seed source, as described below. The crystal end faces were antireflection coated over 532–670 nm and 1.2–1.3 μm; it was found that the residual $\sim$14% Fresnel reflections at the idler wavelength (3.15–3.77 μm) provided sufficient feedback for the crystal to operate as a monolithic oscillator above intensities of 35 MW/cm^2.

A number of commercial 5 mW AlGaInP multi-quantum well semiconductor laser diodes (Hitachi HL6312G), emitting around 637 nm, were tested as potential seed sources. Several of the diodes could be current tuned across almost 50 GHz in a single mode, with the optical bandwidth measured to be below the 250 MHz instrument resolution of the highest resolution interferometer available. Typically, the diodes emitted in excess of 8 mW at the maximum rated current, but were operated at lower currents within the single mode tuning range.

The performance of the diodes was examined by observing the transmission through a 5 GHz Fabry–Pérot interferometer while the diode current was scanned. Result obtained using one of the diodes, which was characterised by a threshold current of 45 mA

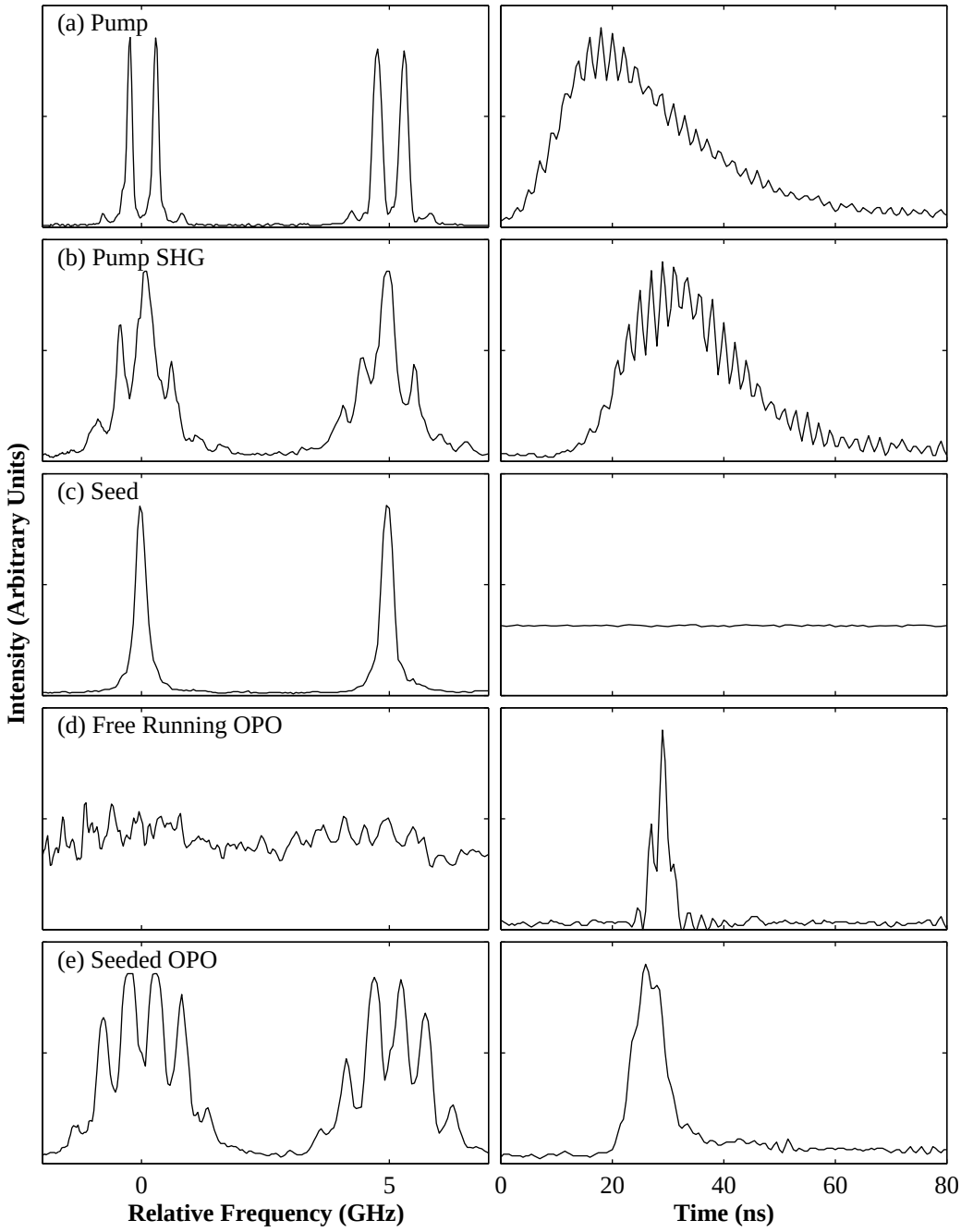

Figure 7.7: Spectral (left) and temporal (right) performance of a 532 nm pumped, injection seeded monolithic PPLN OPO and its pump source. The spectral profiles were taken from the fringe patterns produced by a 5 GHz FSR Fabry–Pérot interferometer. (a) Fundamental 1.064 μm Nd : YAG laser; (b) second harmonic at 532 nm; (c) cw laser diode seed source at 637 nm; (d) unseeded monolithic OPO; (e) seeded OPO.

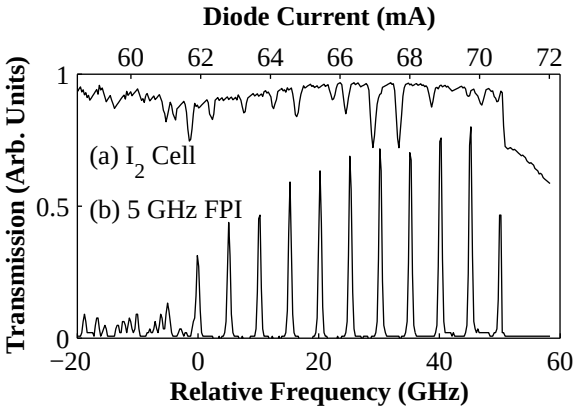

Figure 7.8: Spectral performance of a tuneable semiconductor diode laser, used as a seed source, emitting around 637 nm. (a) Relative absorption spectrum in a 30 cm long I_2 cell. (b) Transmission through a 5 GHz FSR Fabry–Pérot interferometer, used to calibrate the scan.

and a maximum current rating of 85 mA, are presented in figure 7.8. The regular spacing between 62 mA and 71 mA indicated a continuous single mode scan, as mode hops, visible for currents below 62 mA, were manifested by discontinuities in the transmission spectrum and intensity. The increase in the interferometer transmission peak heights resulted from the current dependence of the laser diode power. From the data, a frequency tuning rate with diode current of 5.7 GHz/A was calculated. A temperature tuning rate of 0.2 nm/°C was specified by the manufacturer's data sheet, but the diodes were operated at room temperature without active temperature control.

The spectroscopic performance of the diodes was tested by measuring absorption spectra of I_2, which has been previously used to establish tuned OPO spectral characteristics [219]. Figure 7.8 (a) shows a scan obtained by passing the diode beam through a 30 cm in-house built gas cell that contained an unspecified amount of I_2 vapour. An approximately normalised spectrum was obtained by subtracting the linear slope of output intensity with diode current from the scanned spectrum. The strength of the absorption peaks was of the order of 15% but could have been increased if a higher gas concentration, or a multiple pass cell configuration, had been adopted. Absolute frequency calibration of the diodes using the absorption spectrum was not attempted.

The emission spectrum from a diode at constant current is shown in figure 7.7 (c) on page 126. The power from the diodes was constant except for small long term temperature and power supply drifts. To protect the laser diodes from interference and destruction by back reflections from the OPO, the seed was passed through a tuneable optical isolator (Isowave Inc, I-80-T4M) and a fused silica prism.

The free running OPO operated with a spectral bandwidth of 45 GHz, with considerable shot to shot variation. A spectral measurement using a 5 GHz FSR Fabry–Pérot interferometer is shown in figure 7.7 (d), in which no structure is discernible because of overlapping analysing interferometer orders. When pumped around 1.5 times threshold, the OPO generated signal pulses of approximately 2 ns duration, with an oscillatory structure attributable to the mode beating structure on the Nd : YAG laser pulse.

Seeding of the OPO was achieved by spatially combining the 637 nm seed and 532 nm OPO pump radiation using a dielectric coated 45° beam steering mirror for 532 nm. Injection seeding reduced the signal optical bandwidth to 5–6 peaks, with a combined optical bandwidth of 1.8 GHz, as shown in figure 7.7 (e). This multiple mode structure was consistent with that expected for a multimode pumped OPO seeded at the non-resonant wavelength; each peak was due to the seed radiation interacting with a spectral peak of the pump radiation. Seeding resulted in a reduction of the $1/e^2$ pulse build-up time from 7.7 ns to 3.8 ns with respect to the pump pulse.

Frequency tuning the seed wavelength, by adjusting the laser diode current, resulted in seeding on adjacent groups of modes similar to those shown in figure 7.7 (e). The groups were separated by ≈3.3 GHz, in close agreement with the 3.6 GHz spacing expected for longitudinal modes of the monolithic resonator at the idler wavelength. The minimum seed power necessary for successful optical bandwidth control was deduced by reducing the seed power at the OPO using neutral density filters until seeding became unsuccessful. Seed powers as low as 0.2 μW were found to result in successful seeding.

The monolithic OPO was operated at repetition rates between 1 and 5 kHz. At higher pulse repetition frequencies, the reduced pump pulse energy was insufficient to overcome the OPO threshold. Above 2.5 kHz, average pump powers in excess of 750 mW inside the OPO crystal resulted in visible photorefractive damage in the form of strong pump scattering and significantly degraded OPO performance. These photorefractive effects could be eliminated by heating the crystal above 100°C, but this shifted the OPO gain beyond the wavelength range of the seed laser diodes. Chopping the pump beam using a 50–50 duty cycle optical chopper to reduce the average power was also effective in eliminating photorefraction up to the highest repetition rate used.

At a pulse repetition rate of 1 kHz, pump pulse energies of up to 330 μJ were available. During early experiments, the crystal face at the $\Lambda = 10.3\,\mu$m track useable for injection seeding at 637 nm experienced partial damage, resulting in degraded output energies on this track. Nonetheless, figure 7.9 (a) illustrates the performance improvement observed with injection seeding. Injection seeding reduced the oscillation threshold from 150 mW to 120 mW. At the same time, the maximum signal output power increased from

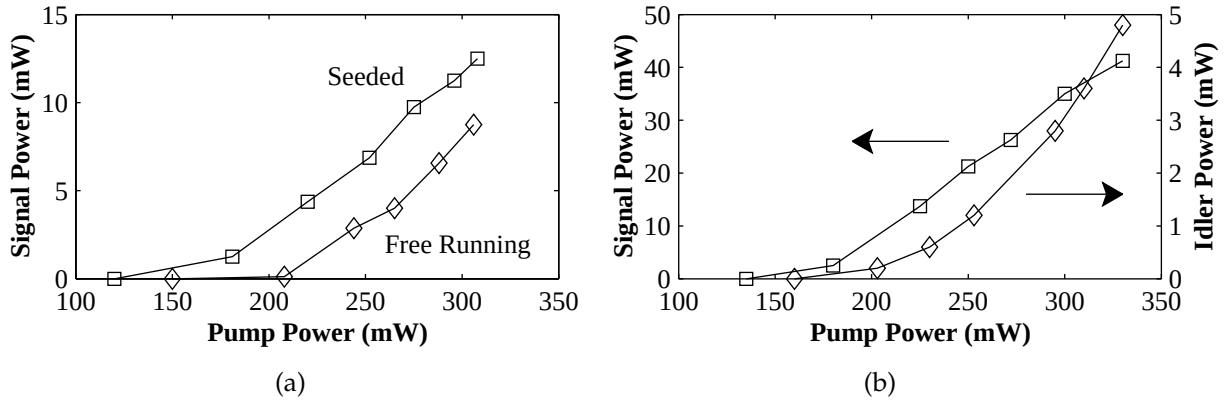

Figure 7.9: Output power of a high repetition rate 532 nm pumped monolithic PPLN OPO, as a function of pump power. (a) Free running broadband (diamonds) and injection seeded narrowband (squares) performance at 637 nm, on partially damaged track. (b) Signal (squares) and idler (diamonds) output power at 624 nm and 3.6 μm on an undamaged crystal track. The OPO was operating at a pulse repetition frequency of 1 kHz.

9 mW to 12 mW at the peak pump power of 308 mW. This represented a small increase in slope efficiency from 5.6% to 6.3%. Unseeded operation of an adjacent track, operating at a signal wavelength of 624 nm under otherwise identical conditions, demonstrated similar thresholds, but generated peak signal and idler powers of 41 mW and 4.8 mW, respectively, at a pump power of 330 mW, as shown in figure 7.9 (b). These values correspond to a signal slope efficiency of 19.5%. Assuming a similar relative performance on an undamaged track where seeding would be possible, signal and idler output powers of 50 mW and 7 mW were expected without further modifications to the experimental apparatus.

10 Hz Results

The multiple mode spectrum of the fundamental 1.064 μm Nd : YAG spectrum precluded seeded OPO optical bandwidths below 1.8 GHz. In order to demonstrate single longitudinal mode operation of the OPO, the second harmonic of the injection seeded Continuum PL7000 laser was used. This laser delivered 14 ns pump pulses with bandwidths below the measurement limit of the highest resolution Fabry–Pérot interferometer available, and operated at 10 Hz pulse repetition frequency. The pump beam was focused using a 500 mm focal length achromat and the monolithic OPO crystal placed 40 mm beyond the waist to ensure the pump filled the available crystal volume and matched the pump conditions of the high repetition rate OPO. A half wave plate and polariser combination allowed smooth variable control of the pump pulse energy at the OPO up to

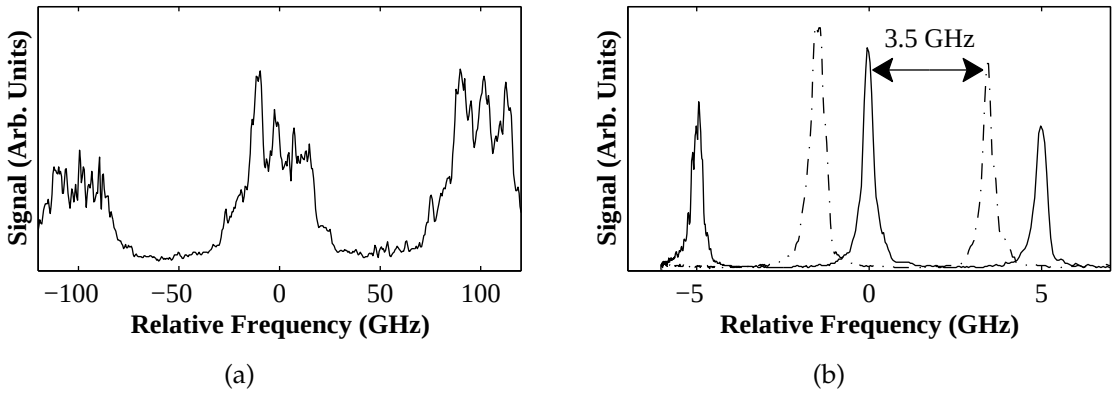

Figure 7.10: Signal spectra of a 532 nm pumped, injection seeded, 10 Hz monolithic PPLN OPO. (a) Line profile through the fringe pattern produced by a 100 GHz FSR Fabry–Pérot interferometer for the unseeded OPO. (b) Fringe pattern produced by a 5 GHz interferometer for the seeded monolithic OPO. The dashed line indicates seeding on an adjacent cavity mode.

1 mJ.

Seeding was again effective, as shown in figure 7.10. The optical bandwidth of the free-running OPO was measured to be 45 GHz using a Fabry–Pérot interferometer with a 100 GHz FSR. The free running monolithic OPO spectra were similar for the high repetition rate multimode and single mode 10 Hz pump lasers. Figure 7.10 (b) shows the output of the seeded OPO, measured with a 5 GHz interferometer, where the measured bandwidth of 250 MHz was limited by the resolution of the interferometer. Tuning of the seed laser frequency resulted in seeding on adjacent monolithic OPO cavity modes, shown as a dashed line in figure 7.10 (b). The adjacent seeding modes were separated by 3.5 GHz, in good agreement with the predicted 3.6 GHz separation of longitudinal modes of the idler resonant monolithic OPO cavity. Simultaneous seeding on two adjacent cavity modes was implemented using two seed laser diodes operating on closely matched emission wavelengths. The seed beams were spatially combined using a 50% reflective silver mirror and co-propagated with the pump beam to seed the monolithic OPO crystal. Independent adjustment of the two diode currents was used to simultaneously tune the seed sources to cavity modes.

It was hoped that the dual wavelength seeding would permit a differential absorption spectroscopy measurement to be carried out in I_2 using the single mode seeded monolithic OPO. However, even when the diode was current tuned to an I_2 absorption and the OPO crystal temperature tuned such that seeding was successful, no absorption of the OPO radiation within the I_2 cell could be detected. The crystal damage, mentioned above, hindered further attempts at absorption spectroscopy using this OPO.

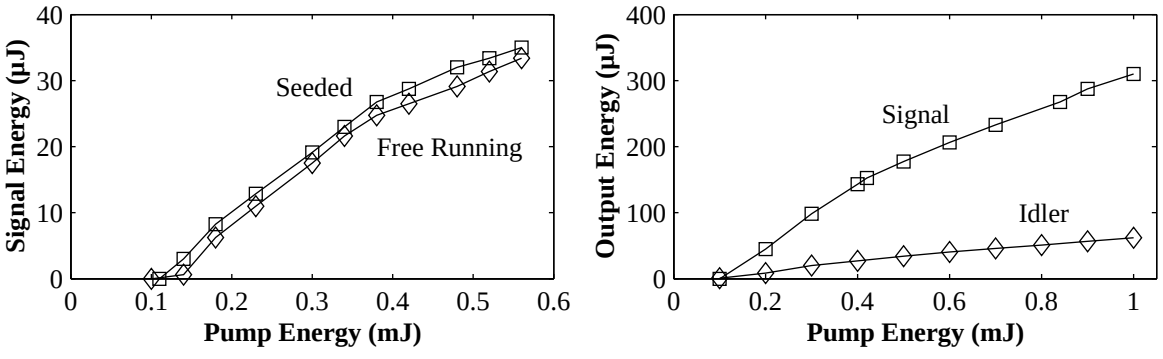

(a) (b)

Figure 7.11: Output pulse energy performance of a 532 nm pumped, injection seeded, 10 Hz monolithic PPLN OPO, as a function of pump power. (a) Free running broadband (diamonds) and injection seeded single longitudinal mode (squares) performance at 637 nm, on partially damaged track. (b) Signal (squares) and idler (diamonds) output energy at 624 nm and 3.6 μm on an undamaged crystal track.

The efficiency for seeding on a single mode using the damaged crystal track is shown in figure 7.11 (a). The 100 μJ threshold measured for this configuration was not appreciably affected by seeding, but the maximum signal output pulse energy on the partially damaged track was increased from 33 μJ to 35 μJ, at a pump pulse energy of 570 μJ. The $1/e^2$ pulse build-up time was reduced by $\sim$2 ns. On an adjacent undamaged track, at a signal wavelength of 624 nm, maximum unseeded signal and idler pulse energies of 310 μJ and 61 μJ were measured at the maximum pump pulse energy of 1 mJ, as shown in figure 7.11 (b). The thresholds were similar to those measured on the damaged track.

7.4 Conclusion

A high repetition rate diode pumped Nd : YAG laser was constructed, and its applicability to pumping narrow optical bandwidth OPOs was demonstrated. Under cw operation, the laser generated up to 10.7 W output power. In Q-switched mode, the implementation of a prelase technique, by tilting the Q-switch, and an intracavity étalon narrowed the optical bandwidth of the laser from $\sim$25 GHz to two cavity modes separated by 600 MHz, with a reduction in output pulse energy of around 10%. At a repetition rate of 5 kHz, the narrowband 1.064 μm pulse energy was 550 μJ.

As discussed in chapter 2, the laser material Nd : YLF was known to be less susceptible to thermal lensing, and was potentially a more appropriate gain material in the configurations reported here. A small number of 1% at. doped Nd : YLF crystals were tested

in the laser cavity configuration shown in figure 7.1 on page 118. Laser outputs of up to 8.1 W and 6.5 W, for the π and σ polarisations at respectively 1.047 μm and 1.053 μm, were measured under cw operation. The beam spatial profiles were qualitatively superior to those of the corresponding Nd : YAG laser. Despite these improvements, a viable pump source could not be built using Nd : YLF, as the laser rods suffered catastrophic thermal fracture under largely varying operating conditions. It was anticipated that a modified laser configuration, and careful attention to the thermal loading and heat extraction in the laser rod, could reduce the risk of fracture and permit the prelase Q-switch technique to be applied to Nd : YLF.

The Nd : YAG laser was used to drive 1.064 μm and 532 nm pumped PPLN OPOs. The 1.064 μm pumped OPO signal optical bandwidth was reduced to a single longitudinal mode by incorporation of an intracavity étalon, except at the longest 1.726 μm signal wavelength where the gain bandwidth diverged as the OPO approached degeneracy. The OPO generated around 0.5 W single mode signal output at repetition rates between 5 kHz and 20 kHz, with slope efficiencies of around 27%. The relative performance between free running and étalon narrowed OPOs was similar to that observed in chapter 5 for 10 Hz pumped PPLN OPOs.

Frequency doubling of the Nd : YAG laser allowed a 532 nm pumped monolithic PPLN OPO to be demonstrated. Injection seeding was successfully demonstrated at the non-resonant signal wavelength using semiconductor diode lasers. The diodes were tuned by current over 50 GHz in a single mode, verified by transmission spectra of a Fabry–Pérot interferometer, and simultaneous seeding on adjacent monolithic OPO cavity modes was accomplished. The multiple spectral mode nature of the pump resulted in a seeded OPO optical bandwidth of 18 GHz, reduced from the free running optical bandwidth of 45 GHz. At 1 kHz repetition rate, the free running monolithic OPO generated around 41 mW signal and 5 mW idler for 330 mW pump. The use of an injection seeded 10 Hz pump source enabled single mode seeded output to be demonstrated, with a 1 mJ pump generating signal (idler) pulse energies of 310 μJ (62 μJ).

Chapter 8

Continuous-Wave Intracavity OPOs

The intensities required for efficient nonlinear optical conversion, including in optical parametric oscillators (OPO), are often not as readily available in continuous-wave (cw) systems as they are under pulsed illumination, such as reported in earlier chapters. To reduce the threshold, cavities resonating two or three of the nonlinear optical interaction fields may be constructed, but the multiple resonator mode constraints can result in fluctuating amplitude and spectral output due to mechanical disturbances in these pump enhanced, doubly resonant, and triply resonant cavities. Placing the OPO within the cavity of the drive laser gives access to the high resonating fields, so that intracavity, singly resonant OPOs (ICSROs) may be constructed. Using a beam splitter to separate the resonant cavities gives more control over the design parameters of the laser and OPO cavities. A schematic diagram for a generic ICSRO, as implemented in this chapter, is shown in figure 8.1. The laser head and OPO construction considerations are thereby correlated and optimisation of operating parameters such as focusing and output coupling, at the

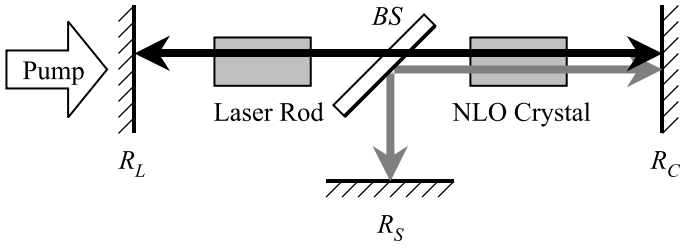

Figure 8.1: Schematic for an intracavity OPO. The laser resonant cavity (black arrow) was formed by laser high reflector R_L and the common mirror R_C, while the signal radiation (grey arrow) resonated between mirrors R_S and R_C. The beam splitter BS was used to discriminate between the wavelengths. In this configuration, the laser rod was end-pumped through the laser high reflector.

laser or resonated OPO wavelength, becomes more difficult to implement. This chapter presents results from an optimisation, in particular, to reduce the influence of thermal lensing in the laser rod and nonlinear optical crystal on the resonated modes. Characterisation of the diode pumped $Nd:YVO_4$ laser head is presented in 8.1, including a number of investigations to determine the strength of the thermal lens. The performance results of cavity designs tested for a PPRTA ICSRO are given in section 8.2. The work presented in this chapter was carried out at the School of Physics and Astronomy, University of St Andrews (St Andrews, Scotland), under the supervision of Prof. Malcolm Dunn.

8.1 $Nd:YVO_4$ Laser

The performance of previously implemented PPLN and PPRTA ICSRO cavities had been found to be limited by thermal lensing causing dynamic instabilities. It was assumed that the principal contributions to the thermal lensing were due to the short pump absorption depth in $Nd:YVO_4$ and the thermal characteristics of PPLN [155]. The thermal lensing behaviour of the laser head was investigated without the ICSRO crystal to isolate the effects caused by laser and nonlinear optical elements. The existing laser head mechanical design was retained.

8.1.1 Laser Construction

The gain material used was a 0.5% at. $Nd:YVO_4$ rod (CASIX Inc, China), of dimensions $3 \times 3 \times 10$ mm. Due to the short pump $\sim$2 mm absorption depth in $Nd:YVO_4$, virtually all of the pump radiation was absorbed within the rod. The rod was housed in a water-cooled brass mount, with indium foil to assist heat transfer between laser rod and mount. The rod end faces were antireflection coated at both the 808 nm pump and 1.064 μm laser wavelengths. Micrometer controlled translation of the rod mount allowed for fine adjustments of the laser rod position within the laser cavity.

The laser rod was pumped by a 20 W fibre coupled diode laser array (SDL, Inc), operating at 808 nm, coupled in through the laser high reflector R_L as shown in figure 8.1. The output from the delivery fibre was collimated and focused using single layer MgF_2 antireflection coated aspheric collimating (Melles Griot 01 LAG 005/067, $f = 18.0$ mm) and focusing (Melles Griot 01 LAG 001/067, $f = 12.0$ mm) lenses. The lens positions were adjusted to focus the diode pump radiation to a waist of 220 μm at the entrance face of the $Nd:YVO_4$ rod.

The pump diode was characterised by a threshold current of 10.5 A and a maximum output power of 17.1 W at 30 A drive current. A coupling efficiency of 95% was as-

Table 8.1: $Nd:YVO_4$ laser performance as a function of output coupler reflectivity. The maximum pump power was 16.2 W.

Output Coupler Reflectivity (%)	Threshold Pump Power (W)	Output Power (W)	Slope Efficiency (%)	Intracavity Power (W)
99	0.13	3.30	20.5	330
98	0.14	5.93	36.9	295
95	0.27	6.25	39.2	120
90	0.55	7.97	50.9	76
85	0.60	7.92	50.8	49
78	1.03	7.80	51.4	31
32	3.04	4.90	37.2	4.3

sumed through the collimating, focusing, and laser high reflector optics, yielding up to 16.2 W incident on the $Nd:YVO_4$ rod. The diode array was mounted on a water cooled block, with the temperature regulated recirculating water used to simultaneously tune the diode wavelength and remove excess heat from both the diode array and the laser rod mount. The diode laser wavelength tuned at 0.3 nm/°C with an optical bandwidth of around 4 nm (full width to $1/e^2$ level). Due to the wide pump absorption bandwidth of $Nd:YVO_4$, no variation in laser performance was observed when the coolant temperature was varied between 10°C and 30°C. For the remaining experiments, the temperature was set arbitrarily to 16.5°C, resulting in the diode radiation being centred at 807.5 nm.

The laser performance was measured in a near hemispherical resonator, comprising a plane high reflector and a 200 mm concave output coupler. The cavity length was chosen to be 165 mm. The cavity was constructed using a number of output coupling optics with reflectivities between 32% and 99%, and the threshold and output power at maximum pump power were measured in each configuration. The laser performance is summarised in table 8.1. The highest laser output power of 7.97 W was obtained using the 90% reflective output coupler, with a threshold of 0.55 W (slope efficiency 51%). Almost identical performance was measured with the 85% reflective optic. Of relevance to ICSROs is the intracavity power available for nonlinear optical conversion, and a maximum intracavity field of up to 328 W was obtained using the 99% reflective output coupler.

The data of table 8.1 were used to evaluate the laser performance and compare it to the theory derived in chapter 2. In the low-loss $L \ll 1$ approximation, the threshold power $P_{p,\mathrm{thr}}$ in equation (2.10) may be expressed as $P_{p,\mathrm{thr}} \propto (L - \ln R)$, where R is the reflectivity of the output coupler. Figure 8.2 (a) shows the measured thresholds in such a Findlay–Clay analysis. Treating the cavity round trip loss coefficient L and the pump mode radius w_p as variable parameters, a least squares line of best fit was calculated for

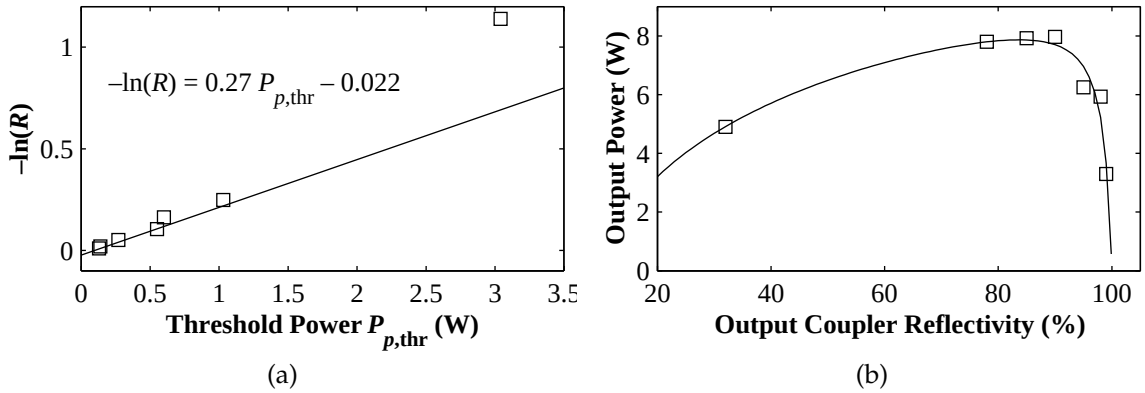

(a) (b)

Figure 8.2: Nd : YVO_4 laser performance compared to theoretical developments of section 2.1. (a) Findlay–Clay analysis, equation (2.10), of threshold power $P_{p,\mathrm{thr}}$ against $-\ln R$. (b) Output power as a function of output coupler reflectivity, with a fit from equation (2.11).

the data. The best fit through the complete data set yielded cavity losses $L = 7.6\%$ and a pump waist $w_p = 320\,\mu$m. The fit line shown in figure 8.2 (a) was obtained by excluding the data point from the 32% reflective output coupler from the fit, which yielded $L = 2.2\%$ and $w_p = 380\,\mu$m. Figure 8.2 (b) shows the output power as a function of output coupler reflectivity R, with a fitted line from equation (2.11). The fitted parameters were $L = 1.5\%$, $w_p = 380\,\mu$m, and small-signal gain $\gamma_0 = 1.4 \times 10^3\,\mathrm{m}^{-1}$ within a gain length of $l_c = 0.9\,$mm. Using equation (2.2), this gain corresponded to around 10 W pump. These considerations indicated that some improvement in the pump laser would be possible, such as pump and laser mode volume matching, but a more detailed study was not undertaken.

8.1.2 Thermal Lensing

Significant thermal lensing effects had been observed to limit the power scalability in earlier ICSRO experiments performed using this laser head. An investigation was therefore undertaken to ascertain the extent of thermal lensing within the laser rod, using a number of different strategies. These are described below, and included resonated mode spot size deductions, direct measurements using probe beams, and stability limits on resonator modes. The results were quantitatively somewhat inconsistent, but it was concluded that the thermal lens was aberrated, with the focal length no shorter than $f_{\mathrm{Th}} \sim 200\,$mm and influenced more strongly by the pump power than the intracavity circulating field. The expected thermal lens was also estimated using equation (2.19). It was assumed that $P_{\mathrm{abs}} = 2\,$W power was absorbed within 3 mm of the laser rod, which, together with the

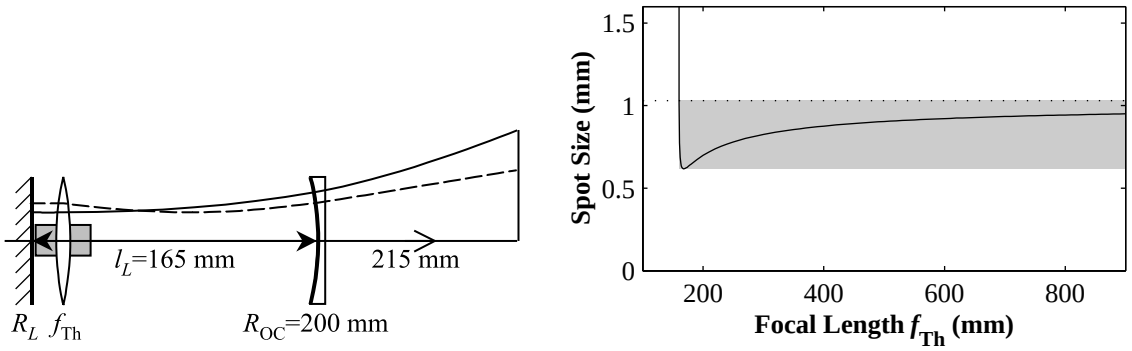

(a) (b)

Figure 8.3: (a) Laser cavity mode for Nd : YVO_4 laser, without (solid line) and with (dashed) thermal lens f_{Th}, and propagation to measurement plane. (Not to scale.) (b) Modelled spot size at measurement plane, as a function of thermal lens focal length. The spot size with no thermal lensing was 1.03 mm (dotted line), and the cavity was unstable for $f_{\mathrm{Th}} < 160$ mm. The shaded region marks stable thermal lens focal lengths and beam spot sizes.

material parameters tabulated in table 2.1 on page 23, predicted a thermal lens of focal length $f_{\mathrm{Th}} = 150$ mm. However, the uniform pump absorption approximation made in deriving equation (2.19) was likely to lead to somewhat inaccurate predictions, due to the short pump absorption depth and the low thermal conductivity leading to a spatially varying thermal load.

Spot Size Considerations

The *ABCD* matrix formalism, described in section 2.3, was used to model the resonated mode of the laser cavity and its propagation beyond the output coupler, and the results compared to experimental values of output beam spot sizes measured using a CCD camera. Correlation between measured and modelled spot sizes was expected to yield a method for determining the effective thermal lens focal length under different operating conditions. This technique has previously been used to measure the thermal lensing of Nd : YAG and Nd : YLF under lasing conditions [31, 192].

The resonated mode, and its propagation through the concave output coupler (radius of curvature $R_{\mathrm{OC}} = 200$ mm, refractive index $n = 1.43$, thickness $d = 6$ mm) and 215 mm free space to a measurement plane, was modelled as shown in figure 8.3 (a), which is not drawn to scale. A 10 mm long rod of refractive index $n = 2.0$ was included at the plane high reflector R_L. The solid line in figure 8.3 (a) indicates the resonant mode size in the absence of thermal lensing. A variable thermal lens f_{Th} was then included within the laser rod; the dashed line illustrates the effect of the lens on the resonated mode. The

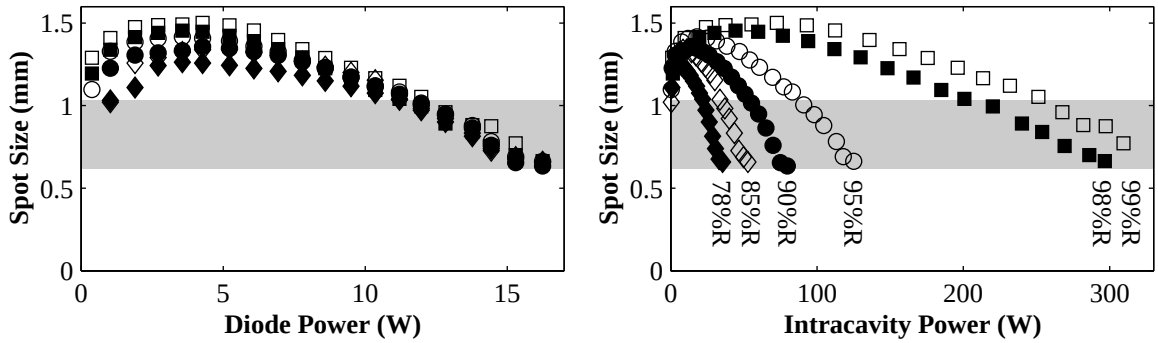

(a) (b)

Figure 8.4: $Nd:YVO_4$ laser spot sizes measured using a CCD camera, as a function of (a) pump diode power and (b) intracavity laser power, for a range of different output couplers. The shaded regions indicate the range of spot sizes predicted by the thermal lens cavity modelling as in figure 8.3.

spot sizes were not sensitive to the exact position of the lens.

The modelled spot size at the observation plane is shown in figure 8.3 (b) as a function of the thermal lens focal length. The spot size in the absence of thermal lensing was predicted to be 1.03 mm; this decreased to 0.62 mm at $f_{\mathrm{Th}} = 168$ mm, and for $f_{\mathrm{Th}} < 160$ mm, the cavity was predicted to be unstable.

The $Nd:YVO_4$ laser cavity was constructed using six different output couplers, with reflectivities between 99% and 78%. For each optic, the laser spot size was measured using a CCD camera (Pulnix TM-520, with Photon Inc, BeamPro frame capturing software) placed 215 mm from the output coupler of the resonator, and the laser output power was recorded, from which the intracavity power was deduced. Figure 8.4 shows the measured spot sizes as a function of pump diode power and as a function of intracavity power. The close agreement between the lines corresponding to different output coupler reflectivities in figure 8.4 (a) indicated that the pump radiation was a more significant influence on the thermal lensing than the intracavity power, especially above 10 W pump power. This was attributed to the high thermal loading in the 220 μm pump spot size and the short pump absorption depth of $Nd:YVO_4$, and indicated that even at the highest intracavity powers, absorption at the laser wavelength was negligible.

Just above threshold, the measured beam spot sizes matched the predicted value of 1 mm in the absence of thermal lensing, but the data at moderate pump powers were not consistent with the modelling of figure 8.3 for any focal length thermal lens. At pump powers above 12 W, the measured spot sizes decrease consistently from 1.01 ± 0.04 mm at 12 W to 0.65 ± 0.02 mm at 16 W for all output couplers. From figure 8.3, this would

indicate that a thermal lens of focal length $f_{\mathrm{Th}} \sim 180\,\mathrm{mm}$ was generated at the highest pump power used.

The experiment was repeated with an intracavity lens of focal length 88 mm, placed 60 mm from the high reflector. This additional optic effectively increased the system sensitivity under short focal length thermal lensing conditions, reduced the resonated mode spot size within the $\mathrm{Nd} : \mathrm{YVO_4}$ rod, and rendered the cavity stable even with thermal lens focal lengths as short as 50 mm. The experimental results indicated similar trends of the variation in spot size being principally determined by the diode pump power, but again the measured spot sizes could not be satisfactorily reconciled with cavity modelling.

Beam Quality Correction

One possible reason for the discrepancy between the modelled and measured spot sizes was that the laser may have resonated on a higher order spatial mode, whereas the modelling assumed the $\mathrm{TEM_{00}}$ fundamental transverse mode. The ratio between measured and modelled spot sizes would be given, to a first approximation, by the M^2 beam quality parameter. To investigate this effect, the M^2 beam quality of the laser output was determined by measuring the laser spot sizes about a focus formed by a 400 mm focal length lens placed 340 mm beyond the output coupler of the laser. The spot sizes $w(z)$ were fitted to the Gaussian beam propagation formula given in table 2.2, treating M^2 as a fitting parameter.

The laser was found to operate with $M^2 \sim 1$ at pump powers below 5 W, with an increase to $M^2 \sim 2.5$ near the highest pump powers used, with the beam spatial mode remaining qualitatively smooth and circular. Similar measurements were obtained using the 95% and 90% reflective output couplers, from which it was concluded that the intracavity power was again less influential than the pump power, allowing the M^2 values to be applied to the spot size data of all output couplers. However, even after accounting for the beam quality, the measured spot sizes could not be satisfactorily reconciled with the modelling, and this lack of agreement between measured and predicted spot sizes prevented a thermal lens focal length being determined by this method. The most likely conclusion was that the thermal lens within the $\mathrm{Nd} : \mathrm{YVO_4}$ rod was aspherical and potentially aberrated.

Stability Considerations

The rapid qualitative deterioration of the mode associated with an almost unstable cavity, visible in figure 8.3 (b) as a diverging spot size when $f_{\mathrm{Th}} < 162$, motivated an attempt to

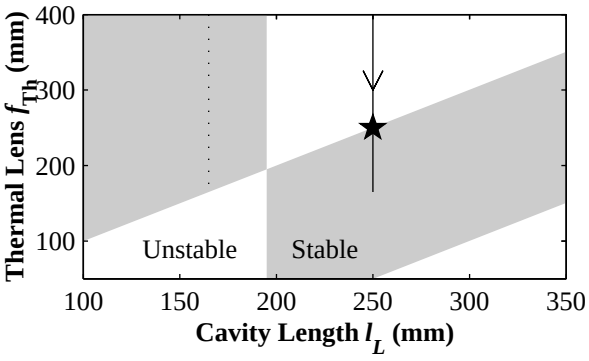

Figure 8.5: $Nd:YVO_4$ laser resonator stability regions (shaded), for different thermal lens focal lengths f_{Th} and cavity lengths l_L. The dotted line indicates the stability region shaded in figure 8.3 (b) for $f_{Th} > 162\,mm$ at a cavity length $l_L = 165\,mm$. The solid arrow indicates the progression also marked in figure 8.6 for an arbitrary cavity length of $l_L = 250\,mm$.

use such stability considerations to find bounding limits for the thermal lens. A similar procedure was used by Sennaroglu [41], where, by translating a lens within a plane–plane cavity and observing the pump power at which the cavity became unstable with different lens positions, the thermal lens could be deduced. In another experiment, the same author established the fractional heat loading by the pump to be 40% in a 3% at. doped $Nd:YVO_4$ laser [39] using such a technique.

The laser resonator was modelled to find stable laser cavity configurations for different resonator lengths l_L and thermal lens focal lengths f_{Th}, shown as shaded regions in figure 8.5. The specific case illustrated in figure 8.3 (b) is marked as a dotted line. For cavity lengths shorter than the radius of curvature of the output coupler, $l_L < R_{OC}$, the cavity modelling predicted that, to a good approximation, the cavity remained stable provided the spherical focal length of the thermal lens exceeded the cavity length, $f_{Th} > l_L$. For cavity lengths longer than R_{OC}, a thermal lens satisfying $(l_L - R_{OC}) < f_{Th} < l_L$ is required to maintain cavity stability.

The laser cavity was constructed with a number of different lengths l_L between 100 mm and 350 mm, using 90% and 99% reflective output couplers. Cavity lengths longer than 319 mm for the 90%, and 338 mm for the 99% reflective output coupler, did not lase at all. For each cavity length, the beam was monitored using a CCD camera, and the diode pump power and laser output power at the extremes of stable operation were recorded. The results for the 90% reflective output coupler are shown in figure 8.6.

The performance was divided into three regions by cavity length. Short cavities with $l_L < 195\,mm$ were found to be stable at all pump and laser powers used, in agreement with the spot size measurements performed at 165 mm described in the previ-

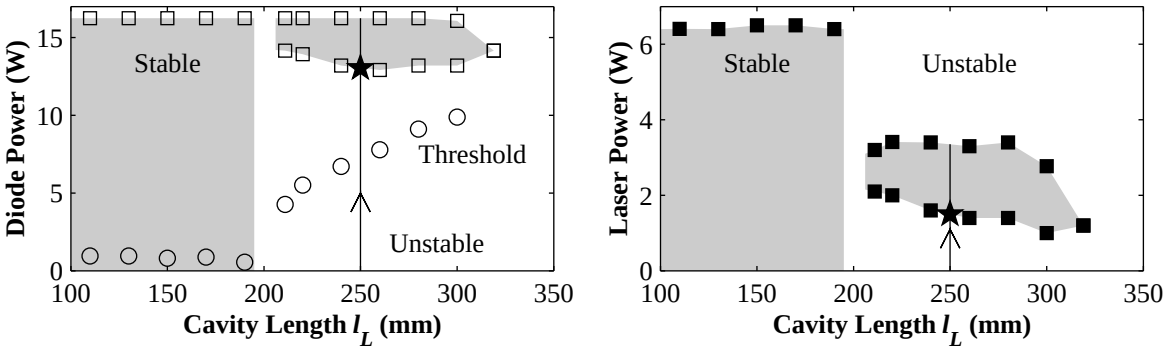

Figure 8.6: Nd : YVO_4 laser cavity stability and performance with cavity length, using a 90% reflective output coupler. Squares illustrate (a) the pump diode power and (b) the laser output power bounding the regions of stable operation (shaded). Circles, pump power required to reach laser threshold. The arrows indicate the progression also marked in figure 8.5 for an arbitrary cavity length of $l_L = 250\,\text{mm}$. The focal length of the thermal lens decreased with increasing pump and laser power, and the star denotes where the cavity became stable.

ous section. From figure 8.5, it was concluded that the thermal lens focal length under these conditions was $f_{\text{Th}} > 200\,\text{mm}$. For a narrow range of cavity lengths between $195 < l_L < 206\,\text{mm}$, the Nd : YVO_4 laser did not operate at all. This was attributed to the nearly confocal cavity configuration, for which modelling also predicted that no stable mode exists. Stable modes again existed for cavity lengths in excess of 206 mm. In agreement with figure 8.5, these cavity lengths were unstable near threshold, and pump powers above ∼13 W and laser powers above 2 W were necessary to yield a stable mode. The solid arrows in figures 8.5 and 8.6, at an arbitrary cavity length of $l_L = 250\,\text{mm}$, indicate the progression from the laser being unpumped, to reaching threshold with an unstable mode, to the cavity becoming stable as the thermal lens focal length became short enough. The star denotes the transition to a stable cavity, which corresponded to a thermal lens of $f_{\text{Th}} = l_L = 250\,\text{mm}$, occurring at 13 W diode power. Comparing figures 8.5 and 8.6, it should be concluded that the lens was dependent on the cavity length l_L due to the relation $f_{\text{Th}} > (l_L - R_{\text{OC}})$; such a behaviour was thought unlikely.

The high laser oscillation threshold evident in figure 8.6 (a) for $l_L > 200\,\text{mm}$ resulted in changed operating conditions, since the extracted power was reduced as compared to short cavities. Thermal lensing measurements published in the literature are typically different under lasing and non-lasing conditions. This effect, and the separate contributions from the pump power and intracavity resonated field, could not be separated in this analysis.

Probe Laser

A method commonly used to determine the thermal lensing in a laser rod is to observe the lens effect on a probe laser of a different wavelength passed through the rod and cavity. From the changes in probe beam spot size, an effective thermal lens can be deduced [192, 197, 298, 299]. Since the measurement technique is passive, the lensing can be measured under different operating conditions, including nonlasing conditions relevant to the pulse build-up period in Q-switched systems. Interference between the front and back faces of the laser rod have been used to determine aberrations in Nd : YAG with He–Ne probe lasers [29, 299]. The aberrations were observed to lead to Bessel-like and annular output beams, with the effects being stronger in Nd : YVO_4 than in Nd : YAG. In reference [191], data from a Twyman–Green interferometer were used to analyse the optical phase front distortions of end pumped Nd : YAG and Nd : YLF rods. The investigation presented in this section was not intended to yield phase information.

The laser rod was probed under both lasing and nonlasing conditions using a He–Ne probe laser and under nonlasing conditions using Nd : YAG, and Nd : YLF probe lasers. Recording images using a He–Ne laser was complicated by the presence of multiple interference fringes from reflections of other cavity optics. The coincidence of the Nd : YAG probe with the laser wavelength precluded this laser from being used for experiments under lasing conditions, and under nonlasing conditions the laser rod was observed to act as an amplifier for the probe beam.

Images obtained by double passing a 40 mW Nd : YLF probe laser (Spectra Physics Inc), polarised parallel to the Nd : YVO_4 laser radiation, through the laser rod under nonlasing conditions are shown in figure 8.7. The 1.047 μm Nd : YLF probe wavelength was close to the reflection peak of the high reflector R_L coating, but sufficiently distinct from the 1.064 μm laser wavelength to prevent amplification in the rod. With no pumping, the $\sim$0.5 mm $1/e^2$ radius probe beam traversed the laser rod without aberration. At around 8 W pump power, the probe beam was focused to a smaller spot. Increased pump power led to the formation of concentric rings about the central probe spot, as illustrated in figure 8.7 (c) and (d). From the measurements of probe beam spot sizes, a thermal lens focal length of $f_{\mathrm{Th}} \sim 250$ mm was deduced for pump powers above 12 W, based on the size of the central spot. The origin of the concentric rings at higher powers was not investigated further, but was assumed to be related to higher order aberrations such as those reported by Jabczyński [29].

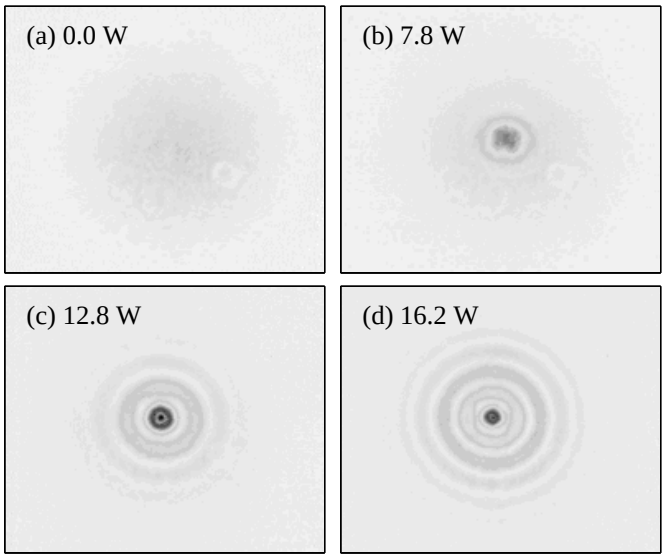

Figure 8.7: $Nd:YVO_4$ laser thermal aberrations, recorded using an Nd : YLF probe laser, under nonlasing conditions. (a) $Nd:YVO_4$ rod unpumped; (b) 7.8 W pump; (c) 12.8 W pump; and (d) at 16 W diode pump power.

Thermal Lensing Conclusions

The thermal lens measurements gave some insight into the $Nd:YVO_4$ rod characteristics under different operating conditions. Inasmuch as the experimental results were consistent, it was concluded that the focal length of the thermal lens within the rod was $f_{\mathrm{Th}} \sim 200\,\mathrm{mm}$ at the highest pump powers used, principally determined by the pump diode power, and that aspheric aberrations seemed to play a significant role in determining the laser cavity resonant mode. This limit on the spherical part of the thermal lens was sufficient to allow ICSRO cavities to be designed such that the resonated mode was insensitive to thermal lensing in the laser rod.

8.2 Intracavity OPO

The periodically poled $RbTiOAsO_4$ (PPRTA) crystal used in the ICSRO cavities was supplied by Crystal Associates, cut at $\theta = 90^\circ$ and $\phi = 0^\circ$ and poled with period $\Lambda = 39.6\,\mu$m, suitable for $\lambda_3 = 1.064\,\mu$m pumped OPO generating signal and idler wavelengths of $\lambda_2 = 1.53\,\mu$m and $\lambda_1 = 3.50\,\mu$m respectively, at room temperature. The crystal had dimensions $20 \times 10 \times 3\,$mm (length $\times$ breadth $\times$ thickness). Some relevant material properties of RTA are given in section 3.4.3. Temperature tuning using this crystal had been

published previously [155, 156] and was not repeated here. The signal resonant ICSROs were constructed using the $Nd:YVO_4$ laser head described in the previous section, in different cavity configurations, shown in figure 8.8.

8.2.1 Single Lens Cavity

The cavity configuration shown in figure 8.8 (a) had been previously demonstrated [155] and served as a benchmark performance cavity. Dichroic beam splitters BS, coated for 10° angle of incidence with high reflectivity at $1.504\,\mu$m and antireflection coated at $1.047\,\mu$m, were used to separate the laser and signal resonant cavities. Two beam splitters were used in series in the signal cavity to obtain adequate extinction of the residual laser reflections and prevent coupled cavity effects.

The near concentric signal cavity was formed between the signal high reflector R_S and common mirror R_C, both concave with $R_S = R_C = 200\,\text{mm}$ radius of curvature, and separated by a cavity length $d_S = 399\,\text{mm}$. The signal mode waist size w_2 is illustrated in figure 8.9 as a function of signal cavity length d_S, the only variable parameter in this case. The cavity length was extended until the spot size within the PPRTA crystal was sufficiently small, on the order of $50\,\mu$m, for the OPO threshold to be reached. As can be seen from figure 8.9 (b), the resulting signal cavity is close to the edge of stability, and adjustments of a few hundred μm were sufficient to make the OPO cavity unstable.

The laser resonator, shown in figure 8.10, was formed between a plane laser high reflector R_L and the $R_C = 200\,\text{mm}$ common mirror. In order to obtain a suitably small waist within the nonlinear optical crystal, a lens of focal length $f_L = 50.2\,\text{mm}$ was included within the laser cavity. The spot size w_L within the $Nd:YVO_4$ laser rod, and the waist w_3 within the PPRTA crystal, are shown in figure 8.10 (b) and (c), respectively, as a function of common mirror displacement. The distance between high reflector R_L and lens f_L was $d_L = 207\,\text{mm}$, and since $d_L \gg f_L$, its precise value did not substantially affect the resonated mode sizes. By contrast, the common arm length d_C changed the spot size within the laser rod as well as both the laser and signal mode waists within the PPRTA crystal. This dependence made the resonator alignment somewhat nontrivial. The successful configuration, with $d_L = 207\,\text{mm}$ and $d_C = 259\,\text{mm}$, resulted in a laser waist size of $w_3 \approx 50\,\mu$m within the PPRTA crystal, and a spot size $w_L \approx 250\,\mu$m within the $Nd:YVO_4$ rod.

A sample idler power efficiency curve, measured through the common mirror R_C and therefore accounting for only half of the generated idler, is shown in figure 8.11. The idler power was extremely sensitive to small changes in cavity configuration, especially

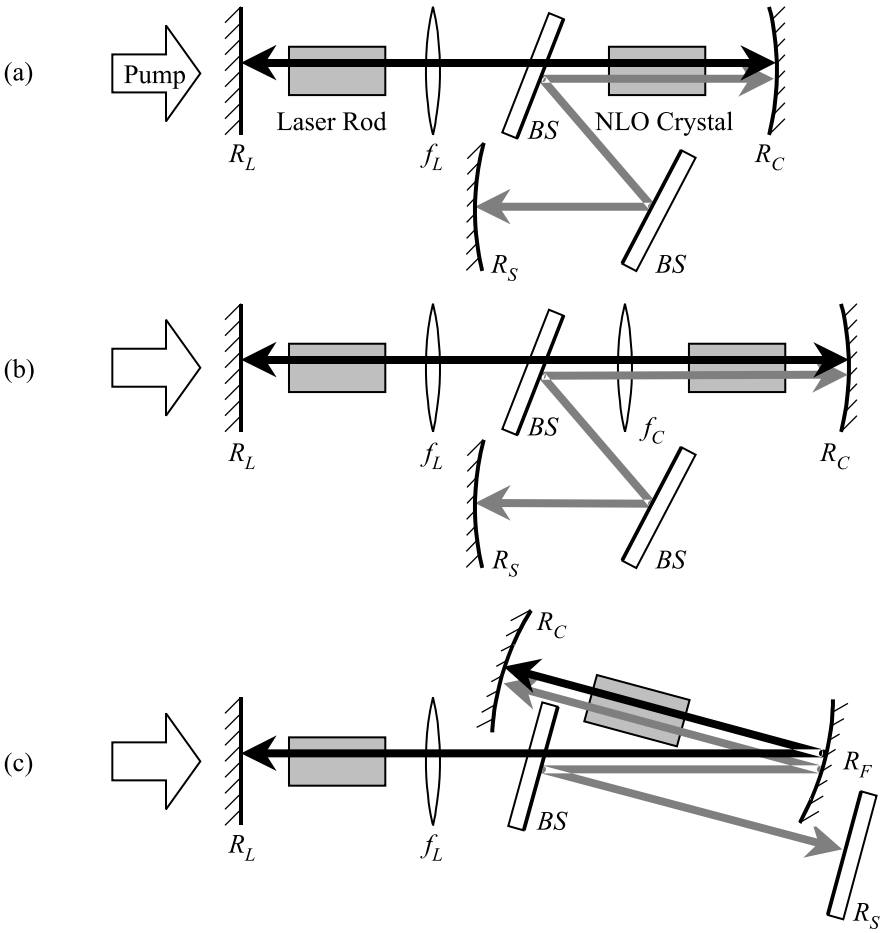

Figure 8.8: Continuous-wave intracavity OPO cavities described in this chapter. (a) Single lens cavity. The laser cavity was formed between laser high reflector R_L and common mirror R_C with intracavity lens f_L, while the signal radiation resonated between signal high reflector R_S and R_C, via two beam splitters BS. (b) Telescope cavity, where an additional lens f_C was inserted into the common laser and signal branch to tailor the spot size within the nonlinear optical crystal. (c) Folded cavity with folding mirror R_F in place of f_C.

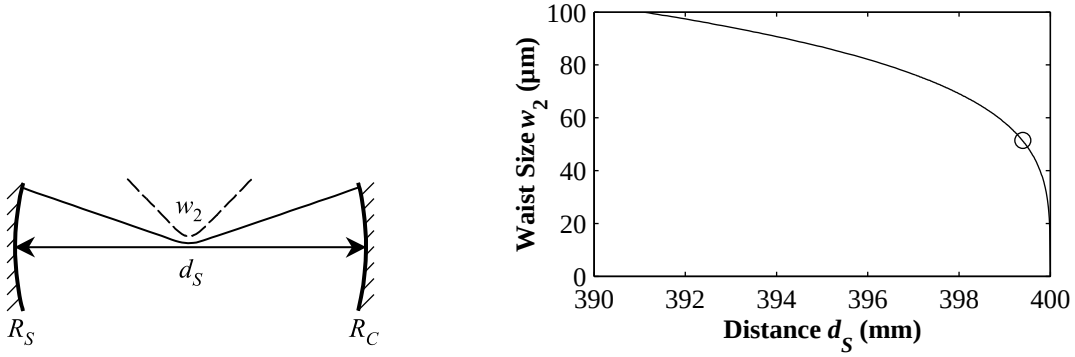

(a) (b)

Figure 8.9: (a) Signal cavity mode with $R_C = R_S = 200\,\text{mm}$. The resonated mode is indicated by the solid line (dashed, 3× magnified). (b) Signal waist size w_2 in the nonlinear optical crystal as a function of signal cavity length. The configuration adopted is indicated by the circle, with a resulting waist size of $w_2 = 50\,\mu\text{m}$.

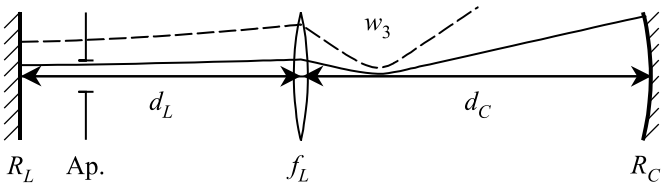

(a)

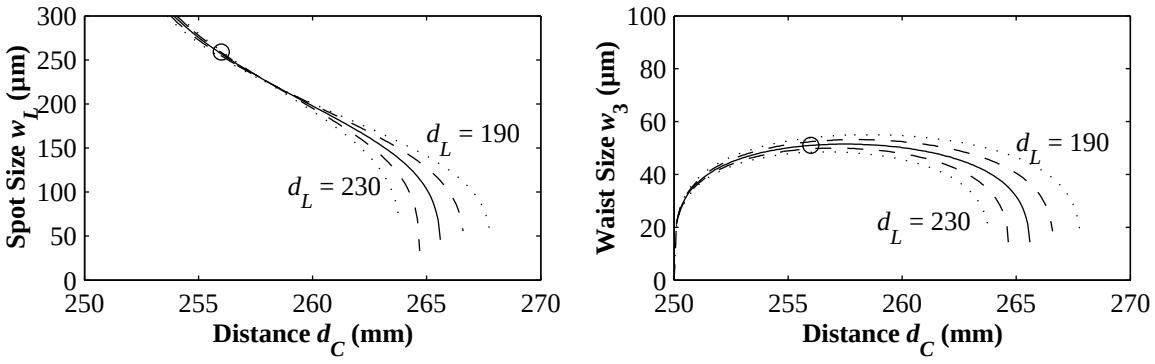

(b) (c)

Figure 8.10: (a) Laser cavity with intracavity lens and $R_L = \infty$, $f_L = 50.2\,\text{mm}$, and $R_C = 200\,\text{mm}$. The resonated mode is indicated by the solid line (dashed, 3× magnified). Ap, aperture. (b) Laser spot size w_L within laser rod and (c) laser waist w_3 within nonlinear optical crystal for different optic spacings. The configuration adopted is indicated by the circle, with a resulting spot in the laser rod $w_L \approx 250\,\mu\text{m}$ and waist within the nonlinear optical crystal of $w_3 \approx 50\,\mu\text{m}$.

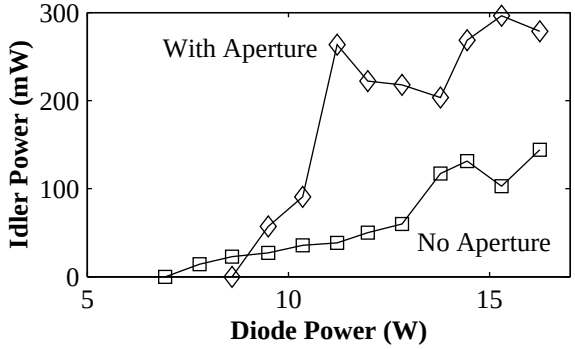

Figure 8.11: Sample idler power measured through common mirror R_C for the single lens ICSRO cavity shown in figure 8.8 (a), with (squares) and without (diamonds) an intracavity aperture, as a function of pump diode power.

the alignment of mirror R_C, and pump power. It was found that an improvement in performance could be obtained by adding an aperture with a diameter of $\sim$800 μm near the laser rod, as shown in figure 8.10. This improvement was observed for all cavity configurations used, and subsequent results were taken with this aperture.

The highest output power obtained from the ICSRO was 478 mW at 14.4 W pump diode power, while the lowest OPO threshold observed was 3.5 W. The unpredictable behaviour evident in figure 8.11 was always observed with this cavity and motivated the search for improved cavity configurations. The single lens OPO configuration presented a number of additional undesirable characteristics, including relaxation oscillations, drift, and hysteretic intolerance to cavity disruptions. Relaxation oscillations in ICSROs were treated theoretically by Turnbull *et al.* [153], and are a common phenomenon of intracavity frequency conversion systems [115, 154, 198, 300, 301]. Their suppression requires the polarisations and spatial hole burning characteristics to be controlled.

A sample of such characteristic spiking is shown in figure 8.12 (a), where the relaxation oscillations were actively triggered using a 2.5 kHz slotted disc optical chopper, placed within the common branch of the cavity. The time axis was measured relative to the opening of the chopper. In the thin line, the ICSRO was blocked from oscillating, but the cavity left otherwise unchanged.

A number of external factors are known to exacerbate relaxation oscillations, including optical or mechanical disturbances to the optical cavity. The use of PPLN as the nonlinear optical material in such an ICSRO results had previously resulted in more severe relaxation oscillations [155]. The single lens cavity PPRTA ICSRO was also observed to exhibit drifts over time periods of several seconds. Figure 8.12 (b) shows the relative

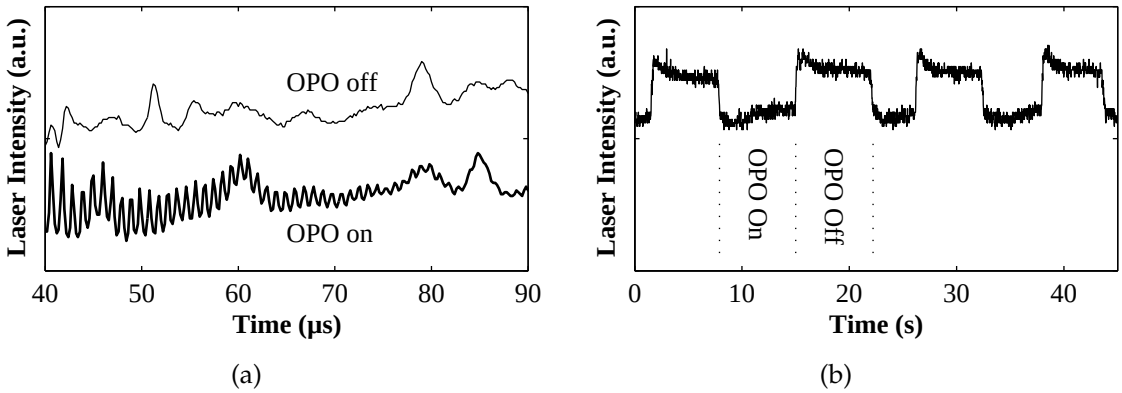

Figure 8.12: Temporal behaviour of the laser intensity for the single lens cavity ICSRO. (a) Relaxation oscillations, triggered by an optical chopper, visible as spikes in the intensity profile of the laser field when the ICSRO is on (heavy line) and absent when the ICSRO is off (thin line). (b) ICSRO spontaneously cycling on and off, over periods of seconds. a.u., Arbitrary units.

intracavity laser intensity as the OPO spontaneously switched between above threshold and below threshold. This phenomenon was assumed to arise from cyclic changes in thermal loading within the laser rod and PPRTA crystal. These undesirable performance characteristics were not further investigated in this work, since each was attributed, at least in part, to the cavity design.

8.2.2 Resonator Design

Compensation of thermal lensing by the addition of intracavity lenses has been successfully demonstrated by a number of authors [154, 196, 197, 298]. Telescope laser resonators comprising two intracavity lenses have been shown to provide the necessary flexibility of resonated mode size and compensation of thermal lensing with small adjustments of the lens spacing, without introducing additional diffraction losses [302, 303]. The design of such resonators has been treated analytically [302], and also by an empirical approach based on the $ABCD$ matrix treatment [28]. For the present case, the $ABCD$ method was found to be sufficient.

A two mirror signal cavity such as that illustrated in figure 8.9 may be treated analytically without difficulty. For a cavity of length L and mirror curvatures R_1 and R_2, we may define stability parameters for each optic $i = 1, 2$ as $g_i = (1 - L/R_i)$ [46, 186, 187, 208]. The cavity will be stable provided $g_1 g_2 < 1$ and have optimum stability with respect to perturbations when $g_1 g_2 = 1/2$. The curvature $R(z)$ of the Gaussian mode must match the mirror curvature at $z = \pm L/2$, from which the waist w_0 can be calculated. For $R_1 = R_2 = 200\,\text{mm}$, the condition $g_1 g_2 = 1/2$ yielded an optimum cavity length of

$L = 341$ mm with a waist $w_0 = 185\,\mu$m. By comparison, the requirement for $w_0 \leq 50\,\mu$m required a cavity length of $L \geq 399$ mm, as illustrated in figure 8.9, resulting in a cavity parameter product $g_1 g_2 \geq 0.997$. To simultaneously satisfy the conditions $g_1 g_2 = 1/2$ and $w_0 = 50\,\mu$m would have necessitated mirrors with curvature radii of 14.6 mm and a cavity length of 25 mm. Since these values were unpractical, it was concluded that a more complex signal cavity configuration, with an additional focusing element, was necessary.

The mode size constraints were taken to be as follows. The laser mode size w_L within the laser rod should satisfy $150 \leq w_L \leq 200\,\mu$m to provide good mode matching between pumped and laser volumes. A laser mode radius smaller than $100\,\mu$m was to be avoided, since such a small volume was expected to intensify the thermal lensing in the laser rod. In the PPRTA crystal, both the laser and signal modes were to have waist sizes of $w_3 \approx w_2 \approx 50\,\mu$m. The validity of the $50\,\mu$m waist condition was verified experimentally by constructing a cavity design with $100\,\mu$m waists within the nonlinear optical crystal, which only barely reached threshold. The spot sizes within the laser rod and nonlinear optical crystal were modelled for different cavity optic spacings about the design points to establish tolerances to mechanical and thermo-optical changes within the resonator. The choice of mirrors, beam splitters, and lenses was restricted by available optics; in particular, plane or 200 mm concave cavity end mirrors, and plane beam splitters.

Since the $Nd:YVO_4$ thermal lensing investigations discussed in section 8.1 did not yield fully consistent measurements of the lens focal length, and any thermal lens in the PPRTA crystal was not studied, lensing compensation was not possible. The cavities were thus designed such that the resonated mode sizes exhibited minimal sensitivity to thermal lensing within the laser rod and the nonlinear optical crystal. In practice, this was achieved by placing each thermal lens at a mode waist, where its effect on the resonated mode remained insignificant until its focal length became comparable to the focal lengths of the optics forming the waist.

Two approaches were chosen, as shown in figure 8.8 (b) and (c) on page 145. In the first design, an intracavity lens was added to the common branch of laser and signal cavities; in the second, a curved folding mirror was employed to the same effect.

8.2.3 Telescope Cavity

In order to obtain the desired $w_2 = 50\,\mu$m signal waist within the nonlinear optical crystal, the common laser and signal branch was modified to include an additional lens f_C. The laser lens f_L was still required to allow independent control of the laser mode within the laser rod and nonlinear optical crystal. The signal cavity with additional lens is shown

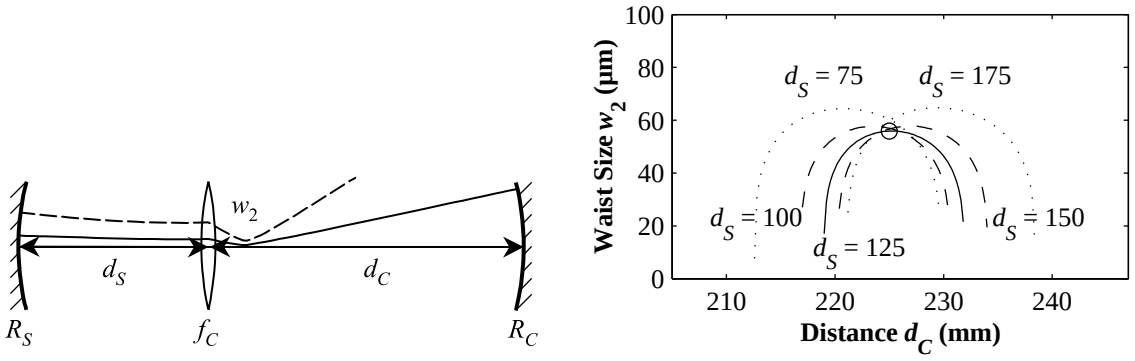

Figure 8.13: (a) Signal cavity with an $f_C = 25.4\,\text{mm}$ intracavity lens and $R_S = R_C = 200\,\text{mm}$. The resonated signal mode volume is indicated by the solid line (dashed, 3× magnified). (b) Signal waist size w_2 in the nonlinear optical crystal for different combinations of optic spacings. The configuration adopted is indicated by the circle, with a resulting waist size of $w_2 = 56\,\mu\text{m}$.

in figure 8.13 (a); given end mirror curvatures $R_S = R_C = 200\,\text{mm}$, a lens of focal length $f_C = 25.4\,\text{mm}$ was found to be adequate. To find the optimum spacings d_S and d_C, the waist size was calculated for a number of combinations of these, figure 8.13 (b). From the figure, a spacing $d_S = 125\,\text{mm}$ was chosen, for which the cavity was stable within the range $219 \leq d_C \leq 232\,\text{mm}$. The largest waist size, at the centre of the stability region where $d_C = 225\,\text{mm}$, was $w_2 = 56\,\mu\text{m}$. Other choices of d_S lead to larger waist sizes at the centre of the stability region.

The layout of the laser cavity was then designed to conform with the f_C, R_C and d_C parameters determined by the signal cavity, as well as the plane laser high reflector R_L. The laser cavity is illustrated in figure 8.14 (a). It was found that, of commercially available focal lengths, a lens with $f_L = 88.3\,\text{mm}$ yielded an acceptable resonating mode, provided the distances d_L and d_T were suitably chosen. The resulting spot size w_L at the laser rod, close to R_L, is shown in figure 8.14 (b) for a number of combinations of d_L and d_T. Figure 8.14 (c) illustrates the waist size w_3 within the nonlinear optical crystal for the same configurations. The waist w_3 within the PPRTA crystal was significantly affected only by choice of d_L, whereas the mode size w_L within the laser rod was influenced by both distances. A choice of $d_L = 125\,\text{mm}$ and $d_T = 150\,\text{mm}$, marked in the figures by a circle, was made for the telescope cavity. The resulting spot sizes were $w_L = 165\,\mu\text{m}$ and $w_3 = 52\,\mu\text{m}$.

The laser cavity was constructed in the configuration shown in figure 8.14 (a), initially without the intracavity OPO crystal, using a plano–convex singlet for f_L and a bi-convex singlet for f_C. Both lenses were antireflection coated in the near-infrared region (New-

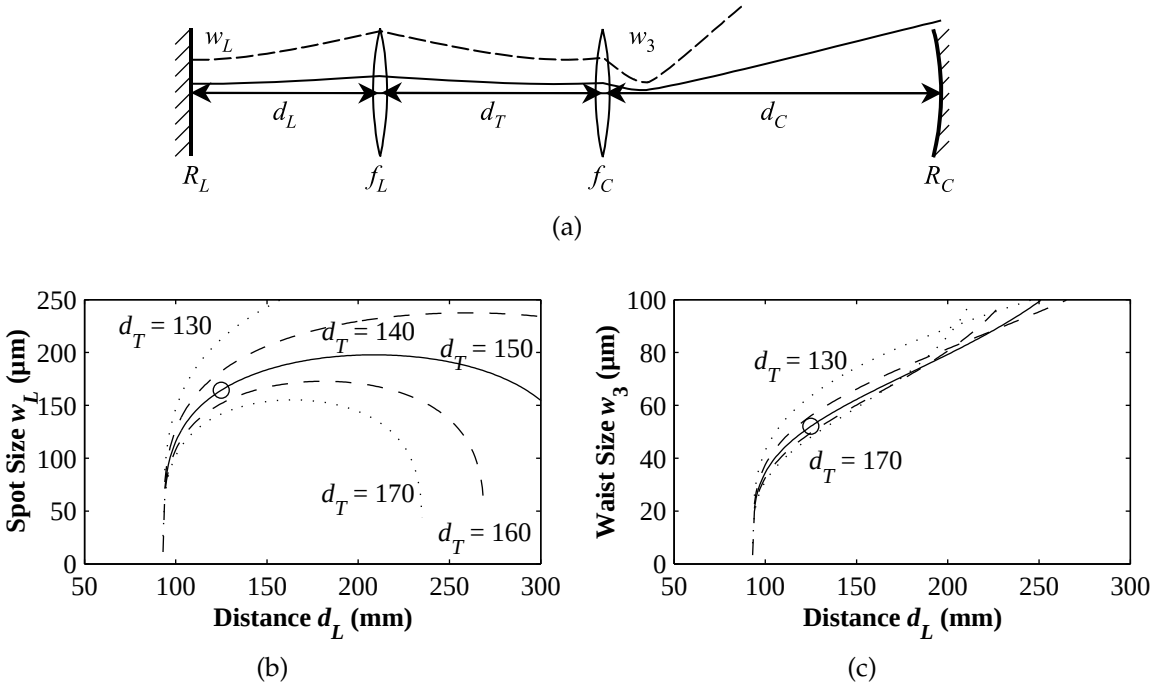

Figure 8.14: (a) Laser cavity with two intracavity lenses $f_L = 88.3\,\text{mm}$, $f_C = 25.4\,\text{mm}$, and $R_L = \infty$, $R_C = 200\,\text{mm}$. The resonated laser mode is indicated by the solid line (dashed, $3\times$ magnified). (b) Laser spot size w_L within laser rod and (c) laser waist w_3 within nonlinear optical crystal for different optic spacings. The configuration adopted is indicated by the circle, with a resulting spot in the laser rod of $w_L = 165\,\mu\text{m}$ and waist within the nonlinear optical crystal of $w_3 = 52\,\mu\text{m}$.

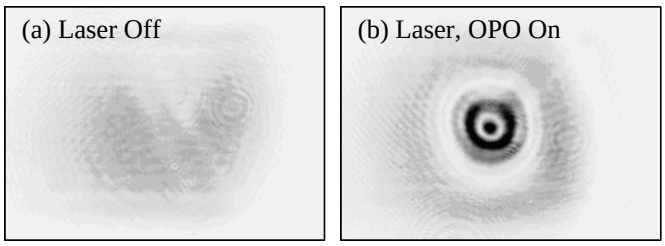

Figure 8.15: Far-field images of He–Ne probe laser passing through the PPRTA crystal. (a) Unpumped; (b) 16.2 W pump incident on Nd : YVO_4 rod, with both laser and ICSRO above threshold.

port AR.18), resulting in estimated losses of ∼0.5% at the laser and ∼1% at the signal wavelength, per surface. Using a 90% reflective output coupler in place of R_C, an output power of 6 W was obtained, in a beam with a smooth, circular spatial distribution. This was compared to the 8 W generated from a short near hemispherical cavity described in section 8.1, verifying that the longer cavity was stable and did not introduce substantial additional losses. The beam splitters (BS), PPRTA crystal, and high reflector R_S were added to complete the ICSRO system illustrated in figure 8.8 (b). The sensitivity to the common mirror position R_C, demonstrated by the narrow curve in figure 8.13 (b) was verified experimentally, with a ∼3 mm shift in position of R_C being sufficient to prevent the OPO from operating.

A diode pump power threshold of 11.2 W was measured for the ICSRO. At the highest diode pump power of 16.2 W, the OPO operated inconsistently and was sensitive to mechanical vibrations, although an aperture near the laser rod was found to improve its performance. The performance stability was further improved with a 50% duty cycle optical chopper inserted in the laser cavity between f_L and f_C. As this improvement was not observed when chopping only the signal branch, the performance instability was attributed to laser radiation-induced thermal lensing within the PPRTA crystal. As confirmation of significant thermal loading within the PPRTA crystal, interference fringes between the crystal faces were recorded using a He–Ne probe laser, with results shown in figure 8.15 for the system unpumped and at 16.2 W pump power. A quantitative analysis was not attempted. The high ICSRO threshold and low output power was, in part, attributed to losses from the interfaces of the intracavity lenses. This motivated replacing the lens f_C by a folding mirror R_F, as outlined in the following section, and the telescope design was not pursued further.

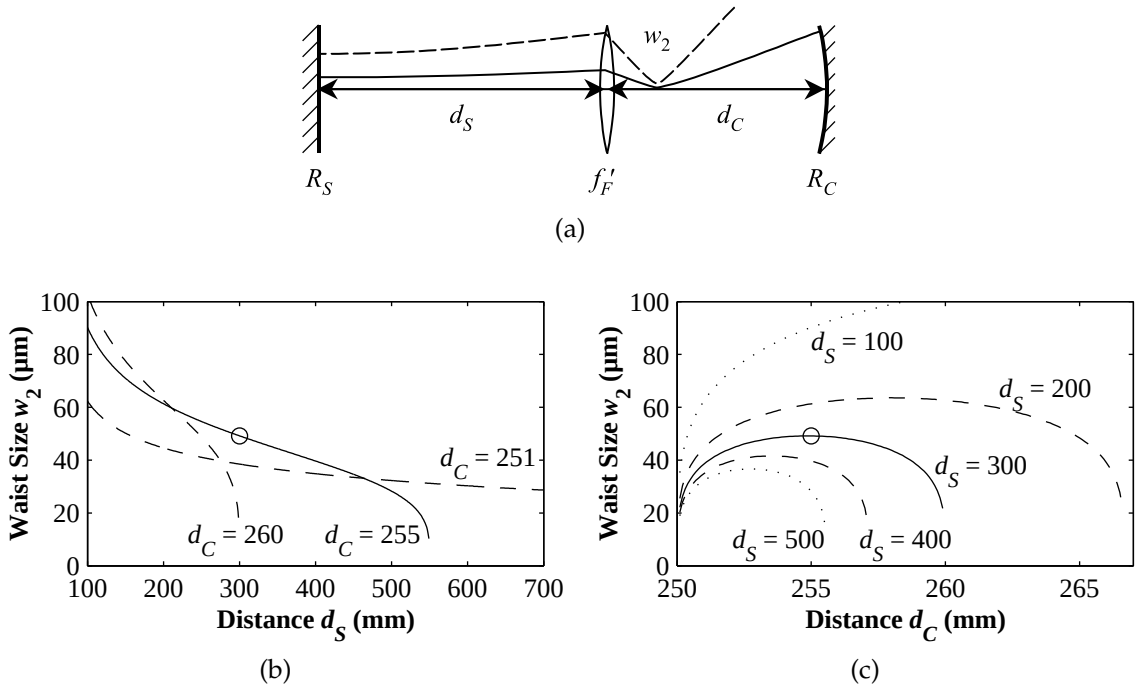

Figure 8.16: (a) Signal cavity with folding mirror R_F modelled as lens $f_F' = 50\,\text{mm}$. The resonated signal mode is indicated by the solid line (dashed, $3\times$ magnified). (b) and (c) Signal waist size w_2 in the nonlinear optical crystal for different combinations of optic spacings. The configuration adopted, with $w_2 = 50\,\mu$m, is indicated by the circle.

8.2.4 Folded Cavity

The availability of concave mirrors custom coated for high reflectivity at both the $1.064\,\mu$m laser and $1.53\,\mu$m signal wavelengths provided a pathway to reduce the passive optical loss introduced by the common lens f_C. The resulting folded cavity, shown in figure 8.8 (c), was similar to bow tie cavities often employed in Ti : sapphire and similar lasers [122]. As in such cavities, the signal high reflector R_S was replaced by a plane optic (in practice, one of the beam splitters BS), which allowed the signal waist size w_2 within the nonlinear optical crystal to be finely controlled by the position of R_S. Other design parameters, such as the requirement for a $w_3 \approx 50\,\mu$m laser mode waist within the nonlinear optical crystal and a $w_L = 200\,\mu$m spot at the laser rod, remained unchanged.

In terms of $ABCD$ cavity modelling, the folding mirror of curvature R_F was equivalent to a lens of focal length $f_F' = R_F/2$, so that the effective signal cavity was as shown in figure 8.16 (a). One of the considerations of the folding mirror cavity was the incidence angle θ_F of the folding mirror R_F, since increasing angles of incidence increased the asymmetry of the resonated mode. In practice, the smallest angle allowed by the

physical constraint of the resonated beams clipping the nonlinear optical crystal mount was used, corresponding to an angle of $\theta_F \approx 20^\circ$. The resulting small astigmatism, expected to be on the order of $(1 - \cos\theta_F) = 6\%$, was disregarded in the cavity modelling.

Of the available optics, a mirror with a radius of curvature of $R_F = 100\,\text{mm}$ ($f'_F = 50\,\text{mm}$) was chosen for the folding mirror. The resonated mode waist w_2 within the nonlinear optical crystal is shown in figure 8.16 (b) and (c) for different combinations of lengths d_S and d_C. From the figure, it can be seen that a choice of $d_C \approx (f'_F + R_C) = 250\,\text{mm}$ (within 2%) yielded an approximately collimated beam to the plane high reflector R_S, and a large insensitivity to its position. Based on the modelling, spacings of $d_C = 255\,\text{mm}$ and $d_S \sim 300\,\text{mm}$ were chosen, resulting in a signal mode waist of 50 μm within the crystal.

For the laser cavity, the choice of intracavity lens f_L was found to be somewhat arbitrary, and $f_L = 150\,\text{mm}$ yielded the required laser cavity mode sizes. By choosing $d_L \approx f_L$, the spot sizes w_L and w_3 depended only weakly on the distance d_T between the laser lens and the folding mirror. The resulting laser cavity is shown in figure 8.17 (a) for $d_C = 255\,\text{mm}$, with panels (b) and (c) showing the variations in spot sizes w_L and w_3, for different optic spacings d_T and d_L. As mentioned above, the cavity behaviour is sensitive to d_C, and an extension to $d_C = 260\,\text{mm}$ would have caused the stability curves of figures 8.17 (b) and (c) to be compressed into the range $220 \leq d_T \leq 450\,\text{mm}$ while maintaining the same qualitative shape. Such an extension of d_C would have enlarged the spot size within the laser rod to $w_L \sim 250\,\mu\text{m}$. Based on these considerations, a spacing of $d_T = 400\,\text{mm}$, suitably near the centre of the stability regions for any $255 \leq d_C \leq 260\,\text{mm}$, was chosen. The combination of $d_L = 150\,\text{mm}$, $d_T = 400\,\text{mm}$, and $d_C = 255\,\text{mm}$ yielded a spot size within the laser rod of $w_L = 180\,\mu\text{m}$ and a waist within the nonlinear optical crystal of $w_3 = 46\,\mu\text{m}$.

The folded cavity ICSRO system was constructed as illustrated in figure 8.8 (c). For ease of alignment, a 90% reflective plane mirror was placed between the laser rod and lens f_L; the output of the plane–plane laser so formed was used for alignment of lens f_L and mirrors R_F and R_C. The signal cavity was aligned using the non-phase matched second harmonic of the pump radiation generated within the PPRTA crystal as an alignment beam.

In agreement with the modelled curves, the performance of the folded cavity ICSRO was found to depend critically on the precise alignment of the folding R_F and common R_C mirrors, and on the spacing d_C between them. The best performance corresponded to the shortest stable d_C, which may have been due to the 180 μm design laser mode size within the $\text{Nd}:\text{YVO}_4$ rod being smaller than optimum. Similarly, the optimum signal cavity high reflector R_S position was empirically found to differ from the modelling, with

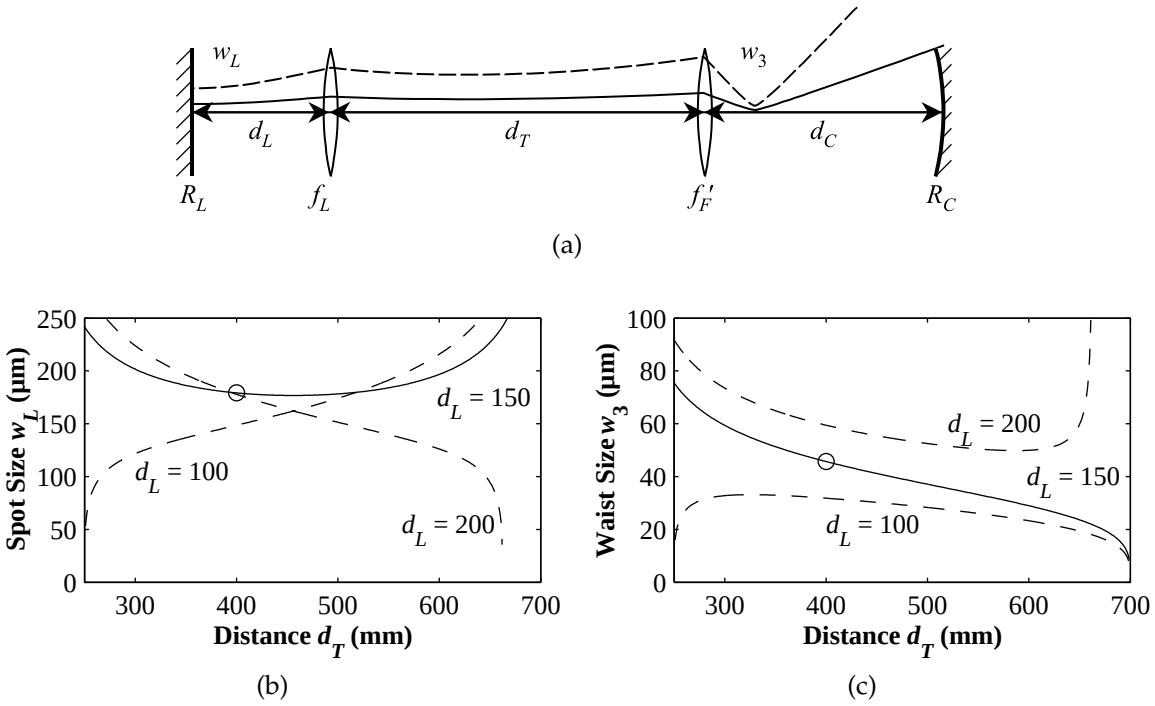

Figure 8.17: (a) Laser cavity, with intracavity lens $f_L = 150$ mm and folding mirror R_F modelled as lens $f_F' = 50$ mm, for $d_C = 255$ mm. The resonated laser mode is indicated by the solid line (dashed, $3\times$ magnified). (b) Laser spot size w_L within laser rod and (c) laser waist size w_3 within the nonlinear optical crystal for different combinations of optic spacings. The configuration adopted is indicated by the circle, with a resulting spot in the laser rod of $w_L = 180\,\mu$m and waist within the nonlinear optical crystal of $w_3 = 46\,\mu$m.

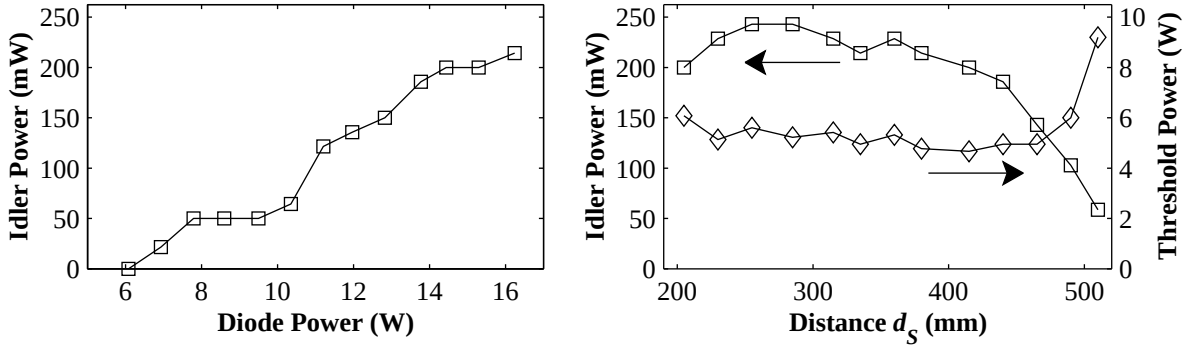

(a) (b)

Figure 8.18: Performance of the folded ICSRO cavity, shown in figure 8.8 (c), measured through common mirror R_C. (a) Output idler power for signal high reflector distance $d_S = 285\,\text{mm}$, as a function of pump diode power. (b) Idler power (squares) and ICSRO threshold (diamonds), as a function of signal high reflector position d_S.

$d_S = 285\,\text{mm}$ resulting in the best performance. The ICSRO performance was improved by the insertion of an 800 μm aperture near the laser rod.

With this cavity configuration, a laser threshold pump power of 0.4 W was measured, comparable to that of the short laser cavity discussed in section 8.1. The ICSRO had a threshold of 4.5 W, with a distinct improvement in performance above 12 W pump power. The idler output power through the common mirror R_C is shown in figure 8.18 (a). The idler amplitude stability was measured to be $\pm 10\,\text{mW}$ on a time scale of seconds, and $\pm 40\,\text{mW}$ over several minutes. In this case, the fused silica substrate of R_F did not transmit the 3.5 μm idler wavelengths, but employing CaF_2 or a similar long wavelength transmissive material for R_F optic would allow all of the generated idler to be readily extracted as useful radiation.

As an indication of the validity of the cavity modelling, the ICSRO performance was measured as a function of the distance d_S between the folding mirror and the signal high reflector. The measured idler output power and ICSRO threshold are shown in figure 8.18 (b). The data indicated that the cavity was stable for $200 \leq d_S \leq 500\,\text{mm}$, in close agreement with figure 8.16 (b), from which a signal mode spot size within the nonlinear optical crystal of $35 \leq w_2 \leq 60\,\mu$m was deduced.

To verify that this cavity was suitably insensitive to thermal lensing, it was modelled with the addition of two effective thermal lenses, one within the laser rod and the other within the nonlinear optical crystal. It was found that thermal lensing in the PPRTA changed the spot sizes by less than 3% for focal lengths as short as 200 mm. A thermal lens f_{Th} within the $\text{Nd}:\text{YVO}_4$ rod had a greater impact on the cavity mode, as the lens

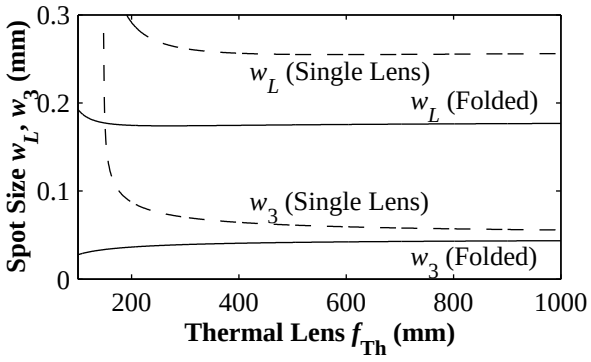

Figure 8.19: Effect of $Nd:YVO_4$ thermal lens f_{Th} on laser mode size within laser rod w_L and PPRTA crystal w_3. Solid line, folded cavity; dashed line, single lens cavity of section 8.2.1.

occurred close to, but not precisely at, a waist of the laser mode. The solid lines of figure 8.19 indicate the effects of f_{Th}. The $w_L = 180\,\mu$m spot size within the laser rod changed by less than 2%, whereas the $w_3 \approx 46\,\mu$m within the nonlinear optical crystal was reduced by up to 17% for thermal lens focal lengths of 200 mm. By comparison, such a thermal lens in the single lens cavity of section 8.2.1 caused changes in w_L and w_3 spot sizes of 10% and 45% respectively, indicated by the dashed lines. The tightening of the waist within the nonlinear optical crystal produced by increased thermal lensing in the laser rod was expected to be more likely to lead to a broader stable operating regime, with the nonlinear conversion depleting the intracavity field more strongly with shorter f_{Th}.

8.3 Conclusion

Bounds on the thermal lens to be tolerated by the cavity design were established by investigating the $Nd:YVO_4$ optical aberrations in a linear cavity without the nonlinear crystal. In this configuration, the laser head gave 7.9 W output power for 16 W pump. Modelling and measurements of resonator mode sizes and of the edge of stability provided a lower bound of $f_{Th} \geq 200$ mm, similar to the 150 mm lens predicted by the thermal modelling of section 2.1.5. Beam quality measurements and qualitative investigations using probe lasers led to the conclusion that the thermal aberrations were not purely spherical. In all cases, the pump power was the dominant factor influencing the thermal effects. This was attributed to the $\sim$50 kW/cm^3 thermal load generated by the 16 W pump diode, more than two orders of magnitude higher than the estimated thermal load induced by absorption of the intracavity field.

A previously developed ICSRO cavity design, incorporating a PPRTA nonlinear op-

tical crystal and $Nd:YVO_4$ laser head, was observed to suffer from dynamic instabilities. The design was modified to include an additional focusing element, permitting cavities with stable modes, with design point waists of $w_L = 200\,\mu$m in the laser rod and $w_3 = w_2 = 50\,\mu$m in the nonlinear optical crystal, to be built. Although the highest one-way idler power of 240 mW was lower than the highest 478 mW measured in the single lens cavity, the final folded cavity ICSRO performance was more repeatable and less sensitive to mechanical and optical changes in the cavity. Further development of this cavity design, in terms of optimised mode sizes, was expected to yield improved powers. By choosing an infrared transmissive substrate for the folding mirror (for example CaF_2, ZnSe, or ZnS) all of the generated idler could be readily extracted from the cavity, whereas in the single lens cavity an additional dichroic element would be necessary.

Chapter 9

Conclusions and Future Directions

The work presented in this thesis demonstrated the applicability of passive line narrowing techniques to quasi-phase matched nanosecond optical parametric oscillators (OPOs). Two configurations were investigated: inclusion of an intracavity étalon; and the use of a grazing incidence diffraction grating. The techniques yielded single longitudinal mode operation of periodically poled lithium niobate (PPLN) and periodically poled $KTiOPO_4$ (PPKTP) OPOs. The high nonlinear optical gain of PPLN made it the material of choice for low pulse energy OPOs generating signal and idler outputs in the 10–100 μJ range, while the higher damage threshold of PPKTP allowed mJ class pulses to be generated. For both crystals, line narrowing by a grazing incidence diffraction grating resulted in consistent single mode operation, with reliable tuning and the potential of cavity length stabilisation using an active feedback loop. By contrast, an intracavity étalon was found to be easier to implement and cause less degradation of the OPO performance, but single mode operation could not be sustained near degeneracy, where the gain bandwidth was sufficiently large to allow oscillation on multiple étalon modes.

A 1.064 μm pumped, étalon narrowed PPLN OPO generated up to 83 μJ single longitudinal mode signal radiation in the 1.5–1.8 μm wavelength range, compared to 130 μJ in the free running configuration. The reduced performance was in effect due to a doubled oscillation threshold, attributed to walkoff and loss effects within the étalon. Similar trends were observed in a visible pumped PPKTP OPO, where insertion of an étalon increased the threshold from 0.23 mJ to 0.41 mJ, and decreased the signal output energy, at a wavelength of 770 nm, from 149 μJ to 44 μJ.

The grazing incidence diffraction grating configuration yielded single longitudinal mode signal outputs with high thresholds but high slope efficiencies (30%–40%). The grazing incidence OPOs could be tuned substantially beyond the acceptance bandwidth of the nonlinear optical crystal, a phenomenon that has been observed by other authors.

Around 150 μJ were generated in PPLN and 370 μJ in PPKTP, at wavelengths between 1.5 μm and 1.8 μm; the corresponding idler wavelengths ranged between 2.6 μm and 3.7 μm. At the 620–640 nm signal wavelength range of a 532 nm pumped grazing incidence diffraction grating PPLN OPO, up to 10 μJ single mode signal radiation was generated, restricted by the onset of monolithic resonance within the crystal. These output energies were amplified in separate amplifier stages. A PPKTP optical parametric amplifier (OPA) generated 2.15 mJ of single mode signal radiation at 1.69 μm and 1.18 mJ of idler at 2.88 μm. In the visible, a Perylene red doped solid state laser amplifier generated up to 115 μJ.

The results from the grazing incidence OPOs reported here compared favourably with other similar OPOs previously reported. OPOs based on β-BaB_2O_4 with a grazing incidence diffraction grating have shown efficiencies of only a few percent, even when dual walkoff compensating crystals were used [181, 219]. Bulk KTP offered better efficiency but high thresholds [183]. The OPOs reported here had both higher slope efficiency (40% compared to 20% in KTP) and lower threshold fluences (55 MW cm^{-2} compared to 80 MW cm^{-2}) than similar devices based on KTP. A grazing incidence PPLN OPO was reported [161] with a broader spectral bandwidth (9 GHz compared to 250 MHz) and lower output pulse energy (50 μJ compared to 170 μJ). Coupled cavities have been demonstrated to yield more efficient grazing incidence OPOs by reducing the effective output coupling, but the increased cavity complexity can make continuous single mode tuning more difficult.

Substantial development and improvement of the devices investigated in this work is needed before their spectral performance become sufficiently reliable for commercial or spectroscopic applications. The efficiency of the OPOs could be optimised with regard to cavity output coupling, pumping configuration, and choice of the resonated wave. The implementation of amplifier stages could be further used to enhance the output of such systems.

One important consideration, not addressed in detail in this work, is the continuous tunability of the OPO output. Etalon narrowed OPOs may be tuned by adjusting the étalon tilt, the temperature of solid étalons, or the mirror spacing of air spaced étalons. Tuning of a grazing incidence diffraction grating cavity was demonstrated in chapter 5. For continuous tunability of the single longitudinal mode output, the cavity length must be varied synchronously, necessitating cavity locking schemes, briefly investigated here. Tuning beyond the gain bandwidth of the OPO can be accomplished by changes in crystal temperature or poling period. Fan gratings, yielding a continuous variation in poling period with crystal translation, have been demonstrated [75, 131, 163], but these

may yield spatially chirped beams if large interaction volumes are used.

The plane parallel polished faces and residual reflectivity at the idler wavelength were observed to support monolithic resonance within the PPLN and PPKTP OPOs. This phenomenon limited the pulse energy range over which single longitudinal mode operation could be achieved using passive line narrowing techniques. Monolithic resonance was suppressed in one case by polishing the crystal faces at Brewster's angle, leading to good performance of a grazing incidence PPKTP OPO, with low reflection losses at all three interacting wavelengths. In a high pulse energy 532 nm pumped PPKTP OPO, the monolithic OPO generated up to 3.74 mJ of signal radiation at 770 nm and 0.81 mJ of idler at 1.7 μm, performing almost as well as the highest output energies from linear external cavity OPOs of 4.06 mJ signal and 1.17 mJ idler. A monolithic PPLN OPO, pumped by a compact diode pumped Nd : YAG laser, was investigated in another experiment; such devices are potentially efficient, robust, and suitable for field measurements. Injection seeding at the non-resonant signal wavelength using a 637 nm single mode diode laser, including seeding on adjacent cavity modes and dual wavelength seeding, was demonstrated, yielding narrowband output limited by the pump spectral bandwidth.

With the aim of developing a compact, efficient pump source for such OPOs, a custom built, high repetition rate Q-switched diode pumped Nd : YAG laser was constructed. The optical bandwidth was reduced from $\sim$25 GHz to two longitudinal modes separated by 600 MHz using an intracavity étalon in conjunction with a passive prelase Q-switching technique. The laser generated up to 670 μJ pulse energy at 1.064 μm when operated at 5 kHz, and up to 300 μJ at 1 kHz after frequency doubling to 532 nm in LiB_3O_5. Both wavelengths were used to pump PPLN OPOs. Nd : YAG is well suited for such pump configurations and has been well researched, but other materials such as Nd : YLF may offer advantages in terms of thermal beam degradation and energy storage.

Thermal lensing was investigated in this work in a continuous wave (cw) Nd : YVO_4 pumped intracavity periodically poled $RbTiOAsO_4$ (PPRTA) OPO, where lensing was observed in both the Nd : YVO_4 and PPRTA crystals. Gain saturation leads to cw OPOs commonly operating on a single longitudinal mode without additional intracavity spectral filters, and the spectral characteristics of this OPO were not investigated.

In the investigations presented here, the magnitude of the lensing could not be quantified accurately. A cavity insensitive to thermal lensing in the laser rod and nonlinear optical crystal was systematically designed and constructed. The ICSRO reliably generated 214 mW of 3.50 micro m idler in one beam, with a similar power expected in the opposite direction that could be extracted if appropriate mirror substrates were used. Further optimisation of the interacting mode volumes within the laser rod and nonlinear

crystal is possible, and implementing the design criteria for optimised ICSRO output is also expected to yield improvements in output power.

These initial investigations indicate that the development of passively line narrowed quasi-phase matched OPOs into practical sources suitable for spectroscopy or other applications is possible. The engineering flexibility for quasi-phase matching any wavelength within the transparency range of the nonlinear optical material, together with the inherent applicability of passive band pass filters at all wavelengths, makes such OPOs attractive for spectral regions where conventional lasers or sources suitable for injection seeding are not available. This applies equally to existing, less widely researched, periodically poled materials including $LiTaO_3$ [65] and isomorphs of KTP [72, 73], as well as new nonlinear optical materials, the search for which is ongoing.

Appendix A

Publications Arising

Journal Publications

Glenn W. Baxter, **Philip Schlup**, Iain T. McKinnie, Jonas Hellström and Fredrik Laurell, "Single-mode near-infrared optical parametric oscillator–amplifier based on periodically poled $KTiOPO_4$," *Applied Optics* **38**, 6659–6662 (2001).

Philip Schlup, Glenn W. Baxter and Iain T. McKinnie, "Single-mode visible and mid-infrared periodically poled lithium niobate optical parametric oscillator amplified in Perylene red doped poly(methyl methacrylate)," *Optics Communications* **184**, 225-230 (2000).

Philip Schlup, Glenn W. Baxter and Iain T. McKinnie, "High pulse energy and single-frequency optical parametric oscillators based on periodically poled $KTiOPO_4$," *OSA Trends in Optics and Photonics Vol. 34, Advanced Solid State Lasers,* Hagop Injeyan, Ursula Keller and Christopher Marshall, eds. (Optical Society of America, Washington DC, 2000), 355-360.

Glenn W. Baxter, **Philip Schlup** and Iain T. McKinnie, "Efficient single frequency high repetition rate PPLN OPO pumped by a prelase *Q*-switched diode-pumped Nd:YAG laser," *Applied Physics B* **70**, 301-304 (2000).

Philip Schlup, Glenn W. Baxter and Iain T. McKinnie, "Single-mode near- and mid-infrared periodically poled lithium niobate optical parametric oscillator," *Optics Communications* **176**, 267–271 (2000).

Philip Schlup, Stuart D. Butterworth and Iain T. McKinnie, "Single mode, singly-resonant pulsed periodically poled lithium niobate optical parametric oscillator," *Applied Optics* **38**, 7398–7401 (1999).

Philip Schlup, Stuart D. Butterworth and Iain T. McKinnie, "Efficient single-frequency pulsed periodically poled lithium niobate optical parametric oscillator," *Optics Communications* **154**, 191–195 (1998).

Conference Presentations

Philip Schlup, Glenn W. Baxter, Iain T. McKinnie, Jonas Hellström and Fredrik Laurell, "Single mode near infrared optical parametric oscillator–amplifier based on periodically poled $KTiOPO_4$," *Conference on Lasers and Electro Optics 2001* (Baltimore, USA, May 2001), paper CThJ5.

Glenn W. Baxter, **Philip Schlup** and Iain T. McKinnie, "Efficient, single-mode, visible and infrared periodically poled lithium niobate OPOs," *Conference on Lasers and Electro-Optics /Europe 2000*, (Nice, France, September 2000), paper CThH3.

Philip Schlup, Glenn W. Baxter and Iain T. McKinnie, "High pulse-energy and single frequency optical parametric oscillators based on periodically poled $KTiOPO_4$," *Advanced Solid State Lasers 2000* (Davos, Switzerland, February 2000), paper WD6.

Philip Schlup, Glenn W. Baxter, Iain T. McKinnie and Stuart D. Butterworth, "Efficient single-frequency pulsed PPLN OPO," *Conference on Lasers and Electro-Optics 1999* (Baltimore, USA, May 1999), session CMG5.

Philip Schlup, Stuart D. Butterworth and Iain T. McKinnie, "Single mode, 1.45–1.59 μm tuneable periodically poled lithium niobate optical parametric oscillator," *Australasian Conference on Optics, Lasers and Spectroscopy 1998* (Christchurch, New Zealand, December 1998), paper Thu2b-4.

Philip Schlup, Stuart D. Butterworth and Iain T. McKinnie, "Efficient single frequency pulsed periodically poled lithium niobate optical parametric oscillator," *Electronics New Zealand Conference 1998*, (Dunedin, New Zealand, September 1998).

Appendix B

Locking Circuit

The circuit diagram for the dual sample-and-hold PID feedback circuit, as used in section 5.2.5, is shown in figure B.1. The ac-coupled, buffered and amplified signals from the photodiode elements were sampled by the NE5537 sample-and-hold amplifiers U4 and U11 during the sampling gate, with different holding capacitor RC time constants offered by combinations of the DIP switches S1 and S2. The algebraic difference between the integrated pulses was determined by op-amp U7. A variable voltage offset could be added via R38, and, after optional inversion, the error signal was processed using the proportional–integral–derivative (PID) circuit of op-amps U16, U17, U18. The low 10 Hz repetition rate of the laser rendered the derivative error signal ineffectual and it was not used in practice. The sample and clamp wave forms were generated by a Stanford Research Systems model DG535 digital delay / pulse generator.

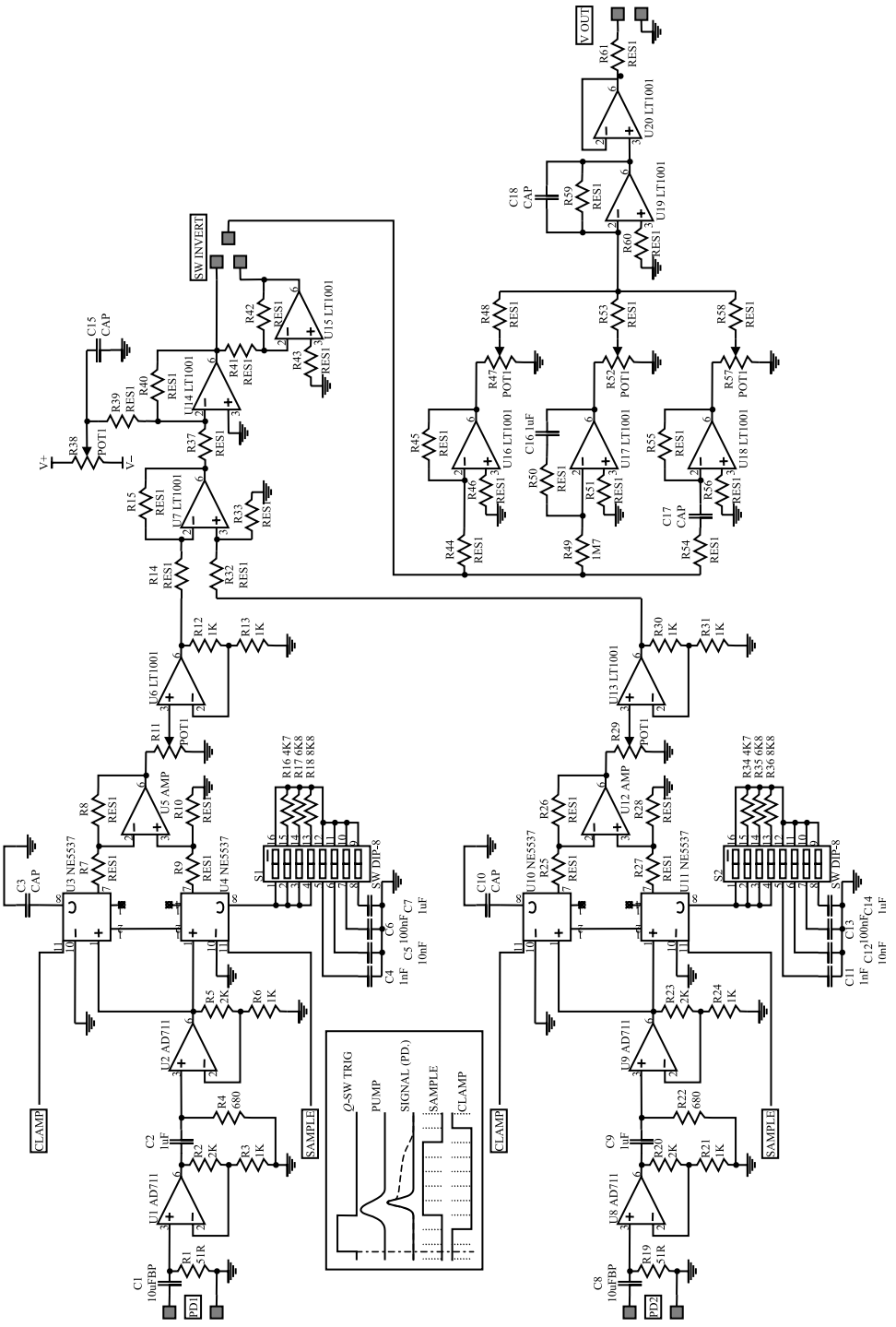

Figure B.1: PID Circuit diagram.

References

[1] T. H. Maiman, "Stimulated optical radiation in ruby masers," *Nature* **187**, 493–494 (1960).

[2] W. Koechner, "Solid-State Laser Engineering" (5th ed), *Springer Series in Optical Sciences*, Springer-Verlag, Berlin (1999).

[3] J. E. Geusic, H. M. Marcos and L. G. Van Uitert, "Laser oscillation in Nd-doped yttrium aluminum, yttrium gallium and gadolinium garnets," *Applied Physics Letters* **4**, 182–184 (1964).

[4] S. E. Christensen, H. C. Kapteyn, M. M. Murnane and S. Backus, "A simple high power compact intracavity frequency-doubled Q-switched Nd:$Y_3Al_5O_{12}$ laser," *Review of Scientific Instruments* **73**, 1994–1997 (2002).

[5] T. J. Axenson, N. P. Barnes, D. J. Reichle Jr and E. E. Koehler, "High-energy Q-switched 0.946-μm solid-state diode pumped laser," *Journal of the Optical Society of America B* **19**, 1535–1538 (2002).

[6] W. A. Clarkson, R. Koch and D. C. Hanna, "Room-temperature diode-bar-pumped Nd:YAG laser at 946 nm," *Optics Letters* **21**, 737–739 (1996).

[7] N. Moore, W. A. Clarkson, D. C. Hanna, S. Lehmann and J. Bosenberg, "Efficient operation of a diode-bar-pumped Nd:YAG laser on the low-gain 1123-nm line," *Applied Optics* **38**, 5761–5764 (1999).

[8] M. Pierrou, F. Laurell, H. Karlsson, T. Kellner, C. Czeranowsky and G. Huber, "Generation of 740 mW of blue light by intracavity frequency doubling with a first-order quasi-phase-matched $KTiOPO_4$ crystal," *Optics Letters* **24**, 205–207 (1999).

[9] N. P. Barnes, D. J. Gettemy, L. Esterowitz and R. E. Allen, "Comparison of Nd 1.06 and 1.33 μm operation in various hosts," *IEEE Journal of Quantum Electronics* **QE-23**, 1434–1451 (1987).

[10] D. C. Hanna, B. Luther-Davies and R. C. Smith, "Single longitudinal mode selection of high power actively Q-switched lasers," *Opto-Electronics* **4**, 249–256 (1972).

[11] C. F. Rae, J. A. C. Terry, B. D. Sinclair, M. H. Dunn and W. Sibbett, "Single-frequency, end-pumped Nd:YLF laser excited by a 12-mJ diode-laser array," *Optics Letters* **17**, 1673–1675 (1992).

[12] P. J. Hardman, W. A. Clarkson and D. C. Hanna, "Efficient operation of an acousto-optically-induced unidirectional and single-frequency *Q*-switched Nd:YLF ring laser," *OSA Trends in Optics and Photonics, Advanced Solid State Lasers* (Optical Society of America, Washington, DC) **16**, 236–240 (1999).

[13] H. H. Kee, G. P. Lees and T. P. Newson, "Narrow linewidth CW and *Q*-switched erbium-doped fibre loop laser," *Electronics Letters* **34**, 1318–1319 (1998).

[14] T. Crawford, C. Lowrie and J. R. Thompson, "Prelase stabilization of the polarization state and frequency of a *Q*-switched, diode-pumped, Nd:YAG laser," *Applied Optics* **35**, 5861–5869 (1996).

[15] C. Bollig, W. A. Clarkson and D. C. Hanna, "Stable high-repetition-rate single-frequency *Q*-switched operation by feedback suppression of relaxation oscillation," *Optics Letters* **20**, 1383–1385 (1995).

[16] A. Agnesi, S. Dell'Acqua and G. C. Reali, "1.5 Watt passively *Q*-switched diode-pumped cw Nd:YAG laser," *Optics Communications* **133**, 211–215 (1997).

[17] Y. Yashkir and H. M. van Driel, "Passively *Q*-switched 1.57-μm intracavity optical parametric oscillator," *Applied Optics* **38**, 2554–2559 (1999).

[18] J. Song, C. Li and K. Ueda, "Thermal influence of saturable absorber in passively *Q*-switched diode-pumped cw Nd:YAG / Cr^{4+}:YAG laser," *Optics Communications* **177**, 307–316 (2000).

[19] N. N. Il'ichev, E. S. Gulyamova and P. P. Pashinin, "Passive *Q*-switching of a neodymium laser by a Cr^{4+}:YAG crystal switch," *Quantum Electronics* **27**, 972–977 (1997).

[20] G. Xiao and M. Bass, "A generalized model for passively *Q*-switched lasers including excited state absorption in the saturable absorber," *IEEE Journal of Quantum Electronics* **33**, 41–44 (1997).

[21] A. Sennaroglu, "Continuous-wave power transmission and thermal lensing of a saturable absorber subject to excited-state absorption," *Applied Optics* **38**, 3334–3337 (1999).

[22] T. Kurobori, N. Shoumura and N. Takeuchi, "*Q*-switching of a cw-pumped Nd:YAG laser with an LiF:F_2^- crystal," *Optics Communications* **58**, 409–412 (1986).

[23] Y.-F. Chen, Y.-P. Lan and S.-C. Wang, "Modeling of diode-end-pumped *Q*-switched solid-state lasers: influence of energy-transfer upconversion," *Journal of the Optical Society of America B* **19**, 1558–1563 (2002).

[24] M. Pollnau, P. J. Hardman, M. A. Kern, W. A. Clarkson and D. C. Hanna, "Upconversion-induced heat generation and thermal lensing in Nd:YLF and Nd:YAG," *Physical Review B* **58**, 16076–16092 (1998).

[25] Y. Guyot, H. Manaa, J. Y. Rivoire, R. Moncorgé, N. Garnier, E. Descroix, M. Bon and P. Laporte, "Excited-state-absorption and upconversion studies of Nd^{3+}-doped single crystals $Y_3Al_5O_{12}$, $YLiF_4$, and $LaMgAl_{11}O_{19}$," *Physical Review B* **51**, 784–799 (1995).

[26] D. P. Devor, L. G. DeShazer and R. C. Pastor, "Nd:YAG quantum efficiency and related radiative properties," *IEEE Journal of Quantum Electronics* **25**, 1863–1873 (1989).

[27] M. P. MacDonald, T. Graf, J. E. Balmer and H. P. Weber, "Reducing thermal lensing in diode-pumped laser rods," *Optics Communications* **178**, 383–393 (2000).

[28] J. K. Jabczyński, "Modeling of diode pumped laser with pump dependent diffraction loss," *Optics Communications* **182**, 413–422 (2000).

[29] J. K. Jabczyński, K. Kopczyński and A. Szczęśniak, "Thermal lensing and thermal aberration investigations in diode-pumped lasers," *Optical Engineering* **35**, 3572–3578 (1996).

[30] T. Y. Fan, "Heat generation in Nd:YAG and Yb:YAG," *IEEE Journal of Quantum Electronics* **29**, 1457–1459 (1993).

[31] J. Frauchiger, P. Albers and H. P. Weber, "Modeling of thermal lensing and higher order ring mode oscillation in end-pumped cw Nd:YAG lasers," *IEEE Journal of Quantum Electronics* **28**, 1046–1056 (1992).

[32] A. K. Cousins, "Temperature and thermal stress scaling in finite-length end-pumped laser rods," *IEEE Journal of Quantum Electronics* **28**, 1057–1069 (1992).

[33] R. Wynne, J. L. Daneu and T. Y. Fan, "Thermal coefficients of the expansion and refractive index in YAG," *Applied Optics* **38**, 3282–3284 (1999).

[34] A. L. Harmer, A. Linz and D. R. Gabbe, "Fluorescence of Nd^{3+} in lithium yttrium fluoride," *Journal of Physics and Chemistry of Solids* **30**, 1483–1491 (1969).

[35] T. M. Pollak, W. F. Wing, R. J. Grasso, E. P. Chicklis and H. P. Jenssen, "CW laser operation of Nd:YLF," *IEEE Journal of Quantum Electronics* **18**, 159–162 (1982).

[36] J. E. Murray, "Pulsed gain and thermal lensing of Nd:$LiYF_4$," *IEEE Journal of Quantum Electronics* **19**, 488–491 (1983).

[37] W. A. Clarkson, P. J. Hardman and D. C. Hanna, "High-power diode-bar end-pumped Nd:YLF laser at 1.053 μm," *Optics Letters* **23**, 1363–1365 (1998).

[38] R. A. Fields, M. Birnbaum and C. L. Fincher, "Highly efficient Nd:YVO_4 diode-laser end-pumped laser," *Applied Physics Letters* **51**, 1885–1886 (1987).

[39] A. Sennaroglu, "Experimental determination of fractional thermal loading in an operating diode-pumped Nd:YVO_4 minilaser at 1064 nm," *Applied Optics* **38**, 3253–3257 (1999).

[40] Y. F. Chen, L. J. Lee, T. M. Huang and C. L. Wang, "Study of high-power diode-end-pumped Nd:YVO_4 laser at 1.34 μm: influence of Auger upconversion," *Optics Communications* **163**, 198–202 (1999).

[41] A. Sennaroglu, "Influence of neodymium concentration on the strength of thermal effects in continuous-wave diode-pumped Nd:YVO_4 lasers at 1064 nm," *Optical and Quantum Electronics* **32**, 1307–1317 (2000).

[42] K. Du, D. Li, H. Zhang, P. Shi, X. Wei and R. Diart, "Electro-optically Q-switched Nd:YVO_4 slab laser with high repetition rate and a short pulse width," *Optics Letters* **28**, 87–89 (2003).

[43] M. D. Skeldon, R. B. Saager and W. Seka, "Quantitative pump-induced wavefront distortions in laser-diode- and flashlamp-pumped Nd:YLF laser rods," *IEEE Journal of Quantum Electronics* **35**, 381–386 (1999).

[44] F. J. Duarte (ed.), "Tunable Lasers Handbook," Academic Press, New York (1995).

[45] M. D. Rahn and T. A. King, "Comparison of laser performance of dye molecules in sol-gel, polycom, ormosil, and poly(methyl methacrylate) host media," *Applied Optics* **34**, 8260–8271 (1995).

[46] O. Svelto, "Principles of Lasers" (4th ed), translated by D.C. Hanna, Plenum Press, New York (1998).

[47] P. A. Franken, A. E. Hill, C. W. Peters and G. Weinreich, "Generation of optical harmonics," *Physics Review Letters* **7**, 118–119 (1961).

[48] Y. X. Fan, R. C. Eckardt, R. L. Byer, C. Chen and A. D. Jiang, "Beta-phase barium borate optical parametric oscillator," *Conference on Lasers and Electro-Optics* Technical Digest (Optical Society of America, Washington, DC) , paper ThU4 (1986).

[49] Y. X. Fan, R. C. Eckardt, R. L. Byer, J. Nolting and R. Wallenstein, "Visible BaB_2O_4 optical parametric oscillator pumped at 355 nm by a single-axial-mode pulsed source," *Applied Physics Letters* **53**, 2014–2016 (1988).

[50] L. K. Cheng, W. R. Bosenberg and C. L. Tang, "Broadly tunable optical parametric oscillation in β-BaB_2O_4," *Applied Physics Letters* **53**, 175–177 (1988).

[51] B. T. Mathias and J. P. Reimeika, *Physics Review* **76**, 1886 (1949).

[52] G. D. Boyd, R. C. Miller, K. Nassau, W. L. Bond and A. Savage, *Applied Physics Letters* **5**, 234 (1964).

[53] R. L. Byer, R. L. Herbst, R. S. Feigelson and W. L. Kway, "Growth and application of [01·4] $LiNbO_3$," *Optics Communications* **12**, 427–429 (1974).

[54] F. C. Zumsteg, J. D. Bierlein and T. E. Gier, "$K_xRb_{1-x}TiOPO_4$: a new nonlinear optical material," *Journal of Applied Physics* **47**, 4980–4985 (1976).

[55] C. Chen, Y. Wu, A. Jiang, B. Wu, G. You, R. Li and S. Lin, "New nonlinear-optical crystal: LiB_3O_5," *Journal of the Optical Society of America B* **6**, 616–621 (1989).

[56] L. E. Myers, R. C. Eckardt, M. M. Fejer, R. L. Byer, W. R. Bosenberg and J. W. Pierce, "Quasi-phase-matched optical parametric oscillators in bulk periodically poled $LiNbO_3$," *Journal of the Optical Society of America B* **12**, 2102–2116 (1995).

[57] J. A. Armstrong, N. Bloembergen, J. Ducuino and P. S. Pershan, "Interactions between light waves in a nonlinear dielectric," *Physics Review* **127**, 1918–1939 (1962).

[58] O. Levi, T. J. Pinguet, T. Skauli, L. A. Eyres, K. R. Parameswaran, J. S. Harris Jr, M. M. Fejer, T. J. Kulp, S. E. Bisson, B. Gerard, E. Lallier and L. Becouarn, "Difference frequency generation of 8-μm radiation in orientation-patterned GaAs," *Optics Letters* **27**, 2091–2093 (2002).

[59] M. M. Fejer, G. A. Magel, D. H. Jundt and R. L. Byer, "Quasi-phasematched second harmonic generation: tuning and tolerances," *IEEE Journal of Quantum Electronics* **28**, 2631–2654 (1992).

[60] M. Yamada, N. Nada, M. Saitoh and K. Watanabe, "First-order quasi-phase matched $LiNbO_3$ waveguide periodically poled by applying an external field for efficient blue second-harmonic generation," *Applied Physics Letters* **62**, 435–436 (1993).

[61] L. E. Myers and W. R. Bosenberg, "Periodically poled lithium niobate and quasi-phase-matched optical parametric oscillators," *IEEE Journal of Quantum Electronics* **33**, 1663–1672 (1997).

[62] S. N. Zhu, Y. Y. Zhu, Z. Y. Zhang, H. Shu, H. F. Wang, J. F. Hong, C. Z. Ge and N. B. Ming, "$LiTaO_3$ crystal periodically poled by applying an external pulsed field," *Journal of Applied Physics* **77**, 5481–5483 (1995).

[63] J.-P. Meyn and M. M. Feyer, "Tunable ultraviolet radiation by second-harmonic generation in periodically poled lithium tantalate," *Optics Letters* **22**, 1214–1216 (1997).

[64] T. Hatanaka, K. Nakamura, T. Taniuchi, H. Ito, Y. Furukawa and K. Kitamura, "Quasi-phase-matched optical parametric oscillation with periodically poled stoichiometric $LiTaO_3$," *Optics Letters* **25**, 651–653 (2000).

[65] T. Südmeyer, J. Aus der Au, R. Paschotta, U. Keller, P. G. R. Smith, G. W. Ross and D. C. Hanna, "Femtosecond fiber-feedback optical parametric oscillator," *Optics Letters* **26**, 304–309 (2001).

[66] J.-P. Meyn, M. E. Klein, D. Woll, R. Wallenstein and D. Rytz, "Periodically poled potassium niobate for second-harmonic generation at 463 nm ," *Optics Letters* **24**, 1154–1156 (1999).

[67] Q. Chen and W. P. Risk, "Periodic poling of $KTiOPO_4$ using an applied electric field," *Electronics Letters* **30**, 1516–1517 (1994).

[68] Q. Chen and W. P. Risk, "High efficiency quasi-phasematched frequency doubling waveguides in $KTiOPO_4$ fabricated by electric field poling," *Electronics Letters* **32**, 107–108 (1996).

[69] G. Rosenman, A. Skliar, M. Oron and M. Katz, "Polarization reversal in $KTiOPO_4$ crystals," *Journal of Physics D: Applied Physics* **30**, 277–282 (1997).

[70] H. Karlsson and F. Laurell, "Electric field poling of flux grown $KTiOPO_4$," *Applied Physics Letters* **71**, 3474–3476 (1997).

[71] W. P. Risk and G. M. Loiacono, "Periodic poling and waveguide frequency doubling in $RbTiOAsO_4$," *Applied Physics Letters* **69**, 311–313 (1996).

[72] H. Karlsson, F. Laurell and L. K. Cheng, "Periodic poling of $RbTiOPO_4$ for quasi-phase matched blue light generation," *Applied Physics Letters* **74**, 1519–1521 (1999).

[73] G. Rosenman, A. Skliar, Y. Findling, P. Urenski, A. Englander, P. A. Thomas and Z. W. Hu, "Periodically poled $KTiOAsO_4$ crystals for optical parametric oscillation," *Journal of Physics D: Applied Physics* **32**, L49–L52 (1999).

[74] M. Yamada and K. Kishima, "Fabrication of periodically reversed domain structure for SHG in $LiNbO_3$ by direct electron beam lithography at room temperature," *Electronics Letters* **27**, 828–829 (1991).

[75] Y. Ishigame, T. Suhara and H. Nishihara, "$LiNbO_3$ waveguide second-harmonic-generation device phase matched with a fan-out domain-inverted grating," *Optics Letters* **16**, 375–377 (1991).

[76] M. L. Bortz, M. Fujimura and M. M. Fejer, "Increased acceptance bandwidth for quasi-phasematched second harmonic generation in $LiNbO_3$ waveguides," *Electronics Letters* **30**, 34–35 (1994).

[77] V. Pruneri, J. Webjörn, P. St. J. Russell and D. C. Hanna, "532 nm pumped optical parametric oscillator in bulk periodically poled lithium niobate," *Applied Physics Letters* **67**, 2126–2128 (1995).

[78] S. J. Brosnan and R. L. Byer, "Optical parametric oscillator threshold and linewidth studies," *IEEE Journal of Quantum Electronics* **QE-15**, 415–431 (1979).

[79] Y. Tang, C. F. Rae, C. Rahlff and M. H. Dunn, "Low-threshold, high-efficiency, widely tunable infrared source from a KTP-based optical parametric oscillator," *Journal of the Optical Society of America B* **14**, 3442–3451 (1997).

[80] L. E. Myers, R. C. Eckardt, M. M. Fejer, R. L. Byer and W. R. Bosenberg, "Multigrating quasi-phase-matched optical parametric oscillator in periodically-poled $LiNbO_3$," *Optics Letters* **21**, 591–593 (1996).

[81] D. H. Jundt, "Temperature-dependent Sellmeier equation for the index of refraction, n_e, in congruent lithium niobate," *Optics Letters* **22**, 1553–1555 (1997).

[82] V. Pruneri, S. D. Butterworth and D. C. Hanna, "Low-threshold picosecond optical parametric oscillator in quasi-phase-matched lithium niobate," *Applied Physics Letters* **69**, 1029–1031 (1996).

[83] S. D. Butterworth, P. G. R. Smith and D. C. Hanna, "Picosecond Ti:sapphire-pumped optical parametric oscillator based on periodically poled $LiNbO_3$," *Optics Letters* **22**, 618–620 (1997).

[84] K. C. Burr, C. L. Tang, M. A. Arbore and M. M. Fejer, "Broadly tunable mid-infrared femtosecond optical parametric oscillator using all-solid-state pumped periodically poled lithium niobate," *Optics Letters* **22**, 1458–1460 (1997).

[85] K. C. Burr, C. L. Tang, M. A. Arbore and M. M. Fejer, "High-repetition-rate femtosecond optical parametric oscillator based on periodically poled lithium niobate," *Applied Physics Letters* **70**, 3341–3343 (1997).

[86] C. McGowan, D. T. Reid, Z. E. Penman, M. Ebrahimzadeh, W. Sibbett and D. H. Jundt, "Femtosecond optical parametric oscillator based on periodically poled lithium niobate," *Journal of the Optical Society of America B* **15**, 694–701 (1998).

[87] L. Lefort, K. Puech, S. D. Butterworth, G. W. Ross, P. G. R. Smith, D. C. Hanna and D. H. Jundt, "Efficient, low-threshold synchronously-pumped parametric oscillation in periodically-poled lithium niobate over the 1.3 μm to 5.3 μm range," *Optics Communications* **152**, 55–58 (1998).

[88] T. Graf, G. McConnel, A. I. Ferguson, E. Bente, D. Burns and M. D. Dawson, "Synchronously pumped optical parametric oscillation in periodically poled lithium niobate with 1-W average output power," *Applied Optics* **38**, 3324–3328 (1999).

[89] A. Robertson, M. E. Klein, M. A. Tremont, K.-J. Boller and R. Wallenstein, "2.5-GHz repetition-rate singly resonant optical parametric oscillator synchronously pumped by a mode-locked diode oscillator amplifier system," *Optics Letters* **25**, 657–659 (2000).

[90] M. J. Missey, V. Dominic, L. E. Myers and R. C. Eckardt, "Diffusion-bonded stacks of periodically poled lithium niobate," *Optics Letters* **23**, 664–666 (1998).

[91] M. Missey, V. Dominic, P. Powers and K. L. Schepler, "Aperture scaling effects with monolithic periodically poled lithium niobate optical parametric oscillators and generators," *Optics Letters* **25**, 248–250 (2000).

[92] A. Agnesi, E. Piccinini, G. C. Reali and C. Solcia, "All-solid-state picosecond tunable source of near-infrared radiation," *Optics Letters* **22**, 1415–1417 (1997).

[93] K. W. Aniolek, P. E. Powers, T. J. Kulp, B. A. Richman and S. E. Bisson, "Cavity ringdown laser absorption spectroscopy with a 1 kHz mid-infrared periodically poled lithium niobate optical parametric generator / optical parametric amplifier," *Chemical Physics Letters* **302**, 555–562 (1999).

[94] G. Breitenbach, S. Schiller and J. Mlynek, "81% Conversion efficiency in frequency-stable continuous-wave parametric oscillation," *Journal of the Optical Society of America B* **12**, 2095–2101 (1995).

[95] R. S. Conroy, C. F. Rae, G. J. Friel, M. H. Dunn, B. D. Sinclair and J. M. Ley, "Compact low-threshold *Q*-switched intracavity optical parametric oscillator," *Optics Letters* **23**, 1348–1350 (1998).

[96] U. Bäder, J.-P. Meyn, J. Bartschke, T. Weber, A. Borsutzky, R. Wallenstein, R. G. Batchko, M. M. Fejer and R. L. Byer, "Nanosecond periodically poled lithium niobate optical parametric generator pumped at 532 nm by a single-frequency passively *Q*-switched Nd:YAG laser," *Optics Letters* **24**, 1608–1610 (1999).

[97] R. S. Conroy, C. F. Rae, M. H. Dunn, B. D. Sinclair and J. M. Ley, "Compact, actively *Q*-switched optical parametric oscillator," *Optics Letters* **24**, 1614–1616 (1999).

[98] M. J. Missey, V. Dominic, P. E. Powers and K. L. Schepler, "Periodically poled lithium niobate monolithic nanosecond optical parametric oscillators and generators," *Optics Letters* **24**, 1227–1229 (1999).

[99] M. Taya, M. C. Bashaw and M. M. Fejer, "Photorefractive effects in periodically poled ferroelectrics," *Optics Letters* **21**, 857–859 (1996).

[100] B. Sturman, M. Aguilar, F. Agulló-López, V. Pruneri and P. G. Kazansky, "Photorefractive nonlinearity of periodically poled ferroelectrics," *Journal of the Optical Society of America B* **14**, 2641–2649 (1997).

[101] V. Pruneri, S. D. Butterworth and D. C. Hanna, "Highly efficient green-light generation by quasi-phase-matched frequency doubling of picosecond pulses from an amplified mode-locked Nd:YLF laser," *Optics Letters* **21**, 390–392 (1996).

[102] M. Oron, M. Katz, D. Eger, G. Rosenman and A. Skliar, "Highly efficient blue light generation in flux grown $KTiOPO_4$ periodically poled by an electric field," *Electronics Letters* **33**, 807–809 (1997).

[103] A. Englander, R. Lavi, M. Katz, M. Oron, D. Eger, E. Lebiush, G. Rosenman and A. Skliar, "Highly efficient doubling of a high-repetition-rate diode-pumped laser with bulk periodically poled KTP," *Optics Letters* **22**, 1598–1599 (1997).

[104] A. Arie, G. Rosenman, V. Mahal, A. Skliar, M. Oron, M. Katz and D. Eger, "Green and ultraviolet quasi-phase-matched second harmonic generation in bulk periodically-poled $KTiOPO_4$," *Optics Communications* **142**, 265–268 (1997).

[105] S. Wang, V. Pasiskevicius, F. Laurell and H. Karlsson, "Ultraviolet generation by first-order frequency doubling in periodically poled $KTiOPO_4$," *Optics Letters* **23**, 1883–1885 (1998).

[106] A. Arie, G. Rosenman, A. Korenfeld, A. Skliar, M. Oron, M. Katz and D. Eger, "Efficient resonant frequency doubling of a cw Nd:YAG laser in bulk periodically poled $KTiOPO_4$," *Optics Letters* **23**, 28–30 (1998).

[107] V. Pasiskevicius, S. Wang, J. A. Tellefsen, F. Laurell and H. Karlsson, "Efficient Nd:YAG laser frequency doubling with periodically poled KTP," *Applied Optics* **37**, 7116–7119 (1998).

[108] T. Kartaloğlu, K. G. Köprülü, O. Aytür, M. Sundheimer and W. P. Risk, "Femtosecond optical parametric oscillator based on periodically poled $KTiOPO_4$," *Optics Letters* **23**, 61–63 (1998).

[109] G. M. Gibson, M. Ebrahimzadeh, M. J. Padgett and M. H. Dunn, "Continuous-wave optical parametric oscillator based on periodically poled $KTiOPO_4$ and its application to spectroscopy," *Optics Letters* **24**, 397–399 (1999).

[110] D. Woll, J. Schumacher, A. Robertson, M. A. Tremont, R. Wallenstein, M. Katz, D. Eger and A. Englander, "250 mW of coherent blue 460-nm light generated by single-pass frequency doubling of the output of a mode-locked high-power diode laser in periodically poled KTP," *Optics Letters* **27**, 1055–1057 (2002).

[111] G. M. Gibson, G. A. Turnbull, M. Ebrahimzadeh, M. H. Dunn, H. Karlsson, G. Arvidsson and F. Laurell, "Temperature-tuned difference-frequency mixing in periodically poled $KTiOPO_4$," *Applied Physics B* **67**, 675–677 (1998).

[112] K. Fradkin, A. Arie, A. Skliar and G. Rosenman, "Tunable midinfrared source by difference frequency generation in bulk periodically poled $KTiOPO_4$," *Applied Physics Letters* **74**, 914–916 (1999).

[113] K. Fradkin, A. Arie, A. Skliar and G. Rosenman, "Erratum: Tunable midinfrared source by difference frequency generation in bulk periodically poled $KTiOPO_4$ [Appl. Phys. Lett. 74, 914 (1999)]," *Applied Physics Letters* **74**, 2723 (1999).

[114] A. Garashi, A. Arie, A. Skliar and G. Rosenman, "Continuous-wave optical parametric oscillator based on periodically poled $KTiOPO_4$," *Optics Letters* **23**, 1739–1741 (1998).

[115] M. Ebrahimzadeh, G. A. Turnbull, T. J. Edwards, D. J. M. Stothard, I. D. Lindsay and M. H. Dunn, "Intracavity continuous-wave singly resonant optical parametric oscillators," *Journal of the Optical Society of America B* **16**, 1499–1511 (1999).

[116] T. J. Edwards, G. A. Turnbull, M. H. Dunn and M. Ebrahimzadeh, "Continuous-wave, singly-resonant, optical parametric oscillator based on periodically poled $KTiOPO_4$," *Optics Express* **6**, 58–63 (2000).

[117] J. Hellström, V. Pasiskevicius, F. Laurell and H. Karlsson, "Efficient nanosecond optical parametric oscillators based on periodically poled KTP emitting in the 1.8–2.5-μm spectral region," *Optics Letters* **24**, 1233–1235 (1999).

[118] J. Hellström, V. Pasiskevicius, H. Karlsson and F. Laurell, "High-power optical parametric oscillation in large-aperture periodically poled $KTiOPO_4$," *Optics Letters* **25**, 174–176 (2000).

[119] H. Karlsson, F. Laurell, P. Henriksson and G. Arvidsson, "Frequency doubling in periodically poled $RbTiOAsO_4$," *Electronics Letters* **32**, 556–557 (1996).

[120] Z. W. Hu, P. A. Thomas, J. Webjörn and G. M. Loiacono, "Domain inversion in $RbTiOAsO_4$ using electric field poling," *Journal of Physics D: Applied Physics* **29**, 1681–1684 (1996).

[121] D. T. Reid, Z. Penman, M. Ebrahimzadeh, W. Sibbett, H. Karlsson and F. Laurell, "Broadly tunable infrared femtosecond optical parametric oscillator based on periodically poled $RbTiOAsO_4$," *Optics Letters* **22**, 1397–1399 (1997).

[122] T. J. Edwards, G. A. Turnbull, M. H. Dunn, M. Ebrahimzadeh, H. Karlsson, G. Arvidsson and F. Laurell, "Continuous-wave singly resonant optical parametric oscillator based on periodically poled $RbTiOAsO_4$," *Optics Letters* **23**, 837–839 (1998).

[123] D. J. M. Stothard, M. Ebrahimzadeh and M. H. Dunn, "Low-pump-threshold continuous-wave singly resonant optical parametric oscillator," *Optics Letters* **23**, 1895–1897 (1998).

[124] H. Karlsson, M. Olson, G. Arvidsson, F. Laurell, U. Bäder, A. Borsutzky, R. Wallenstein, S. Wickström and M. Gustafsson, "Nanosecond optical parametric oscillator based on large-aperture periodically poled $RbTiOAsO_4$," *Optics Letters* **24**, 330–332 (1999).

[125] G. T. Kennedy, D. T. Reid, A. Miller, M. Ebrahimzadeh, H. Karlsson, G. Arvidsson and F. Laurell, "Near- to mid-infrared picosecond optical parametric oscillator based on periodically poled $RbTiOAsO_4$," *Optics Letters* **23**, 503–505 (1998).

[126] P. Loza-Alvarez, D. T. Reid, M. Ebrahimzadeh, W. Sibbett, H. Karlsson, P. Henriksson, G. Arvidsson and F. Laurell, "Periodically poled $RbTiOAsO_4$ femtosecond optical parametric oscillator tunable from 1.38 to 1.58 μm," *Applied Physics B* **68**, 177–180 (1999).

[127] M. Peltz, U. Bäder, A. Borsutzky, R. Wallenstein, J. Hellström, H. Karlsson, V. Pasiskevicius and F. Laurell, "Optical parametric oscillators for high pulse energy and high average power operation based on large aperture periodically poled KTP and RTA," *Applied Physics B* **73**, 663–670 (2001).

[128] W. R. Bosenberg, A. Drobshoff, J. I. Alexander, L. E. Myers and R. L. Byer, "93% pump depletion, 3.5-W continuous-wave, singly resonant optical parametric oscillator," *Optics Letters* **21**, 1336–1338 (1996).

[129] M. E. Klein, D.-H. Lee, J.-P. Meyn, K.-J. Boller and R. Wallenstein, "Singly resonant continuous-wave optical parametric oscillator pumped by a diode laser," *Optics Letters* **24**, 1142–1144 (1999).

[130] M. E. Klein, C. K. Laue, D.-H. Lee, K.-J. Boller and R. Wallenstein, "Diode-pumped singly resonant continuous-wave optical parametric oscillator with wide continuous tuning of the near-infrared idler wave," *Optics Letters* **25**, 490–493 (2000).

[131] S. E. Bisson, K. M. Armstrong, T. J. Kulp and M. Hartings, "Broadly tunable, mode-hop-tuned cw optical parametric oscillator based on periodically poled lithium niobate," *Applied Optics* **40**, 6049–6055 (2001).

[132] U. Strößner, J.-P. Meyn, R. Wallenstein, P. Urenski, A. Arie, G. Rosenman, J. Mlynek, S. Schiller and A. Peters, "Single-frequency continuous-wave optical parametric oscillator system with an ultrawide tuning range of 550 to 2830 nm," *Journal of the Optical Society of America B* **19**, 1419–1424 (2002).

[133] J. Falk, "Instabilities in the doubly resonant parametric oscillator: A theoretical analysis," *IEEE Journal of Quantum Electronics* **QE-7**, 230–235 (1971).

[134] R. C. Eckardt, C. D. Nabors, W. J. Kozlovsky and R. L. Byer, "Optical parametric oscillator frequency tuning and control," *Journal of the Optical Society of America B* **8**, 646–667 (1991).

[135] A. J. Henderson, M. J. Padgett, F. G. Colville, J. Zhang and M. H. Dunn, "Doubly-resonant optical parametric oscillators: tuning behaviour and stability requirements," *Optics Communications* **119**, 256–264 (1995).

[136] R. Al-Tahtamouni, K. Bencheikh, R. Storz, K. Schneider, M. Lang, J. Mlynek and S. Schiller, "Long-term stable operation and absolute frequency stabilization of a doubly resonant parametric oscillator," *Applied Physics B* **66**, 733–739 (1998).

[137] M. Scheidt, B. Beier, K.-J. Boller and R. Wallenstein, "Frequency-stable operation of a diode-pumped continuous wave $RbTiOAsO_4$ optical parametric oscillator," *Optics Letters* **22**, 1287–1289 (1997).

[138] I. D. Lindsay, G. A. Turnbull, M. H. Dunn and M. Ebrahimzadeh, "Doubly resonant continuous-wave optical parametric oscillator pumped by a single-mode diode laser," *Optics Letters* **23**, 1889–1891 (1998).

[139] A. J. Henderson, P. M. Roper, L. A. Borschowa and R. D. Mead, "Stable, continuously tunable operation of a diode-pumped doubly resonant optical parametric oscillator," *Optics Letters* **25**, 1264–1266 (2000).

[140] B. Scherrer, I. Ribet, A. Godard, E. Rosencher and M. Lefebvre, "Dual-cavity doubly resonant optical parametric oscillators: demonstration of pulsed single-mode operation," *Journal of the Optical Society of America B* **17**, 1716–1729 (2000).

[141] K. Schneider, P. Kramper, S. Schiller and J. Mlynek, "Toward an optical synthesizer: a single-frequency parametric oscillator using periodically poled $LiNbO_3$," *Optics Letters* **22**, 1293–1295 (1997).

[142] M. Scheidt, M. E. Klein and K.-J. Boller, "Spiking in pump enhanced idler resonant optical parametric oscillators," *Optics Communications* **149**, 108–112 (1998).

[143] D. Chen, D. Hinkley, J. Pyo, J. Swenson and R. Fields, "Single-frequency low-threshold continuous-wave 3-μm periodically poled lithium niobate optical parametric oscillator," *Journal of the Optical Society of America B* **15**, 1693–1697 (1998).

[144] S. Schiller, K. Schneider and J. Mlynek, "Theory of an optical parametric oscillator with resonant pump and signal," *Journal of the Optical Society of America B* **16**, 1512–1524 (1999).

[145] D. C. Edelstein, E. S. Wachman and C. L. Tang, "Broadly tunable high repetition rate femtosecond optical parametric oscillator," *Applied Physics Letters* **54**, 1728–1730 (1989).

[146] A. Kaz and L. R. Marshall, "Continuous wave diode-pumped lasers and parametric oscillators," *Conference on Lasers and Electro-Optics* Technical Digest (Optical Society of America, Washington, DC) **11**, 244–245 (1993).

[147] T. Debuisschert, J. Raffy, J.-P. Pocholle and M. Papuchon, "Intracavity optical parametric oscillator: study of the dynamics in pulsed regime," *Journal of the Optical Society of America B* **13**, 1569–1587 (1996).

[148] F. G. Colville, M. H. Dunn and M. Ebrahimzadeh, "Continuous-wave, singly resonant, intracavity parametric oscillator," *Optics Letters* **22**, 75–77 (1997).

[149] G. A. Turnbull, T. J. Edwards, M. H. Dunn and M. Ebrahimzadeh, "Continuous-wave singly-resonant intracavity parametric oscillator based on periodically-poled $LiNbO_3$," *Electronics Letters* **33**, 1817–1818 (1997).

[150] T. J. Edwards, G. A. Turnbull, M. H. Dunn and M. Ebrahimzadeh, "High-power, continuous-wave, singly resonant, intracavity optical paremetric oscillator," *Applied Physics Letters* **72**, 1527–1529 (1998).

[151] M. K. Oshman and S. E. Harris, "Theory of optical parametric oscillation internal to the laser cavity," *IEEE Journal of Quantum Electronics* **QE-4**, 491–502 (1968).

[152] T.-B. Chu and M. Boyer, "Intracavity single resonance optical parametric oscillator," *Journal de Physique* **45**, 1599 (1984).

[153] G. A. Turnbull, M. H. Dunn and M. Ebradimzadeh, "Continuous-wave, inctracavity optical parametric oscillators: an analysis of power characteristics," *Applied Physics B* **66**, 701–710 (1998).

[154] G. A. Turnbull, D. J. M. Stothard, M. Ebrahimzadeh and M. H. Dunn, "Transient dynamics of cw intracavity singly resonant optical parametric oscillators," *IEEE Journal of Quantum Electronics* **35**, 1666–1672 (1999).

[155] D. J. M. Stothard, P.-Y. Fortin, M. Ebrahimzadeh and M. H. Dunn, "Comparison of periodically-poled $LiNbO_3$ and $RbTiOAsO_4$ as nonlinear media in continuous-wave optical parametric oscillators pumped internal to an all-solid-state Nd:vanadate laser," *Conference on Lasers and Electro-Optics* Technical Digest (Optical Society of America, Washington, DC) , 536–537 (2001).

[156] A. Carleton, D. J. M. Stothard, M. Ebrahimzadeh and M. H. Dunn, "Continuous-wave singly resonant optical parametric oscillator based on periodically-poled $RbTiOAsO_4$," *Conference on Lasers and Electro-Optics* Technical Digest (Optical Society of America, Washington, DC) , 421–422 (2002).

[157] J. G. Haub, R. M. Hentschel, M. J. Johnson and B. J. Orr, "Controlling the performance of a pulsed optical parametric oscillator: a survey of techniques and spectroscopic applications," *Journal of the Optical Society of America B* **12**, 2128–2141 (1995).

[158] G. W. Baxter, M. A. Payne, B. D. W. Austin, C. A. Halloway, J. G. Haub, Y. He, A. P. Milce, J. F. Nibler and B. J. Orr, "Spectroscopic diagnostics of chemical processes: applications of tunable optical parametric oscillators," *Applied Physics B* **71**, 651–663 (2000).

[159] K. Schneider, S. Schiller, J. Mlynek, F. Kühnemann, A. Hecker, A. E. E. Martis and W. Urban, "Photoacoustic trace gas detection using a broadly-tunabel single-frequency cw parametric oscillator," *OSA Trends in Optics and Photonics, Advanced Solid State Lasers* (Optical Society of America, Washington, DC) **19**, 259–261 (1998).

[160] G. W. Baxter, Y. He and B. J. Orr, "A pulsed optical parametric oscillator, based on periodically poled lithium niobate (PPLN), for high-resolution spectroscopy," *Applied Physics B* **67**, 753–756 (1998).

[161] C.-S. Yu and A. H. Kung, "Grazing-incidence periodically poled $LiNbO_3$ optical parametric oscillator," *Journal of the Optical Society of America B* **16**, 2233–2238 (1999).

[162] B. A. Richman, K. W. Aniolek, T. J. Kulp and S. E. Bisson, "Continuously tunable, single-longitudinal-mode, pulsed mid-infrared optical parametric oscillator based on periodically poled lithium niobate," *Journal of the Optical Society of America B* **17**, 1233–1239 (2000).

[163] P. E. Powers, T. J. Kulp and S. E. Bisson, "Continuous tuning of a continuous-wave periodically poled lithium niobate optical parametric oscillator by use of a fan-out grating design," *Optics Letters* **23**, 159–161 (1998).

[164] M. J. T. Milton, T. D. Gardiner, F. Molero and J. Galech, "Injection-seeded optical parametric oscillator for range-resolved DIAL measurements of atmospheric methane," *Optics Communications* **142**, 153–160 (1997).

[165] G. Ehret, A. Fix, V. Weiß, G. Poberaj and T. Baumert, "Diode-laser-seeded optical parametric oscillator for airborne water vapor DIAL application in the upper troposphere and lower stratosphere," *Applied Physics B* **67**, 427–431 (1998).

[166] G. W. Baxter, "Injection-seeded optical parametric oscillators for spectroscopy," *Macquarie University*, Sydney, Australia, PhD Thesis, (1998).

[167] J. E. Bjorkholm and H. G. Danielmeyer, "Frequency control of a pulsed optical parametric oscillator by radiation injection," *Applied Physics Letters* **15**, 171–173 (1969).

[168] Y. He, G. W. Baxter and B. J. Orr, "Locking the cavity of a pulsed periodically poled lithium niobate optical parametric oscillator to the wavelength of a continuous-wave injection seeder by an "intensity-dip" method," *Review of Scientific Instruments* **70**, 3203–3213 (1999).

[169] L. B. Kreuzer, "Single mode oscillation of a pulsed singly resonant optical parametric oscillator," *Applied Physics Letters* **15**, 263–265 (1969).

[170] J. F. Young, R. B. Miles, S. E. Harris and R. W. Wallace, "Pump linewidth requirement for optical parametric oscillators," *Journal of Applied Physics* **42**, 497–498 (1971).

[171] X. Long, G. A. Pasmanik, D. G. Peterson, A. A. Shilov and I. Yakovlev, "Tunable narrow bandwidth high energy IR OPO/OPA," *OSA Trends in Optics and Photonics, Advanced Solid State Lasers* (Optical Society of America, Washington, DC) **19**, 265–268 (1998).

[172] G. Robertson, A. Henderson and M. H. Dunn, "Efficient, single-axial mode oscillation of a beta barium borate optical parametric oscillator pumped by an excimer laser," *Applied Physics Letters* **62**, 123–125 (1993).

[173] W. R. Leeb, "Losses introduced by tilting intracavity etalons," *Applied Physics* **6**, 267–272 (1975).

[174] H. Daussy, R. Dumanchin and O. de Witte, "Fabry–Perot with short pulse lasers: spectral selection and spectral analysis in dye lasers," *Applied Optics* **17**, 451–458 (1978).

[175] I. Shoshan, N. N. Danon and U. P. Oppenheim, "Narrowband operation of a pulsed dye laser without intracavity beam expansion," *Journal of Applied Physics* **48**, 4495–4497 (1977).

[176] M. G. Littman and H. J. Metcalf, "Spectrally narrow pulsed dye laser without beam expander," *Applied Optics* **17**, 2224–2227 (1978).

[177] M. G. Littman, "Single-mode pulsed tunable dye laser," *Applied Optics* **23**, 4465–4468 (1984).

[178] P. McNicholl and H. J. Metcalf, "Synchronous cavity mode and feedback wavelength scanning in dye laser oscillators with gratings," *Applied Optics* **24**, 2757–2761 (1985).

[179] K. W. Kangas, D. D. Lowenthal and C. H. Muller III, "Single-longitudinal-mode, tunable, pulsed Ti:sapphire laser oscillator," *Optics Letters* **14**, 21–23 (1989).

[180] W. R. Bosenberg and D. R. Guyer, "Single-frequency optical parametric oscillator," *Applied Physics Letters* **61**, 387–389 (1992).

[181] L. A. W. Gloster, I. T. McKinine, Z. X. Jiang, T. A. King, J. M. Boon-Engering, W. E. van der Veer and W. Hogervorst, "Narrow-band β-BaB_2O_4 optical parametric oscillator in a grazing-incidence configuration," *Journal of the Optical Society of America B* **12**, 2117–2121 (1995).

[182] J. M. Boon-Engering, L. A. W. Gloster, W. E. van der Veer, I. T. McKinnie, T. A. King and W. Hogervorst, "Highly efficient single-longitdinal mode β-BaB_2O_4 optical parametric oscillator with a new cavity design," *Optics Letters* **20**, 2087–2089 (1995).

[183] W. R. Bosenberg and D. R. Guyer, "Broadly tunable, single-frequency optical parametric frequency-conversion system," *Journal of the Optical Society of America B* **10**, 1716–1722 (1993).

[184] J. Mes, M. Leblans and W. Hogervorst, "Single-longitudinal-mode optical parametric oscillator for spectroscopic applications," *Optics Letters* **27**, 1442–1444 (2002).

[185] A. E. Siegman, "Lasers," University Science Books, Mill Valley, CA (1986).

[186] J. T. Verdeyen, "Laser Electronics," Prentice-Hall, New Jersey (1995).

[187] B. A. E. Saleh and M. C. Teich, "Fundamentals of Photonics," John Wiley & Sons, New York (1991).

[188] D. Findlay and R. A. Clay, *Physics Letters* **20**, 277–278 (1966).

[189] B. Luther-Davies, "An electro-optically Q-switched actively mode-locked Nd:YLF laser with feedback stabilised pre-lase," *Optics Communications* **57**, 345–349 (1986).

[190] M. E. Innocenzi, H. T. Yura, C. L. Fincher and R. A. Fields, "Thermal modeling of continuous-wave end-pumped solid-state lasers," *Applied Physics Letters* **56**, 1831–1833 (1990).

[191] C. Pfistner, R. Weber, H. P. Weber, S. Merazzi and R. Gruber, "Thermal beam distortions in end-pumped Nd:YAG, Nd:GSGG, and Nd:YLF rods," *IEEE Journal of Quantum Electronics* **30**, 1605–1615 (1994).

[192] P. J. Hardman, W. A. Clarkson, G. J. Friel, M. Pollnau and D. C. Hanna, "Energy-transfer upconversion and thermal lensing in high-power end-pumped Nd:YLF laser crystals," *IEEE Journal of Quantum Electronics* **35**, 647–655 (1999).

[193] K. W. Aniolek, R. L. Schmitt, T. J. Kulp, B. A. Richman, S. E. Bisson and P. E. Powers, "Microlaser-pumped periodically poled lithium niobate optical parametric generator–optical parametric amplifier," *Optics Letters* **25**, 557–559 (2000).

[194] I. O. Musgrave, W. A. Clarkson and D. C. Hanna, "Detailed study of thermal lensing in Nd:YVO_4 under intense diode end-pumping," *Conference on Lasers and Electro-Optics* Technical Digest (Optical Society of America, Washington, DC) , 171–172 (2001).

[195] A. A. Kaminskii, "Laser Crystals" (2nd ed), *Springer Series in Optical Sciences*, Springer-Verlag, Berlin (1990).

[196] M. Armstrong, X. Zhu, S. Gracewsky and R. J. D. Miller, "Development of a 25 W TEM_{00} diode-pumped Nd:YLF laser," *Optics Communications* **169**, 141–148 (1999).

[197] H. Vanherzeele, "Thermal lensing measurement and compensation in a continuous-wave mode-locked Nd:YLF laser," *Optics Letters* **13**, 369–371 (1988).

[198] P. J. Hardman, W. A. Clarkson and D. C. Hanna, "High-power diode-bar-pumped intracavity-frequency-doubled Nd:YLF ring laser," *Optics Communications* **156**, 49–52 (1998).

[199] H. Kogelnik and T. Li, "Laser beams and resonators," *Applied Optics* **5**, 1550–1567 (1966).

[200] A. E. Siegman, "New developments in laser resonators," *SPIE* **1224**, 2–14 (1990).

[201] M. Schubert and B. Wilhelmi, "Nonlinear Optics and Quantum Electronics," John Wiley & Sons, New York (1986).

[202] F. Zernike and J. E. Midwinter, "Applied Nonlinear Optics," John Wiley & Sons, New York (1973).

[203] J. E. Midwinter and J. Warner, "The effects of phase matching method and of uniaxial crystal symmetry on the polar distribution of second-order non-linear optical polarisation," *British Journal of Applied Physics* **16**, 1135–1142 (1965).

[204] R. W. Boyd, "Nonlinear Optics," Academic Press, San Diego, CA (1992).

[205] D. A. Kleinman, "Nonlinear dielectric polarisation in optical media," *Physics Review* **126**, 1977–1979 (1962).

[206] J. F. Nye, "Physical Properties of Crystals, Their Representation by Tensors and Matrices," Oxford University Press, Oxford (1957).

[207] V. G. Dmitriev, G. G. Gurzadyan and D. N. Nikogosyan, "Handbook of Nonlinear Optical Crystals," Springer-Verlag, Berlin (1991).

[208] E. Hecht, "Optics" (2nd ed), Addison-Wesley Publishing Company, Reading, MA (1987).

[209] R. D. Guenther, "Modern Optics," John Wiley & Sons, New York (1990).

[210] J. M. Manley and H. E. Rowe, "General energy in nonlinear reactances," *Proceedings of the IRE* **47**, 2115 (1959).

[211] G. G. Gurzadian, V. G. Dmitriev and D. N. Nikogosian, "Handbook of Nonlinear Optics" (3rd ed), Vol. 64 in *Springer Series in Optical Sciences*, Springer-Verlag, Berlin (1999).

[212] A. V. Smith, W. J. Alford, T. D. Raymond and M. S. Bowers, "Comparison of a numerical model with measured performance of a seeded, nanosecond KTP optical parametric oscillator," *Journal of the Optical Society of America B* **12**, 2253–2267 (1995).

[213] N. P. Barnes, "Tunable mid-infrared sources using second-order nonlinearities," *International Journal of Nonlinear Optical Physics* **1**, 639–672 (1991).

[214] J. A. Giordmaine, "Mixing of light beams in crystals," *Physics Review Letters* **8**, 19–20 (1962).

[215] P. D. Maker, R. W. Terhune, M. Nicenoff and C. M. Savage, "Effects of dispersion and focusing on the production of optical harmonics," *Physics Review Letters* **8**, 21–22 (1962).

[216] D. A. Roberts, "Simplified characterization of uniaxial and biaxial nonlinear optical crystals: A plea for standardization of nomenclature and conventions," *IEEE Journal of Quantum Electronics* **28**, 2057–2074 (1992).

[217] P. Jain, "Noncollinear phase matching in a β-barium borate optical parametric oscillator," *University of Otago*, Dunedin, New Zealand, MSc Thesis, (2000).

[218] A. M. L. Oien, I. T. McKinnie, P. Jain, N. A. Russell, D. M. Warrington and L. A. W. Gloster, "Efficient, low-threshold collinear and noncollinear β-barium borate optical parametric oscillators," *Optics Letters* **22**, 859–861 (1997).

[219] J. M. Boon-Engering, W. E. van der Veer, E. A. J. M. Bente and W. Hogervorst, "Scanning and locking of a single longitudinal mode β-BaB_2O_4 OPO in a grazing incidence configuration," *Optics Communications* **136**, 261–266 (1997).

[220] G. Rosenman, K. Garb, A. Skliar, M. Oron, D. Eger and M. Katz, "Domain broadening in quasi-phase-matched nonlinear optical devices," *Applied Physics Letters* **73**, 865–867 (1998).

[221] T. Kartaloğlu, Z. G. Figen and O. Aytür, "Simultaneous phase matching of optical parametric oscillation and second-harmonic generation in aperiodically poled lithium niobate," *Journal of the Optical Society of America B* **20**, 343–350 (2003).

[222] D.-H. Lee, M. E. Klein, J.-P. Meyn, P. Groß, R. Wallenstein and K.-J. Boller, "Self-injection-locking of a CW-OPO by intracavity frequency-doubling the idler wave," *Optics Express* **5**, 114–119 (1999).

[223] P. Loza-Alvarez, D. T. Reid, P. Faller, M. Ebrahimzadeh and W. Sibbett, "Simultaneous second-harmonic generation and femtosecond-pulse compression in aperiodically poled $KTiOPO_4$ with a $RbTiOAsO_4$-based optical parametric oscillator," *Journal of the Optical Society of America B* **16**, 1553–1560 (1999).

[224] T. Beddard, M. Ebrahimzadeh, T. D. Reid and W. Sibbett, "Five-optical-cycle pulse generation in the mid infrared from an optical parametric oscillator based on aperiodically poled lithium niobate," *Optics Letters* **25**, 1052–1054 (2000).

[225] S. Guha, F.-J. Wu and J. Falk, "The effects of focusing on parametric oscillation," *IEEE Journal of Quantum Electronics* **QE-18**, 907–912 (1982).

[226] J. A. C. Terry, Y. Cui, Y. Yang, W. Sibbett and M. H. Dunn, "Low-threshold operation of an all-solid-state KTP optical parametric oscillator," *Journal of the Optical Society of America B* **11**, 758–769 (1994).

[227] G. W. Baxter, J. G. Haub and B. J. Orr, "Backconversion in a pulsed optical parametric oscillator: evidence from injection-seeded sidebands," *Journal of the Optical Society of America B* **14**, 2723–2730 (1997).

[228] G. Arisholm and K. Stenersen, "Optical parametric oscillator with non-ideal mirrors and single- and multi-mode pump beams," *Optics Express* **4**, 183–192 (1999).

[229] G. D. Boyd and D. A. Kleinman, "Parametric interaction of focused Gaussian light beams," *Journal of Applied Physics* **39**, 3597–3639 (1968).

[230] J. G. Haub, M. J. Johnson, A. J. Powell and B. J. Orr, "Bandwidth characteristics of a pulsed optical parametric oscillator: application to degenerate four-wave mixing spectroscopy," *Optics Letters* **20**, 1637–1639 (1995).

[231] M. Bass and E. W. Van Stryland, "Handbook of Optics II" (2nd ed), McGraw-Hill, New York (1994).

[232] J. D. Beasley, "Thermal conductivities of some novel nonlinear optical materials," *Applied Optics* **33**, 1000–1004 (1994).

[233] Y. Cui, M. H. Dunn, C. J. Norrie, W. Sibbett, B. D. Sinclair, Y. Tang and J. A. C. Terry, "All-solid-state optical parametric oscillator for the visible," *Optics Letters* **17**, 646–648 (1992).

[234] D. L. Fenimore, K. L. Schepler, D. Zelmon, S. Kück, U. B. Ramabadran, P. von Richter and D. Small, "Rubidium titanyl arsenate difference-frequency generation and validation of new Sellmeier coefficients," *Journal of the Optical Society of America B* **13**, 1935–1940 (1996).

[235] J. D. Bierlein and H. Vanherzeele, "Potassium titanyl phosphate: properties and new applications," *Journal of the Optical Society of America B* **6**, 622–633 (1989).

[236] I. Shoji, T. Kondo, A. Kitamoto, M. Shirane and R. Ito, "Absolute scale of second-order nonlinear-optical coefficients," *Journal of the Optical Society of America B* **14**, 2268–2294 (1997).

[237] L. K. Cheng, L. T. Cheng, J. Galperin, P. A. M. Hotsenpiller and J. D. Bierlein, "Crystal growth and characterization of $KTiOPO_4$ isomorphs from the self-fluxes," *Journal of Crystal Growth* **137**, 107–115 (1994).

[238] S. P. Velsko, M. Webb, L. Davis and C. Huang, "Phase-matched harmonic generation in lithium triborate (LBO)," *IEEE Journal of Quantum Electronics* **27**, 2182–2192 (1991).

[239] D. T. Reid, M. Ebrahimzadeh and W. Sibbett, "Design criteria and comparison of femtosecond optical parametric oscillators based on $KTiOPO_4$ and $RbTiOAsO_4$," *Journal of the Optical Society of America B* **12**, 2168–2179 (1995).

[240] G. J. Edwards and M. Lawrence, "A temperature-dependent dispersion equation for congruently grown lithium niobate," *Optical and Quantum Electronics* **16**, 373 (1984).

[241] S. Wang, V. Pasiskevicius, J. Hellström, F. Laurell and H. Karlsson, "First-order type II quasi-phase-matched UV generation in periodically poled KTP," *Optics Letters* **24**, 978–980 (1999).

[242] N. E. Yu, J. H. Ro, M. Cha, S. Kurimura and T. Taira, "Broadband quasi-phase-matched second-harmonic generation in MgO-doped periodically poled $LiNbO_3$ at the communications band," *Optics Letters* **27**, 1046–1048 (2002).

[243] M. Sato, T. Hatanaka, S. Izumi, T. Taniuchi and H. Ito, "Generation of 6.6-μm optical parametric oscillation with periodically poled $LiNbO_3$," *Applied Optics* **38**, 2560–2563 (1999).

[244] D. H. Jundt, M. M. Fejer and R. L. Byer, "Optical properties of lithium-rich lithium niobate fabricated by vapor transport equilibration," *IEEE Journal of Quantum Electronics* **26**, 135–138 (1990).

[245] L. Lefort, K. Puech, G. W. Ross, Y. P. Svirko and D. C. Hanna, "Optical parametric oscillation out to 6.3 μm in periodically poled lithium niobate under strong idler absorption," *Applied Physics Letters* **73**, 1610–1612 (1998).

[246] D. J. Gettemy, W. C. Harker, G. Lindholm and N. P. Barnes, "Some optical properties of KTP, $LiIO_3$ and $LiNbO_3$," *IEEE Journal of Quantum Electronics* **24**, 2231–2237 (1988).

[247] K. Kato, "Parametric oscillation at 3.2 μm in KTP pumped at 1.064 μm," *IEEE Journal of Quantum Electronics* **27**, 1137–1140 (1991).

[248] G. Hansson, H. Karlsson, S. Wang and F. Laurell, "Transmission measurements in KTP and isomorphic compounds," *Applied Optics* **39**, 5058–5069 (2000).

[249] J. C. Jacco and G. M. Loiacono, "Nature of the infrared spectrum in band-edge region of $KTiOPO_4$," *Applied Physics Letters* **58**, 560–561 (1991).

[250] K. Fradkin-Kashi, A. Arie, P. Urenski and G. Rosenman, "Characterization of optical and nonlinear properties of periodically-poled $RbTiOAsO_4$ in the mid-infrared range via difference-frequency generation," *Applied Physics B* **71**, 251–255 (2000).

[251] L. K. Cheng, L.-T. Cheng, J. D. Bierlein, F. C. Zumsteg and A. A. Ballman, "Properties of doped and undoped crystals of single domain $KTiOAsO_4$," *Applied Physics Letters* **62**, 346–348 (1993).

[252] B. Boulanger, J.-P. Fève, G. Marnier, B. Ménaert, X. Cabriol, P. Villeval and C. Bonnin, "Relative sign and absolute magnitude of $d^{(2)}$ nonlinear coefficients of KTP from second-harmonic-generation measurements," *Journal of the Optical Society of America B* **11**, 750–757 (1994).

[253] H. Vanherzeele and J. D. Bierlein, "Magnitude of the nonlinear optical coefficients of $KTiOPO_4$," *Optics Letters* **17**, 982–984 (1992).

[254] T. Y. Fan, C. E. Huang, B. Q. Hu, R. C. Eckardt, Y. X. Fan, R. L. Byer and R. S. Feigelson, "Second harmonic generation and accurate index of refraction measurements in flux-grown $KTiOPO_4$," *Applied Optics* **26**, 2390–2394 (1987).

[255] H. Liao, H. Y. Shen, Z. D. Zheng, T. Q. Lian, Y. P. Zhou, C. H. Huang, R. R. Zeng and G. F. Yu, "Accurate values for the index of refraction and the optimum phase match parameters in a flux grown $KTiOPO_4$ crystal," *Optics and Laser Technology* **20**, 103–104 (1988).

[256] K. Kato, "Second-harmonic and sum-frequency generation to 4950 and 4589 Åin KTP," *IEEE Journal of Quantum Electronics* **QE-24**, 3–4 (1988).

[257] D. W. Anthon and C. D. Crowder, "Wavelength dependent phase matching in KTP," *Applied Optics* **27**, 2650–2652 (1988).

[258] H. Vanherzeele, J. D. Bierlein and F. C. Zumsteg, "Index of refraction measurements and parametric generation in hydrothermally grown $KTiOPO_4$," *Applied Optics* **27**, 3314–3316 (1988).

[259] V. A. Dyakov, V. V. Krasnikov, V. I. Pryalkin, M. S. Pshenichnikov, T. B. Razumikhina, V. S. Solomatin and A. I. Kholodnykh, "Sellmeier equation and tuning characteristincs of KTP crystal frequency converters in the 0.4–4.0 μm range," *Soviet Journal of Quantum Electronics* **18**, 1059–1060 (1988).

[260] B. Boulanger, J.-P. Fève, G. Marnier, C. Bonnin, P. Villeval and J. J. Zondy, "Absolute measurement of quadratic nonlinearities from phase-matched second-harmonic generation in a single KTP crystal cut as a sphere," *Journal of the Optical Society of America B* **14**, 1380–1386 (1997).

[261] M. Katz, D. Eger, M. B. Oron and A. Hardy, "Refractive dispersion curve measurement of $KTiOPO_4$ using periodically segmented waveguides and periodically poled crystals," *Journal of Applied Physics* **90**, 53–58 (2001).

[262] K. Kato and E. Takaoka, "Sellmeier and thermo-optic dispersion formulas for KTP," *Applied Optics* **41**, 5040–5044 (2002).

[263] K. Kato, "Temperature insensitive SHG at 0.5321 μm in KTP," *IEEE Journal of Quantum Electronics* **28**, 1974–1976 (1992).

[264] W. Wiechmann, S. Kubota, T. Fukui and H. Masuda, "Refractive-index temperature derivatives of potassium titanyl phosphate," *Optics Letters* **18**, 1208–1210 (1993).

[265] B. Boulanger, I. Rousseau, J.-P. Fève, M. Maglione, B. Ménaert and G. Marnier, "Optical studies of laser-induced gray-tracking KTP," *IEEE Journal of Quantum Electronics* **35**, 281–286 (1999).

[266] B. Boulanger, J.-P. Fève and Y. Guillien, "Thermo-optical effect and saturation of nonlinear absorption induced by gray tracking in a 532-nm-pumped KTP optical parametric oscillator," *Optics Letters* **25**, 484–486 (2000).

[267] G. Hansson, H. Karlsson and F. Laurell, "Unstable resonator optical parametric oscillator based on quasi-phase-matched $RbTiOAsO_4$," *Applied Optics* **40**, 5446–5451 (2001).

[268] J.-P. Fève, B. Boulanger, O. Pacaud, I. Rousseau, B. Ménaert, G. Marnier, P. Villeval, C. Bonnin, G. M. Loiacono and D. N. Loiacono, "Phase-matching measurements and Sellmeier equations over the complete transparence range of $KTiOAsO_4$, $RbTiOAsO_4$, and $CsTiOAsO_4$," *Journal of the Optical Society of America B* **17**, 775–780 (2000).

[269] G. R. Morrison, M. Ebrahimzadeh, C. F. Rae and M. H. Dunn, "Diode-pumped, *Q*-switched, 1.321 μm Nd:YLF laser and its frequency doubling," *Optics Communications* **118**, 55–60 (1995).

[270] H. Schnitzler, U. Fröhlich, T. K. W. Boley, A. E. M. Clemen, J. Mlynek, A. Peters and S. Schiller, "All-solid-state tunable continuous-wave ultraviolet source with high spectral purity and frequency stability," *Applied Optics* **41**, 7000–7005 (2002).

[271] H. Mao, B. Wu, C. Chen, D. Zhang and P. Wang, "Broadband optical parametric amplification in LiB_3O_5," *Applied Physics Letters* **62**, 1866–1868 (1993).

[272] G. Robertson, M. J. Padgett and M. H. Dunn, "Continuous-wave singly resonant pump-enhanced type II LiB_3O_5 optical parametric oscillator," *Optics Letters* **19**, 1735–1737 (1994).

[273] K. Kato, "Tunable UV generation to 0.2325 μm in LiB_3O_5," *IEEE Journal of Quantum Electronics* **26**, 1173–1175 (1990).

[274] Y. Kong, Z. Xu, Y. Zhou, D. Deng, X.-A. Zhu and L.-A. Wu, "The compound cavity optical parametric oscillator: Theory and experiment," *IEEE Journal of Quantum Electronics* **34**, 439–446 (1998).

[275] M. Ebrahimzadeh, A. J. Henderson and M. H. Dunn, "An excimer-pumped β-BaB_2O_4 optical parametric oscillator tunable from 354 nm to 2.370 μm," *IEEE Journal of Quantum Electronics* **26**, 1241–1252 (1990).

[276] J. Pinard and J. F. Young, "Interferometric stabilisation of an optical parametric oscillator," *Optics Communications* **4**, 425–427 (1972).

[277] T. K. Minton, S. A. Reid, H. L. Kim and J. D. McDonald, "A scaning, single mode, $LiNbO_3$, optical parametric oscillator," *Optics Communications* **69**, 289–293 (1989).

[278] K. Puech, L. Lefort and D. C. Hanna, "Broad tuning around degeneracy in a singly resonant synchronously pumped parametric oscillator by means of a diffraction grating," *Journal of the Optical Society of America B* **16**, 1533–1538 (1999).

[279] W. R. Bosenberg, W. S. Pelouch and C. L. Tang, "High-efficiency and narrow-linewidth operation of a two-crystal β-BaB_2O_4 optical parametric oscillator," *Applied Physics Letters* **55**, 1952–1954 (1989).

[280] C. Palmer, "Diffraction Grating Handbook" (4th ed), Richardson Grating Laboratory, New York (2000).

[281] K. Liu and M. G. Littman, "Novel geometry for single mode scanning of tunable lasers," *Optics Letters* **6**, 117–119 (1981).

[282] T. D. Raymond, P. Esherick and A. V. Smith, "Widely tunable single-longitudinal-mode pulsed dye laser," *Optics Letters* **14**, 1116–1118 (1989).

[283] S. T. Yang and S. P. Velsko, "Frequency-agile kilohertz repetition-rate optical parametric oscillator based on periodically poled lithium niobate," *Optics Letters* **24**, 133–135 (1999).

[284] T. J. Kane, A. C. Nilsson and R. L. Byer, "Frequency stability and offset locking of a laser-diode-pumped Nd:YAG monolithic nonplanar ring oscillator," *Optics Letters* **12**, 175–177 (1987).

[285] P. Schlup, S. D. Butterworth and I. T. McKinnie, "Efficient single-frequency pulsed periodically poled lithium niobate optical parametric oscillator," *Optics Communications* **154**, 191–195 (1998).

[286] S. Wu, V. A. Kapinus and G. A. Blake, "A nanosecond optical parametric generator / amplifier seeded by an external cavity diode laser," *Optics Communications* **159**, 74–79 (1999).

[287] P. E. Powers, K. W. Aniolek, T. J. Kulp, B. A. Richman and S. E. Bisson, "Periodically poled lithium niobate optical parametric amplifier seeded with the narrowband filtered output of an optical parametric generator," *Optics Letters* **23**, 1886–1888 (1998).

[288] Y. Lu, J. Zheng, Y. Lu, N. Ming and Z. Xu, "Frequency tuning of optical parametric generator in poled optical superlattice $LiNbO_3$ by electro-optic effect," *Applied Physics Letters* **74**, 123–125 (1999).

[289] S. Haidar, T. Usami and H. Ito, "Nd:YAG-pumped periodically poled $LiNbO_3$ optical parametric generator seeded with the narrowband output of a 532-nm pumped optical parametric generator," *Applied Optics* **41**, 5656–5659 (2002).

[290] S. Schiller and R. L. Byer, "Quadruply-resonant optical parametric oscillation in a monolithic total-internal-reflection resonator ," *Journal of the Optical Society of America B* **10**, 1696 (1993).

[291] M. Vaidyanathan, R. C. Eckardt, V. Dominic, L. E. Myers and T. P. Grayson, "Cascaded optical parametric oscillations," *Optics Express* **1**, 49–53 (1997).

[292] P. Schlup, I. T. McKinnie and S. D. Butterworth, "Single-mode, singly resonant, pulsed periodically poled lithium niobate optical parametric oscillator," *Applied Optics* **38**, 7398–7401 (1999).

[293] P. Schlup, G. W. Baxter and I. T. McKinnie, "Single-mode near- and mid-infrared periodically poled lithium niobate optical parametric oscillator," *Optics Communications* **176**, 267–271 (2000).

[294] J. Hellström, "Nanosecond optical parametric oscillators and amplifiers based on periodically poled $KTiOPO_4$," *Royal Institute of Technology*, Stockholm, Sweden, PhD Thesis, (2001).

[295] R. G. Batchko, D. R. Weise, T. Plettner, G. D. Miller, M. M. Fejer and R. L. Byer, "Continuous-wave 532-nm-pumped singly resonant optical parametric oscillator based on periodically poled lithium niobate," *Optics Letters* **23**, 168–170 (1998).

[296] P. Schlup, G. W. Baxter and I. T. McKinnie, "Single-mode visible and mid-infrared periodically poled lithium niobate OPO amplified in perylene red doped poly(methyl methacrylate)," *Optics Communications* **184**, 225–230 (2000).

[297] G. W. Baxter, P. Schlup and I. T. McKinnie, "Efficient, single-frequency, high repetition rate, PPLN OPO pumped by a prelase *Q*-switched diode-pumped Nd:YAG laser," *Applied Physics B* **70**, 301–304 (2000).

[298] G. Cerullo, S. de Silvestri and V. Magni, "High efficiency, 40 W cw Nd:YLF laser with large TEM_{00} mode," *Optics Communications* **93**, 77–81 (1992).

[299] J. K. Jabczyński, "Investigations of thermal aberrations in Nd:YAG laser end-pumped by 10 W fiber coupled diode bar," *Optica Applicata* **26**, 151–158 (1996).

[300] I. Paiss, A. Englander and R. Lavi, "Efficient, mid-IR long pulse generation with an intra-cavity PPLN OPO," *OSA Trends in Optics and Photonics, Advanced Solid State Lasers* (Optical Society of America, Washington, DC) **19**, 253–255 (1998).

[301] D. W. Anthon, D. L. Sipes, T. J. Pier and M. R. Ressl, "Intracavity doubling of cw diode-pumped Nd:YAG lasers with KTP," *IEEE Journal of Quantum Electronics* **28**, 1148–1157 (1992).

[302] D. C. Hanna, C. G. Sawyers and M. A. Yuratrich, "Telescopic resonators for large-volume TEM_{00}-mode operation," *Optical and Quantum Electronics* **13**, 493–507 (1981).

[303] D. C. Hanna, C. G. Sawyers and M. A. Yuratrich, "Large volume TEM_{00} mode operation of Nd:YAG lasers," *Optics Communications* **37**, 359–362 (1981).

Acknowledgements

Physics Crew

University of Otago, Dunedin, New Zealand
BSc (Hons) 1994–1997, PhD 1998–2003

Supervision, Encouragement, and Support
Iain McKinnie

The Art of Play, Laboratory Help, Proofreading
and Letting Me Land the Model Plane Once Before the Crash
Glenn Baxter

Additional Supervision, Thesis Corrections
Don Warrington

Post-Doctoral Support and Simple Explanations of Complicated Things	William Wadsworth Stuart Butterworth
Workshop Wizard	Peter Stroud
Secretarial Stuff	Helen Wreford Trish Knox Brenda Tustin Margaret Sykes
Motorcycles, ze-Bang-Bangs, DVDs	Chris Rawle
LaTeX Support Dudes	Jan Diettrich Nick Thomas
SSD Discussions, Aloha Connection	Maile Giffin
Fellow Student Support	Richard White Chris Lee

Workshop

David Hardisty	Dale Watts
Myles Thayer	Barbara Buchanan
Peter Simpson	Robin Gledhill
Solid State Dye Sample	Industrial Research Ltd

Sweden Crew
Kongl Tekniska Högskolan, Stockholm, Sweden
PPKTP Collaboration—Visit March 2000

Poling of PPKTP Crystal	Jonas Hellström
Collaboration and Hospitality	Fredrik Laurell Håkan Karlsson

Australia Crew

Macquarie University, Sydney, NSW, Australia
Research Visit September 2000–December 2000

Supervision and Arrangement	Brian Orr
Locating Lab Equipment, Table Tennis	Yabai He
Laser Tech Support Dude	Matt Johnson
Cafe 142, Sydney Transport Advice	Richard Shorten
Flatting and Food Tips	Therese Photios David Photios

SCOTLAND CREW

UNIVERSITY OF ST ANDREWS, ST ANDREWS, FIFE, SCOTLAND
WORSFOLD SCHOLARSHIP JANUARY 2001–JULY 2001

SUPERVISION AND ARRANGEMENT	MALCOLM DUNN
ALL STYLE	DAVE STOTHARD
MOST SOCIAL BUNCH OF PHYSICISTS	ALISON CARLETON IAN LINDSAY TOM EDWARDS COSTAS PETRIDIS
SUSHI, COASTAL BOULDERING IN SLEET	DUSTY SPATES
DREAMS OF "DREARY END"	THELMA MITCHELL

DEANS COURT

MARIE-CARMEN NEIPP LOPEZ	KATRINE KRAUSE-JENSEN
MARK CLIFFORD	SEAN ODENEAL
JUSTIN LAWRENCE	

SHOWTIME	CAST, CREW, BAND "COMPANY"

AMERICA CREW

COHERENT TECHNOLOGIES INC, LAFAYETTE, COLORADO, USA
RESEARCH VISIT OCTOBER 2001–DECEMBER 2002

SUPERVISION AND ARRANGEMENT	IAIN MCKINNIE SAMMY HENDERSON TIM CARRIG
FOOD, FUN, FRIENDSHIP	SCOTT CHRISTENSEN JESSICA FRANZ-CHRISTENSEN
HOSPITALITY MADISON STEAMBOAT SPRINGS	JULIE AND JOHN FRANZ DIANNE AND LAU CHRISTENSEN
POLISHIN' TURDS	JOHN KOROSHETZ
LASER MODEL GURU	SEPP UNTERNAHRER
ONE OF GOD'S BETTER PEOPLE...	JENNY KEENE
FOUNDING MEMBER, PALS SOCIETY	SARAH THOMPSON
MATLAB GEEK	SARA TUCKER

LAB JOCKS

MARK KUKLA	ERIC SCHNEIDER
AMY SULLIVAN	GREG WAGNER
DOUG GWIN	

SPECIAL THANKS	ANNE HICKLAND
KIWI ACCENTS AND PAVLOVA	ROBYN MILNE JANE CROSBIE

Real Life Crew

For Everything
Mum, Dad, Esthi, Tiwa, Tiwa (ii), Trini, and All the Family

Winning at Pool, D&D, Bowling, and Proofing Materials Properties
Andrew Tagg

On-Line / General Support and Yummy Food
Aynia Noever

International Support	Kate Paulin
Wild Side of Life	Cameron Wilkie
Missing that Hermitian Conjugate	Dougal McQueen
Rides Home after Band	Johanna Brusse
Amiga, Young Ones and Red Dwarf Nostalgia	Chris Edwards

Thanks To

Nicola Gibson	Rebecca Emslie
Hayley Meiklejohn	Kathryn McAuley
Amy Hammond	Marion de Lambert
Carol Foote	Llew Samuel
Applied Physics (With Wings)	Dion Buchanan
	John Penno
	Jenny Quelch

Production

Word Processing	Microsoft Word 97 / XP
Typesetting	LaTeX v3.14159 (MiKTeX 1.20e) Palatino 11 / 10 pt
Graphics	Matlab 5.1 / 5.2 (PostScript)
Diagrams	Microsoft PowerPoint 97 / XP CorelDRAW 7.0
References	Microsoft Excel / VBA 6.3 DOS / QuickBASIC 4.5
Hardware	AcerNote Light Compaq Presario 2702TW

*inclusion of company or institutional logo does not imply endorsement for this work trademarks and registered trademarks are properties of their resective owners

Reasons for 64/32 Restrictions, No. 3:

System DLLs such as Kernel32.dll, User32.dll, and Gdi32.dll expect only one instance per process, either 32-bit or 64-bit. For example, User32.dll stores a pointer to an array of function pointers into the PEB at startup, and those functions are called through user mode APCs initiated by Win32k.sys. If a process contained two copies of User32.dll, Win32k.sys would not be able to decide which one to call. The WOW64 emulator stores its own table of function pointers in the PEB64, which thunk the parameters then make calls through the 32-bit function pointer table in the PEB32, so Win32k.sys does not have to disambiguate whether the window is 32-bit or 64-bit.

($\mathcal{G}$) 20563.200302142307M